



HAL
open science

Marine ageing and fatigue of carbon/epoxy composite propeller blades

Antoine Le Guen-Geffroy

► **To cite this version:**

Antoine Le Guen-Geffroy. Marine ageing and fatigue of carbon/epoxy composite propeller blades. Mechanical engineering [physics.class-ph]. Université de Bretagne occidentale - Brest, 2019. English. NNT : 2019BRES0104 . tel-02612622v2

HAL Id: tel-02612622

<https://theses.hal.science/tel-02612622v2>

Submitted on 20 May 2020

HAL is a multi-disciplinary open access archive for the deposit and dissemination of scientific research documents, whether they are published or not. The documents may come from teaching and research institutions in France or abroad, or from public or private research centers.

L'archive ouverte pluridisciplinaire **HAL**, est destinée au dépôt et à la diffusion de documents scientifiques de niveau recherche, publiés ou non, émanant des établissements d'enseignement et de recherche français ou étrangers, des laboratoires publics ou privés.

THESE DE DOCTORAT DE

L'UNIVERSITE
DE BRETAGNE OCCIDENTALE
COMUE UNIVERSITE BRETAGNE LOIRE

ECOLE DOCTORALE N° 598

Sciences de la Mer et du littoral

Spécialité : Mécanique, génie mécanique, mécanique des fluides et
énergétique

Par

Antoine LE GUEN-GEFFROY

Marine ageing and fatigue of carbon/epoxy composite propeller blades

Thèse présentée et soutenue à Plouzané, le 19/12/2019

Unité de recherche : Laboratoire de Comportement des Structures en Mer, Unité RDT, Ifremer

Rapporteurs avant soutenance :

Christian BERGGREEN
Christian HOCHARD

Associate professor, Technical University of Denmark
Professeur des Universités, HDR, Université Aix Marseille

Composition du Jury :

Christophe BALEY
Christian BERGGREEN
Christian HOCHARD
Lenaïk BELEC
Thomas BONNEMAINS
Peter DAVIES

Professeur des universités, IRDL
Associate professor, Technical University of Denmark
Professeur des Universités, HDR, Université Aix Marseille
Maitre de conférence, Université de Toulon
Maitre de conférence, UBO
Chercheur, HDR, IFREMER

Président

Directeur de thèse

Invité(s)

Bertrand HABERT
Pierre-Yves LE GAC

Direction Générale de l'Armement
Ingénieur de recherche, IFREMER

Tuteur DGA
Co-encadrant de thèse

Marine ageing and fatigue of carbon/epoxy composite propeller blades

Vieillessement en milieu marin et fatigue des pales d'hélices en composite carbone/époxy

Antoine LE GUEN-GEFFROY

March 11, 2020

Abstracts

English abstract

The current document presents the long term seawater ageing effect on the fatigue properties of carbon fibre reinforced epoxy marine propeller blades. Seawater uptake in the resin and the composite was identified to correspond to a Fickian diffusion. Calculations of the mass to saturation of the composite based on that of the resin reveal the presence of water in the composite's porosities.

Accelerated ageing of the pure resin highlighted three ageing phenomena: oxidation, plasticization and physical ageing. The last two were mechanically characterised separately and coupled with one another. Above all, it was shown that the presence of seawater accelerated the physical ageing kinetics by reducing the relaxation time.

The composite was studied under different quasistatic and cyclic loadings. Few effects of seawater have been found for tensile stresses on fibre oriented loadings. This was not the case for transversely loaded composite that showed non-negligible decrease of the mechanical properties for both static and fatigue loadings. This was also the case for flexure loading which was studied under four-point flexure. This latter test method was particularly studied due to the particular induced damage.

The composite was studied under two delamination loadings: crack opening and in-plane shear. It was observed that seawater decreased the critical strain energy release rates for both load cases as well as the fatigue resistance of both crack modes.

Finally, the effect of physical ageing on the composite was studied and found to be non-negligible, demonstrating the necessity of taking it into account for both ageing and mechanical design.

Résumé en Français

Les travaux présentés dans ce document portent sur l'étude du vieillissement en milieu marin d'un composite carbone époxy pour applications pales d'hélice de navires. La caractérisation de la prise en eau dans la résine pure et le composite a montré un comportement Fickien. La présence d'eau dans les porosités du composite a également été mise en évidence analytiquement.

Le vieillissement accéléré de la résine a mis en évidence trois phénomènes : l'oxydation, le vieillissement physique et la plastification. L'effet mécanique des ces deux derniers a été particulièrement étudié. La présence d'eau et donc d'une résine plastifiée a eu l'effet d'accélérer le vieillissement physique.

L'effet du vieillissement accéléré sur le composite a ensuite été étudié sous différentes sollicitations quasi-statiques et de fatigue. Peu d'effets de l'eau ont été relevés pour les sollicitations de traction sur des orientations sens fibres. Cependant, des pertes plus importantes des propriétés mécaniques ont été observées en traction sens transverse aussi bien en statique que en fatigue. Ces mêmes résultats ont été trouvés sous sollicitations de flexion grâce à l'essai de flexion quatre points. Ce dernier a été discuté du fait de l'endommagement qu'il provoque.

Enfin, le composite a été étudié sous sollicitations de délaminage suivant deux modes de fissuration : ouverture et cisaillement dans le plan. La présence d'eau a eu pour effet de diminuer l'énergie de fissuration dans les deux modes. Ce même résultat a été trouvé sous chargement de fatigue.

L'influence du vieillissement physique sur les propriétés mécaniques du composite a également été démontré, son effet étant négatif, il nécessite d'être pris en compte.

Remerciements

S'il y a bien une chose à laquelle j'ai du mal à m'atteler, ce sont les remerciements. J'ai tellement peur de ne pas réussir à retranscrire ma gratitude envers toutes les personnes qui ont fait de cette thèse ce qu'elle a été, que les mots me sont difficiles à formuler. Je me lance.

And I would like to start by the main person behind this whole PhD thesis, Peter Davies. Peter have been a real guide for me from the very beggining untill the last days of this PhD thesis (and beyond) in terms of technical, scientific and professional aspects. Thank you for everything, you are a real legend for all you gave me. Ensuite je voudrais remercier Pierre-Yves Le Gac sans qui cette thèse n'aurait pas le même visage et moi non plus. Puis Bertrand Habert qui a su suivre et alimenter cette thèse, m'ouvrir certaines portes et a toujours eu un regard et un avis pertinent sur ce travail. Je voudrais vous remercier tous les trois pour la confiance que vous m'avez donné dans la réalisation de ce travail.

Il n'y aurait aujourd'hui pas de publication de ce travail sans l'amont des examinateurs qui ont validé cette thèse. Tout d'abord je voudrais remercier mes deux rapporteurs, fait non voulus, ce sont tous les deux des Christian. I would like to first thank Christian Berggreen for his time, his precious reviewing and relevant questions and remarks, I was very honoured and thankfull having you. Je remercie également Christian Hochard d'avoir accepté d'être rapporteur de cette thèse et ainsi m'accorder tout ce temps d'évaluation. Ensuite je voudrais remercier Christophe Baley d'avoir accepté, tout d'abord, de prendre les reines de la soutenance et de la présider d'une façon bienveillante, mais également de m'avoir suivi tout au long de la thèse. Merci enfin à Lenaïk Belec ainsi que Thomas Bonnemains pour leur temps, leurs remarques et leur intéressement dans ce travail. Merci à vous tous.

Nombreux sont ceux qui ont contribué à cette thèse. Je pense particulièrement à Maelenn et Maël qui ont toujours su se rendre disponibles et que je remercie beaucoup pour leur temps et leurs précieux conseils. Je pense également aux techniciens du laboratoire LCSM: Nicolas Lacotte, Mickael Premel Cabic et Luc Riou qui ont tous les trois apporté beaucoup. Je voudrais remercier Nicolas Gayet qui a également réalisé l'ensemble des prises de vue au MEB de l'Ifremer.

Trois ans de thèse c'est aussi l'occasion de collaborer et rencontrer des personnes de différents horizons. Je pense d'abord à Malick Diakhate qui a réalisé le traitement des

données d'émission acoustique et avec qui j'ai apprécié échanger et collaborer. Je pense aux personnes faisant parti du projet FabHéli (dont vous découvrirez les détails plus loin dans le document) avec qui j'ai pu échanger. Je pense également à Anthony Foulon travaillant chez Mistras, toujours disponible et d'une grande aide. Je remercie également M. Jean-Pierre Gros de chez Sicomin pour sa disponibilité, et les précieuses informations dont il a su me faire part.

Maintenant, je voudrais faire un clin d'œil à l'ensemble des personnes du bâtiment Coriolis (LCSM et LDCM), particulièrement ceux qui m'ont supporté dans le bureau, je pense surtout à Tatianna avec qui j'ai fait un bon bout de chemin et que j'ai vu terminer sa thèse. J'ai du mal à hiérarchiser tout ça donc je vais d'abord vous remercier tous, que ce soit pour votre aide scientifique et technique mais aussi pour votre soutien durant ces trois ans. Je souhaite bon courage à Olivier pour la suite de son projet. Benoit, j'espère qu'on se croiera en Y à l'avenir. Nolwenn et Justine, vous êtes formidables, merci pour tout. Bon courage à Morgan pour la suite. Christophe, Pierre-Yves, Arnaud merci pour votre disponibilité et votre aide. J'ai aussi une grosse pensée pour tous les thésards Ifremer et pas Ifremer, passés et futurs (Corentin, Alin, Morgane, Antoine, Cédric, Yoan, Quentin, Romain, Gauthier, Alban).

Aussi, je n'aurais pas tenu ces trois ans sans mon entourage. Je ne compte pas les soirées à bière et malt avec Paul, Roxane, Jo et François. J'ai une grosse pensée aussi pour tous mes amis d'enfance de Saint Malo qui m'ont dit être fiers de moi. Les gars, je suis tout aussi fier de ce que vous êtes devenus et de ce que vous avez accompli.

Le plus facile est de remercier ma famille. En effet, je ne pense pas qu'il y ai besoin d'expliquer en quoi vous êtes tous aussi importants pour moi. Je pense que vous en êtes conscient de vous même. Malgré tout, il y a quelqu'un qui m'a soutenu à la fois dans les bons et les mauvais moment, à qui j'ai raconté les réussites et les échecs de ce travail et qui a toujours su me soutenir particulièrement sur la fin de ces trois ans, ma chérie: Anaïs. Tu m'as été si précieuse. Faire tout ça sans toi n'aurait pas été la même histoire.

Objet de restitution de ces travaux, je te laisse maintenant, lecteur, à ta lecture.

À mon père.

Contents

Abstracts	iii
Remerciements	vii
Detailed summary	xiii
Introduction	1
Context of the study	1
Climate change	1
Marine propellers	3
Marine renewable energies	5
1 State of the art	9
1.1 Composite materials used in the marine domain	9
1.1.1 Fibre reinforcements	9
1.1.2 Polymer matrices	10
1.1.3 Manufacturing processes for composite fabrication	11
1.2 Ageing of carbon fibre reinforced epoxy	13
1.2.1 Seawater and polymer composites	13
1.2.2 Physical ageing of epoxy	16
1.3 Fatigue of fibre reinforced composites	17
1.3.1 Fatigue of composites, the effect of seawater	17
1.3.2 Statistical analysis and models	21
1.3.3 Delamination fatigue	24
1.4 Conclusions	29
2 Materials and methods	31
2.1 Materials	31
2.1.1 Resin	31
2.1.2 Composites	35
2.1.3 Sizing	37
2.2 Test methods	37

2.2.1	Ageing methods	37
2.2.2	Tests on the materials	38
3	Water diffusion	51
3.1	Resin	51
3.2	Composite	56
3.3	Prediction for a real blade structure	62
3.4	Conclusion	66
4	Accelerated ageing of the resin	69
4.1	Plasticization and physical ageing	69
4.1.1	Ageing mechanisms in the resin	69
4.1.2	Kinetics of physical ageing on the resin	71
4.1.3	Plasticization of the resin	84
4.2	Effect of physical ageing on composite	89
4.2.1	Effect of physical ageing on the composite transverse tensile properties	90
4.2.2	Evaluation of the influence of physical ageing on interlaminar shear strength	90
4.3	Conclusion	91
5	Seawater ageing of composite materials	93
5.1	Load cases for propeller blades	93
5.2	Tensile loading	97
5.2.1	Effect of seawater	97
5.3	Cyclic four point flexure loading	109
5.3.1	Effect of load frequency	109
5.3.2	Effect of long-term seawater ageing	113
5.4	Conclusion	134
6	Composite under delamination loading	137
6.1	Seawater ageing under mode I	137
6.1.1	Quasistatic loading	137
6.1.2	Fatigue loading	140
6.2	Seawater ageing under mode II	143
6.2.1	Quasistatic loading	143
6.2.2	Fatigue loading	147
6.3	Effect of physical ageing	150
6.3.1	Mode I	150
6.3.2	Mode II	152
6.4	Discussion	157
6.5	Conclusion	162
	Conclusion	165

A	Extended French abstract	171
A.1	Introduction	171
A.2	Prise en eau dans le résine et le composite	174
A.3	Plastification et vieillissement physique sur la résine pure	178
A.4	Vieillissement à long terme du composite	181
A.5	Composite sous chargement critique : délaminage	184
A.6	Perspectives	187
A.6.1	Méthodes et essais expérimentaux	187
A.6.2	Matériaux	189
A.6.3	Aspect vieillissement	190
B	Identification procedures using scilab code	193
C	Data processing using R	201
D	Water uptake of the infused composite	207
E	Crack gauges	211
F	Schematic drawings of the immersed fatigue fixtures	217
	List of figures	225
	List of tables	227
	List of acronyms	230
	Tabular abstract of experiments	231
	Bibliography	248

General Introduction

The main objective of this thesis is to investigate the effect of long-term exposure to seawater on the mechanical properties of a carbon fibre reinforced polymer under static and cyclic loads, in order to assist the development of marine structures. This introduction will first present the context of the thesis, and describe the applications considered.

Context of the study

Climate change

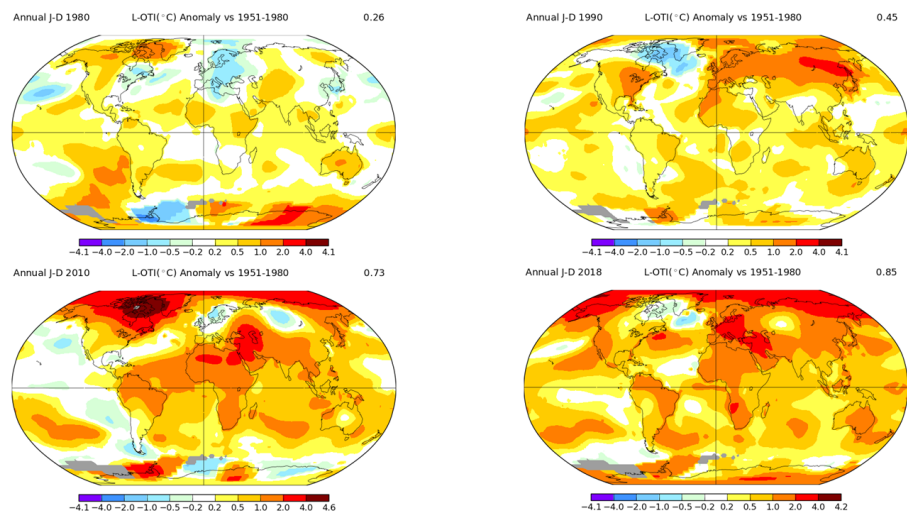


Figure 1 – Global mean temperature anomaly in 1980, 1990, 2010 and 2018. Reference temperature is taken from 1951 to 1980 [1,2]

The impact of human beings on the environment has accelerated during the last decades. The main criterion used to assess this today is temperature increase, see Figure 1. The reason for the temperature to increase can be directly linked to the greenhouse gas levels as shown in Figure 2 from the Climate change synthesis report of 2014 [3]. However, due to industrial development and population increase, the production of greenhouse gases

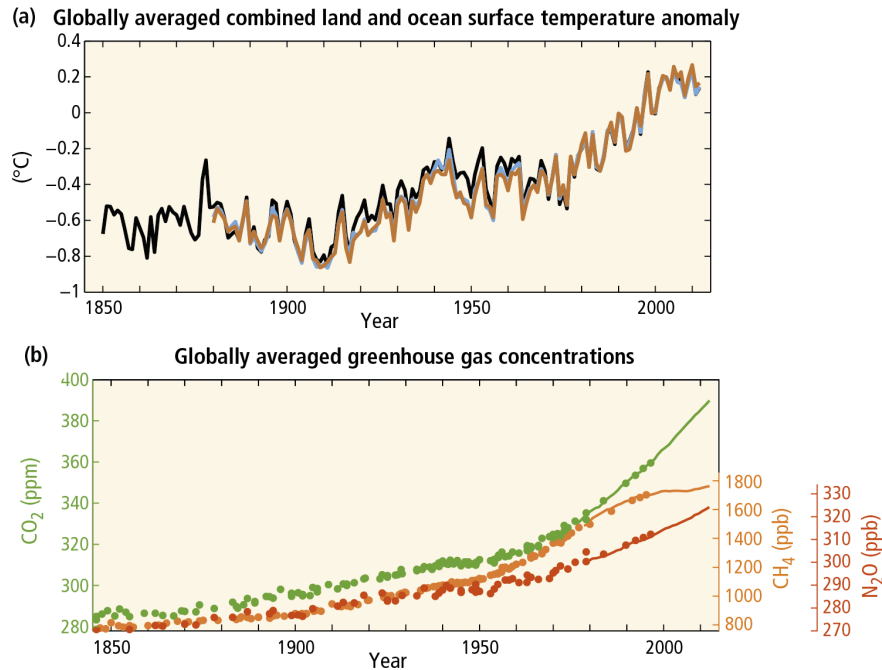


Figure 2 – Increase of global temperature (a) and greenhouse gas concentrations (b) [3]

has reach such levels that the temperature increase is becoming critical.

In order to reduce this trend, an increasing number of policies are aimed at limiting the carbon dioxide emissions and some governments have signed agreements to this effect. Possible solutions to reduce the greenhouse gases production include reduction of urban energy consumption, the development of non-emitting energies (mainly pushed by renewable energies), low emitting transports and even low emitting agricultural techniques.

In this way, the main trend in the transport industry is to reduce the fuel consumption, as has been done in the car industry for several decades, pushed by the European Union emission standards for example. For the marine transport industry, the goal is the same. One way to improve motor boat efficiency is to work on propeller design, and the replacement of metal blades by composites is part of this approach. This allows weight reduction, but in addition, an increase in engine efficiency is expected thanks to the unique properties of composite materials compared to their metallic equivalents. The ways to improve boat efficiency thanks to composite propeller design will be discussed in the next chapter.

Energy production is also a sector that produces many greenhouse gases. In this domain though, there is considerable effort towards trying to produce renewable energies. These energies rely on converting renewable resources such as wind, solar power, thermal or, mostly of interest here, marine power. For wind power, the best-known technology is wind turbines, which convert the kinetic energy of wind into electrical energy using a generator activated by rotor blades that can reach over 100m in diameter.

Marine propellers

The first official in-service marine propeller is often attributed to the screw propeller fitted on the SS Archimedes, a 237 registered tonnage vessel. Before this, other engineers and scientists had proposed concepts for different propeller technologies as reported in [4, 5]. Initially, the patent for a propeller, obtained by English inventor Francis Pettit Smith in 1836, consisted of a one-turn screw with only one thread made out of wood, Figure 3. Smith started with a prototype of a two-turn screw, but, following an incident in February 1837, half of the two-turn screw broke off. This resulted in a positive result as it increased the boat's speed. Later, the patent was modified and the one-turn screw was cut once again in half but with the addition of another thread. This is the first appearance of what will be referred to later as propeller blades [4].

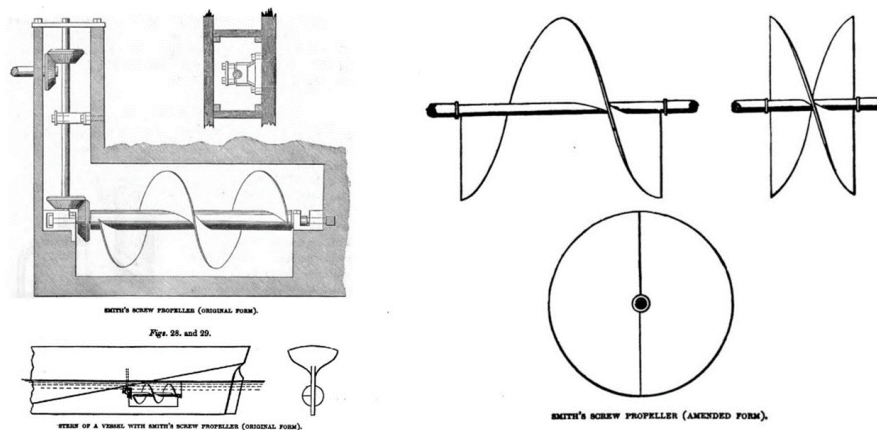


Figure 3 – Francis Pettit Smith first (left) and amended (right) patent for the first marine screw propeller, taken from [4]

Since then, propellers have improved significantly. The fourth edition of the Marine Propellers and propulsion book by John Carlton [5] compiles the knowledge in this domain up to 2019. The main advances were made in the design of the blades, which increased propulsion efficiency. Advances in materials also play a role in the durability of such mechanical parts. Figure 4 shows the main options for fabrication of propellers. It can be noted that among the 14 different options presented on this figure, 12 are metal based. In fact, even today, the marine propeller domain is dominated by metallic materials.

Besides having advantages, such as good mechanical properties or excellent biofouling resistance, the metallic propellers have many disadvantages. One of the main problems encountered with metallic propellers is corrosion, often limited by using anodes on the boat's hull or by optimizing alloy composition.

Metal propellers also have the disadvantage of high manufacturing costs. This is especially true for large-scale propellers for container, long course transport or military boats, which have propellers of large diameters. Each propeller has a different design, so the manufacturing process is not scalable to high production rates. Manufacturers usually

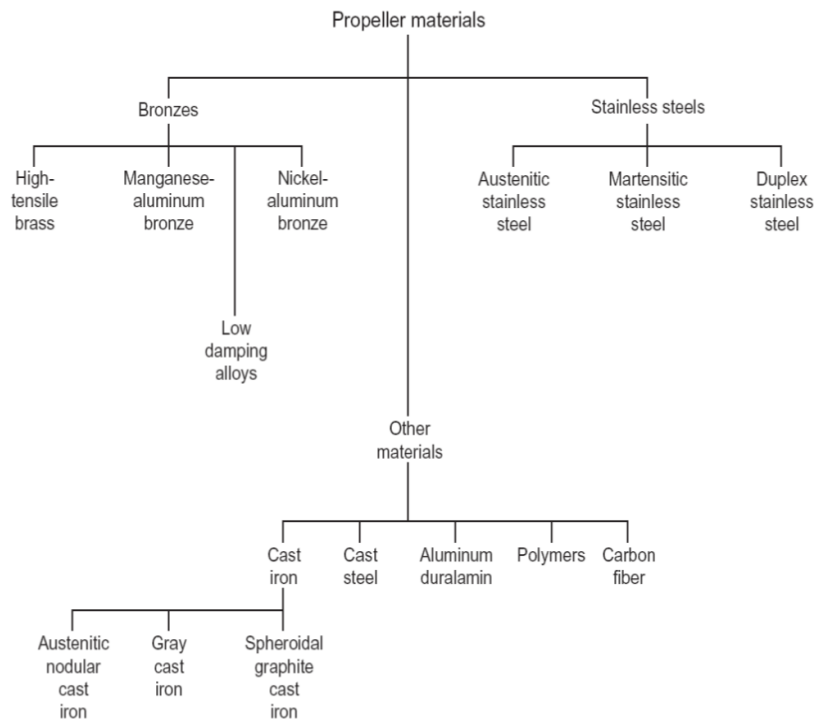


Figure 4 – The different materials used to fabricate marine propellers from [5]

produce one silica sand mould in order to manufacture one propeller. After casting and demoulding, the quality standards require adjusting of the outer surface. Dimensions are measured and the surface is milled to the design size. These manufacturing steps make the propeller a high cost element of the final boat price.

Marine propellers also encounter cavitation erosion. Cavitation results from the low pressure zones and high velocity created by the foil design of the propellers. This turns water from liquid to a gaseous state. Figure 5 shows cavitation occurring on a metallic propeller tested in a cavitation tank, described by Asnaghi et al. in [6]. The implosion of cavitation bubbles creates shock-waves that little by little erode the propeller surface leading to major damage.

Composite materials such as carbon fibre reinforced polymers (CFRP) have been studied in recent years in order to find solutions to the previously cited drawbacks of metallic propellers. The integration of composite materials in marine propellers applies mainly to the blades. In fact, most of the proposed manufacturing concepts rely on the use of composite propeller blades fixed to a metallic hub linked to the propulsion-shaft. With this manufacturing solution in mind, the cost of such propellers should decrease, as the same blade geometry is replicated to fabricate each propeller. The maintenance cost would also be minimized in theory, as a failure of one blade would mean that only one blade would need to be replaced. In the case of metallic propellers, a blade failure could mean that the entire propeller needs to be changed if no repair is possible. Another advantage of composite propellers is their resistance to corrosion. This should be a major advantage

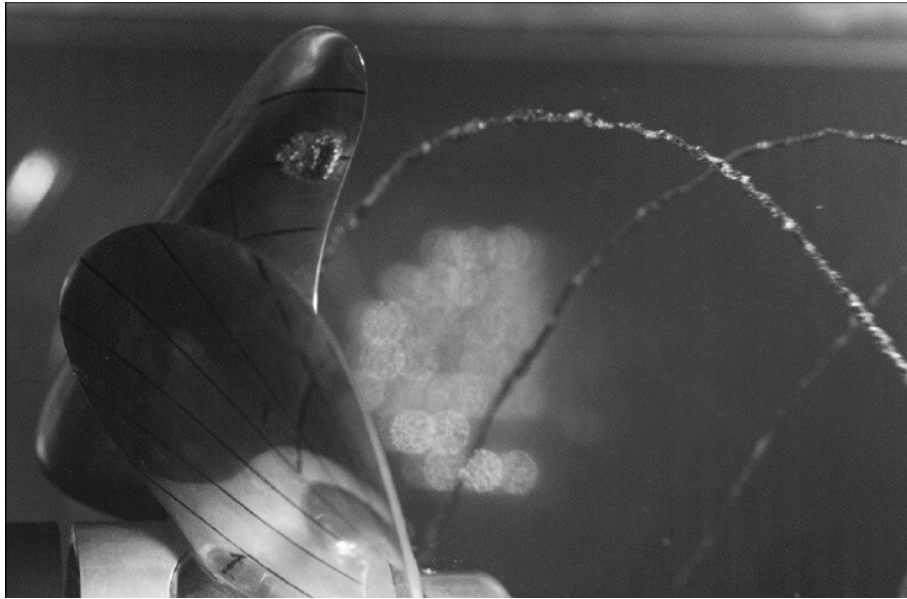


Figure 5 – Example of tip and surface cavitation from [6]

compared to their metallic equivalents. One particularity of the composite propellers that is encouraging further research and development nowadays is their expected benefits in reducing the boat's fuel consumption. In fact, their main biggest difference compared to metallic propellers is their weight. As an example reference, Nakashima[®] retrofitted a 2 meter diameter metal propeller with composite reducing its weight from 715 to 422kg. This weight reduction is over 40%.

Another advantage of composite propellers is their morphing ability thanks to fibre orientation optimisation. This has been the focus of both experimental [7–9] and numerical studies [10–17]. By optimizing the blade angle at the different boat's speeds, both a decrease of the needed engine power and a reduction of the cavitation are expected [7,9–11]. Other optimisations can be made, as shown by Kishore et al. for vibrations [18].

Today, while short fibre reinforced polymer propellers are being developed and commercialized (see PropPulse[®] and Piranha Propellers[®]) used on small boats, their use on larger vessels is very limited [19]. A French project named FabHeli which stands for Fabrication d'Hélices en composite (Composite Propeller Manufacturing) was performed by three French companies being LoireTech, Meca, Naval Group with the contribution of AML and Bureau Veritas and part of a DGA Rapid project between 2016 and 2018. The goal of the project was to develop a composite propeller blade for commercial vessels. The project ended with a 1.1 metre propeller prototype fitted on a 30 meters passenger ship. One of the produced blade is shown in Figure 6.

Marine renewable energies

As explained in the first section, there is a considerable interest in developing renewable energies to limit pollution and emissions of greenhouse gases. The oceans present one of the most promising renewable energy resources on earth. The different ways to produce

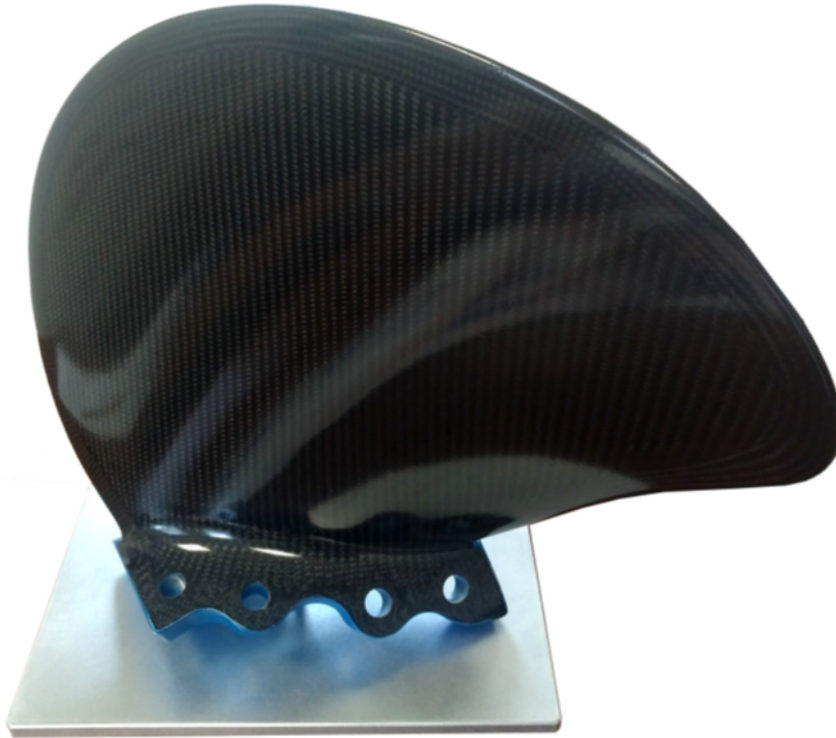


Figure 6 – FabHeli composite propeller blade [20]

energy out of marine resources are tidal, stream/current, wave, thermal gradient and salinity gradient. Offshore wind-turbines are often referred as marine renewable energies. However, offshore wind turbines do not rely on marine energy but on wind energy, it is only their geographical location that is marine-related.

In the tidal domain, a great example is the Barrage de la Rance between Saint Malo and Dinard where a dam was built in 1960s and was the largest tidal barrage for several decades. The principle is to retain seawater from either side and to force water into water turbines to produce electricity. This power plant produces around 500 GWh per year.

Using a similar principle, tidal turbines are being developed [21]. These systems use the power of the constant currents and those created by the tides. One of the most advanced prototypes that were developed, such as Sabella D10 (Figure 7) for example, work in a similar way to wind turbines. A moving rotor uses blades to transform the kinetic energy of water into a rotational movement that is then converted to electricity thanks to a generator.

In the case of tidal turbines, due to the high density of seawater, the blades are more highly loaded than wind blades so they tend to be shorter, up to 10 meters long. Any intervention for maintenance or repair in the regions of high currents is severely limited, so long term reliability is paramount for the commercial viability of these turbines. There is thus a need for high strength, and excellent fatigue resistance. Limited weight for the moving part is beneficial for installation but not the predominant requirement. Therefore, composite materials have been selected in designing most composite blades for



Figure 7 – Sabella D10 tidal turbine (picture from Sabella)

prototypes [22–28]. The tidal turbine industry is in its infancy today. The world’s first tidal farm with 4 turbines was installed North of Scotland recently by Atlantis [29] and is producing electricity, but there are no farms off the French coast yet even though there are projects underway.

Both these applications of composite materials for marine purposes can, in their own way, help to reduce greenhouse gas emissions. However, there is a common problematic for both these subjects:

- The composite materials are immersed in water for long periods of time
- There are complex, cyclic and high stresses induced on the blades

The commercial success of both tidal and propeller blades depends on how long they can survive before being replaced, but today we have very little return from experience. For example, carbon fibres are assumed to be necessary for these applications but glass fibres may be sufficient and considerably less costly.

The present document describes results from a study of the long-term durability of carbon fibre reinforced polymers. Composite materials have been widely used in the marine domain for the last 50 years [30–33]. The main application by volume is for boat hulls, usually made of glass reinforced thermoset composites, but racing yachts are made quasi-exclusively from carbon composites. Military surface vessels and submarines also use large amounts of composites [34].

Concerning the context of this study, it was co-funded by DGA and IFREMER, and carried out in parallel with other ongoing projects. There was a collaboration and exchanges with the DGA RAPID FabHeli project, in particular for the choice of materials for that project. For that, LoireTech graciously supplied composite plates for this study.

In the renewable marine energy area Ifremer has been involved in the use of composites for tidal turbines for over 10 years. The aging of glass fibre reinforced composites was studied by Boisseau [35], then Tual looked at static behaviour and aging of carbon composites [36]. IFREMER is currently a partner in the H2020 REALTIDE project, with Sabella among other partners [37], the scope of which includes measurements on the D10 carbon reinforced blades in service to improve the understanding of real loading conditions.

The present thesis addresses these issues and will be presented as follows:

The first chapter will present the state of the art on the subjects treated.

In the second chapter, the resin and composites studied in this thesis will be described. A single epoxy matrix system was studied, but two manufacturing processes were considered with different areal weights of carbon fibre.

The third chapter treats water uptake characterisation. This chapter is separated into three parts. The first presents the characterisation of the resin's water uptake. The second presents water uptake in the composite. A study of the predictability of water uptake by the composite, based on the resin's behaviour, will be described. Finally, a simple prediction of the water ingress in a real composite propeller blade at different ageing times will be discussed.

The fourth chapter describes a study on the different ageing mechanisms occurring in the pure resin. Two main mechanisms were identified when performing seawater ageing tests on the resin. These two mechanisms will be studied separately first and then coupled.

The fifth chapter deals with the effect of seawater on the fatigue properties. In this study, the composite material was subjected to cyclic tensile and flexural loadings. The damage mechanisms encountered during these tests will be studied by different techniques. In particular, the damage induced during four point flexure tests will be examined by C-scan analysis and X-ray micro-tomography, leading to conclusions on the relevance of fatigue data produced by such a test.

The sixth chapter is a consequence of the failure modes that were identified during the four point flexure tests. In fact, the main failure was during delamination. Therefore, this chapter focuses on the fatigue crack propagation properties of the composite and the influence of seawater ageing on this behaviour.

Finally, the conclusions and the perspectives of this study will be presented.

Chapter 1

State of the art

1.1 Composite materials used in the marine domain

1.1.1 Fibre reinforcements

Composite materials are used in a wide variety of applications going from highly demanding domains such as aerospace to less critical applications such as interior furniture. In the marine domain, fibre reinforced composites have always had a large place. There are applications for recreational applications such as surfboards, windsurf, pleasure boats but also on military and commercial boats [38]. For these applications, three main types of fibres have been used for several decades. The first one, also the cheapest, is glass fibres. These have good mechanical properties and a low price, which makes them a good choice for recreational applications. The second is aramid fibres. The best-known aramid fibre is Kevlar™ from Dupont® but there are other brands and suppliers such as Teijin® or Toray®. These fibres have great abrasion and mechanical resistance but are more expensive and are harder to impregnate which make them more suitable for military applications although they were sometimes used for pleasure boats in highly reinforced areas. The third type of fibre reinforcement is carbon fibre. This latter has high mechanical properties and resistance along with low weight. Even though these fibres are relatively expensive, they are used when good mechanical properties, flexibility and low weight are required. For this reason, they are a first choice when weight is important such as for racing windsurfs and racing yachts, fishing rods, but also when high mechanical resistance is required as in the military domain for example.

There are a number of other synthetic fibre polymers (polypropylene, nylon, polyester for example) with low modulus and less suited to composites, and some high performance fibres (HMPE¹, PBO² and Liquid Crystal Polyester) which are rarely used as composite reinforcement.

Recently, some more “environmental-friendly” fibres have also been studied. For example, vegetal fibres such as hemp and flax are receiving considerable attention [39]. The use of these fibres will undoubtedly increase in the future, in particular for the automotive

¹High Modulus PolyEthylene

²poly(p-phenylene-2,6-benzobisoxazole) also known as the trademark Zylon™



Figure 1.1 – Gwalaz 7 meters multi-hull integrating flax fibres composite hulls, example of an impact on the structure, ©Ifremer

industry, but their strong attraction for water will limit marine applications. Nevertheless, the Kairos “Gwalaz” trimaran used only flax reinforcement, Figure 1.1.

Another possibility is to use basalt fibres, which have similar properties compared to glass fibres but are claimed to have the advantage of lower manufacturing temperatures than glass fibres, resulting in less emission and energy required.

In the case of blades for propellers and tidal turbines, both weight and mechanical resistance are required. For this reason, carbon fibres are a good candidate when designing such highly loaded parts and have been the first choice to date.

1.1.2 Polymer matrices

Reinforcement fibres are only one part of fibre-reinforced composites, the second being the polymeric matrix. The goal of the matrix is to give cohesion to fibres and to distribute stress. In the marine domain, thermosetting matrix resins dominate and three polymers are widely used. Historically the first is unsaturated polyester resin. This resin has good mechanical properties at low cost, and is liquid at the manufacturing stage, which makes it easy to impregnate fibres. Therefore, polyester is often used as the cheapest option, having also the advantage of rapid polymerisation, which is suitable for industrialisation. Polyester resins are widely used in the pleasure boat and leisure industry.

The second resin is vinylester. This has better mechanical properties than polyester but is mainly known for its great resistance to corrosive environments such as in the chemical engineering industry. It is also known to have good resistance to fire and impact.

For this reason, vinyl ester has been a popular choice for military applications. However, these two resins have shown sensitivity to osmosis and hydrolysis [40, 41].

The third resin is based on epoxy chemistry. Epoxies, more expensive than polyesters, have been widely used as a composite matrix for space and aircraft structures, but also in the electronic industry, and they have been adopted in the marine domain for their higher performance and durability.

The epoxy systems are characterized by the triangular epoxide function. This epoxide function is opened in order to be able to cross-link epoxy molecules using different types of curing agents such as anhydride or amine, the latter being represented along with four epoxy functions in Figure 1.2. There are many possible epoxide constituents, each

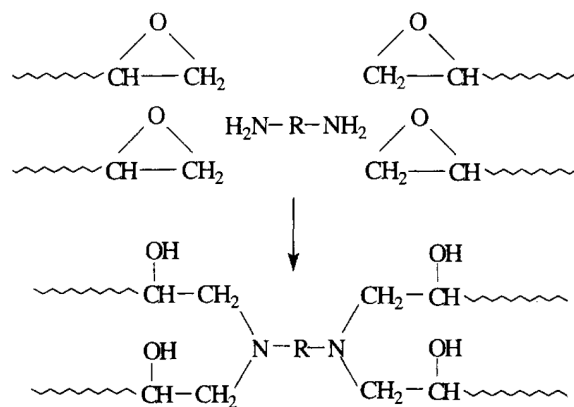


Figure 1.2 – Reaction of amine curing agent with four epoxide groups [42]

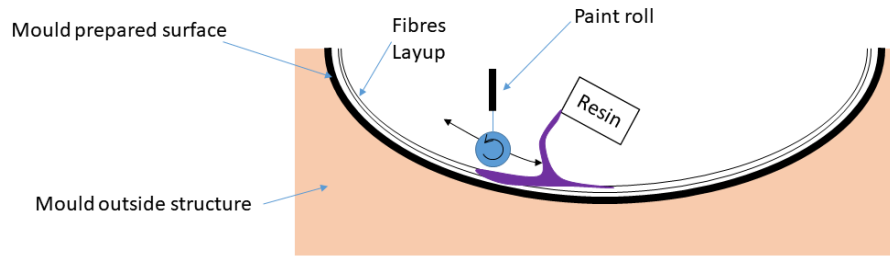
having its own advantages in terms of stability, resistance, ageing behaviour etc. The most widely used epoxides are Diglycidyl ether of Bisphenol A (DGEBA) and Diglycidyl ether of Bisphenol F (DGEBF), although others are also used [42–44].

Epoxy matrices are a good choice for structural application, such as the one considered in this study, as they have good mechanical properties. However, even though carbon fibre reinforced epoxy is known to have great resistance to the marine environment compared to other materials such as metals and wood, it is not insensitive to ageing. This will be discussed in section 1.2.

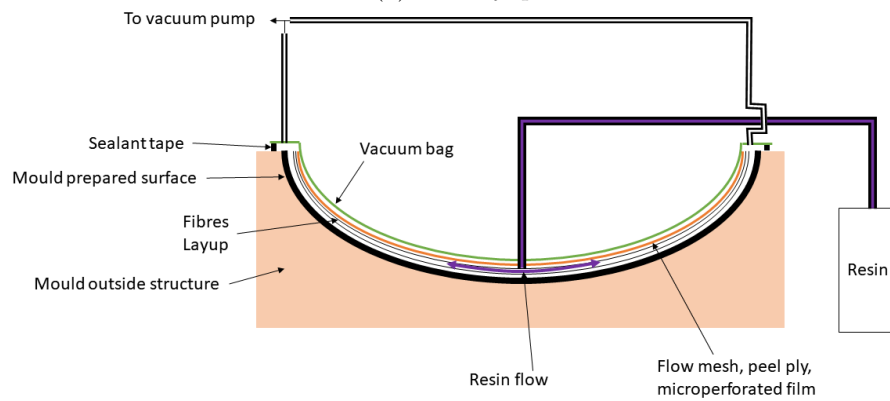
1.1.3 Manufacturing processes for composite fabrication

It must be emphasized that composite material properties depend on their constituents, but also to a large extent on how they are produced. There are several manufacturing processes to manufacture fibre-reinforced composites. In the marine industry, there are traditional methods that are economic but result in lower mechanical properties and for certain parts there are also manufacturing processes similar to those of the aerospace industry, that allow high manufacturing quality but at a much higher cost.

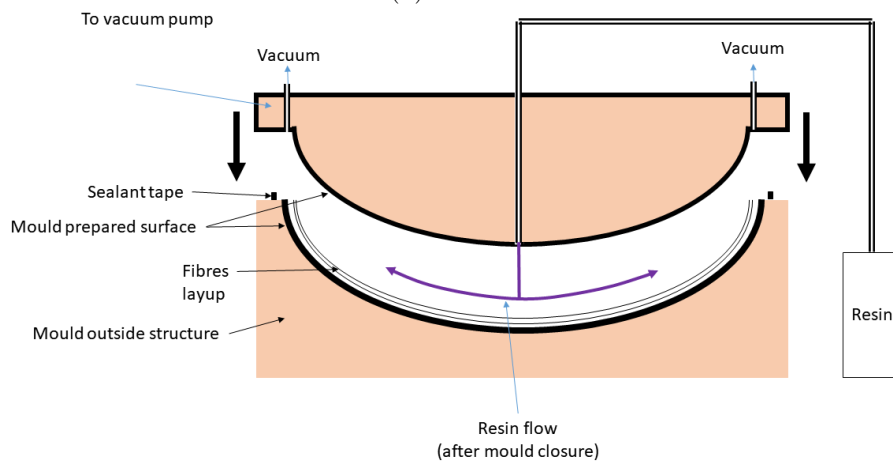
To begin with, the most economical process is wet layup. For this process, fibre reinforcement is placed in a mould. Then resin is prepared and fibres are impregnated with brushes or rollers. This process is used for example for surfboards, and for a major part of the pleasure boat industry, even though infusion is increasingly being used for the



(a) Wet-layup



(b) Infusion



(c) RTM

Figure 1.3 – Different manufacturing process of composite materials (a) wet-layup, (b) infusion, (c) Resin Transfer Moulding (RTM)

latter. The hand layup process can introduce many voids during impregnation and fibre volume ratio is not optimized.

The second process used is infusion. For this process, a preform or a mould is prepared. The fibres are laid according to the required orientations. Then a peel ply, a flow mesh and sometimes a perforated film are placed prior to applying a vacuum bag. Fibres are impregnated thanks to an applied vacuum, as shown in Figure 1.3. It is possible to place the mould in an autoclave in order to increase compaction resulting in a higher fibre volume ratio. This process gives good manufacturing quality along with good composite mechanical properties. However, it is less easy to transpose to mass production. It is being used for windsurf and kitesurf boards using foam cores and also for certain pleasure and large scale yachts. An alternative of the infusion process is the pre-preg process. Here the fibres are replaced by the pre-impregnated layups and the resin feed is removed. This process was developed for the aeronautical industry and is used in the marine industry for highly loaded composite parts such as racing sailboat hulls, masts and other appendices such as foils.

The final manufacturing process that will be presented here is the Resin Transfer Moulding (RTM) process. This process relies on the same principle as the infusion process with the difference that there is a two part rigid mould (usually male-female). The mould is closed after having placed the fibres and either vacuum or an applied pressure is applied to impregnate them. This allows the production of repeatable composite parts with tight dimensional tolerances and good mechanical properties. This process is used in aerospace and for mass production such as the ski industry but does not have many applications in the marine industry to date.

Other composite manufacturing processes exist, such as Automatic Fibre Placement (AFP), filament winding, pultrusion among others [45,46]. Some of these could be envisaged to manufacture turbine blades, but they were not studied here.

The term ‘composite material’ corresponds to a wide variety of multi-phased materials. In fact, there are composites composed of ceramic or metal fibres with ceramic, metallic or organic matrixes, and from a wider point of view, even plywood can be seen as a composite material as it is composed of distinct phases. However, for ease of expression in the rest of this manuscript, the term ‘composite’ will only refer to continuous fibre-reinforced polymers, otherwise it will be specified which type of composite material it will refer to.

1.2 Ageing of carbon fibre reinforced epoxy

1.2.1 Seawater and polymer composites

Diffusion of water in epoxy resin

Although widely used for various marine structures, as discussed previously, composite materials are not completely inert in a marine environment. In fact, seawater diffuses inside composite materials when they are immersed but also when exposed to relative humidity.

The diffusion of water in epoxy has been widely studied and was mathematically described by Fick in 1855 [47]. Fick used the heat conduction equations to develop the

diffusion equation, which bears his name. It is possible to simplify the Fickian equation from its spatial formulation (Eq. (1.1)) to a one-dimensional diffusion equation (Eq. (1.2)) by considering dimensions such that diffusion is considered only in one direction (see [48]) :

$$\Phi = -D \times \overrightarrow{\text{grad}}(C) \quad (1.1)$$

$$M(t) = M_{\infty} \times \left(1 - \left[\frac{8}{\pi^2} \sum_{n=0}^{\infty} \frac{1}{(2n+1)^2} \times \exp\left(\frac{-D(2n+1)^2\pi^2 t}{h^2}\right) \right] \right) \quad (1.2)$$

In the first equation, Φ is the diffusing flux, C is the moisture concentration in space coordinate and D is the diffusion coefficient.

In the second equation, the one that will be used in this thesis, the moisture content M at a time t in seconds is calculated as a function of the moisture content at saturation M_{∞} , the diffusion coefficient D of the material in $mm^2.s^{-1}$ and the specimen's thickness h in millimetres.

For epoxy resins, Fick's diffusion equation is commonly used to describe water ingress with relatively good results [49]. However, it has been shown that cross-linking with different curing agents can result in non-Fickian diffusion behaviour, as for anhydride cured epoxy [49, 50]. Other parameters can induce changes in the diffusion kinetics, such as ageing conditions [51, 52].

The diffusion parameters D and M_{∞} usually follow an Arrhenius behaviour. This means that these parameters are sensitive to the ageing temperature and possibly proportional. This can be used for accelerated ageing tests, allowing rapid determination (several months) of a long-term aged state (several years or decades) of a polymer that can be extrapolated to longer times at lower temperatures. However, increasing the ageing temperature can activate other degradation mechanisms that will not occur at lower temperatures.

Effect of seawater on the mechanical properties of composites

Composite materials used in a marine environment are exposed to harsh conditions, which can lead to changes in the mechanical properties. These may be permanent or reversible

For epoxy polymer, it is well known that plasticization can occur. Water molecules that diffuse into the polymer increase the chain mobility and act like a plasticizer. This results in changes to the mechanical properties such as lower yield stress, increased strain to break and also a decrease of the material's Tg [53–57]. This mechanical change has the particularity of being reversible when water is removed from the polymer. In this way, the polymer chains recover their initial low mobility and recover their initial mechanical properties. Other changes can result in permanent degradation of the matrix such as oxidation and hydrolysis as reported in [58].

Seawater has many effects on the mechanical properties of composites. Concerning the tension behaviour, many results show that exposure to seawater decreases the ultimate tensile strength. This result has been reported for composites of different matrices, fibres, and fibre orientation [28, 59–61]. When tested under compression, the same observations are made [62, 63].

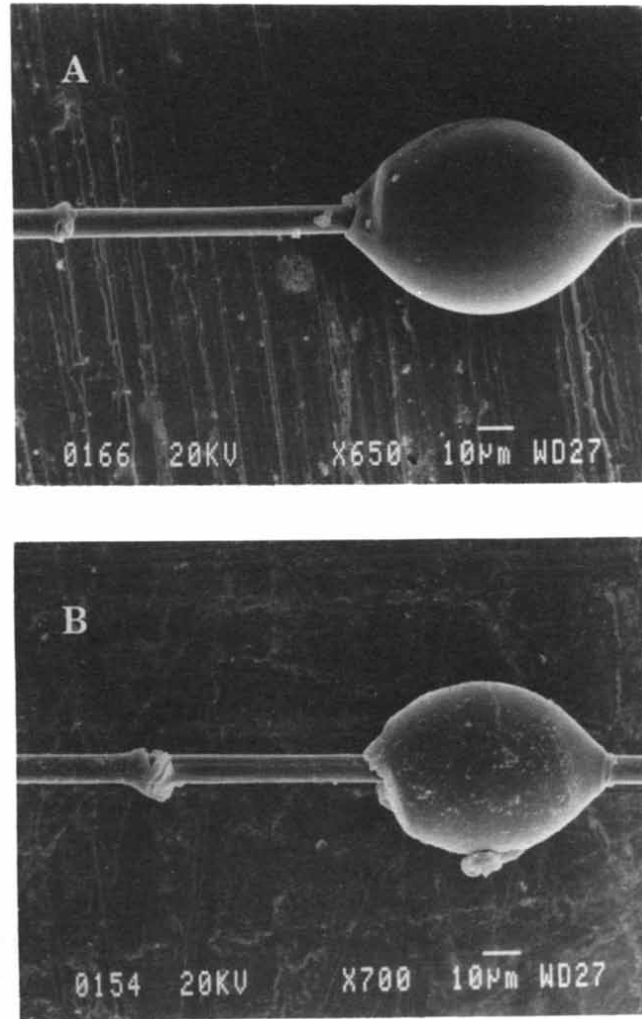


Figure 1.4 – SEM micrographs of debonded carbon fibres dry (A) and exposed to 80°C water for 6 hours (B) [64]

Similar observations have been reported for the interlaminar properties of composites exposed to seawater and humid environment. For the mode I fracture toughness, both increases and decreases have been reported [65–68, 68]. Laplante et al. studied the effect of water absorption on the mode II and mixed mode I and II and recorded lower fracture toughness and a decrease of the fatigue resistance of a carbon epoxy composite [69, 70]. These results were also reported by Asp [71].

Other studies have focused on the interlaminar shear strength, which can be of high importance when looking at the delamination properties of the composites. These studies have recorded once again a decrease after ageing, this time of the interlaminar shear strength [72–75].

Moreover, concerning the interlaminar mechanical properties, it seems that water has an influence on the fibre matrix interfaces. In fact, delamination and shear strength are

properties highly dependent on the fibre matrix interface and the ageing results reported tend to indicate a degradation of these interfaces [64, 65]. Ramirez et al. investigated the fibre debonding resistance of different carbon and glass fibre composites with epoxy and one vinyl ester matrices. Their results showed that water degraded the fibre matrix interface resulting in a decrease of the interfacial shear strength and higher debonding lengths [76]. This was also reported by Biro et al. who performed debonding tests of micro-droplets on single carbon fibres exposed to different hydrothermal conditions and measured losses between 25 and 50% of the interfacial shear strength [77]. In the same study, the SEM analysis of the debonded fibres (Figure 1.4) showed that the specimens exposed to 6h at 80°C in water had a rougher fibre surface. Additional measurements by X-ray spectroscopy indicated that the surface of the fibre was oxidised, which can be expected at these ageing temperatures. Joliff et al. showed the presence of an interphase [78] This interphase may be subjected to degradation during water absorption of the resin. Bradley and Grant had the same conclusions by performing micro-indentation of different composite systems including carbon epoxy that were saturated in seawater [79].

1.2.2 Physical ageing of epoxy

In addition to wet ageing a second mechanism by which glassy materials, such as epoxy, can change with time is physical ageing [80–82]. This particular ageing effect occurs when the polymer is exposed to sub-T_g temperatures. Physical ageing is characterised by many physical changes. Among these is a change in the material's density/free volume, which is a sign of a volumetric relaxation. Another change is seen in the molecular configuration, which is characterized by an enthalpy relaxation.

Physical ageing is often highlighted by two characteristic measurements on Differential

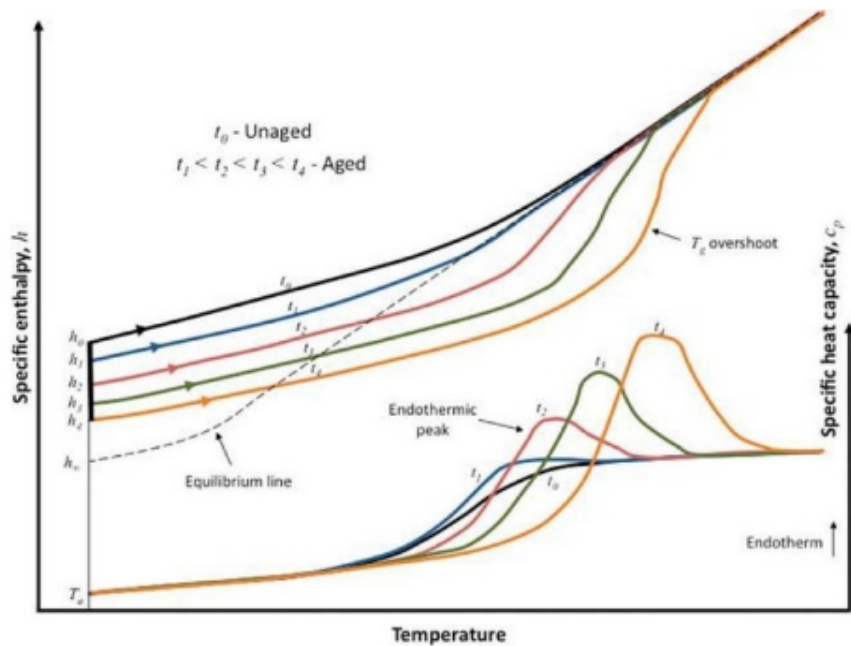


Figure 1.5 – T_g overshoot and endothermic peak as illustrated by [82]

Scanning Calorimetry (DSC) plots; Tg overshoot and the endothermic peak. Tg overshoot, as shown in Figure 1.5, is characterized by a translation of the Tg to higher temperatures as physical ageing increases. The endothermic peak corresponds to a bump on the heat capacity plot appearing just after the Tg also shown in Figure 1.5.

A major aspect of physical ageing is the fact that exposing the material to above-Tg temperature allows a total recovery of the initial state and properties of the epoxy. This phenomenon is known as thermal rejuvenation.

There are multiple effects of physical ageing on the mechanical behaviour of epoxy polymer. The mechanical response of physically aged polymers was widely studied under quasi-static tension [83–88]. These studies led to the conclusion that physical ageing increased yield stress and changed the microscopic failure to a more brittle one, with a decrease in the strain to break.

Chang and Brittain studied the fracture toughness of epoxy resins subjected to physical ageing [86]. Their first conclusion was that physical ageing reduced the fracture toughness. This was confirmed later by Truong and Ennis [89]. The second conclusion was that the crack propagation was stable when the resin was unaged but followed a stick-slip behaviour after ageing. Both these behaviours are coherent with a microstructure that became more brittle with physical ageing. Stick-slip behaviour corresponds to an abrupt crack propagation and arrest that is representative of a brittle material. The reduced strain energy release rate is also coherent with a brittle behaviour as the strain that the resin can undergo is reduced, and therefore the required energy to fracture the resin is less important even though the stress increases.

Kong studied the effect of physical ageing on a prepreg carbon fibre epoxy composite in [83]. His conclusion on the effect of physical ageing on composite materials was that the ultimate tensile strength, tested in the $\pm 45^\circ$ orientation, decreased with ageing time as shown in Figure 1.6.

1.3 Fatigue of fibre reinforced composites

Fatigue of materials has been studied since the middle of the 19th century with the work of August Wöhler. Prior to that, materials were considered as unbreakable if static dimensioning was adequately calculated. However, after a break of a train axle in 1875, this postulate was questioned. Wöhler studied the fatigue behaviour of metals and was the first to introduce what is known today as the Wöhler curve, also known as S-N curve for Stress vs Number of cycles to failure.

Composite materials are often considered fatigue-resistant because of the excellent fatigue properties of glass and carbon fibre reinforcements. However, the introduction of defects such as fibre misalignment, micro/macro voids or different ply orientations can lead to stress concentrations initiating damage that propagate under cyclic loads. This makes the composite materials more or less fatigue-sensitive.

1.3.1 Fatigue of composites, the effect of seawater

Composite materials are highly anisotropic. Therefore, the formation of S-N curves for composite materials differs to that of conventional isotropic materials. This is compli-

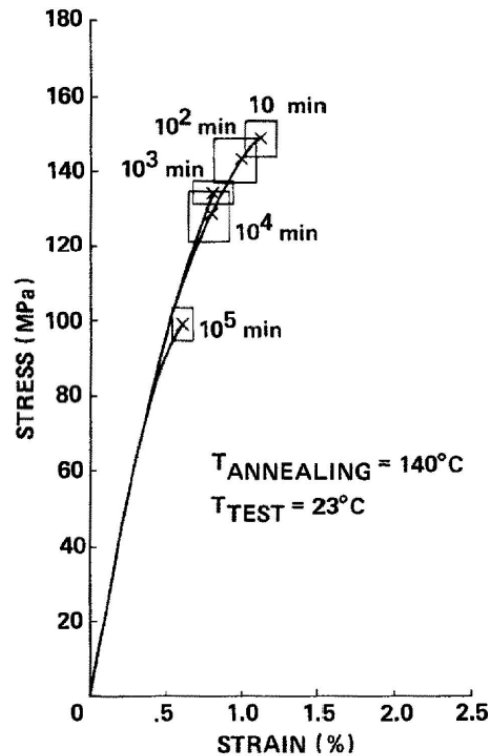


Figure 1.6 – $\pm 45^\circ$ tensile strength of a cfrp prepreg composite as a function of ageing time at 140°C [83]

cated by the fact that composites can vary widely, depending on the type of fibres, the stacking sequence, the manufacturing process or even the fibre/matrix combination and ratios. In addition to these material parameters, the composite can be loaded according to different fibre orientations, stacking sequences and under different load conditions such as tensile, compression, flexure, delamination, different load ratios and sometimes with different stress concentrations (open hole, edge-notched). For this reason, this section will only present briefly the fatigue of composite materials and will mainly focus on the environmental effect. The reader will find many studies and information on the global subject of fatigue of composite materials in the following literature [90–94].

The major part of fatigue studies on composite materials concerns in-plane loading. This ranges from compression-compression to tension-tension, as illustrated by Sims in Figure 1.7, according to different load ratio R as:

$$R = \frac{\sigma_{min}}{\sigma_{max}} \quad (1.3)$$

Many of the aforementioned reports and studies use the rectangular design from the ASTM D3039 [96] and ASTM D3479 [97]/ also in [98–101]. However, in order to channel stress, avoid end-tab failure or to study the effect of stress concentration, other studies have used different designs [102–104].

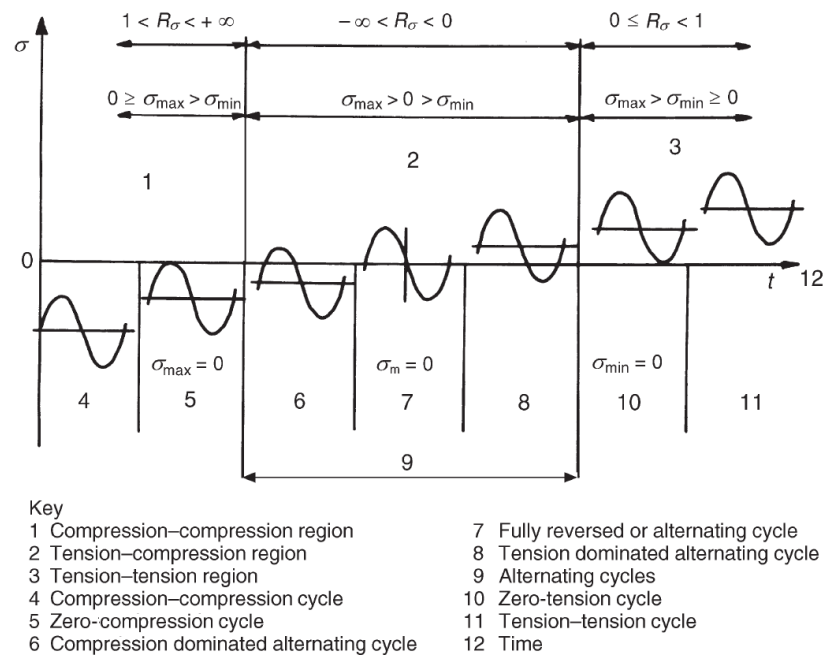


Figure 1.7 – Representation and correspondence of the different load ratios from [95]

The major part of the literature agrees that fatigue damage occurring on fibre-reinforced composite materials happen with the following mechanisms:

- Micro crack of the resin
- Micro-crack reaching fibre/matrix interface
- Delamination
- Fibre breaking
- Total failure

This damage trend is illustrated in Figure 1.8. There is an alternative for final failure though. In fact, the final failure on certain laminated composite may occur at the third stage : delamination. Other studies have investigated the fatigue performance of composite materials under flexural fatigue. As for tensile fatigue, there are no standards for the test of fatigue under flexural loading. Most of the studies use either 3 or 4 point flexure (ASTM D790 [106] and ASTM D6272 [107] standards) [108–110].

Concerning the study of the effect of moisture, and more precisely seawater, on the fatigue behaviour of composites, there is more limited data. Kennedy et al. investigated the effect of seawater on glass-epoxy Quasi-Isotropic (QI) composite under tension-tension fatigue in [111]. After 30 months of immersion at 30°C, they found that the tension-tension SN curve shifted by around 1 decade to lower fatigue lives, with a more pronounced shift for the higher stresses (see Figure 1.9).

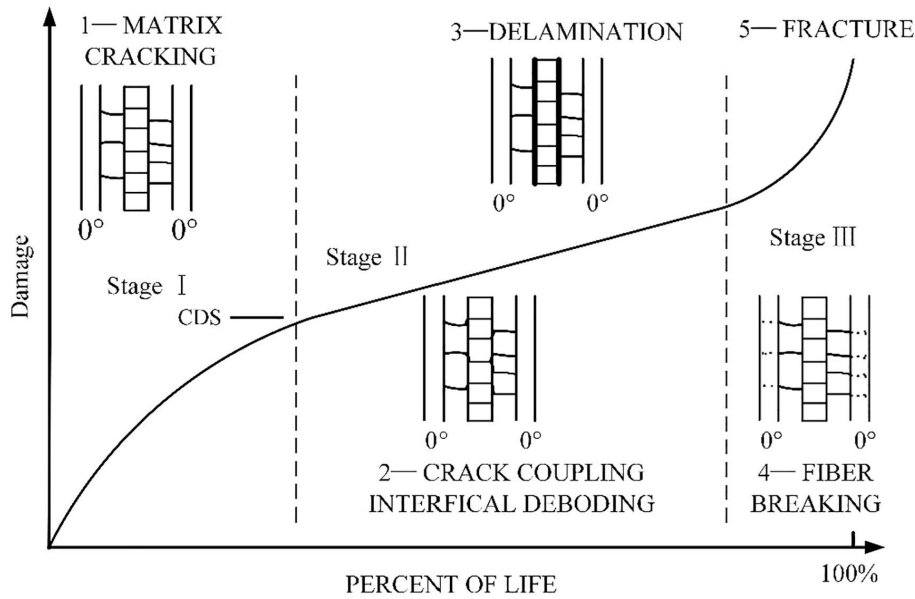


Figure 1.8 – Damage leading to fatigue failure of composite materials from [105]

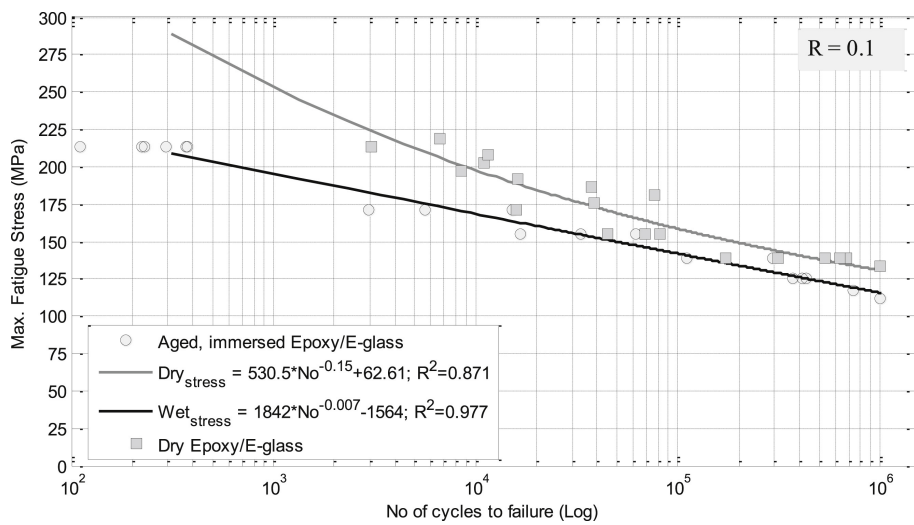


Figure 1.9 – Effect of 30 months at 30°C in seawater on a Quasi-isotropic glass/epoxy composite from [111]

Concerning the effect of water on the fatigue behaviour of CFRP composites, Selzer and Friedrich recorded a decrease of the number of cycles to failure of 7% for a carbon/epoxy composite and also negligible effect on carbon/PEEK [112]. In the same vein, Davies et al. studied the effect of seawater on a unidirectional carbon/epoxy composite under four-point flexure [25]. Their results showed a non-negligible decrease of the fatigue life (Figure 1.10). It is interesting to note that as for GFRP in the Kennedy et al. study, Davies et al. also found a more pronounced shift of the fatigue life for higher maximal stresses.

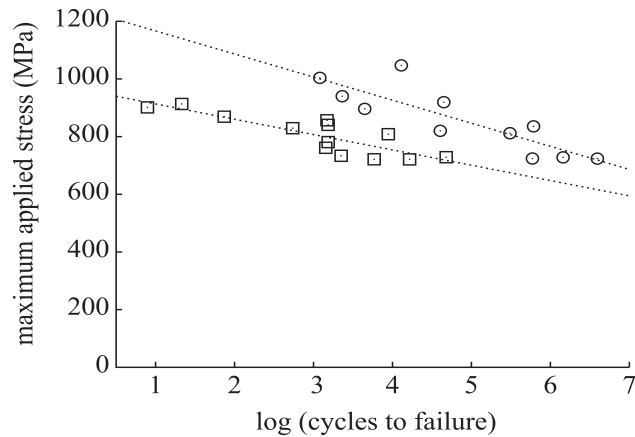


Figure 1.10 – Effect of seawater on CFRP composite under four-point flexure loading [25]

Furrow and Loos have also studied the effect of pure water on the compression behaviour of multiple unidirectional composite unstitched and stitched with Kevlar[®] and glass fibres also comparing to woven 2D and 3D carbon fibre composites [113]. Among the conclusions that stitching decreases compressive strength, they found that after saturation in water, the ultimate compression strength decreased for all materials. When it comes to fatigue loading, they found that all unidirectional composites (stitched and non-stitched) have their fatigue life reduced, once again more pronounced at higher stress levels. Unfortunately, they did not perform the fatigue tests at the saturated level for the woven composites.

Nakada and Miyano applied the Time Temperature Superposition Principle (TTSP) to carbon vinylester, carbon epoxy and glass epoxy composites exposed to water ageing [114]. They performed predictions under three point bending constant strain rate and fatigue tests. They found that for all the different composites, water decreased their fatigue strength. Linking the TTSP to fatigue is possible when considering the damage accumulation theory. In this theory, fatigue failure occurs when fatigue strength, also referred as residual strength, reaches the applied fatigue maximal stress as illustrated by Harris in [115]. However, this theory, as reported by Vassilopoulos and Keller, has the drawback that residual strength often decreases near to final failure compared to the residual stiffness that fluctuates all along the fatigue life as illustrated in Figure 1.11.

1.3.2 Statistical analysis and models

Fatigue investigations on composite materials are often based on a final failure approach. The data obtained are then represented on S-N curves showing the number of cycles to failure as a function of maximal applied stress as shown in Figure 1.12. The ASTM standard practice recommends fitting the obtained data with a linear curve as illustrated on Figure 1.12 by the orange curve and calculated as:

$$\log(N) = A + B\sigma_{max} \quad (1.4)$$

There are other models that were developed in order to describe SN curves [116–118].

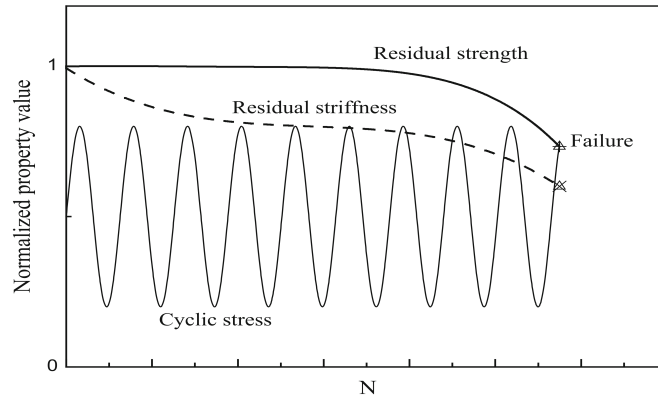


Figure 1.11 – Damage accumulation theory with comparison of residual strength and stiffness trends [90]

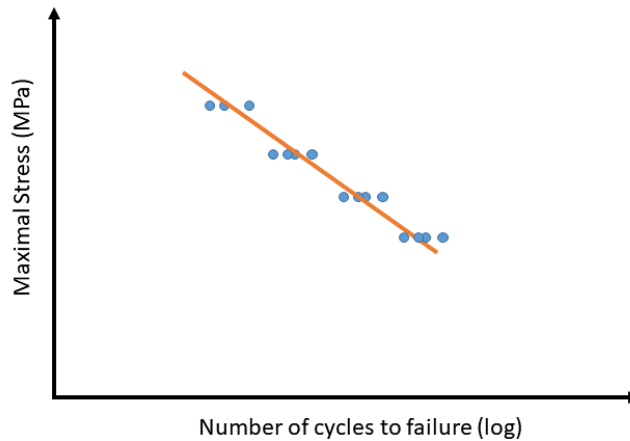


Figure 1.12 – Typical S-N curve and linear fit

In [119], Vassilopoulos and Keller presented different statistical approaches to represent the fatigue data. Two of those were found to present a conservative representation of the fatigue data. These two approaches are Whitney's Pooling Scheme (WPS) and Sendenskyj's wear-out model. Sendenskyj's model has the advantage that it can take into account the quasi-static strength but shows similar results to the WPS approach if the static failure level is not considered.

The WPS approach is a straightforward approach based on a Weibull distribution of the data. The idea is to calculate for each stress level, the Weibull parameters α and \bar{N} which are respectively the shape and scale parameters. The survival probability, noted P , can be calculated at each stress level as a function of the number of cycles, N , as:

$$P(N) = \exp\left(-\left(\frac{N}{\bar{N}}\right)^\alpha\right) \quad (1.5)$$

Figure 1.13 represents an S-N curve with four different stress levels. For illustrating

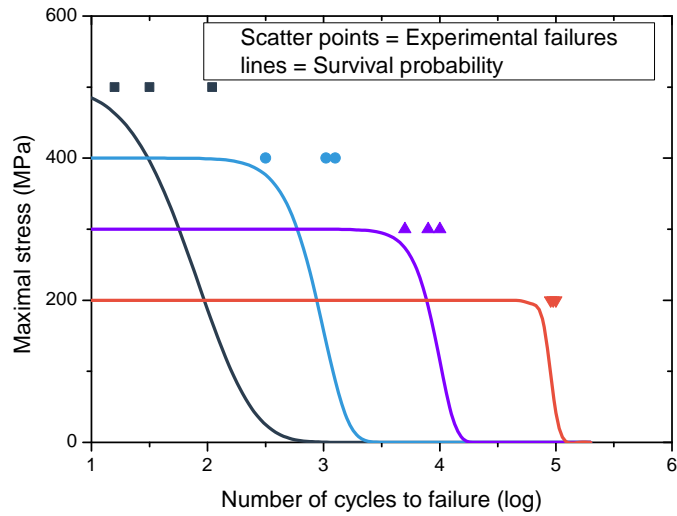


Figure 1.13 – Illustration of the Weibull survival probability on S-N data

purpose, the following fatigue data presented in this section have been created and does not present results from any study. The points represent the recorded failures and the corresponding survival probabilities are shown by the lines. One can see that for high variation, the survival curves are elongated (for example at 500 MPa) and for low variability, the probability rapidly drops (for example at 200 MPa).

At this stage, the whole dataset can be normalized by its respective scale parameter

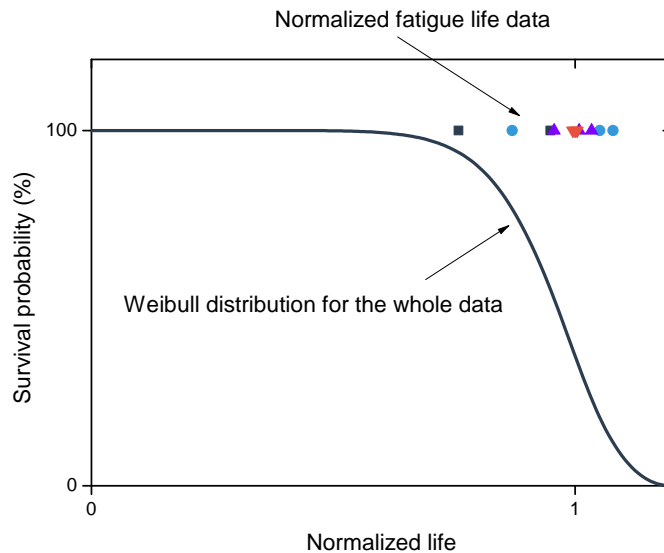


Figure 1.14 – Weibull distribution of normalized data

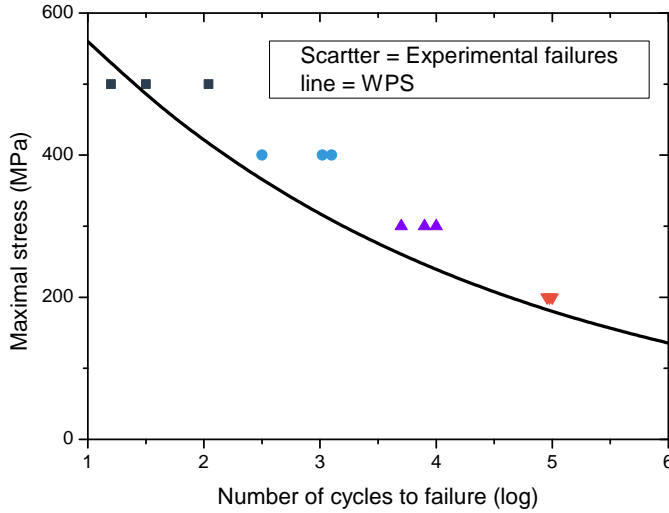


Figure 1.15 – Result of the WPS approach

\bar{N} . This means for example that if the scale parameter found at the 200 MPa stress level is 5, then the three recorded number of cycles to failure are divided by 5. Then the shape parameter, noted α_f , of the Weibull distribution of this entire normalized dataset is calculated as shown in Figure 1.14. The normalized scale parameter should be equal to 1 otherwise adjustments are made and the shape parameter is re-calculated. The WPS curve can finally be calculated as:

$$\sigma_{WPS}(N) = \sigma_0 \left[-\ln(P(N))^{\frac{1}{\alpha_f k}} \right] N^{-\frac{1}{k}} \quad (1.6)$$

In this equation, a value of survival probability $P(N)$ has to be chosen, usually 95%, the parameters σ_0 and $\frac{1}{k}$ are respectively the y-intercept and slope of the linear regression of $\log(\sigma)$ versus $\log(\bar{N}_f)$ with \bar{N}_f corresponding to the adjusted scale parameters at each stress level.

The final WPS can then be represented as shown by Figure 1.15.

1.3.3 Delamination fatigue

Interlaminar crack propagation (delamination) can be one of the weaknesses of laminated composite materials. Delamination corresponds to a de-cohesion of the different composite plies and is usually described according to one of three different loading modes, as illustrated in Figure 1.16. The first mode corresponds to crack opening, the second to in-plane shear and the third to out-of-plane orthogonal shear.

Mode I has received most attention in the literature, as it is the only crack loading with a well-accepted and standardized test procedure. The mode II loading case, on the contrary, has different test methods and even though two of those are standardized, the validity of these tests is often questioned. Mode III is the least studied mode, as there are

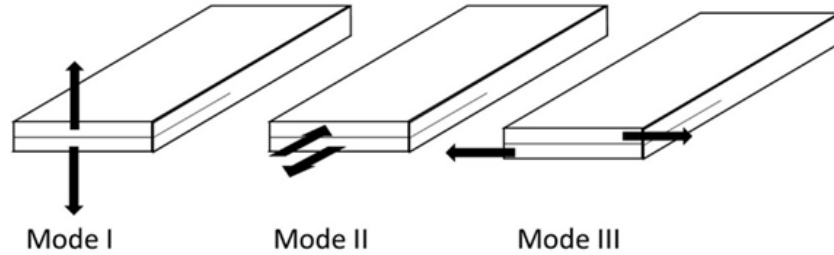


Figure 1.16 – Illustration of the three modes of delamination

no standard test methods and it is harder to perform, although experimental test methods exist [120, 121]. Another well-studied option is mixed mode bending which mixes mode I and mode II. This has the advantage of limiting friction for high mode II ratios but requires a special fixture for the standardized test; the determination of the pure mode II fracture resistance values with this test method relies on an extrapolation.

The fatigue approach that will be followed in this study will only treat pure mode I and “pure” mode II, so the state of the art on this subject will only focus on these two modes.

Fatigue in mode I

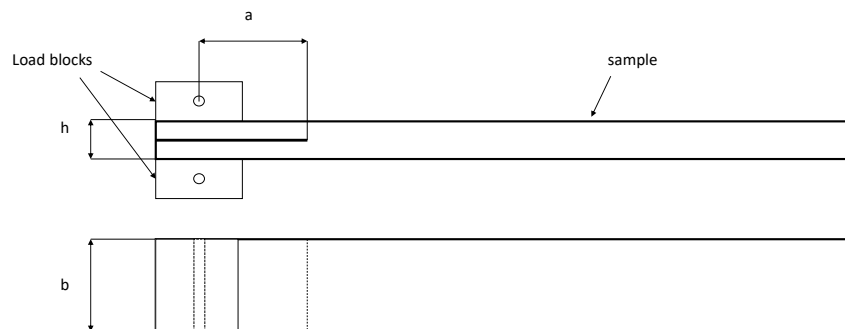


Figure 1.17 – Design of the Double Cantilever Beam standard test

The International and American standards for this test method for pure mode I measurement under static loading are based on the Double Cantilever Beam (DCB) specimen, Figure 1.17 (ASTM D5528 [122] and ISO 15024 [123]). Three data reduction methods for calculation of the energy release rate, G_{Ic} , are presented by the two standards:

- The Modified Beam Theory (MBT) – ASTM & ISO
- The Compliance Calibration (CC) – ASTM & ISO
- The Modified Compliance Calibration (MCC) – ASTM

Round robin tests have compared the three different methods [124,125]. The results from this international round robin is that MBT shows the lowest values of G_{Ic} meaning it is the most conservative value. The equations for these three data reduction methods are presented below:

$$G_{Ic} = \frac{3P\delta}{2b(a + \Delta)} \quad (1.7)$$

$$G_{Ic} = \frac{nP\delta}{2ba} \quad (1.8)$$

$$G_{Ic} = \frac{3P^2C^{\frac{2}{3}}}{2Abh} \quad (1.9)$$

In these equation, P is the load in N, b is the specimen width in mm, a is the crack length in mm, δ is the opening displacement in mm and C is the compliance defined as: $C = \frac{\delta}{P}$. Then, Δ is the crack length correction corresponding to the x-intercept of $C^{\frac{1}{3}}$ versus crack length a , n is the slope of $\log(C)$ versus $\log(a)$ and A is the slope of $\frac{a}{h}$ versus $C^{\frac{1}{3}}$.

For fatigue tests, the ASTM D6115 [126] standard only takes into account the crack onset. The principle is to record the number of cycles for an applied G_I leading to a crack onset. The data obtained are plotted as a G-N curve similar to the S-N plot.

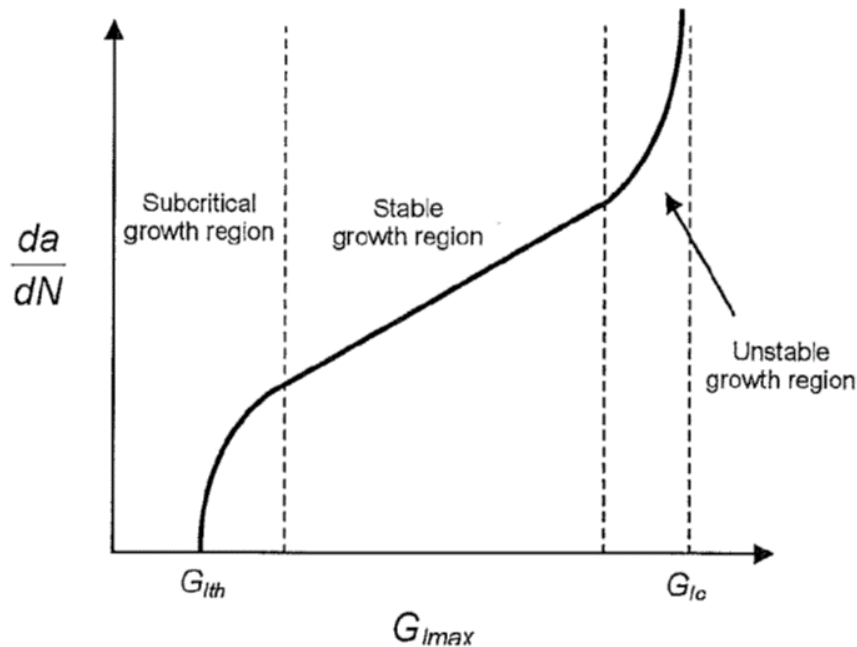


Figure 1.18 – Typical delamination curve according to Paris relation

Recent studies have pushed in the direction of a standardisation for the fatigue crack growth measurement of composite materials [127, 128]. The goal is to measure the crack growth rate, da/dN in mm/cycle, for a variety of applied energy release rates. Several studies have already used this method to study the fatigue under mode I loading of composite materials [66, 129–135]. The data acquired from this approach can be represented as a Paris plot (Figure 1.18) with usually three phases being: unstable, stable and subcritical growth. The axes of the plot are both logarithmic. The linear part of the curve can be expressed as a Paris law:

$$\frac{da}{dN} = kG_{max}^n \quad (1.10)$$

Where $\frac{da}{dN}$ is the crack growth rate, G_{max} is the maximum cyclic energy release rate and k and n are the Paris law parameters. To obtain such plots, the specimens are loaded under constant displacement rate control and crack advance is either measured directly, or calculated from the corresponding measured compliance. At the beginning, the load will be high, leading to the highest crack growth rates. Then, as the crack advances, the load decreases and crack growth rate decreases.

Other studies have tried to perform constant G fatigue tests under mode I and mixed mode loadings [136]. The advantage of such a method is a better evaluation of the crack growth rate at a certain applied energy release rate. However, this method requires a closed loop between measurements and control in order to adjust displacement and/or load; this is not possible on all fatigue test machines. It also requires different G levels to be applied, in order to fully cover the $\frac{da}{dN}$ curve as is done with the displacement-controlled method.

Fatigue in mode II

There are many different test methods that exist for the determination of the critical mode II energy release rate, see Figure 1.19 from [120]. In this figure are presented the Edge Notched Flexure (ENF), the Stabilized Edge Notched Flexure (SENF), the Four point Edge Notched Flexure (4ENF), the Edge Loaded Split (ELS), the Over Notched Flexure (ONF) and finally the Compact Edge-Notched Shear (CENS).

Only two of the aforementioned methods are standardized: the ENF (ASTM D7905 [137]) and the Calibrated ELS (C-ELS) (ISO 15114 [138]). A round robin comparison of these two methods under quasi-static loading, together with the 4ENF and SENF geometries was done by Davies et al. in [139]. The result of this round robin was that none of the different methods showed a significant advantage. The crack instability was underlined for the ENF method, and only one laboratory had satisfactory results for the SENF method.

For fatigue testing, none of these methods is standardized although studies have considered ENF, 4ENF and ELS methods [69, 141–144]. Brunner et al. performed a recent round robin for the standardization of a test procedure for mode II fatigue. This round robin indicated that the C-ELS tests showed more consistent results between the different laboratories [144]. The results from C-ELS tests may also underestimate the fatigue properties but at least these values can be considered as conservative.

From a practical point of view, it is worth mentioning that for similar dimensions between ENF and C-ELS specimens, the effective crack length that can be tested is more

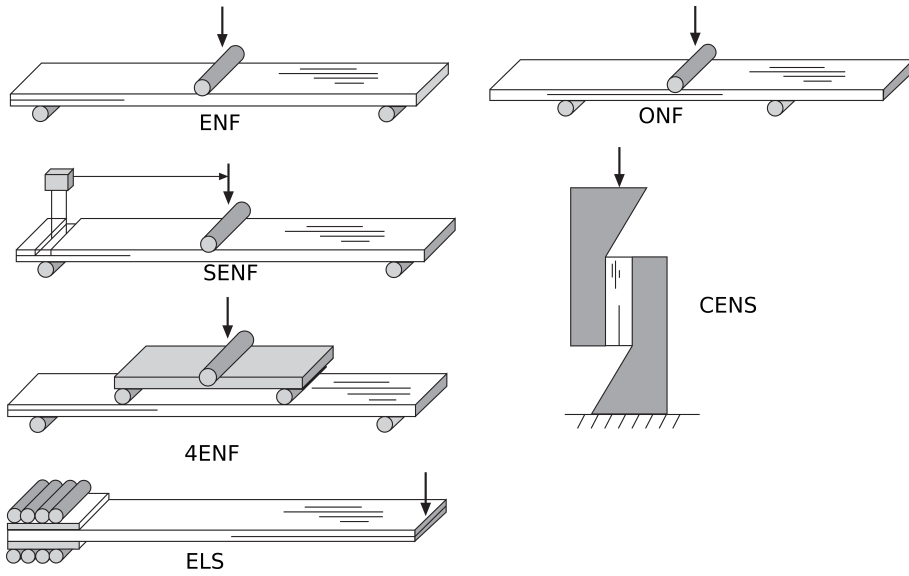


Figure 1.19 – The different test methods for mode II delamination measurement [120]

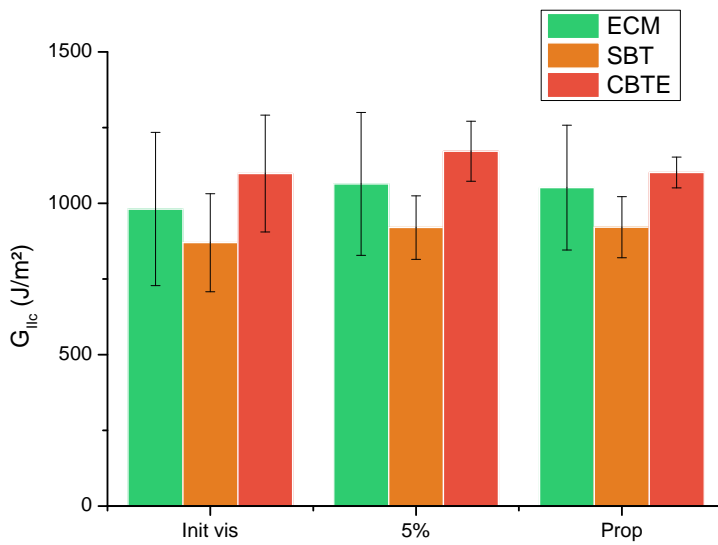


Figure 1.20 – Comparison of data reduction methods according to round robin from [140]

important for the C-ELS, as the ENF is limited to using only one half of the specimen (until the crack approaches the central load point). Therefore, C-ELS seems a better option for propagation fatigue tests. The ENF may be a better choice in order to create G-N curves.

For the test programme described in this thesis, the C-ELS fixture was chosen over ENF and 4ENF geometries for the aforementioned reasons of crack stability, operational

crack length and conservative results.

The C-ELS has three different data reduction methods:

- Experimental Compliance Method (ECM)
- Simple Beam Theory (SBM)
- Corrected Beam Theory using Effective crack length (CBTE)

These data reduction methods were compared for initiation values during the ESIS TC4 round robin, as shown in Figure 1.20.

On this figure are represented the initiation values from visual detection, from the 5% compliance decrease and the mean propagation value. It appears that the CBTE shows the highest values for G_{IIc} calculation. However, it has the lowest scatter for the propagation values. This makes the CBTE method a better candidate for fatigue tests when it is propagation values that are measured. For G-N curves, the SBT could be considered to be at the same level as CBTE, as the deviations obtained for crack initiation toughness are close to each other.

1.4 Conclusions

Both the mentioned applications discussed in the introduction involve coupled durability issues. There are complex and repeated loadings induced in the blades by water flows and bending. However, these cyclic loads are difficult to take into account for dimensioning today due to a lack of data.

In addition to mechanical loading, the composite parts are also exposed to the harsh seawater environment. The effect of long-term exposure of composites to seawater has been studied previously, but only few data exist on the effects on fatigue properties especially when carbon fibres are used. Such studies require both a validated accelerated aging methodology and the availability of test machines for long test sequences in seawater. One of the most frequent failure mods for composites is delamination, and in the case of composite blades subjected to out-of-plane loading it requires special attention. However, if there is limited data on fatigue crack resistance of composite, it is even more limited when considering the influence of long-term exposure to seawater on fatigue delamination. The acquisition and analysis of such data is a major objective of the present study.

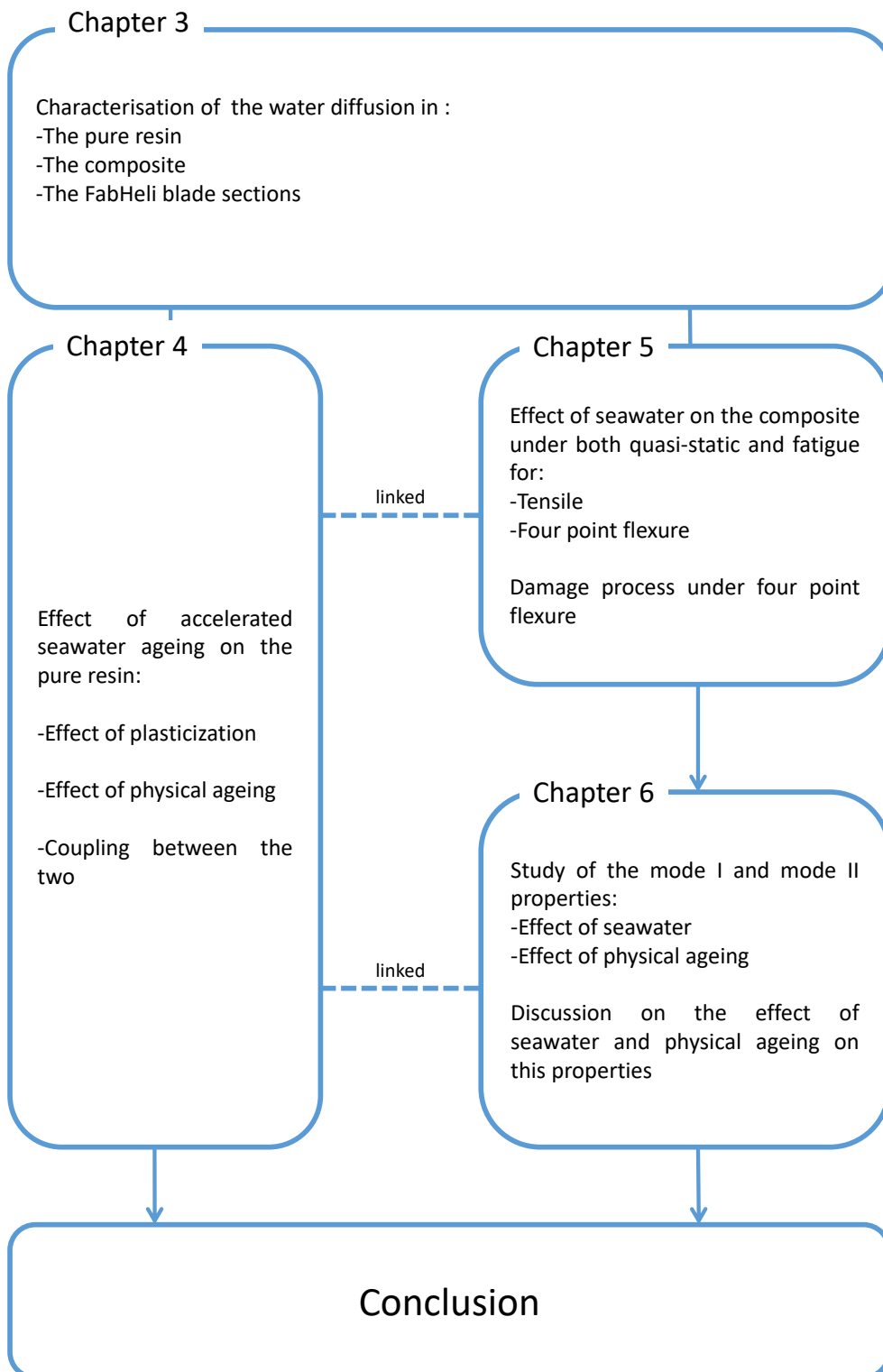


Figure 1.21 – Illustration of the document

Materials and methods

2.1 Materials

The material of interest in this study is a fibre-reinforced polymer (FRP). The reinforcement is carbon fibres and the polymer is a marine grade epoxy. The composite material was studied in two forms that were fabricated using two different processes and with two areal-weights of carbon fibres. First, the epoxy resin will be presented with the fabrication method used to manufacture coupons and specimens. Then the composite will be presented with the two different manufacturing routes.

2.1.1 Resin

The resin studied in this thesis is a commercial epoxy from SicominTM, a French manufacturer, based on three pre-polymers. These are Diglycidyl Ether of Bisphenol F (DGEBF), Diglycidyl Ether of Bisphenol A (DGEBA) and Hexa Diglycidyl Ether. The molecular representation of these three pre-polymers is shown in Table 2.1. There may be other components such as plasticizers or antioxidants. However, as this is a commercial resin, the complete composition is protected by the manufacturer and therefore cannot be completely known.

This resin is designed to work with different hardeners. However, as the main application here concerns marine propellers and tidal turbine blades, which are composed of thick composite parts, the crosslinking reaction must be slow. The reason is that for thick composite parts, more time is needed to impregnate the fibres before curing, and it is important to limit exothermic reactions during the fabrication. Therefore, the hardener used in this study, Table 2.2, is a slow hardener.

This resin system is designed for anaerobic processes such as resin transfer moulding (RTM) or infusion process. To fabricate resin plates, a semi-closed mould was developed during this study with the help of SicominTM (Figure 2.1). It relies on two aluminium plates covered by Teflon tape so that the cast resin can be removed easily from the mould. The two plates are separated by a U-shaped frame of 3 mm in thickness. A silicone tube is placed along the U-frame to make the seal between the two aluminium plates, leaving only a small surface in contact with air during resin curing.

Table 2.1 – Resin's pre-polymer composition

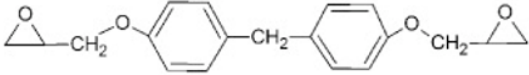
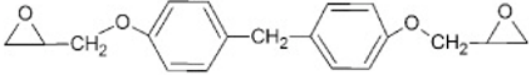
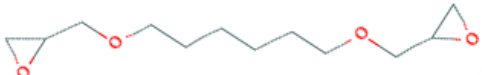
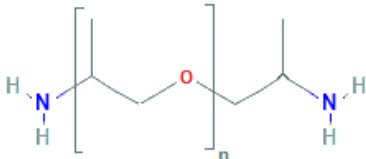
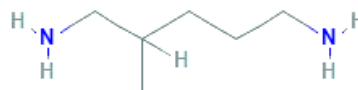
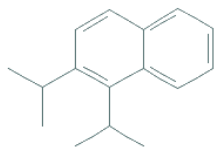
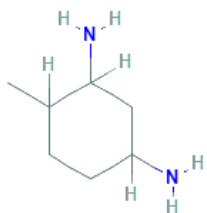
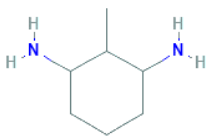
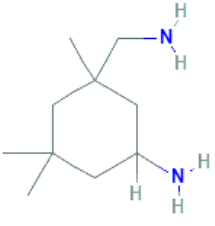
Molecule name	Approx. Composition (in %)	Molecule representation
DGEBF	$50 \leq x < 100$	
DGEBA	$10 \leq x < 25$	
1,6 hexa diglycidylether	$10 \leq x < 25$	



Figure 2.1 – Mould for pure resin

The resin is cured in three steps. First a 24h cure at ambient temperature (20 °C ideally) is required. Then a post-cure of 16 hours at 60 °C is applied. DSC measurements after this post-cure revealed incomplete curing of the resin, so a second post-cure of 2 hours at 120 °C was applied, resulting in a complete cure of the resin. Complete curing is necessary to avoid post curing during accelerated ageing and to obtain reliable data. For example, water uptakes measured on the resin with and without the final post cure showed

Table 2.2 – Resin’s pre-polymer composition

Molecule name	Approx. Composition (in %)	Molecule representation
polyoxypropylène diamine	$25 \leq x < 50$	
2-Methylpentane-1,5diamine	$10 \leq x < 25$	
Diisopropyl naphthalene	$10 \leq x < 25$	
4-Methylcyclohexane-1,3-diamine	$10 \leq x < 25$	
2-Methylcyclohexane-1,3-diamine	$2.5 \leq x < 10$	
3-aminomethyl-3,5,5-trimethylcyclohexylamine	$2.5 \leq x < 10$	

that incomplete curing induced higher water uptake of the resin as shown in Figure 2.2.

A 3-axis CNC machine, shown in Figure 2.3, was used in order to cut resin plates to the desired dimensions.

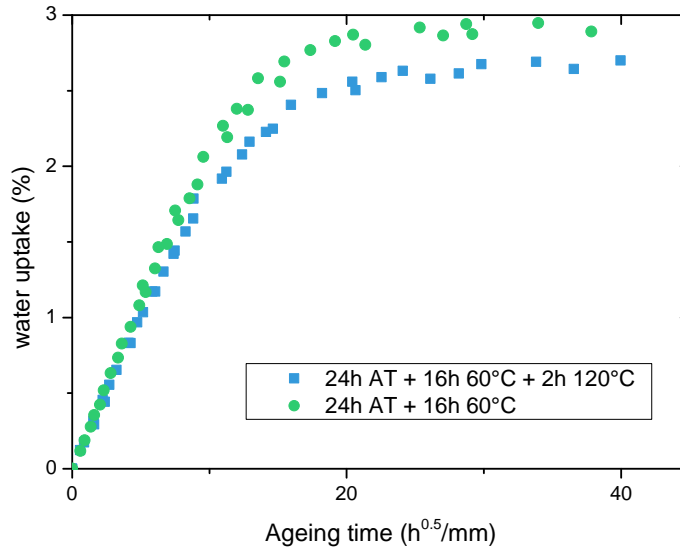


Figure 2.2 – Effect of level of curing on water uptake of the pure resin in seawater at 40 °C

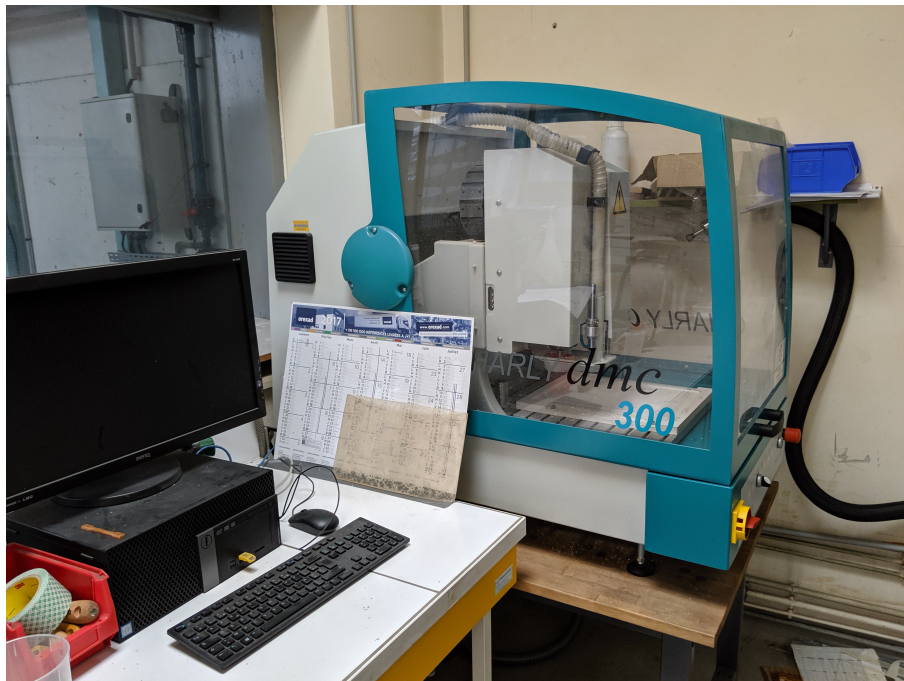


Figure 2.3 – Charlyrobot[®] CNC machine

2.1.2 Composites

Two types of composites were studied, the first type was manufactured with a vacuum-RTM process and the second one by infusion. Both composites were composed of the same fibres and resin. The resin is the one presented in the previous section. The fibres were 12k T700 unidirectional carbon fibres from Torayca™. The RTM composite used a 300 g/m^2 reinforcement and the infused composite used 600 g/m^2 fibres. In order to maintain carbon fibre alignment and facilitate manipulation, the carbon fibres are weaved with 68 tex glass fibres every 5 mm (Figure 2.4). RTM plates were produced by a French manufacturer,



Figure 2.4 – 600 g/m^2 carbon fibre fabric with off-axis glass fibre weaving

LoireTech®. Two stacking sequences of square plates were manufactured by the RTM process. These sequences were 10 ply unidirectional and cross-ply $[0/90/0/90/0]_s$. The resulting dimensions were approximately $(500 \times 500 \times 3.4 \pm 0.1) \text{ mm}^3$. Fibre volume ratio was evaluated by ThermoGravimetric Analysis (TGA) using a burn-off technique under nitrogen atmosphere coupled with density measurements with a helium pycnometer (this will be explained in the next section). The fibre volume ratios of the 6 RTM plates supplied are shown in Figure 2.5. The average fibre volume ratio of the RTM composite plates was $50 \pm 4\%$.

For the infused composite, four different stacking sequences were manufactured by another French manufacturer, FMC®. The four stacking sequences produced were 3 ply unidirectional $[0]_3$; 3 ply crossply $[0/90/0]$; 6 ply unidirectional $[0]_6$ with pre-crack; and finally 6 ply crossply $[0/90/0]_s$. The dimensions of these 6 different stacking sequences are all $500 \times 500 \text{ mm}^2$ square plates but with thicknesses of $1.74 \pm 0.06 \text{ mm}$ for the three ply plates, $3.31 \pm 0.09 \text{ mm}$ for the 6 ply cross-ply plates and $3.5 \pm 0.12 \text{ mm}$ for the pre-cracked unidirectional plates. Even though the cross ply composites produced by the

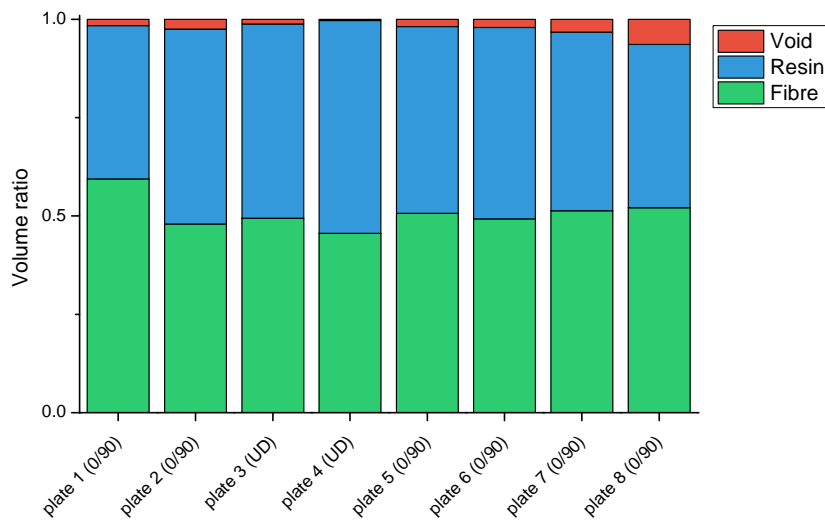


Figure 2.5 – Measured composition of RTM composite plates

two manufacturing methods have similar thicknesses, the unidirectional proportionality is different as the 600 g/m^2 plates have 4 out of 6 plies unidirectional whereas the 300 g/m^2 one has 6 unidirectional out of 10 plies.

Infused composite plates had higher fibre volume ratios as this process allows more compaction. The average fibre volume ratio was measured to be $62 \pm 3 \%$. The summary of these measurements is presented in Figure 2.6.

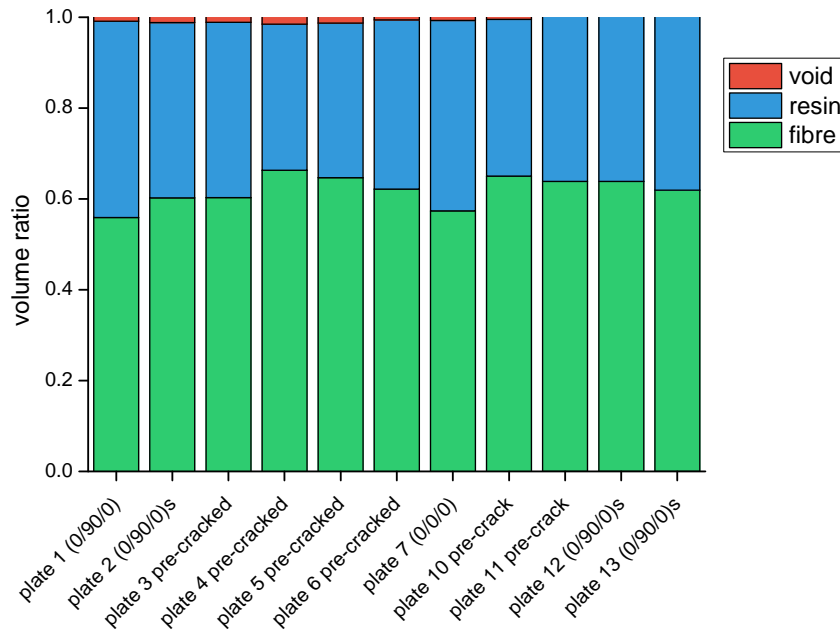


Figure 2.6 – Measured composition of the infused composite plates

The composite plates were cut with a wet diamond saw to the specimen dimensions and all cut surfaces were wet polished to limit rough surfaces that may lead to early failures.

2.1.3 Sizing

The fibres used in both the previously-presented composite differs in term of areal weight. However, the elementary fibres remains the same in both cases. Therefore, the sizing is not expected to change between the two composites. However, the nature of the sizing was not known in this study as these are commercial materials.

2.2 Test methods

This thesis is focussed on seawater ageing effects on composite materials. Different test methods were employed in order to evaluate mechanical properties, but there were also original ageing methods and analyses developed. This section will present the tests, ageing procedures and data processing methods used to carry out this study.

2.2.1 Ageing methods

Accelerated seawater ageing

Seawater ageing of both composite and pure resin specimens was performed in seawater baths, Figure 2.7. Five different temperatures were used in this study: 4, 15, 25, 40 and 60 °C. The seawater baths are filled with natural seawater pumped from the Brest Estuary and it is continuously renewed.

Other wet ageing was performed on the pure resin using temperature and humidity controlled ovens. These ageing studies were carried out at 33, 50 and 75 % relative humidity at 40 °C. The ovens used for this were Memmert® HCP 108 and HPP110.

Physical ageing

Physical ageing was applied in two different ways. The first relates to dry material. This ageing was done in Memmert™ UFE 400 and UFB 500 ovens at 40, 50 and 60 °C. The samples were placed in vacuum bags, as shown in Figure 2.8, in order to limit unwanted reactions such as oxidation.

The second physical ageing method was for the seawater-saturated samples. For these, samples were previously saturated in seawater and then placed in the seawater baths at 15, 25 and 40 °C. For both these ageing conditions, a rejuvenation of the material was performed. This rejuvenation consists of “erasing” physical ageing present in the material by exposing it to above-T_g temperatures. To do so, samples were placed in zip-bags and then immersed in a 90 °C water bath for 5 minutes. Then to quench the material, the zip-bags were immediately plunged in the 15 °C water bath also for 5 minutes.



Figure 2.7 – Temperature-controlled seawater ageing baths

2.2.2 Tests on the materials

Mechanical tests

Most of the mechanical tests performed in this study were based on ASTM and ISO standards. Certain test methods were slightly modified, in particular to enable tests to be performed immersed in water. There are few standards for fatigue tests of polymer matrix composites. ISO 13003 [145] gives indications on the number of specimens per stress level, number of stress/strain levels and indications on stress/strain ratios to be tested. ASTM D6115 [126] presents indications for fatigue under mode I DCB loading and ASTM D3479 [97] for tension-tension fatigue of polymer matrix composites. The majority of the fatigue tests here followed ISO 13003 indications.

Four point bending test The composites were tested in flexure using a four point bending test. Four point was chosen over three point due to the pure flexure induced in the central zone and the reduction in indentation loading. In addition, it is a test that has been performed at Ifremer on various materials on the past, allowing comparison to be made. The four point bending tests were performed according to ASTM D6272. Span to depth was chosen to be 32 to 1. Span to depth value has an influence on failure mode

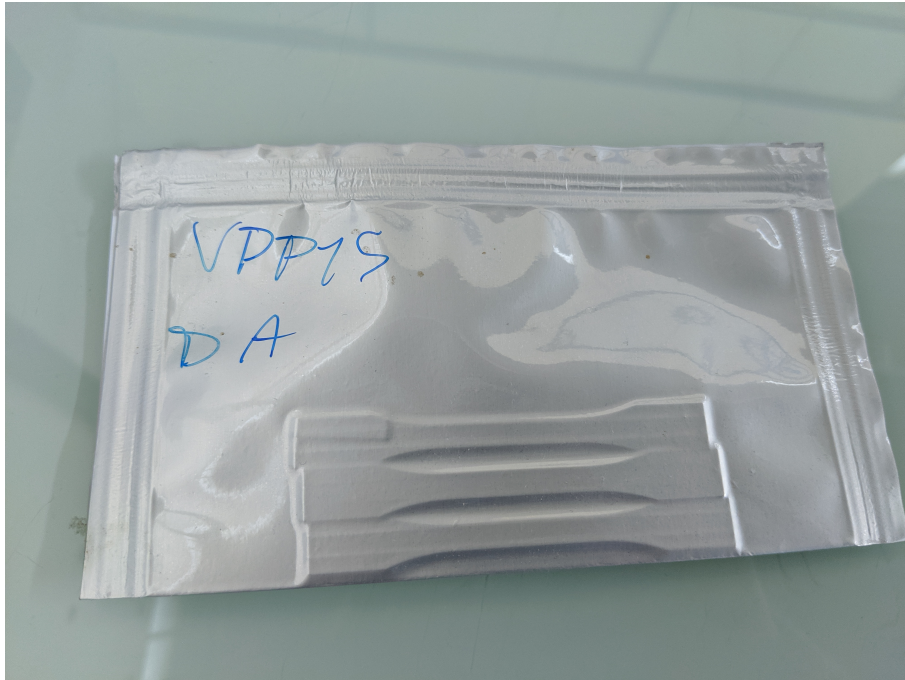


Figure 2.8 – Vacuum bagged resin tensile samples

and modulus measurements. For highly reinforced unidirectional composites, the ASTM standard recommends 16:1, 32:1 or even 60:1 span to depth ratios. Increasing span-to-depth ratio is required to obtain accurate modulus measurements as lower span-to-depth ratios increase shear stresses.

The nominal specimen dimensions were $(125 \times 25 \times 3) \text{ mm}^3$. Static tests were performed at 5 mm.min^{-1} so that a strain rate of 1 \%.min^{-1} was applied to the specimen's outer surfaces. Five specimens were tested for static tests and 3 specimens per stress level for fatigue tests. All four-point flexure tests were performed immersed in renewed natural seawater, at a temperature of $25 \text{ }^\circ\text{C}$ (Figure 2.9). A schematic drawing of the test fixture is shown in Appendix F. The effect of frequency was studied and will be presented later. The load ratio was fixed at $R = 0.1$. Fatigue tests were carried out on two identical Zwick-Roell HC-25 servo-hydraulic test machines. The load-cells were identical SENSOTEC[®] 41E50KN0 load cells with a 50 kN range. Displacement measurements were made with an internal LVDT. The test data was recorded on a Spider 8[™] measurement system using CatmanAP[™] software.

Tensile tests Both the RTM composite and the pure resin were tested in tension. The tensile tests for the composite were performed according to ASTM D3039 [96]. The load speed was 1 mm.min^{-1} . Quasi-static tests were carried out on a 200 kN Instron[™] 5500R electro-mechanical machine. For the fatigue tests a 250 kN MTS[™] servo-hydraulic test machine was used. Fatigue tests were carried out with a load ratio of $R = 0.1$ and a frequency of 1 Hz . The 1 Hz frequency was chosen to limit self-heating. The specimen dimensions were identical for quasi-static and fatigue tests and were $(250 \times 25 \times 3) \text{ mm}^3$ The



Figure 2.9 – Immersed fatigue four point bending test

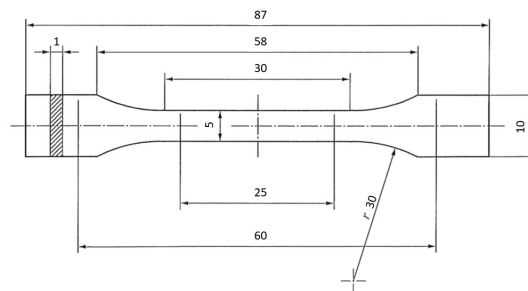


Figure 2.10 – Pure resin tensile specimen's dimensions

pure resin was tested according to the ISO 527-2 standard [146]. The specimen dimensions were those of the 1Ba geometry, with a thickness of 1mm . The dimensions are shown in Figure 2.10. A load speed of $1\text{ mm}\cdot\text{min}^{-1}$ was chosen for pure resin tensile tests. The specimens were tested on an InstronTM 5966 test machine with an InstronTM 2580-500N load cell. The specimens were held by pneumatic grips. Laboratory conditions were controlled at $21 \pm 1\text{ }^{\circ}\text{C}$ and $50 \pm 5\%$ of relative humidity.

For quasi-static tests on resin and composite, strain measurement was made by Digital Image Correlation (DIC). To do so, composite specimens were painted white on one side then graphite powder was sprayed on, so that a random black and white pattern appeared on the specimen. For pure resin specimens, as samples were semi-transparent, only graphite powder was sprayed and samples were illuminated from behind. Examples of the random patterns on composite and pure resin are shown in Figure 2.11.

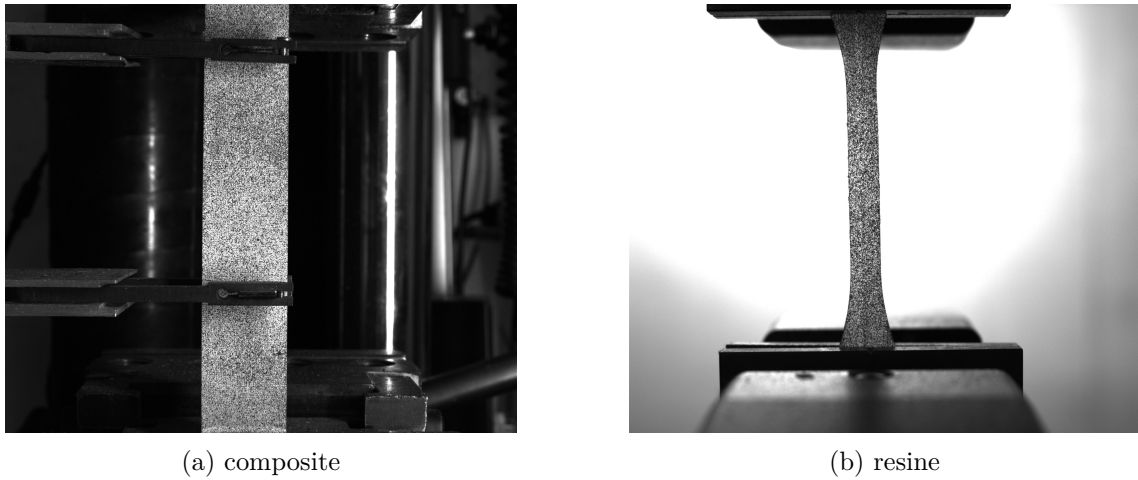


Figure 2.11 – Example of random pattern on composite (a) pure resin (b)

In fatigue tests, specimens were instrumented with an acoustic emission (AE) system. This uses two Micro80™ piezo-electric transducers so that damage can be localised within the specimens and to prevent recording of parasite signals. The acquisition system was a Mistras™ PCI2 and the software was AEwin for PCI2. An example of a specimen with the transducers clamped at the ends is shown in Figure 2.12. Silicone grease is used as a coupling agent between the sample and the sensitive surface of the transducers. Good coupling between the samples and the transducers was verified prior to each test, together with localisation calibration by pencil lead break.

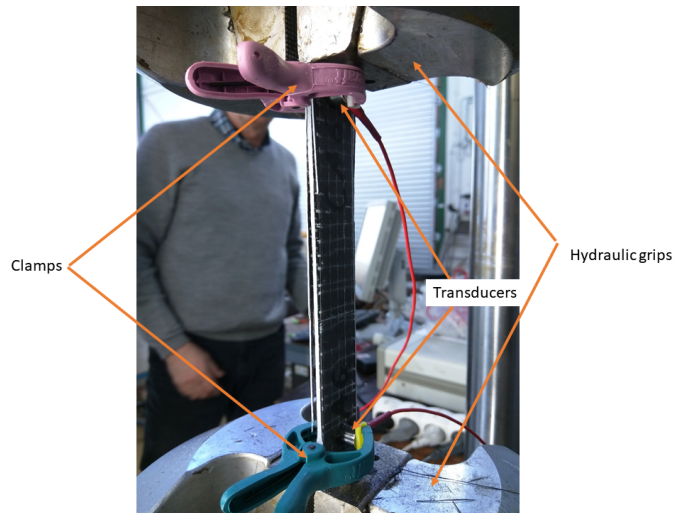


Figure 2.12 – Acoustic emission system on a composite fatigue tensile test

Equipment was already in the laboratory but the test methodology was developed during this study. The data analysis was developed by Malick Diakathe, a researcher from Brest University, working in collaboration to process the AE data acquired during

all tensile fatigue tests.

Interlaminar shear strength Interlaminar shear strength tests were performed according to ISO 14130 [147]. Samples dimension were $(20 \times 5 \times 3) \text{ mm}^3$. The loading rate was 1 mm.min^{-1} at a room temperature of $21 \text{ }^\circ\text{C}$ and 50% relative humidity.

Delamination of the composite

Mode I : Double Cantilever Beam (DCB) The Double Cantilever Beam test configuration was chosen for mode I delamination resistance measurements, according to the ISO 15024 standard [123]. Quasi-static tests were performed on an Instron™ 5966 electromechanical test machine. The load cell was an Instron™ 2580-500N with $\pm 500 \text{ N}$ capacity. The tests were done at $21 \text{ }^\circ\text{C}$ and 50% relative humidity. For quasi-static tests, the crack length measurements were made visually. To do so, one of the edges of each specimen was first painted white with a water-based Posca™ pencil leaving a thin layer of mat paint. During the test, a camera took pictures at one frame per second, measurement of the crack length was reported in post processing. Graph paper was then bonded to the upper-face of DCB specimens allowing a clear indication of crack length as shown in Figure 2.13a. It is sometimes easier to distinguish the crack tip by looking at the negative image as shown in Figure 2.13b.

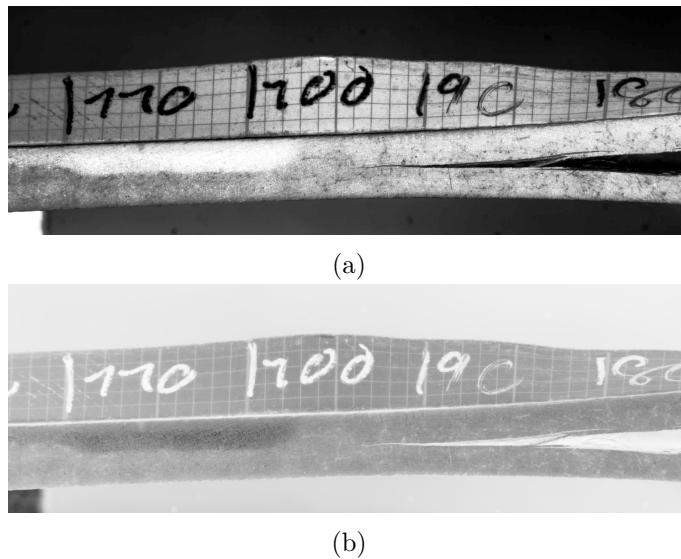


Figure 2.13 – Crack length measurement by visual analysis regular (a) and negative (b) image

The energy release rate was calculated according to the Compliance Calibration (CC) method presented in the ASTM standard. The calculation of G_I in J/m^2 is:

$$G_{Ic} = \frac{nP\delta}{2ba} \quad (2.1)$$

Chapter 2. Materials and methods

In this equation, n is the slope of $\log(C)$ versus $\log(a)$ curve. P is the load in N corresponding to the opening displacement δ in mm and a crack length a in mm with a specimen width of b in mm.

For fatigue tests, crack length was calculated and the calculation will be presented below.

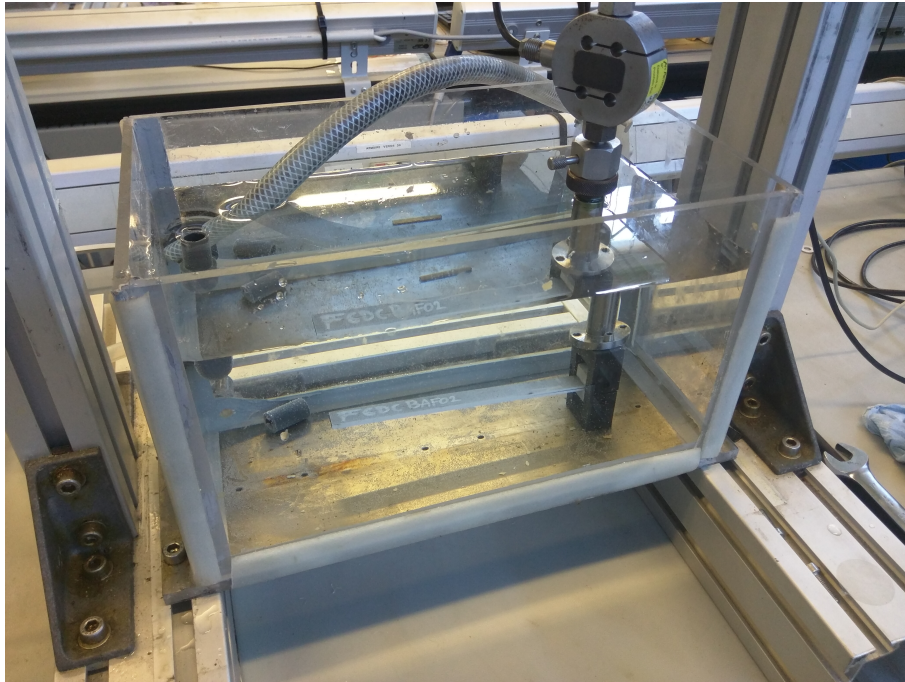


Figure 2.14 – DCB immersed in water fatigue fixture

Fatigue specimens were loaded by electric actuators under displacement control according to ASTM D6115 [126]. The test frequency was 2 Hz and the R ratio was $R = \frac{D_{min}}{D_{max}} = 0.1$. The specimens were loaded for 1 million cycles, load was recorded with a Quantum™ MX 840A acquisition system with CatmanAP™ V5.2.2 software. Displacement was recorded with a NovoTechnik® TR-0100 LVDT and load with an AEP transducers® TS 500 N load cell. The test system was mounted in a small bath, so that tests could be performed immersed in tap water, Figure 2.14. A schematic drawing of the test fixture is shown in Appendix F. This particular setup was developed during this thesis. For the unaged and dried conditions, specimens were tested in air, whereas for the saturated condition they were tested immersed in water, in order to maintain the water content in the sample.

Mode II: Calibrated-End Loaded Split (C-ELS) There are many ways to test composite materials under mode II delamination as discussed in Chapter 1. Among these, the End Loaded Split test was chosen here. This test method is the only official international standard, reference ISO 15114 [138]. It has the advantage of producing stable crack growth provided under usual $\frac{a}{L}$ dimensions ($\frac{a}{L} > 0.55$), and these are close to those of the DCB. It also has the advantage of allowing a longer crack length to be tested compared

to the 3 and 4 End Notch Flexure (3ENF and 4ENF) specimens.

The Corrected Beam Theory with Effective crack length (CBTE) data reduction method was used for quasi-static tests with G_{IIc} obtained using the following expression:

$$G_{IIc} = \frac{9P^2 a_e^2}{4b^2 h^3 E_1} \quad (2.2)$$

Once again, tests could be performed in a specially designed water bath, Figure 2.15. A schematic drawing of the test fixture is shown in Appendix F. This setup was also developed during this study.

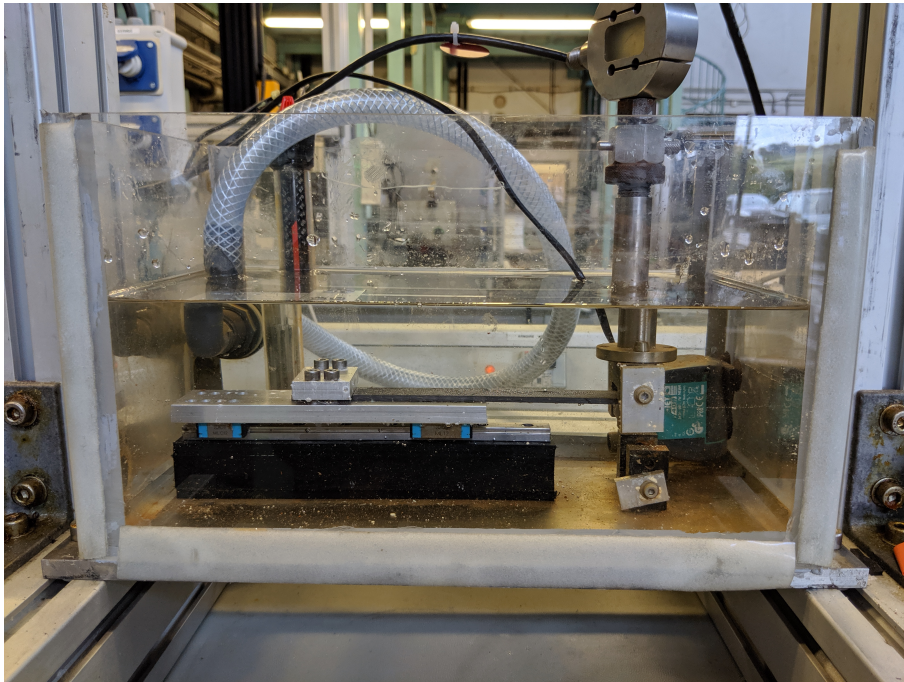


Figure 2.15 – Water immersed C-ELS fatigue fixture

Data reduction of crack fatigue tests A similar data reduction method was used for both mode I and mode II crack fatigue tests. The input data for post-processing was load and displacement: minimum and maximum values were recorded every 2 cycles (min and max data every 1 second for a load frequency of 2 Hz). In addition to these test data, specimen width, b , thickness, h , initial crack length, a_0 , and final crack length, a_f , were measured.

The data analysis was then carried out with an in-house R code that was developed and written in this study. R is capable of a high number of data processes which is an advantage in our case as each fatigue test has 500 000 lines each with 4 columns of data. The main codes are given in Appendix C.

A critical part of the data analysis is the determination of crack length. A preliminary study was performed using crack gauges (Figure 2.16) from Teksym[®] bonded to the



Figure 2.16 – Example of a DCB-100 crack gage from Teksym®

specimens, in order to try to automate the measurement. However, this revealed several problems, in particular the gauge appeared to affect the crack advance resulting in a non-parallel crack propagation. In addition to that, the results from crack measurement versus calculated crack length only showed a small constant shift of the measured crack length. In order to establish da/dn curves, only the trend of crack length as a function of the number of cycles is needed. Then, a constant shift of the crack length value will not change the resulting value of da/dN and as the shift was below 1 mm, it is also expected not to change drastically the value of the calculated energy release rate. More informations on the principle and the results are exposed in Appendix E. The crack length was therefore calculated for the entire number of cycles. For mode I, compliance calibration is used. Compliance is calculated as:

$$C = \frac{\delta_{max} - \delta_{min}}{P_{max} - P_{min}} \quad (2.3)$$

A linear regression of $\log(C)$ versus $\log(a)$ gives the value of the slope n and the intercept d . The value of crack length in mm at each cycle is finally calculated as:

$$a = 10^{\frac{\log(C) - d}{n}} \quad (2.4)$$

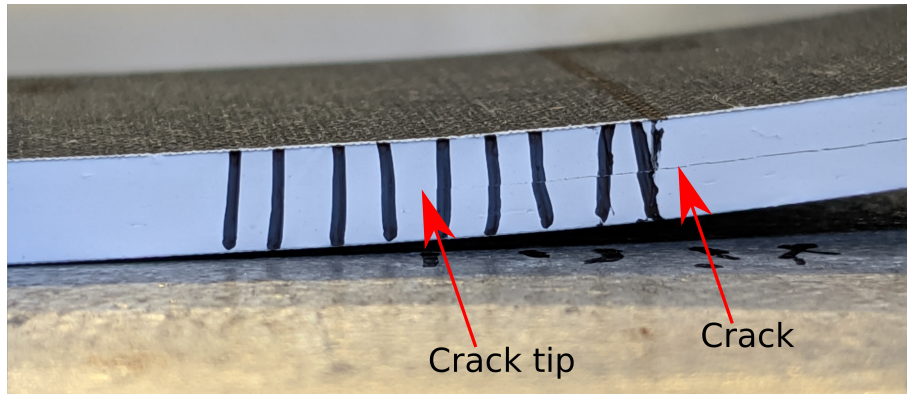


Figure 2.17 – Example ELS specimen being loaded showing the difficulty to measure the crack length precisely

For the mode II delamination, Only the free length L is added to the input data. Compliance is calculated as in Eq. (2.3). It is slightly harder to get the crack length value than for mode I as visual measurements are more difficult (see Figure 2.17). So, crack length is calculated using Eq. (2.5); at $C = C_0$ crack length is equal to a_0 and at $C = C_f$ it is equal to a_f . Then Eq. (2.6) can be written, giving the value of E after simplification

of Eq. (2.7). Finally, Δ_{Clamp} can be calculated by Eq. (2.8 with either (C_f, a_f) or (C_0, a_0) values. At this stage, the value of effective crack length at every cycle can be calculated with Eq. (2.5) and the value of maximal G_{II} at every cycle by the Eq. (2.2) using P as the maximum load for the specific cycle.

$$a_e = \left[\frac{1}{3} \left(2bCh^3E - (L + \Delta_{Clamp})^3 \right) \right]^{\frac{1}{3}} \quad (2.5)$$

$$3(a_f^3 - a_0^3) = \left(2bC_f h^3 E - (L + \Delta_{Clamp})^3 \right) - \left(2bC_0 h^3 E - (L + \Delta_{Clamp})^3 \right) \quad (2.6)$$

$$E = \frac{3(a_f^3 - a_0^3)}{2bC_f h^3 (C_f - C_0)} \quad (2.7)$$

$$\Delta_{Clamp} = \left(2bC_f h^3 E - 3a_f^3 \right)^{\frac{1}{3}} - L \quad (2.8)$$

At this stage, for both mode I and mode II, we have the value of energy release rate with the corresponding crack length value. The value of the crack growth rate is given by the slope of crack length versus number of cycles. To obtain this, $\frac{da}{dN}$ is approximated by a linear regression for every crack length increase of 0.1 mm. This final part was processed on Excel[®].

Physicochemical analyses

Several physicochemical test methods were used to characterise the materials, check their initial state and follow changes with ageing.

Differential Scanning Calorimetry (DSC) Glass transition temperature (Tg) and physical ageing effects were measured by Differential Scanning Calorimetry (DSC). The system is a TA Instrument Q200TM. The heating rate was 10 °C.min⁻¹. Two ramps were performed on each sample, both from -5 to 120 °C, in order to measure Tg and Tgmax. The tests were performed under N₂ gas at a flowrate of 50 mL.min⁻¹.

ThermoGravimetric Analysis (TGA) ThermoGravimetric Analysis (TGA) was used to measured fibre volume ratio. These analyses were performed on a TA Instrument SDT Q600TM. Resin burn-off was carried out under nitrogen, in order not to oxidize carbon fibres. The burn-off conditions were 800 °C for 20 minutes.

Pycnometer Both composite and matrix densities were measured using a Micromeritics AccuPyc IITM 1340 helium pycnometer. Based on TGA and pycnometer values, the fibre, resin and void volume ratios can be calculated with respect to ISO 14127 standard [148]. The equations are:

$$V_f = \frac{m_f \times \rho_c}{\rho_f} \quad (2.9)$$

$$V_r = \frac{(1 - m_f) \times \rho_c}{\rho_r} \quad (2.10)$$

$$V_v = 1 - (V_f - V_r) \quad (2.11)$$

Chapter 2. Materials and methods

The value of fibre mass ratio, m_f , is measured by TGA; ρ_c and ρ_r correspond respectively to composite and resin densities that are measured by the pycnometer and ρ_f was measured to be $1.79 \pm 0.01 \text{ g.cm}^3$. The latter is very close to the manufacturer's datasheet value.

Microstructural analysis

Different inspection techniques were used for quality control, fracture surface examination and damage analysis.

Optical microscopy Optical microscopy was carried out at the IUT de Brest (Brest University). The microscope used was a Keyence VHX 6000[®].

Scanning Electron Microscopy (SEM) Scanning Electron Microscopy (SEM) images of fracture surfaces were taken at Ifremer. The system used is a FEI Quanta 200[™] by Thermo Fisher. Images were taken at $1.5 \cdot 10^{-4} \text{ mbar}$, the maximum vacuum capacity is 10^{-6} mbar . The samples were covered by pure gold with Balzers SCD 400[®] equipment under argon gas. The gold layer was 15 to 20 nm and allowed good reflection of electrons on the specimen's surface without charging. The electron beam is generated by a tungsten filament.

Ultrasonic C-scan In order to control the composite plate's quality and follow damage during interrupted four point bending tests, ultrasonic C-scans were performed. The system is a Sofratest[™] 49944. The transducer used for quality control was an ULTRAN[®] WS 50-5P2, which produces a focal zone of 1.18 by 33.15 mm^2 in water. The measurements with this transducer were taken every millimetre. This transducer was used to map the whole composite plates. A second transducer was used for the interrupted four point flexure tests, an ULTRAN[®] WS 75-10-P76, that produces a smaller focal zone of 0.6 by 16 mm^2 . This transducer allows a more refined measurement and therefore measurements were taken at every 0.3 mm.

X-ray tomography Along with C-scan, a number of interrupted four point flexure tests were also scanned by X-ray tomography, both prior to fatigue tests and after cycling. The measurements were performed at the CRT de Morlaix (Technical Resource Centre of Morlaix). The high-resolution tomography machine is a GE/Phoenix V|tome|xsv. Its power is 240kV with a 2048 by 2048 sensor and minimum 5 μm resolution (Figure 2.18). The measurements performed in this thesis were made at a 10 μm resolution.

The reconstructed volumes were then analysed by VG Studio[™] in order to identify defects and damage present in the material.

Computational processing

Unsupervised data classification Unsupervised data classification or data clustering was used for both acoustic emission (AE) and x-ray tomography data. The code for AE was developed by a researcher from Brest University on Matlab[™] and transposed to R[®].

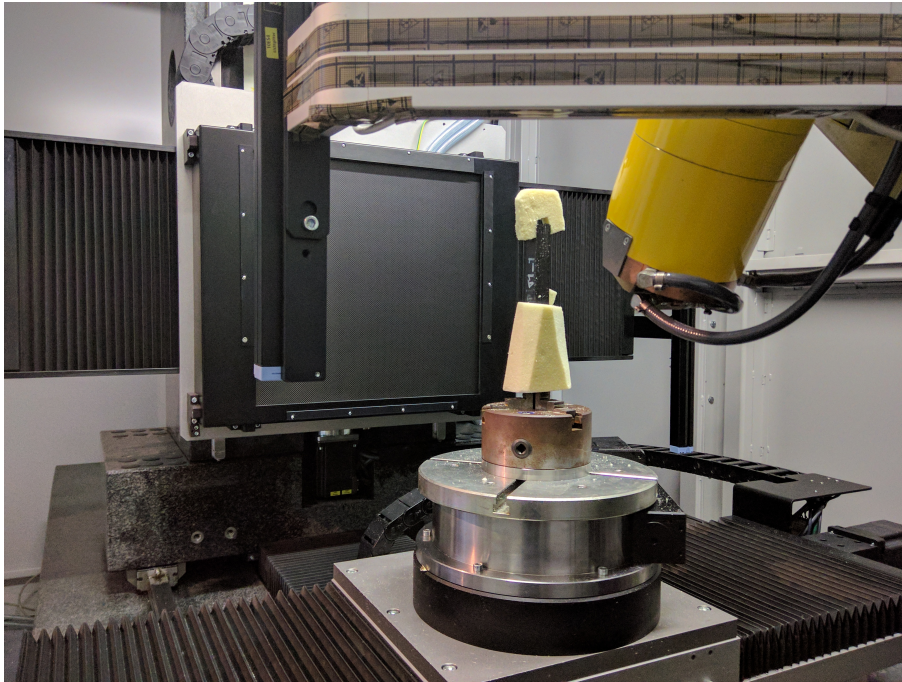


Figure 2.18 – X-ray tomography machine from CRT of Morlaix

The code for the tomography data analysis was developed during this study. The goal of this method is to classify a population of data by similarities. The similarities arise from different properties that correspond here to data measurements such as amplitude, energy or number of counts for AE and void dimensions, orientations, surfaces for tomography data.

The classification was coded on the software R that is part of the CRAN (Comprehensive R Archive Network). R is free software that is well known for its statistics and data mining ability. The code is given in Appendix C.

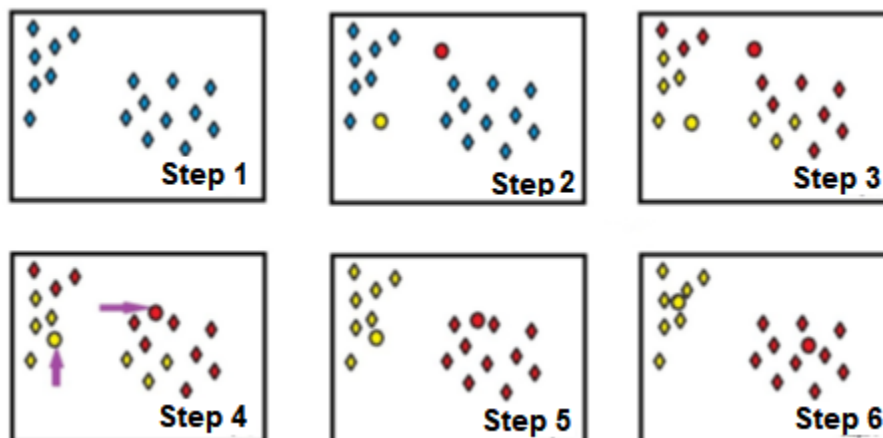


Figure 2.19 – Illustration of k-means clustering on a simple set of data [149]

The principle of the K-means method is illustrated on Figure 2.19. On this figure, a set of data is classified by two clusters. At first, two random centres are created (Step 2). Each data point is attributed to its nearest centre, by calculating the distance of from the data point to each centre and then each data point is attributed to the nearest centre, here illustrated by the red and yellow sub-data sets (Step 3). For each sub-data set, the centre of gravity is calculated and becomes the new sub-data centre, this is step 4. A new matrix of distances of each data point to the new centre is created. The data points are then re-attributed to their respective nearest centre (Step 5). The previous steps are repeated until a convergence is obtained. Then the whole data set is properly clustered.

In this example, an arbitrary number of clusters have been used. In order to optimize the number of clusters, two methods can help determining the optimum number of clusters as seen in Figure 2.20. The signification of these criteria is as follows:

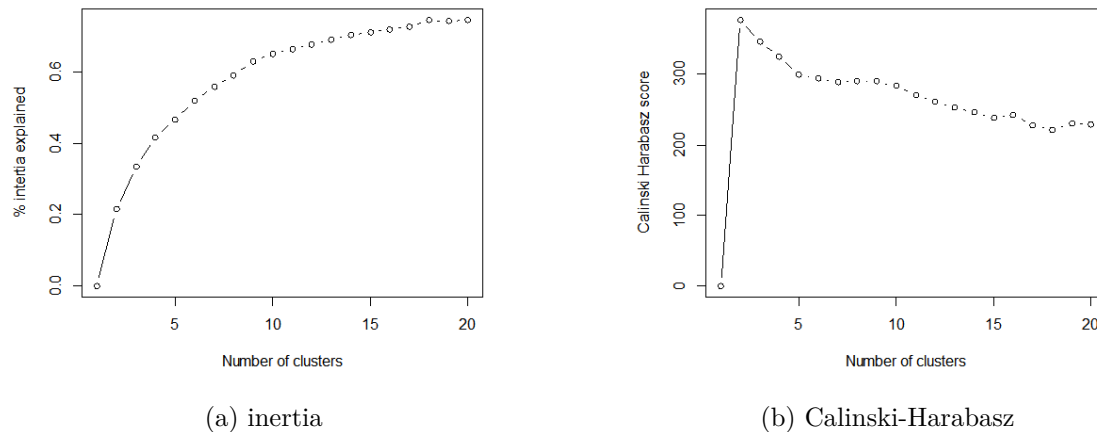


Figure 2.20 – Optimisation of the number of clusters with inertia criterion (a) and Calinski Harabasz criterion (b)

- The first method is to calculate the inertia as a function of cluster number. The number at which adding one cluster does not increase significantly the inertia corresponds to the optimized number of clusters.
- The second method is to calculate the Calinski-Harabasz (CH) value. The CH value is a ratio between cluster distances from one another and the inner distance of the data-points within these clusters. The value of the CH criterion is illustrated in Figure 2.21.

Based on these two criteria, an optimal number of clusters is found and the dataset is clustered with the kmeans function of the R software. The distribution of the different classes as a function of different parameters can then be studied. For example, the association of a cluster of AE data to a specific damage mechanism in the composite can then be defined as in [150–153].

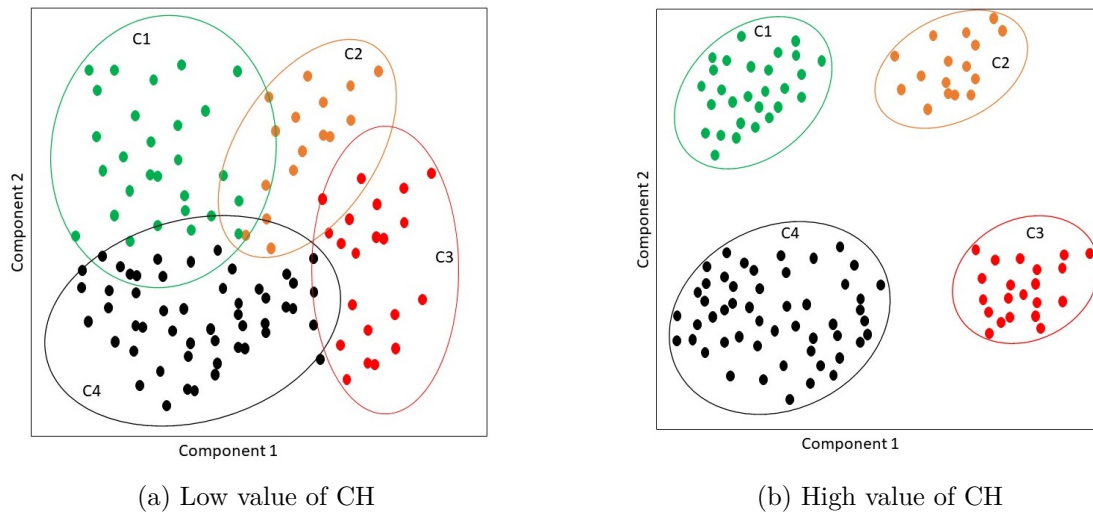


Figure 2.21 – Illustration of the CH criterion: low value (a) high value (b)

Fick, Whitney’s Pooling Scheme and KWW identification Diffusion coefficients and masses at saturation were identified by a least-square method. The one dimensional Fickian equation was written on Scilab™ and fitted with the `leastsq` function. The same function was used to fit the Kolrausch Williams Watts equation for physical ageing.

For Whitney’s Pooling Scheme (WPS) identification, equations from [119], that were explained in Chapter 1, were also coded in Scilab™. Identification of parameters was done with the `fsolve` function. The detailed Scilab codes for Fick, KWW and WPS identification that were developed during this study can be found in Appendix B.

Water diffusion

Tidal turbines and marine propeller blades are designed with lifespans of several decades. Using composite materials to fabricate those systems involves understanding and quantifying the kinetics of diffusion, as water can affect resin and composite mechanical properties. Knowing the kinetics of water diffusion and hence the distribution of water within the composite is essential in order to predict long term mechanical behaviour of composites. In order to examine water ingress, the study focussed on the pure resin first. Then, tests on the composite and comparison between the expected diffusion characteristics based on water diffusion only in the resin and the experimental results are presented. Finally, the diffusion of water into a composite propeller blade has been calculated.

3.1 Resin

At deep sea levels, it is commonly stated that seawater temperature is close to 4 °C, while the temperature of seawater at the surface near the equator region could reach 35 °C or more. In our use cases, tidal turbines are most likely to be immersed in 20-30 meters water depth, which would correspond to temperatures below 15 °C. The propeller blades, on the other hand, could be exposed to high and low temperatures depending on the boat's geographical position. The temperature range seen for these two cases is likely to be between 25 and 4 °C.

In order to accelerate the water ingress in the resin, higher temperatures have been applied. Four different temperatures were used for pure resin ageing tests: 4, 25, 40, and 60 °C. Figure 3.1 shows the water uptake of the neat resin at these four temperatures for a maximum period of 400 days. On this graph, time is expressed as the square root of hours divided by the sample's thickness. This allows a first qualitative evaluation of the diffusion behaviour, particularly whether or not a Fickian behaviour can be identified.

Water uptakes at the different temperatures show the same behaviour. The initial part of the curve shows a linear increase and then reaches a plateau. Superposing the water uptake of 1 and 3 millimeters thick samples on the same graph also shows similar trends, if the x axis is shown as square root of time divided by thickness. From these different characteristics, a Fickian behaviour can be identified as shown in Figure 3.2.

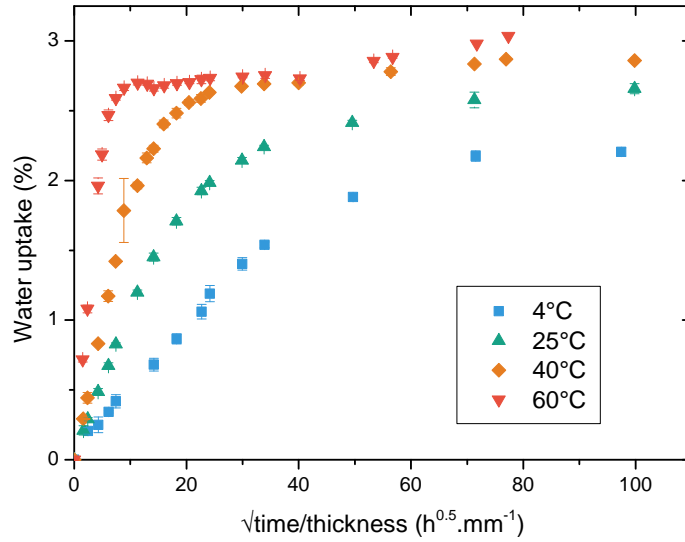


Figure 3.1 – Water uptake of pure resin; 1 mm thick coupons. (error bars are shown for all conditions)

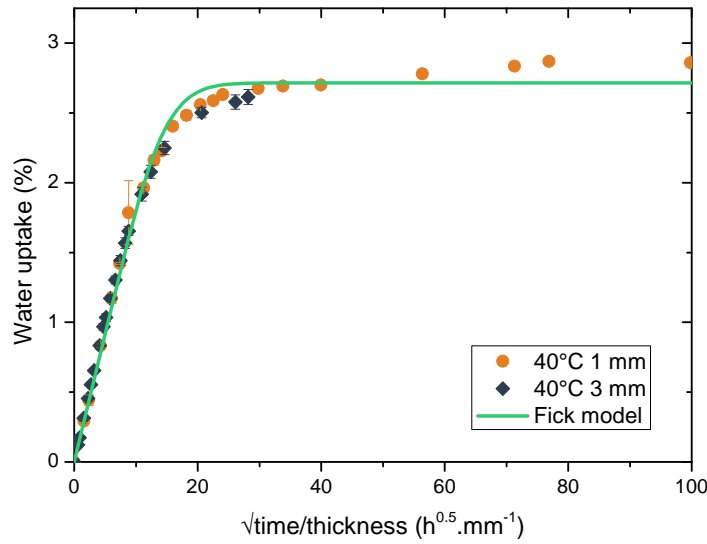


Figure 3.2 – Water uptake of pure resin at 40 °C in seawater

Although the water uptakes seem to follow Fick’s law, there is a small deviation from the plateau for the longer times. This deviation could come from oxidation of the resin. In fact, the samples tend to change colour towards a more yellowish colour that is typi-

cal of oxidation. In addition, Richaud et al. and Delozanne et al. showed that oxidation can create polar groups, in the molecular chains, which may increase the mass to saturation [154, 155]. Figure 3.3 shows the visual aspect of four of the resin samples that were aged for 660 days from 4 to 60 °C. One can see that between 25 and 4 °C, there is no major change in colour whereas at 40 and even more at 60 °C, the resin turned to an orange, near brown, colour. Oxidation is known to be thermally activated. In service seawater would not reach such temperatures and then oxidation will occur at a reduced ageing time. Therefore, Fickian behaviour was retained as the diffusion behaviour for the material.

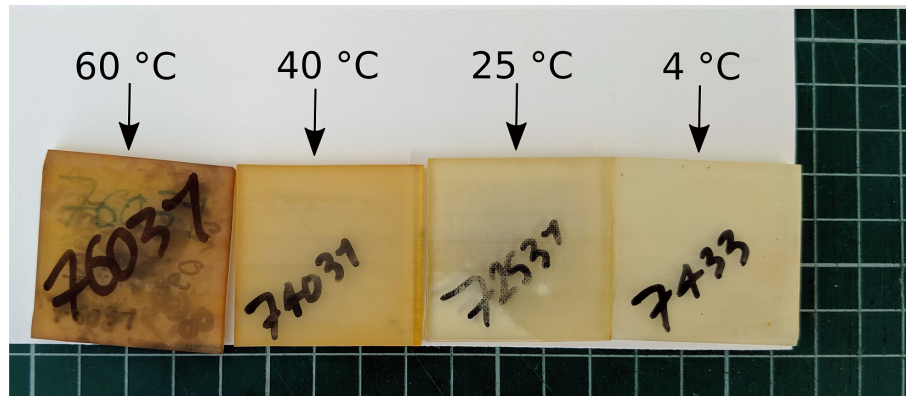


Figure 3.3 – Coupons of 3 mm in thickness aged in seawater for up to 660 days at 60, 40, 25 and 4 °C (from left to right)

The diffusion parameters were calculated for all temperatures. These two parameters are the diffusion coefficient D and the moisture content at saturation M_{∞} . The temperature dependence can be expressed with an Arrhenius law as shown in Figure 3.4 for the diffusion coefficient. Results for the solubility as a function of temperature according to the Arrhenius law are shown in Figure 3.5. The solubility, S_{∞} , in $mol.L^{-1}$ is measured as:

$$S_{\infty} = \frac{M_{\infty}}{M_{H_2O} \times a_w} \times \rho_r \quad (3.1)$$

In this equation M_{∞} is the mass at saturation in %, $M_{H_2O} = 18 g.mol^{-1}$ the molar mass of water, a_w the water activity, here 0.98 for seawater, and finally, ρ_r is the resin density in $g.L^{-1}$.

The activation energy measured for the diffusion coefficient corresponds to published values in the literature, which usually vary between 40 and 70 $kJ.mol^{-1}$ depending on the epoxy chemistry [57, 156, 157]. The reasonable agreement of D and M_{∞} with an Arrhenius law confirms that the accelerated ageing can be used to accelerate diffusion which will occur during the in-service use of the material.

On this graph, we can see that the solubility of the 3 mm thick samples is lower compared to that of the 1 mm. An explanation could come from the void ratios. In fact, measurements of densities on 1 and 3 mm samples showed that the resin density of thinner samples was higher, respectively 1.1739 and 1.1473 $g.cm^{-3}$.

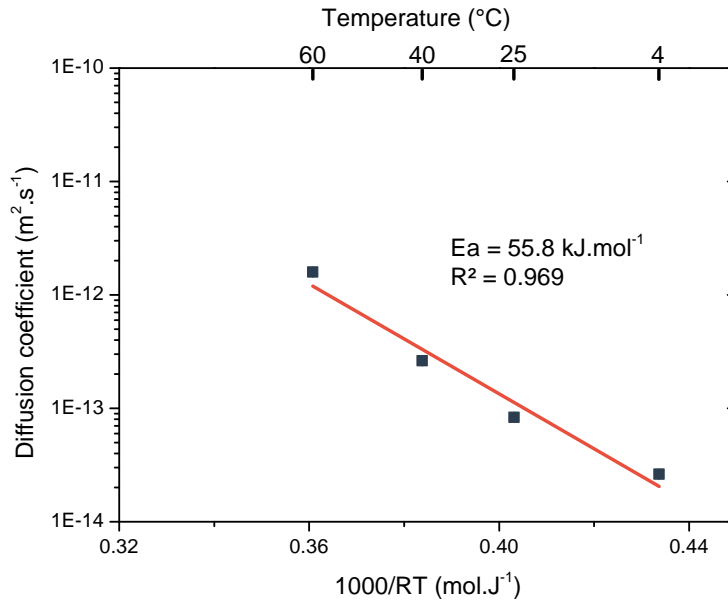


Figure 3.4 – Arrhenius plot of diffusion coefficient for the pure resin in seawater

Additional water uptake measurements were made at different water activities at 40 °C. For these ageing conditions, samples were placed in controlled relative humidity ovens at 33, 50 and 75 % relative humidity. The results are different saturation levels for the four different water activities considered (the fourth condition being a water activity of 0.98 for seawater). All three additional conditions were fitted with a Fick law and showed good agreement (Figure 3.6). This result is not surprising as Fick's diffusion is based on a difference in concentrations between two media. Here, the diffusing media is just less concentrated but the kinetics remain the same.

The main difference here is that by reducing the relative humidity, the mass to saturation decreases.

In conclusion, the water absorption of the pure resin was identified as Fickian even though small deviations could suggest another model of diffusion. The saturation level of the resin is slightly over 2.5 %, which is a typical value for an amine based epoxy resin. The solubility and diffusion coefficient were found to comply with the Arrhenius law for ageing temperatures ranging from 4 up to 60 °C. This indicates the possibility to extrapolate each respective value to lower temperatures. It is now of interest to evaluate whether water ingress in the composite can be predicted from the resin's diffusion behaviour. If so, this could facilitate the prediction of water ingress in composite parts and allow quicker characterization.

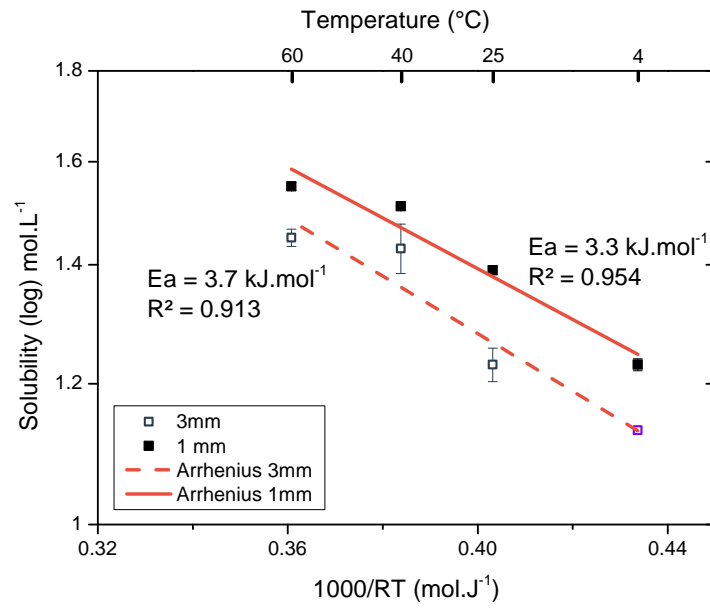


Figure 3.5 – Arrhenius plot of the solubility for the pure resin in seawater

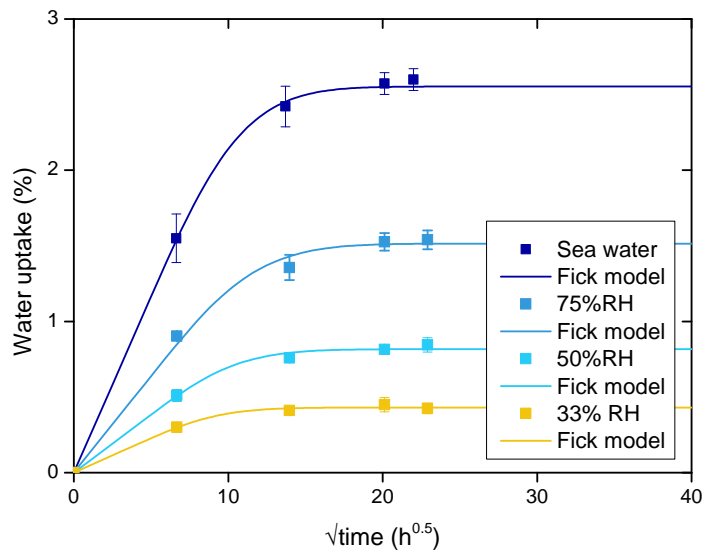


Figure 3.6 – Water uptake on the pure resin at different relative humidities

3.2 Composite

As most of the mechanical tests were performed on the RTM composite, this section will present the results for this composite. The water uptake of the infused composite is detailed in Appendix D.

The water uptake of the resin has been characterized. At this stage, it is necessary to perform the same characterization with the composite, as this is the material in use for the different blade systems; the resin being only one of its constituents. In order to do this, composite coupons have been immersed at the same temperatures as for the resin. The resulting water uptakes were once again in agreement with Fick's diffusion law. Unfortunately this time, only 3 mm thick coupons were available. The water uptake at the four temperatures for a time of up to 400 days are shown in Figure 3.7.

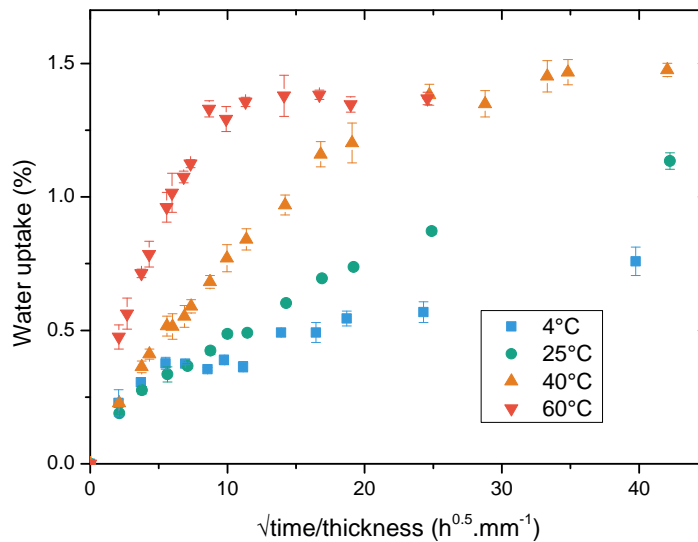


Figure 3.7 – Water uptake of RTM composite immersed in seawater

One can clearly see the accelerating effect of temperature on the diffusivity of the composite. The Fickian behaviour of the diffusion is identified here even though it was not confirmed by the diffusion on two thicknesses as only 3 mm thick samples were studied. The Fickian model showed good agreement with the experimental values. This time though, the mass to saturation appears to be at a lower level than for pure resin, being around 1.5 % at 40 °C (see Figure 3.8).

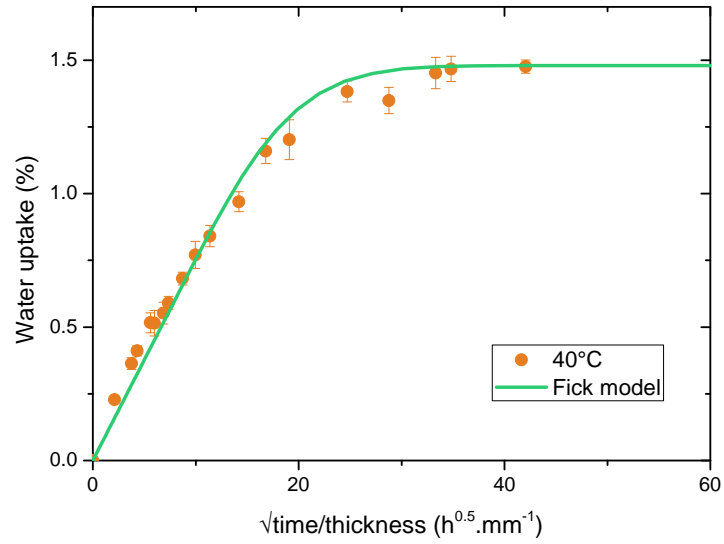


Figure 3.8 – Water uptake of RTM composite in seawater at 40 °C

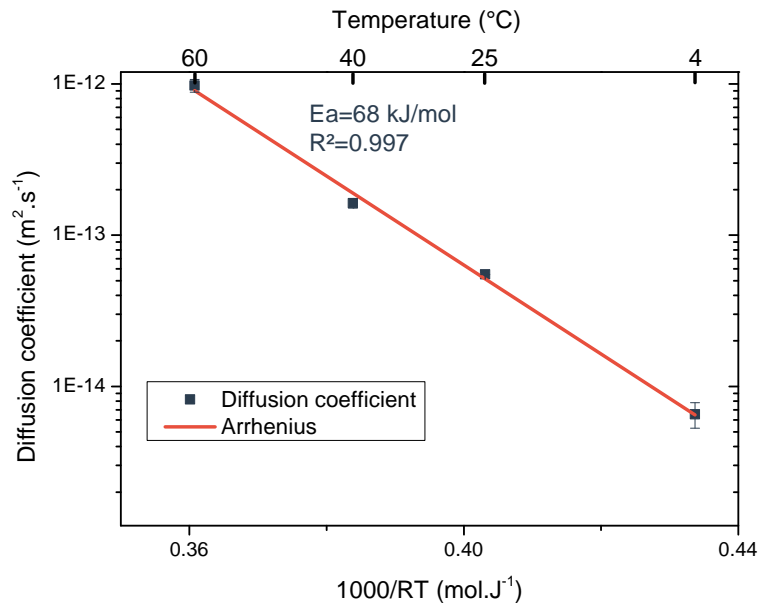


Figure 3.9 – Arrhenius plot of diffusion coefficient for the RTM composite

As with the pure resin, the diffusion parameters dependency on temperature was studied. The temperature dependence of the diffusion coefficient of the composite was found to be in good accordance with an Arrhenius law (Figure 3.9). The measured activation energy is around 68 kJ.mol^{-1} , i.e. 10 kJ.mol^{-1} higher than for the pure resin. This may come from the insulating characteristic of carbon fibres. In addition, one can observe that the diffusion in the composite is slower compared to that of the pure resin. In fact, the theoretical time to saturation can be derived from Eq. (1.2) by considering $M(t)$ equal to M_∞ giving :

$$t_{sat} = \frac{\pi(2h)^2}{16D} \quad (3.2)$$

In this equation, t_{sat} is the time to saturation in seconds with the diffusion coefficient D in $\text{m}^2.\text{s}^{-1}$ and the thickness h in metres. The times to saturation at each temperature are shown in Table 3.1.

Table 3.1 – Theoretical time to saturation of the composite and pure resin for different ageing temperatures

Ageing temperature	Time to saturation for a 3 mm thick immersed plate (days)			
	4 °C	25 °C	40 °C	60 °C
Resin	3122	984	311	51
Composite	12509	2850	501	83

On the other hand, the trend of the solubility as function of temperature has more scatter for the composite (Figure 3.10). The activation energy measured on the solubility of the composite is lower than that of the neat resin, being here 2.7 kJ.mol^{-1} compared to 3.3 kJ.mol^{-1} for the 1 mm thick neat resin. This value is to be taken in the light of this scatter, as the R-square value is here equal to 0.835. However, this value of activation energy is not far from that of the pure resin.

The measured mass to saturation in the composite material is below that of the resin. This is not surprising as it has been shown that water does not diffuse into the carbon fibres. If we consider that water only diffuses into the resin of the composite then the mass at saturation of the composite can be estimated by a simple proportionality calculation:

$$M_{\infty C} = M_{\infty r} \times \omega_r \quad (3.3)$$

$M_{\infty C}$ and $M_{\infty r}$ being respectively the mass to saturation of the composite and the resin and ω_r the resin mass ratio in the composite. Results from this prediction are below the experimental values, underestimating the amount of seawater in the composite at full saturation. These results are shown in Table 3.2.

The characterisation of the composite showed a non-negligible amount of voids (see Chapter 2). The void volume ratio was determined to be around 2.5 %. The presence and amount of voids in the composite plays a role on the mass to saturation as it has been measured by Costa and Rezende [158] and also by Zhang et al. [110]. A new prediction of the mass to saturation can be made considering that voids present in the composite are entirely filled with water. This prediction is calculated as:

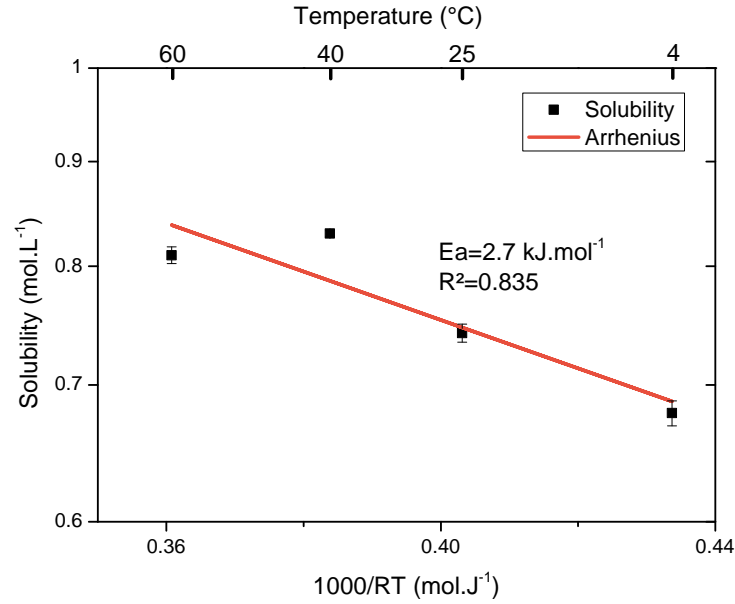


Figure 3.10 – Arrhenius plot of solubility of RTM composite in seawater

$$M_{\infty C} = M_{\infty r} \times \omega_r + \frac{V_v \times \rho_{H_2O}}{\rho_c} \quad (3.4)$$

In this equation, V_v is the void volume ration, ρ_{H_2O} is the water density and ρ_c is the composite density. This time, the prediction overestimates the mass to saturation (see Table 3.2). This suggests that water does not completely fill composite voids.

A last prediction can be made on the proportion of voids filled with water in order to obtain the right prediction of mass to saturation by adding a filling ratio factor $\Phi \in [0, 1]$ to the Eq. (3.4):

$$M_{\infty C} = M_{\infty r} \times \omega_r + \frac{\Phi \times (V_v \times \rho_{H_2O})}{\rho_c} \quad (3.5)$$

According to the values found for Φ , there is an average 25 % of the void volume that has to be considered as filled with water. However, this value could be interpreted in different ways.

In fact, this can signify that only 25 % of the voids present in the composite are filled with water possibly due to their shapes or dimensions. It could also mean that all voids are filled of water to an average 25 % of their volume. It can either be liquid water or it can also be water in a vapour state. This could be possible due to the relative pressure present inside the voids. The nature of the gas in the voids can be questioned though. In fact, as the composite plates are manufactured by vacuum-RTM, the voids can result from trapped vacuum or from resin components vaporising due to the low pressure. The nature of the voids were not investigated during this study but would be an interesting aspect to look at.

Table 3.2 – Prediction and experimental value of mass to saturation of the composite (*estimated values)

Ageing temperature	Moisture content (%)			Ratio of voids to be filled to meet experimental value
	Prediction without voids	Prediction with 100 % filled voids	Experimental value	
4 °C	0.8	2.56	1.2*	0.23
25 °C	0.87	2.63	1.3*	0.25
40 °C	1.01	2.78	1.48	0.28
60 °C	1.03	2.79	1.43	0.23

Another possibility would be that water migrates to the fibre/matrix interface. The nature or fibre sizing would be, in this case, of high impact. Those three different scenarios are illustrated in Figure 3.11. As of now, none of these scenarios has been validated.

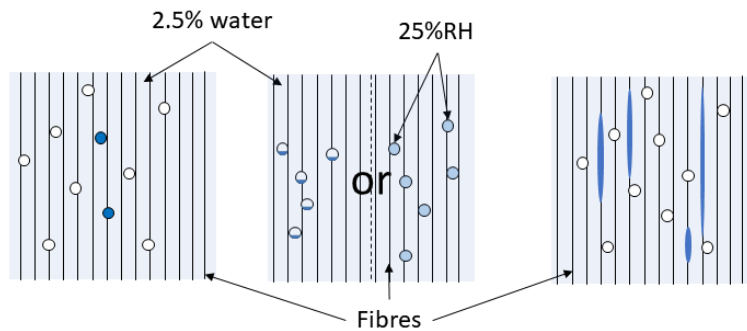


Figure 3.11 – Illustration of the different cases of water in the composite

Several studies suggested equations to predict the diffusion coefficient value by first knowing the resin's diffusion coefficient and the fibre volume ratio. In our case, the different equations have been calculated for the four different ageing temperatures studied for the composite. The calculated values are shown in Table 3.3.

HT, SH and R equations, seem to be more accurate as they have a relative error of respectively 8, 7 and 5 %. However, by comparing the calculated values for each temperature, it appears that SH and R equations give the closest estimates at 25, 40 and 60 °C (see Figure 3.12). The value at 4 °C has been put aside as it was calculated with an estimated value of mass to saturation. Therefore it is not shown in the figure. The Rayleigh equation [160] seems to be the more accurate in predicting the diffusion coefficient for the composite.

$$D_c = D_r \times \frac{1 - v_f - (0.3058 \times v_f^4)}{(1 + v_f - (0.3058 \times v_f^4)) \times (1 - v_f)} \quad (3.6)$$

Chapter 3. Water diffusion

Table 3.3 – Calculated diffusion coefficient according to Dana et al. [159],(* calculated using an extrapolated M_∞ value based on an Arrhenius law)

Ageing temperature	Diffusion coefficient ($\cdot 10^{-13} m^2 \cdot s^{-1}$)						Exp. value
	Halpin Tsai (HP)	Shen-Springer (SS)	Springer Tsai (ST)	Shirrel Halpin (SH)	Rayleigh (R)	Woo Piggott (WP)	
4 °C	0.14	0.06	0.11	0.18	0.17	0.14	0.07*
25 °C	0.43	0.18	0.35	0.56	0.55	0.45	0.55*
40 °C	1.37	0.57	1.10	1.78	1.74	1.43	1.63
60 °C	8.27	3.47	6.67	10.74	10.52	8.64	9.77
Error (%)	6	65	34	7	5	14	-

In this equation, D_c is the diffusion coefficient of the composite, D_r is the diffusion of the resin and v_f is the fibre volume ratio.

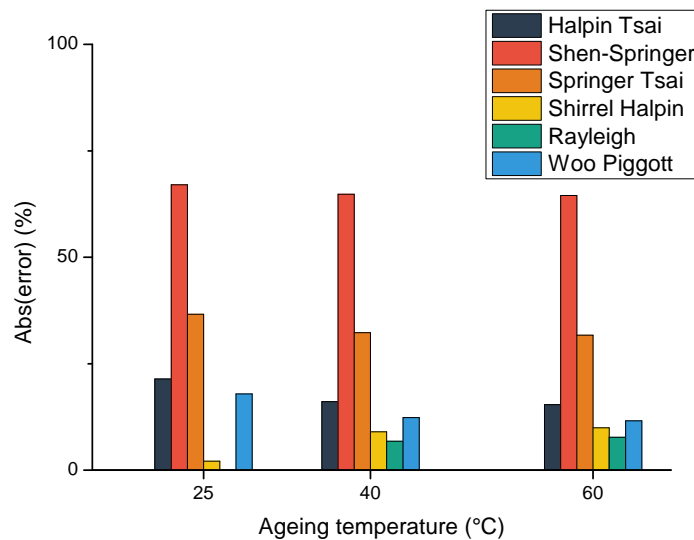


Figure 3.12 – Comparison between predicted values of D and experimental value

The comparison between the activation energies from experiment and from the Rayleigh-calculated diffusion coefficients, shows results that are not far from one another (Figure 3.13). The measured activation energy calculated from the experimental values – without considering the 4 °C – shows good agreement to the Arrhenius law but the activation energy is higher compared to the pure resin. The prediction of D calculated thanks to the Rayleigh equation shows the same activation energy of the resin as calculated from the resin’s diffusivity values (and the fibre volume ratio but that is not temperature-dependent).

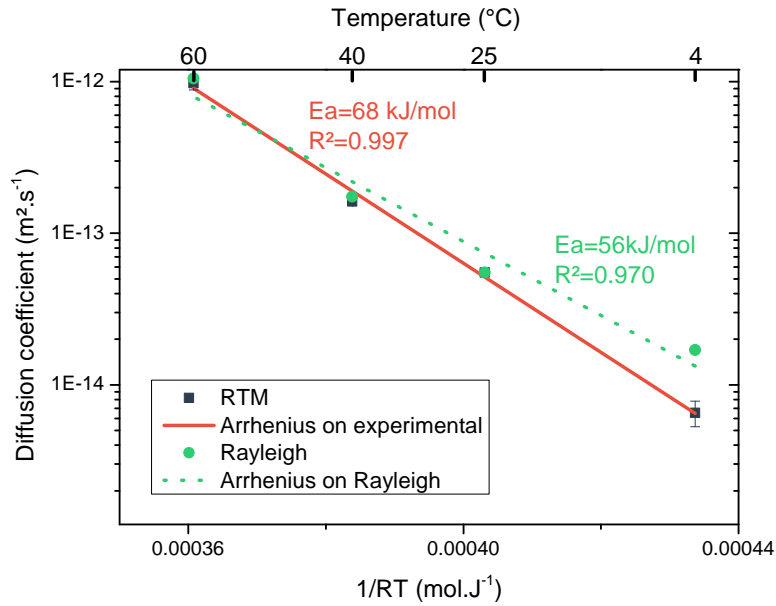


Figure 3.13 – Comparison of experimental and Rayleigh-calculated diffusion coefficients as Arrhenius plot

Therefore, the prediction of the diffusion coefficient using the Rayleigh equation and experimental values for the resin may be possible. Using this prediction will be conservative as the calculated values are slightly above those of the experiment, leading to quicker diffusion.

3.3 Prediction for a real blade structure

The architecture from the FabHéli project was used as a study case to predict the water ingress into a real composite propeller. The global design of one of the propeller's blades is shown in Figure 3.14. The service temperature was chosen as the global average temperature between the sea surface and 300m depth being around 15 °C from [161]. This temperature will be conservative for tidal turbine applications, as lower seawater temperatures are expected, but may be representative of temperatures seen by boats.

The diffusion coefficient of the composite was calculated thanks to the Arrhenius law and was evaluated to be equal to $D_{15\text{ }^{\circ}\text{C}} = 2.10^{-14} \text{ m}^2.\text{s}^{-1}$. For the mass to saturation, it was calculated as in Eq. (3.5). The resin's mass to saturation was calculated by Arrhenius as $M_{\infty r} = 2.35 \%$, the void volume ratio was kept at 2.5 % and filling ratio was fixed at 25 %. The resin's mass ratio was also kept at its measured value of 0.38 from the square plates even though it may change when measured on a complex form such as the propeller blade. This leads to a mass at saturation of the composite of $M_{\infty C} = 1.38 \%$.

Three sections were considered for these estimations. The positions of these sections are shown in Figure 3.15. One can see that, first, the thickness is not constant along the chord of the profile, which is normal for foil profiles, and second the thickness increases

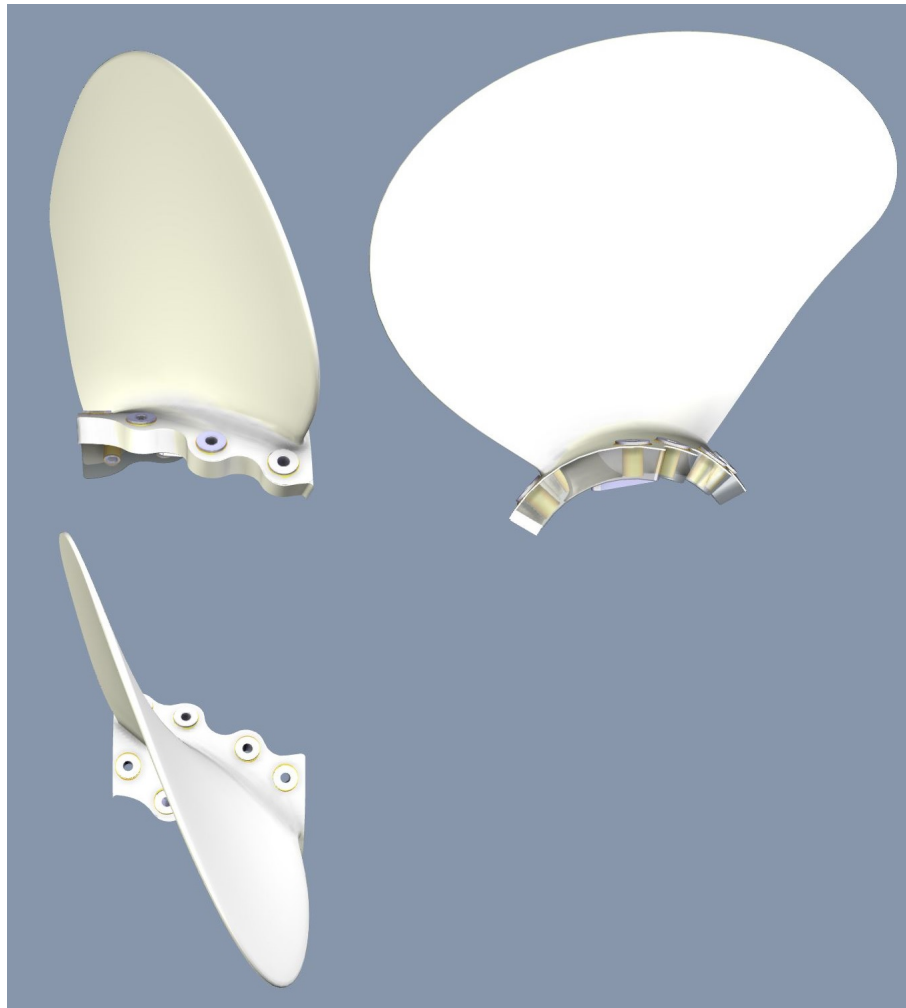


Figure 3.14 – Design of the FabHéli composite blade (the propeller has 5 blades)

closer to the base of the blade. For the calculations, the thickness considered was the maximum along the chord of these three sections. These thicknesses are 17.25, 27.5 and 37,5 mm. The blade was considered to be a monolithic of unidirectional plies although, as shown in the previous picture (Figure 6), there are woven plies on the final blade. Obviously, the ageing condition involves total immersion of the propeller and water is considered to diffuse from both sides. This may not be the case for tidal turbine blades that often have hollow structures with spars for reinforcement as shown in [22,23,162].

A first calculation can be made on the time to saturation of these three sections. The time to saturation of the thinnest to the thickest sections would take respectively 370, 941 and 1751 years. Based on these values, one might consider seawater ageing as negligible for the time of use for these blades in service. However, this time corresponds to the time that it will take to obtain a full saturation of the composite through its entire thickness.

In fact, with an ageing temperature of 15 °C, the thickness that can be saturated in 20 years, considering water on both sides, would be a thickness of approximatively 4 mm.

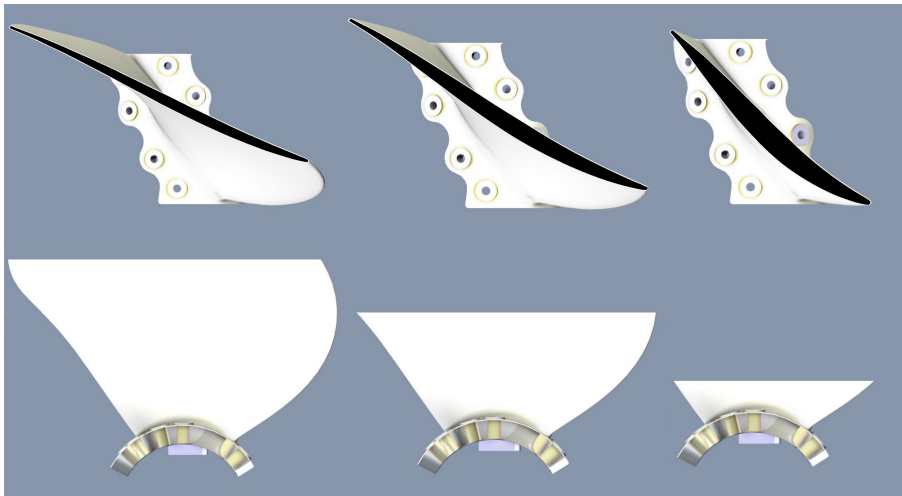


Figure 3.15 – Different propeller blade sections considered for water ingress prediction, section 1 on the left, section 2 in the middle and section 3 on the right

This thickness may be encountered at the leading and trailing edges. This is important as leading and trailing edges are highly sensitive zones of propeller blades and could cause a change in the mechanical/dynamical response of the entire propeller.

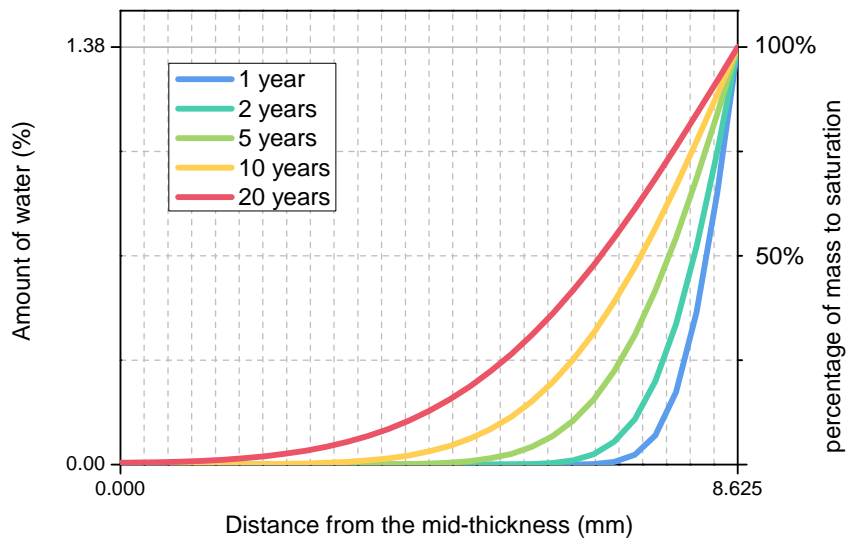


Figure 3.16 – Water profile for the mid-thickness of section 1

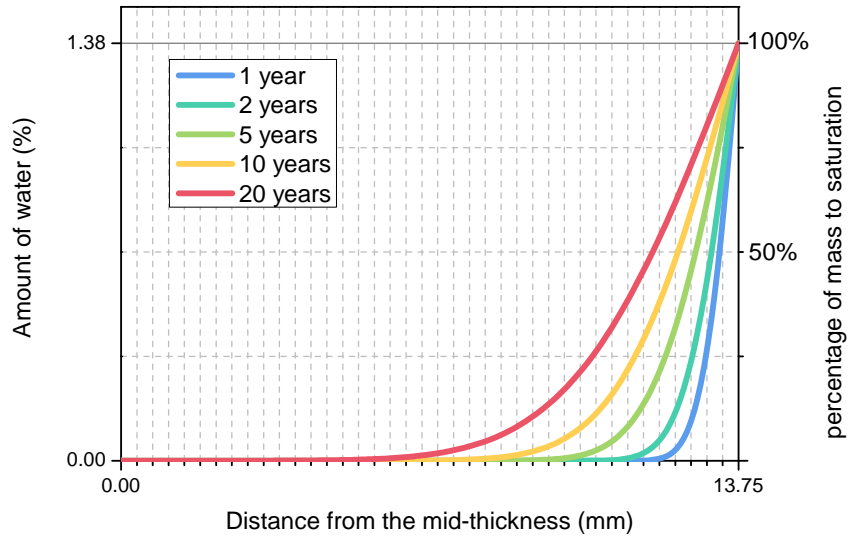


Figure 3.17 – Water profile for the mid-thickness of section 2

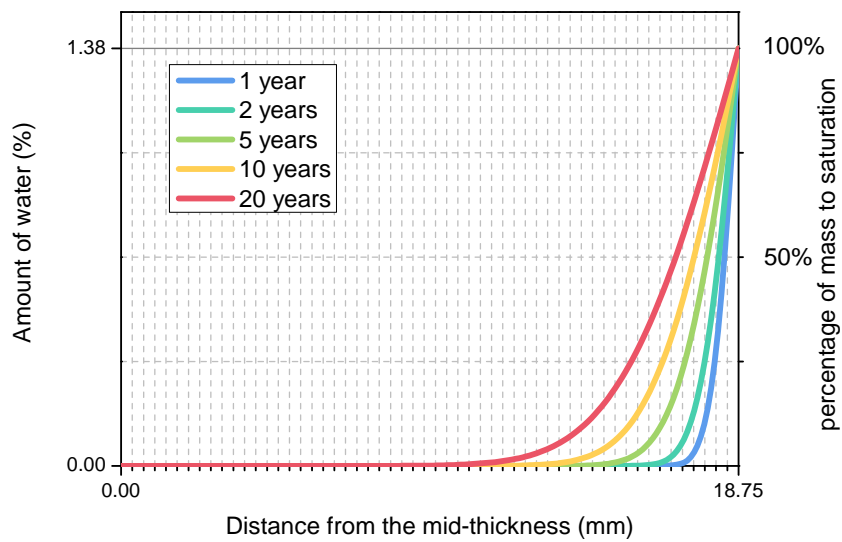


Figure 3.18 – Water profile for the mid-thickness of section 3

An important aspect of the diffusion process is that diffusion is not homogeneous across the thickness. In fact, the water ingress is fast on the outer-surfaces whereas it is significantly slower to reach the mid-thickness. Figure 3.16 to 3.18 show the concentration of water for the three maximum thicknesses with respect to sections from Figure 3.15. The grid of the x-axis represents the thickness of one ply considering it is 0.34 mm thick. The water concentration was calculated for 5 time periods: 1, 2, 5, 10 and 20 years. One can clearly see that the amount of water in the outer plies rapidly increases. In fact, after 1 year of immersion, water starts to reach the fourth composite ply.

The results from these calculations are comforting as they demonstrate that water will not reach the mid-thickness in most of the propeller blade. However, once again, the thicknesses considered here were the maximum thickness of the foil profile. It is possible to see on the previous figures that a significant amount of water does diffuse into the outer plies. This has to be taken into account, as these outer plies are also the most critical ones. First, they are the most highly loaded when the blade undergoes bending loads. Then, due to the thickness reduction needed by the profile design, there are often ply drops, which create highly critical zones with high stress concentration that may play a role in delamination. In addition, for the propeller blade case, the outer plies will be subjected to erosion from cavitation.

Therefore, it is important to evaluate the effect of seawater on the mechanical properties of the composite as, even if it only affects a limited region, it could result in significant changes to the entire blade behaviour.

3.4 Conclusion

This chapter presents the different water diffusion characteristics of the resin and the composite studied in this thesis. The diffusion behaviour, for both pure resin and composite, was found to follow a Fickian behaviour. It was shown that the moisture values at saturation of the pure resin were not sufficient to predict the moisture of the composite and additional microstructural parameters such as voids need to be considered to fully predict composite moisture content. The Rayleigh model showed the best results for predicting diffusion factors of the composite based on its fibre volume ratio and the diffusion coefficient of the resin.

The temperature dependences of the moisture absorption and diffusion coefficients for composite and resin were characterized. Their agreement with an Arrhenius law validates the use of temperature to accelerate ageing for the evaluation of the effect of moisture on the mechanical properties, at least over the range investigated. The effects noted at elevated temperature will be considered as representative of what could be expected at the in-service temperature at time-equivalent periods.

Finally, the water ingress into a real composite propeller blade, which was designed for the FabHeli project, was evaluated. The water ingress was evaluated at the maximal thickness of three sections along the blade's length. The seawater temperature was fixed at 15°C. Considering a time period of twenty years and water on both sides of the propeller, all thicknesses below 4 mm would be saturated. Vibration is an important factor for military purpose but also for civil applications as vibration can wear the transmission chain (shaft, bearings etc.). Trailing and leading edges are highly critical in terms

Chapter 3. Water diffusion

of vibration. Additionally, these zones (edges) are the thinnest parts of the profile. The presence of water in these zones could change the final vibration of the blades and the whole propeller on a wider scale. For greater thicknesses, the water concentration was calculated and showed that even after one year, there was a significant amount of water in the outer-plyes. This water may influence the composite behaviour at the ply scale but also at the blade scale. Therefore, it is necessary to understand and characterize the effect of seawater on the different mechanical properties of the composite.

Accelerated ageing of the resin

4.1 Plasticization and physical ageing

In the previous chapter, the different kinetics of water diffusion of the resin and the composite were presented. When water diffuses into polymers and composites, it can be expected to influence their mechanical properties. The aim of this chapter is to present the different ageing mechanisms that occurred when the seawater ageing tests were carried out on the pure matrix resin.

The main goal of increasing ageing temperature is to accelerate diffusion, as was shown in the previous chapter. Those ageing tests were performed at elevated temperature. In this way, the resin's aged behaviour can be evaluated in a reduced time compared to the real ageing condition. However, increasing the temperature also has the drawback to induce unwanted phenomena. In fact, as will be described below, it was found that instead of having only plasticization, there was also physical ageing occurring during the ageing tests. It will be shown that the presence of seawater in the resin had the effect of accelerating physical ageing.

4.1.1 Ageing mechanisms in the resin

Figure 4.1 presents the main issue when trying to establish the long term behaviour of a resin. Tensile tests on unaged resin show a maximal stress around 56 MPa and a strain at break around 12 %. This tensile curve is shown in grey (#1) in the figure. Although strain at break is also of interest when measured with tensile tests, it will be considered here qualitatively, and emphasis will be placed on the maximum stress. A first ageing performed on the resin was to immerse it in seawater at 40 °C until full saturation (1 month). The presence of water can then be evaluated. This is the dark blue curve (#2) on the graph. Ageing in this condition leads to an increase of the maximal stress from 56 MPa to 64 MPa and a decrease of the strain at break to below 5 %. This is contradictory to what could be expected when performing seawater ageing on epoxy resin as the main ageing recorded in the literature seems to be plasticization [53, 55, 56, 163], which results in higher ductility and lower maximum stress [164–166].

In order to evaluate the reversibility of such ageing effects, the previously seawater

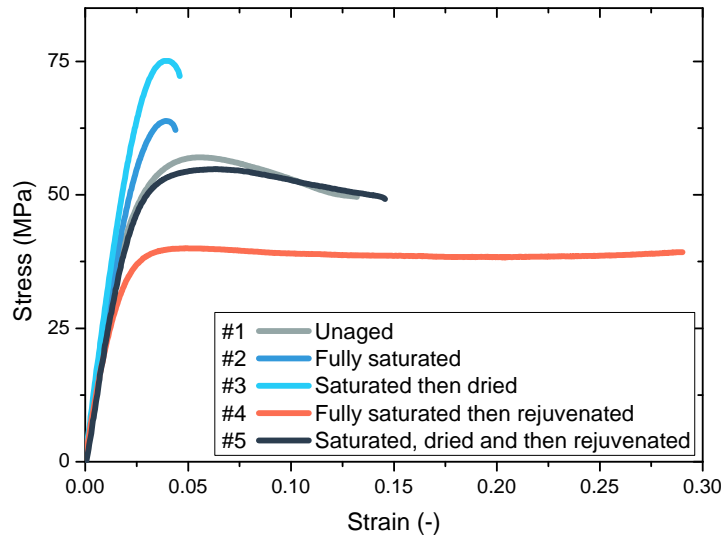


Figure 4.1 – Tensile behaviour of pure resin aged at 40 °C in seawater then dried

aged samples were then dried to constant weight in ovens at 40 °C with desiccant silica gel, the result is shown in Figure 4.1 by the clear blue curve (#3). The resulting samples showed even higher maximal stress at 75 MPa and a strain at break equivalent to the saturated condition. Therefore, the effect of ageing in seawater at 40 °C for three months seems to be irreversible with an increased maximal stress and a decreased strain at break.

Additional investigations involved subjecting the samples to above-T_g temperatures at the two different ageing conditions: saturated and saturated then dried. The mechanical response of the saturated and above-T_g exposed specimen showed a contradictory response compared to the only saturated sample. This response is shown as red curve (#4) in the figure. In fact, for the only saturated condition, maximal stress increased and strain at break decreased, whereas when samples were exposed to above-T_g temperature, the maximal stress dropped to 38 MPa and the strain at break jumped close to 30 %.

The same effect of over-T_g exposure is observed when subjecting dried specimens to above-T_g temperature shown as the black curve (#5) in the figure. The measured maximal stress and strain at break then return to their initial unaged values.

The main conclusion to these tests is that there seem to be two different ageing phenomena occurring at the same time. The first phenomenon appears to be physical ageing which has been defined previously and which is occurring at below-T_g temperature exposures. The second ageing phenomenon is assumed to be plasticization. The next sections will concentrate on the characterisation of these two mechanisms, physical ageing and plasticization, separately. The interactions between them will then be discussed.

4.1.2 Kinetics of physical ageing on the resin

This section will describe the physical ageing occurring in the pure resin during sub-T_g thermal exposures. For this, the characterisation of physical ageing of fully dried resin was performed in inert environment by placing the tensile specimens in vacuum bags; this is the first part of this section. Additional characterisation of the physical ageing was evaluated by performing physical ageing on fully seawater-saturated specimens. The aim is then to evaluate whether or not the presence of seawater plays a role on the kinetics of physical ageing. This will be examined in the second part of this section

Physical ageing of dry resin in inert atmosphere

In order to characterise the kinetics of physical ageing in dried resin, tensile samples were vacuum packed and aged at 40, 50 and 60 °C. The utility of these three temperatures is to characterise the temperature dependency of physical ageing. The presence of physical ageing was also investigated by performing in-situ thermal ageing by DSC to confirm that the observed phenomenon was physical ageing.

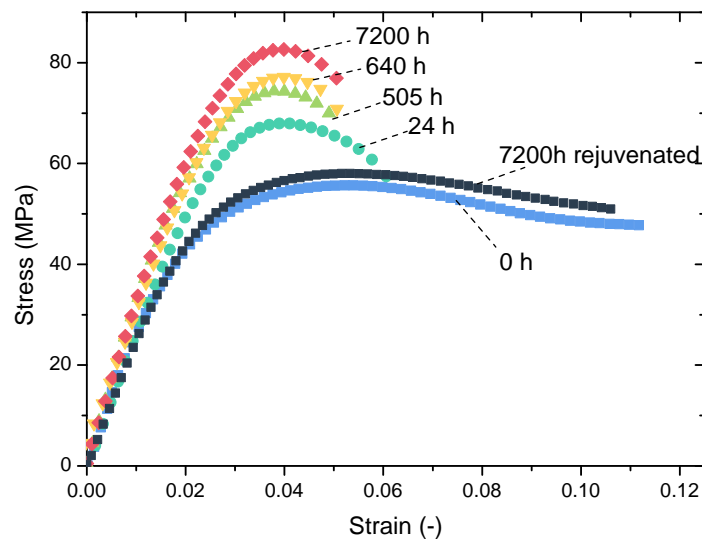


Figure 4.2 – Tensile behaviour of pure resin aged at 40 °C in inert atmosphere

The samples placed in ovens were tested at different ageing times. The ageing time effect at 40 °C is shown in Figure 4.2 for up to 7200 hours (\approx 300 days). It appears that maximal stress progressively increases from a value of 56 MPa reaching 82 MPa after 300 days at 40 °C. Strain at break is also affected by this thermal ageing, rapidly decreasing from 10-12 % to below 6 %. A final batch of 300 day-aged samples was exposed to above-T_g temperature in order to rejuvenate the material. The resulting maximal stress drops back to a value near to the reference while strain to break increases back to the original value.

There is a clear change in fracture mode going from a ductile behaviour to a more brittle one when considering the tensile curves. This can be confirmed by comparing fracture micrographs of the two ageing conditions. Figure 4.3 shows the fractography of four samples with different ageing conditions. The first one is an unaged reference; the second was thermally aged for 640 hours at 40 °C; the third one was aged at 50 °C for 14 hours and the last one was rejuvenated after being aged for 166 hours at 50 °C.

If we try to describe the different fracture modes, they all start with a first “fish-eye” development of around 700 µm in diameter but propagation differs depending on the ageing condition. The roughness of the aged samples is representative of quick and brittle cracking, whereas the unaged and rejuvenated conditions show a mirror fracture surface attributed to a more ductile and slower fracture propagation. This confirms that there is a change in the material’s behaviour induced by thermal ageing independent of the ageing temperature. This also confirms that after being rejuvenated, the initial material behaviour is recovered.

From a physico-chemical point of view, in-situ thermal ageing, performed at 60 °C in the DSC, showed a characteristic enthalpy peak gradually appearing from 4 hours of ageing time. This is shown in Figure 4.4. This peak comes from the relaxation of the resin which was identified in previous studies for physically aged polymers [80].

To characterise and describe the kinetics studied here, it is possible to focus on one mechanical property that is representative of the physical ageing state. Maximal stress has been chosen for this purpose. In Figures 4.5 to 4.7, maximum stress has been plotted as a function of ageing time for ageing temperatures of 40, 50 and 60 °C.

Previous studies on physical ageing [167, 168] used the KWW (Kohlrausch-Williams-Watts) equation in order to describe changes due to physical ageing:

$$\sigma_y(t) = \sigma_0 + \Delta\sigma \times \left(1 - e^{-\left(\frac{t}{\tau}\right)^\beta}\right) \quad (4.1)$$

In this equation, the initial maximal stress σ_0 – meaning without any physical ageing – has been measured experimentally at 56 MPa. The value of maximal stress increase $\Delta\sigma$ was measured experimentally for the 40 °C condition to be 26 MPa. It has been considered equivalent for the 50 and 60 °C conditions even though it could differ. The damping factor $\beta \in [0, 1]$ and the characteristic relaxation time τ are adjusting values in this equation. To determine these two parameters, the least squares method has been used for the three different conditions (see Appendix B). The value of β tends to be close to $\beta = \frac{1}{3}$. This value has been reported in [168], albeit for a different physical ageing marker, and it has been fixed for the rest of the present study. τ , which represents the relaxation time, has been determined for the three different temperatures as the only varying parameter. This means that the changes in behaviour, i.e. initial maximal stress, stress increase and geometry of the change are considered similar independently of the ageing temperature.

The result of this equation is shown for the three different temperatures in their respective figures as a continuous line. Although there are some uncertainties from experimental points, the equation shows a reasonable agreement in describing the mechanical response.

Another representation of these data is to use a logarithmic scale on the x axis. This allows the response of the three different temperatures to be plotted, as shown in Figure 4.8 although it amplifies the x error. On this figure, the accelerating effect of ageing temperature is clearly visible. The higher the ageing temperature, the faster the process.

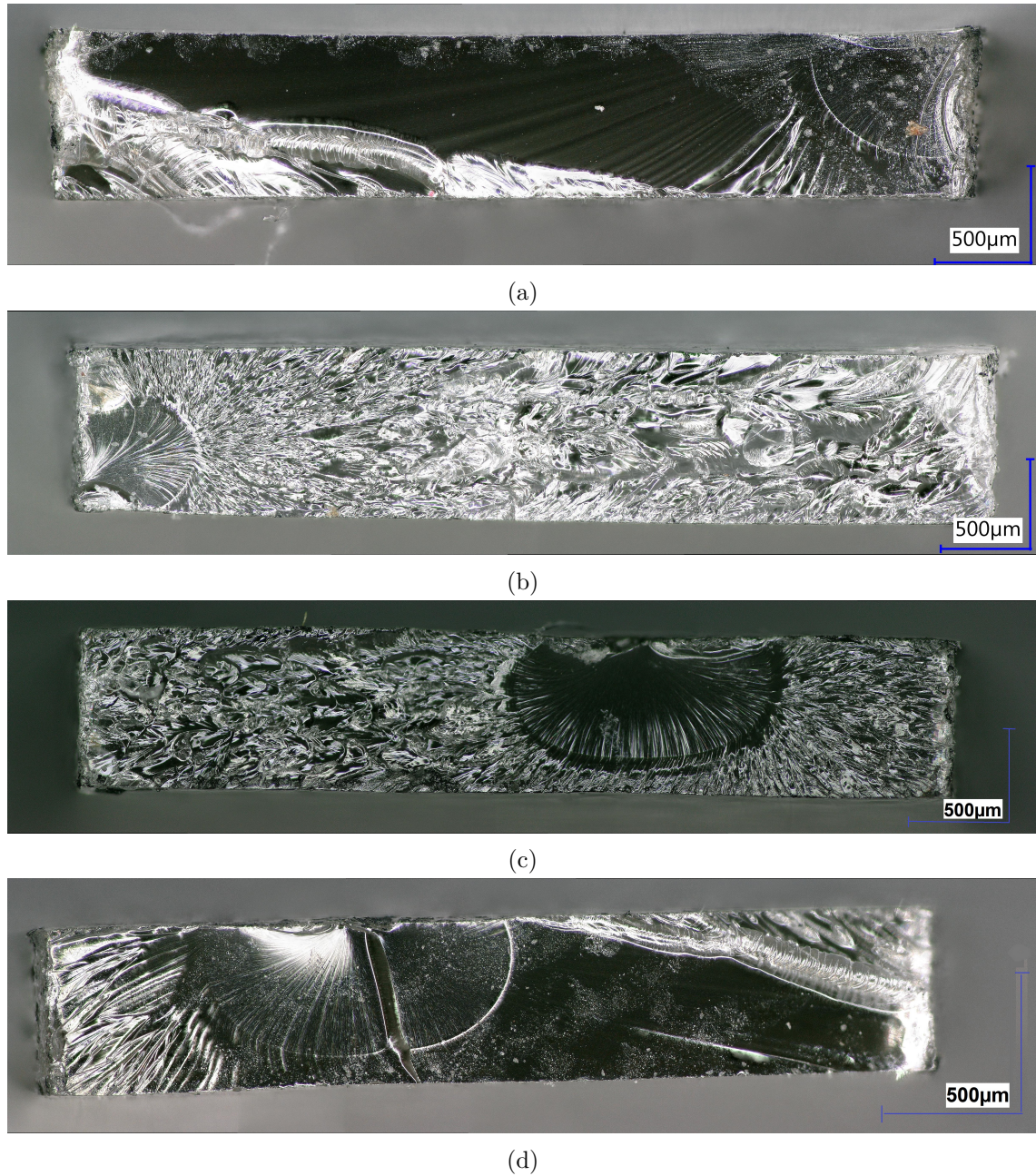


Figure 4.3 – Fracture micrographs from resin tensile test of physically unaged (a) and aged during 620h at 40 °C (b), aged 14 hours at 50 °C (c) and rejuvenated after 166 hours at 50 °C (d).

We can investigate the temperature dependency by applying an Arrhenius plot to the value of τ as plotted in Figure 4.9. It shows that the Arrhenius equation can describe the value of τ with a reasonably good agreement. An activation energy of 108 kJ.mol^{-1} is recorded for the relaxation time. Agreement with an Arrhenius law means that it is

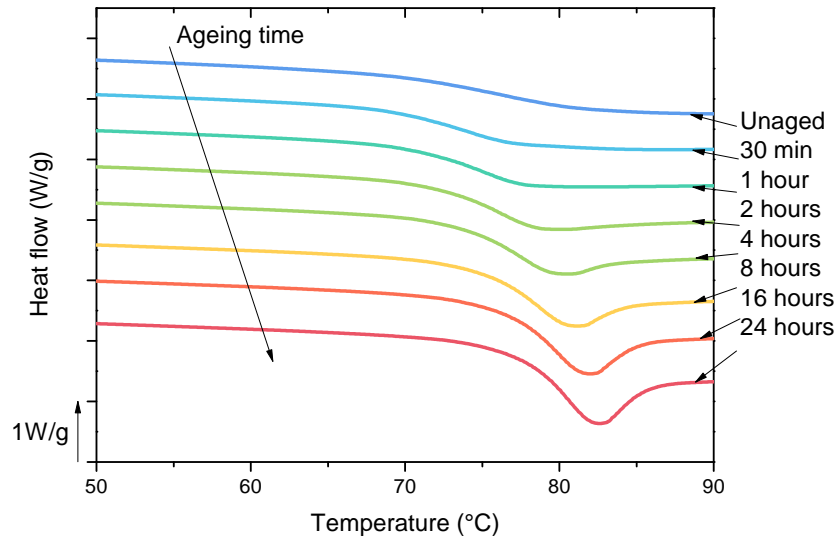


Figure 4.4 – DSC measurements performed on in-situ thermally aged pure dry resin at 60 °C

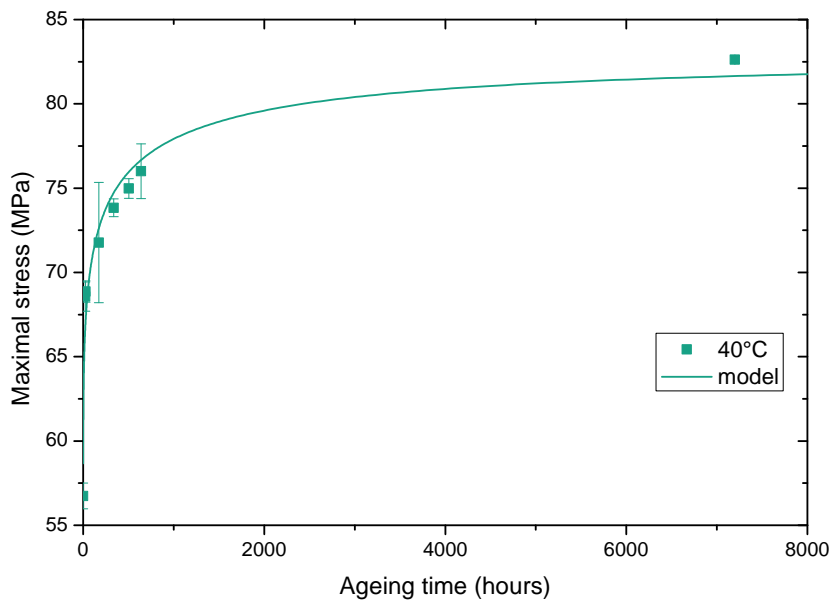


Figure 4.5 – Change of maximal tensile stress during thermal ageing at 40 °C

possible to interpolate the value of τ between 40 and 60 °C. It is also possible to extrapolate τ outside the range of interest –especially below 40 °C in our case– even though care needs to be taken with such values.

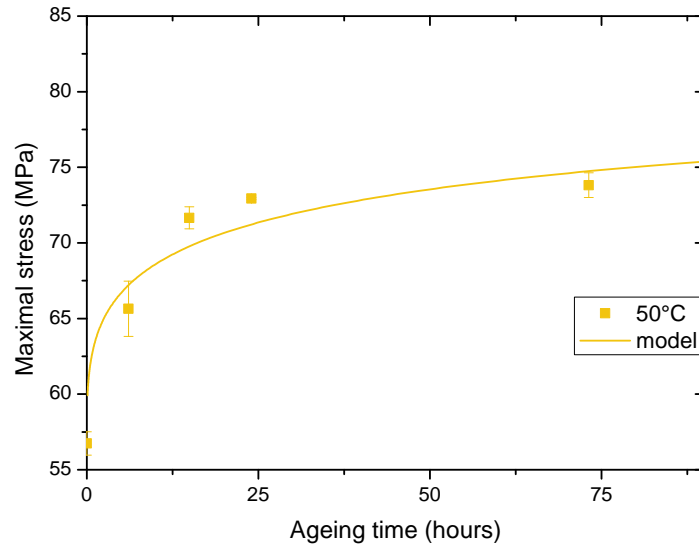


Figure 4.6 – Change of maximal tensile stress during thermal ageing at 50 °C

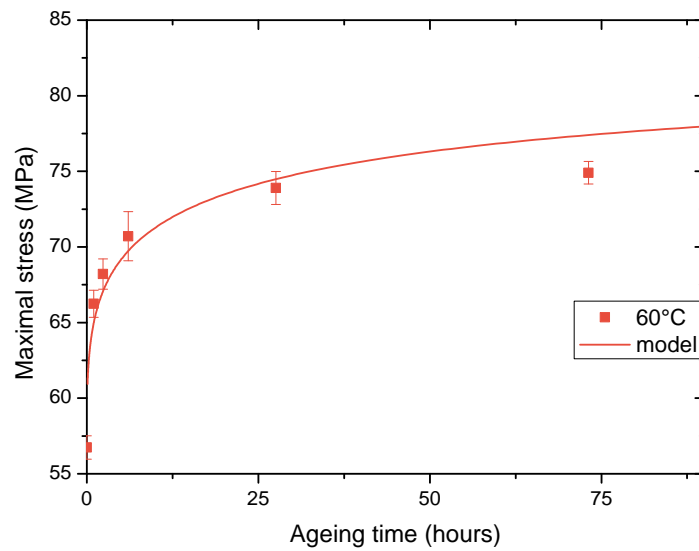


Figure 4.7 – Change of maximal tensile stress during thermal ageing at 60 °C

As a conclusion to this section, the effect of physical ageing has been characterized on the dry resin. The increase in maximal stress can be described by a modified KWW equation and showed good agreement with experimental values. The relaxation time parameter of the equation (τ) was found and could be described by an Arrhenius law,

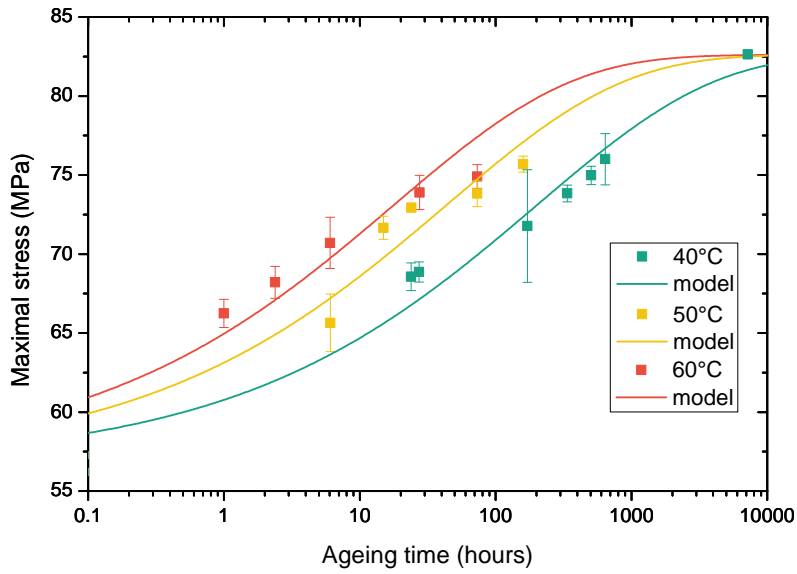


Figure 4.8 – Comparison of the maximal tensile stress changes at 3 different temperatures during thermal ageing

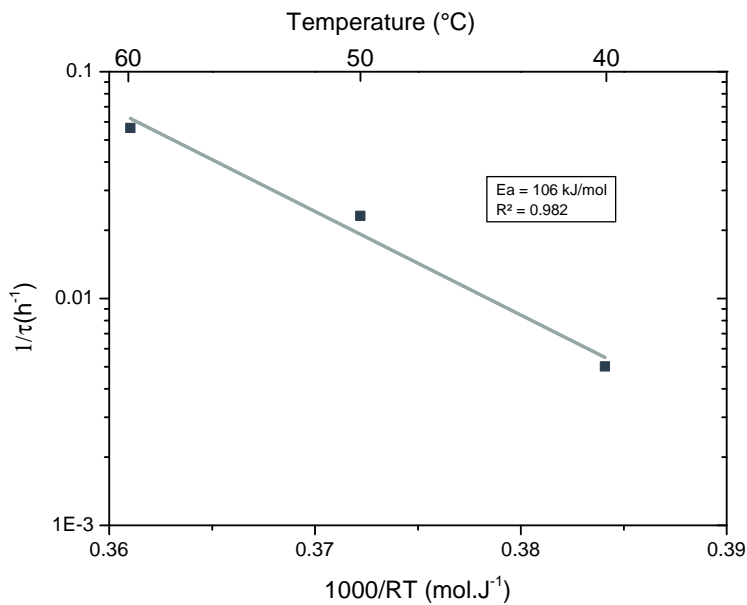


Figure 4.9 – Temperature dependence of τ expressed as an Arrhenius plot

which signifies that physical ageing behaviour can be extrapolated to other temperatures.

The main interrogation now concerns the effect of water absorption on this physical ageing behaviour. This will be investigated in the next section

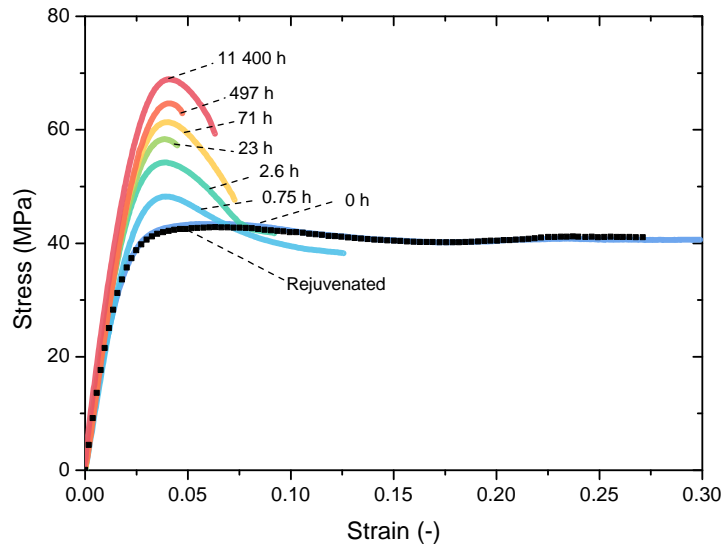
Physical ageing of seawater saturated resin

Figure 4.10 – Tensile behaviour of physically aged fully saturated resin at 40 °C

As a reminder, the aim of this study on the pure resin is to understand its long-term behaviour when exposed to seawater ageing. We showed in the previous section that physical ageing occurred when the dry resin was exposed to sub-T_g temperatures, and this may affect results obtained during accelerated ageing. The effect of this physical ageing on maximal stress was correctly described by a modified KWW equation. During long-term seawater ageing, water diffuses into the resin, as shown in the previous chapter. In order to evaluate the effect of the presence of water in the resin, tensile specimens have been fully saturated in seawater. After saturation, specimens were then immersed in 90 °C seawater for several minutes and then quenched by an immersion in 15 °C seawater. This resulted in a fully saturated and rejuvenated resin, which represents the reference ageing state. Specimens were subsequently exposed to sub-T_g temperature by immersing them into 15, 25 and 40 °C seawater baths and tested at different ageing times.

Tensile tests were performed in the same way as those on the dry resin in the previous section. The mechanical response recorded was found to follow a similar behaviour as for the dry resin. The main difference is a drop of the initial maximal stress, measured here at 43 MPa. This drop of maximal stress as well as the increased strain to break is attributed to resin plasticization but this will be studied in the next sections of this chapter.

The change in the tensile response of the saturated resin thermally aged at 40 °C is shown in Figure 4.10. This time, maximal stress increases from a value of 43 to finish at a value of 69 MPa, which represents here again an increase of 26 MPa. Once again, ductility of the resin is affected as strain at break decreases from over 30 % to less than 7 % after around 500 days at 40 °C. The rejuvenated samples show the same behaviour as unaged specimens; mechanical response is recovered, as shown by the black square points.

The changes in fracture surfaces observed for the dry resin are similar here. The fracture surfaces of the unaged and rejuvenated samples show a mirror-like fracture surface, which is once again attributed to a less brittle fracture. In addition to these fracture surfaces, the surfaces of physically aged resin after 500 hours and 475 days both at 40°C in seawater, are shown in Figure 4.11.

The thermal response of saturated resin was also evaluated by DSC as for the dried

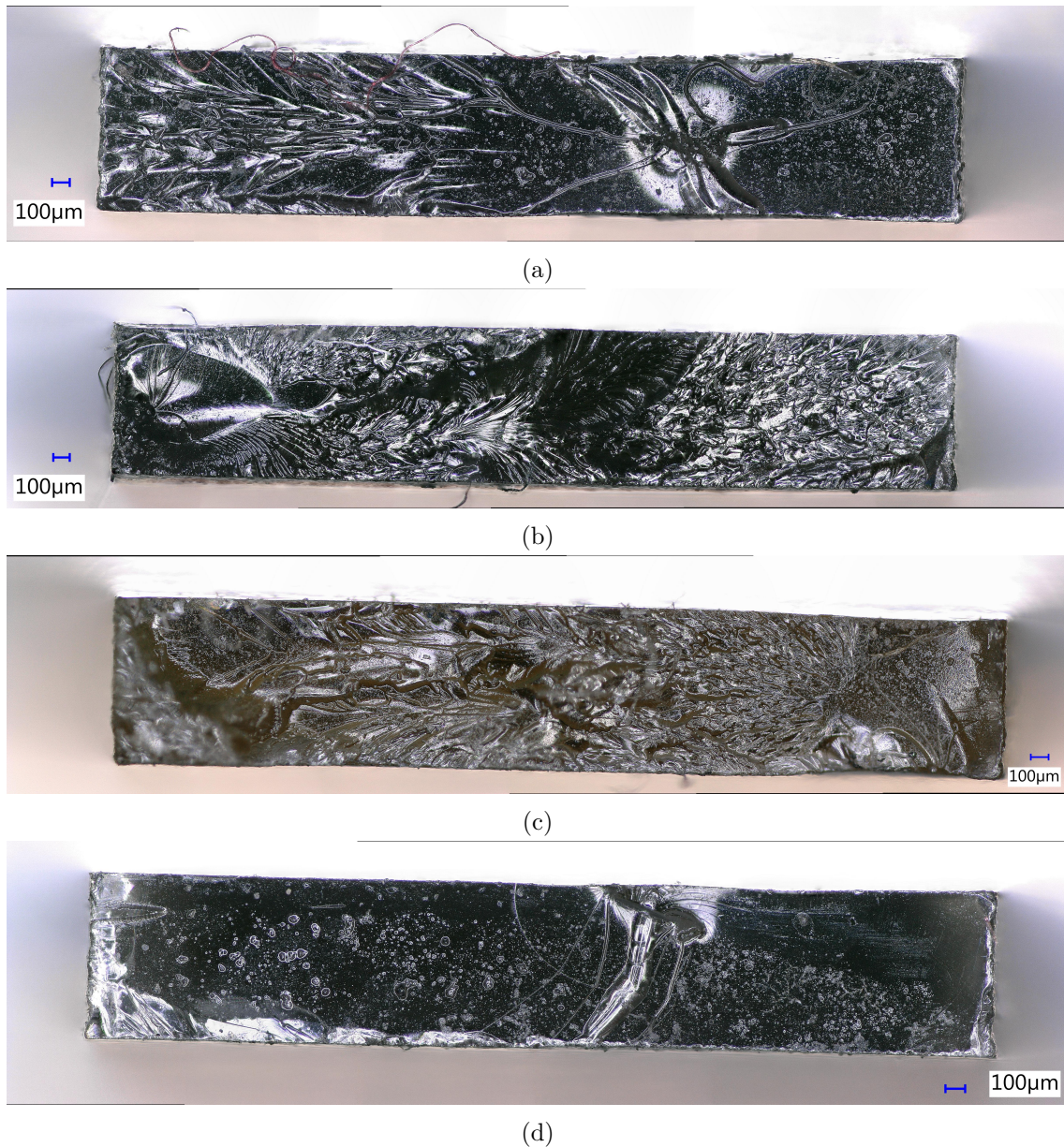


Figure 4.11 – Fracture surfaces for the saturated resin as physically unaged (a), physically aged during 500 hours (b), 475 days (c) and finally, rejuvenated after 500 hours of physical ageing at 40 °C (notice the porous aspect in (c))

Chapter 4. Accelerated ageing of the resin

resin. This time though, in-situ physical ageing was performed at 40°C instead of 60°C as a drop of 15 °C of the Tg was recorded (see Figure 4.12). In order not to lose water during the test, hermetic capsules were used, and a drop of water was placed in the pan to prevent desorption of the resin.

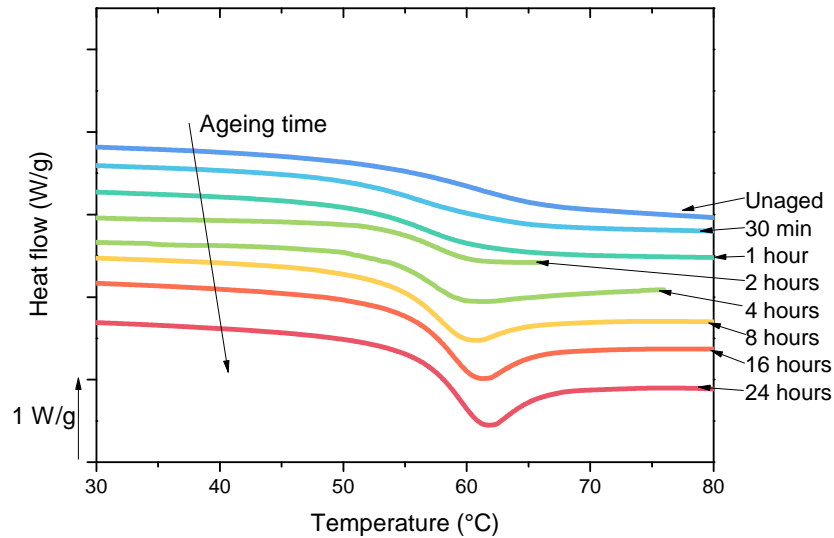


Figure 4.12 – DSC measurements performed on in-situ thermally aged saturated resin at 40 °C

This time, the enthalpy peak attributed to resin relaxation appeared after 8 hours of ageing. A comparison of the physical ageing speed and thermal dependency compared to dry resin was then made. Once again, maximal stress was chosen as the marker to follow ageing level.

Using the previously described equation Eq. (4.1), the increase in maximal stress as a function of ageing time was described. This time, σ_0 was fixed at 43 MPa. The other parameters were left as the values found for the dry resin so that the only parameter expected to be modified is the kinetic parameter (τ).

The change in maximal stress at 15, 25 and 40 °C is shown in Figures 4.13 to 4.15 with their respective KWW model. It appears that the KWW model provides a reasonable description of the changes in maximum stress, as for the dry resin.

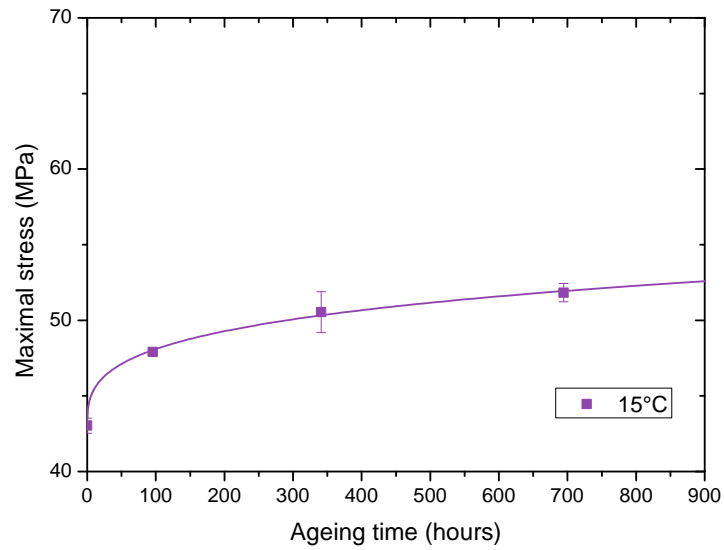


Figure 4.13 – Evolution of maximal stress of saturated resin thermally aged at 15 °C

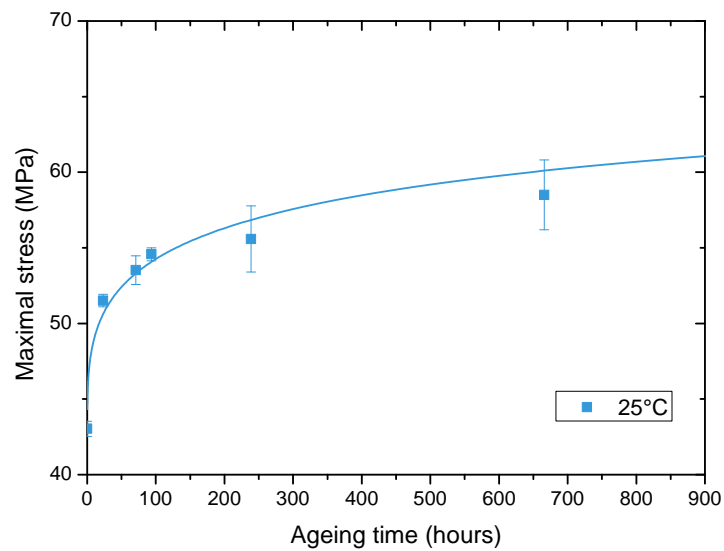


Figure 4.14 – Evolution of maximal stress of saturated resin thermally aged at 25 °C

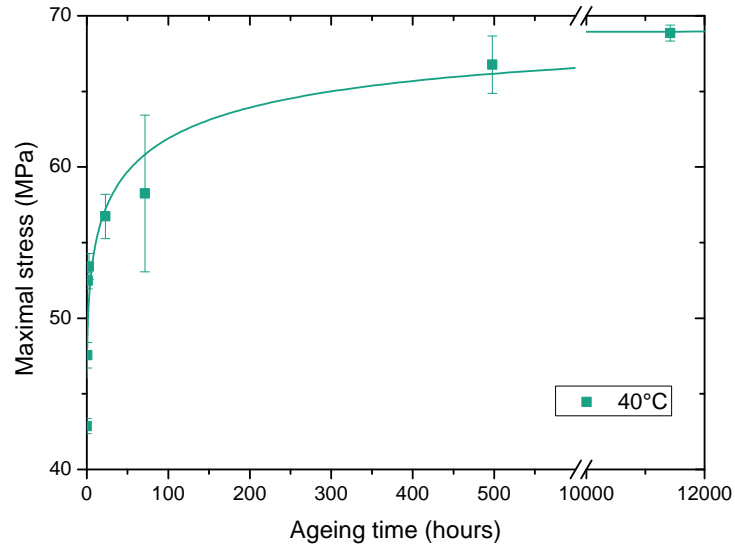


Figure 4.15 – Evolution of maximal stress of saturated resin thermally aged at 40 °C (truncated from 600 to 10000 hours)

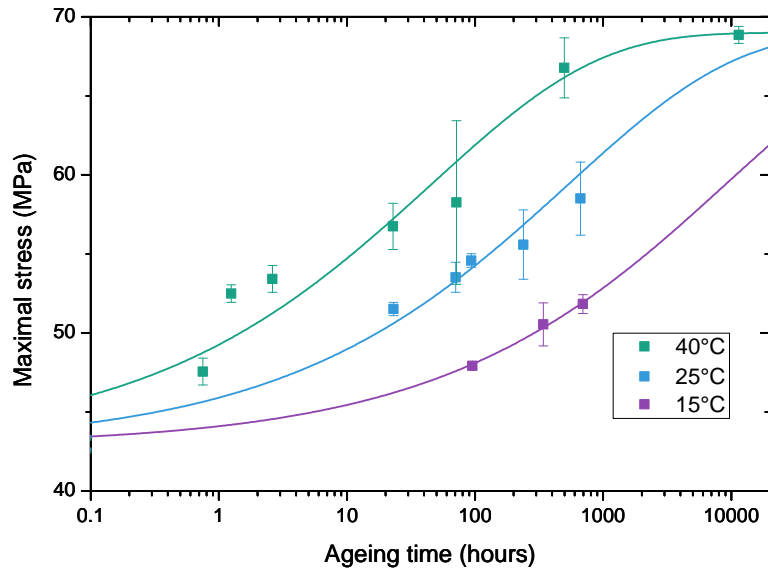


Figure 4.16 – Change in maximal stress as a function of logarithm ageing time, saturated resin

The effect of increasing ageing temperature has the same effect as for the dry resin. The higher the ageing temperature, the faster the maximal stress increases (Figure 4.16). From this observation, it is relevant to suppose that physical ageing occurring on the dry and saturated resin is similar. However, the calculated relaxation times as a function of ageing temperature clearly show that physical ageing is accelerated at the same ageing temperatures.

First, applying the Arrhenius law to the measured values of τ shows a good agreement as shown by the blue points in Figure 4.17. However, the activation energy measured for this condition was found to be 160 kJ.mol^{-1} . This activation energy is almost 60 kJ.mol^{-1} higher than the activation energy of the dry resin. This means that the presence of water modifies the kinetics of physical ageing. From this Arrhenius plot, it is also clear that relaxation time is shorter at $40 \text{ }^\circ\text{C}$ compared to the dry resin.

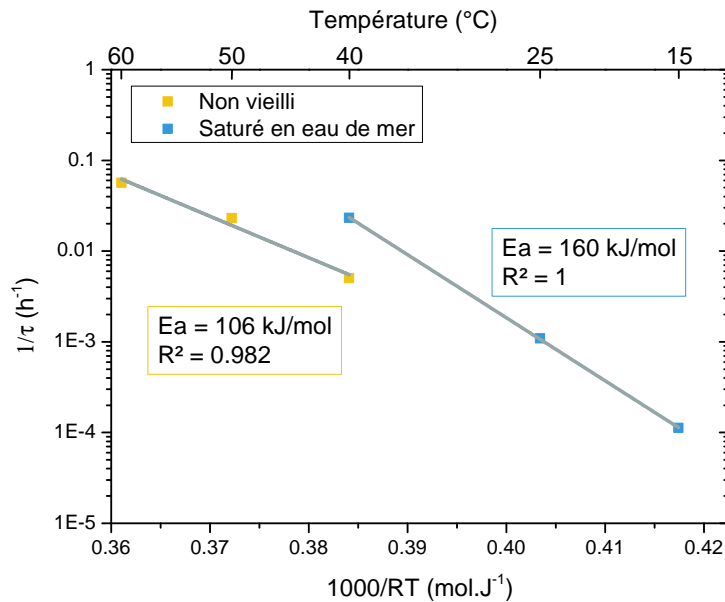


Figure 4.17 – Arrhenius plot of the physical ageing relaxation time for the saturated resin

Figure 4.18 shows DSC plots of the dry and saturated epoxy resins that were thermally aged for 24 hours at $40 \text{ }^\circ\text{C}$. We can see that the characteristic enthalpy signature of physical ageing is clearly visible for the saturated resin. On the contrary, there is no sign of enthalpy peak for the dry resin although there is a double step where the T_g is. This confirms, at least, the difference in relaxation times between the two conditions.

The drop of T_g induced by water absorption will be discussed in the next section. This drop of T_g is measured to be around $15 \text{ }^\circ\text{C}$. An explanation of the change in relaxation time between dry and saturated resin could be this drop of T_g induced by the water. Figure 4.19 addresses this point. On this figure, the difference between the ageing temperature and the respective T_g of the material is plotted on the x axis. If only a drop of T_g could explain the difference between dry and saturated resin, the points would all fall on a single line, which is not the case here. It can therefore be concluded that water absorption induces

Chapter 4. Accelerated ageing of the resin

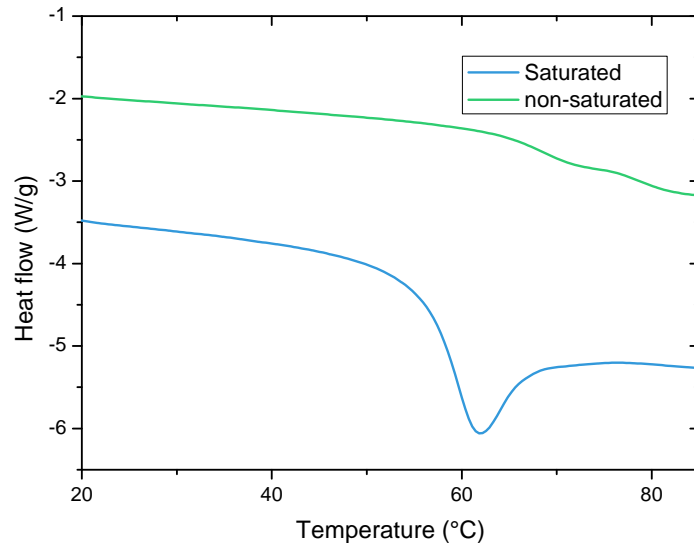


Figure 4.18 – DSC plots of saturated and dry resin thermally aged for 24 hours at 40 °C

more changes in the material when considering physical ageing.

These results raise a problem for the widely-used method of increasing water tempera-

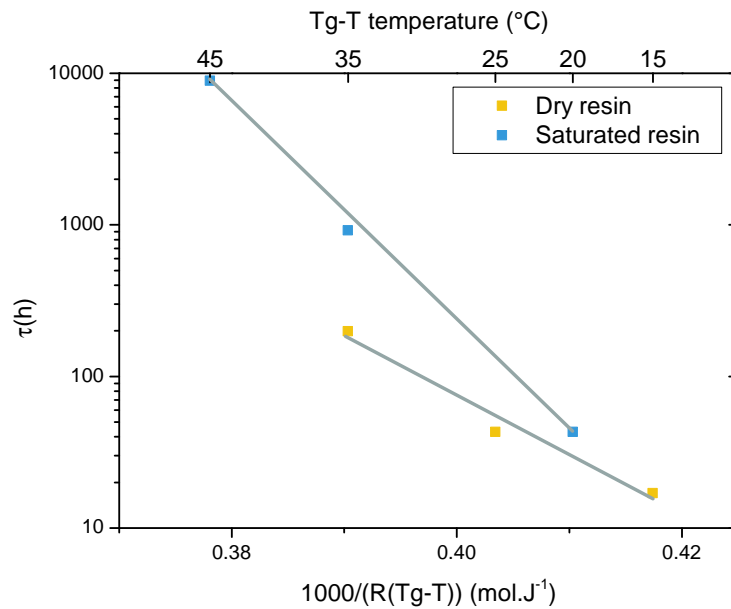


Figure 4.19 – Arrhenius plot of physical relaxation time as a function of ageing temperature with respect to T_g

ture to accelerate seawater ageing. Indeed, by increasing the temperature during seawater ageing, the diffusion kinetics are accelerated but the physical ageing is also faster. There is a question on pre-test conditioning that arises from these results. It would be necessary to either rejuvenate the samples prior to each tests or stock the samples at elevated but below-Tg (15 to 20 °C below) temperatures for several days in order to "physically age" the samples so that it would not change during seawater ageing. However, the state of physical ageing on real structures is not known and can be advanced depending on the storage conditions prior to service.

As a conclusion to these two first sections, we have shown that the epoxy matrix resin undergoes physical ageing when exposed to sub-Tg temperatures for both dry and saturated states. The mechanical effect of physical ageing was evaluated by tensile tests and an embrittlement of the resin was recorded with an increase of maximum stress and a decrease of strain to break. The presence of water in the resin accelerates the physical ageing but temperature dependency is not comparable between dry and saturated resin, as an increase of the activation energy by 60 kJ.mol^{-1} is recorded for the saturated resin. An interesting point is that physical ageing at around 20 °C has the same relaxation time between the dry and the seawater saturated epoxy. Additional characterisations at other ageing temperatures would be needed to confirm this value though, as there are no similar results from such experiments in the literature.

In the next sections, the effect of water on the mechanical properties has been measured. Physical ageing effects were removed, by either rejuvenating the resin before the tensile tests, or by performing ageing tests with a previously physically aged resin.

4.1.3 Plasticization of the resin

In this section, we focus on the plasticization of the resin induced by the presence of water between macromolecular chains. In order to avoid any heterogeneity of the water concentration induced by water profiles, only saturated conditions are considered. To study the impact of the water content, the resin has been aged in seawater and under 50 and 75 % relative humidity. In all cases, a Fickian behaviour was identified. The resulting masses to saturation from these three different water ageing conditions are shown in Table 4.1.

Table 4.1 – Mass to saturation as a function of ageing condition

	Maximum water content (%)
Seawater	2.7
75 % RH	1.7
50 % RH	1

The presence of water between the macromolecular chains increases the chain mobility. It results in a reduction of the Tg of the polymer. As we use different humidity conditions to induce different masses to saturation, different decreases in Tg are observed as shown in Figure 4.20. Here, the Tg drops from a value of 75 °C when the resin is dry, to a minimum value of 61 °C in the case where it has been saturated to 2.7 % weight gain in seawater. The work of Simha-Boyer [169–171] has shown that the reduction in Tg value

can be calculated as a function of water content:

$$\frac{1}{T_g} = \frac{1}{T_{gp}} + A \times \nu_{H_2O} \quad (4.2)$$

$$\text{With } A = \frac{1}{T_{gs}} - \frac{1}{T_{gp}} \quad (4.3)$$

In these equations, T_g in Kelvin is the glass transition temperature of the resin with a known value ν_{H_2O} of water volume ratio. T_{gp} is the glass transition temperature of the dry polymer, T_{gs} is the glass transition temperature of the solvent which is water in our case and its value was taken to be 136 K. This value is questioned in the literature but no clear value has been clearly accepted yet [172–174]. The theoretical value from Eq. (4.3) is shown as a red dashed line in Figure 4.20. It appears that the Simha-Boyer expression is adequate to predict the value of Tg of the resin studied here.

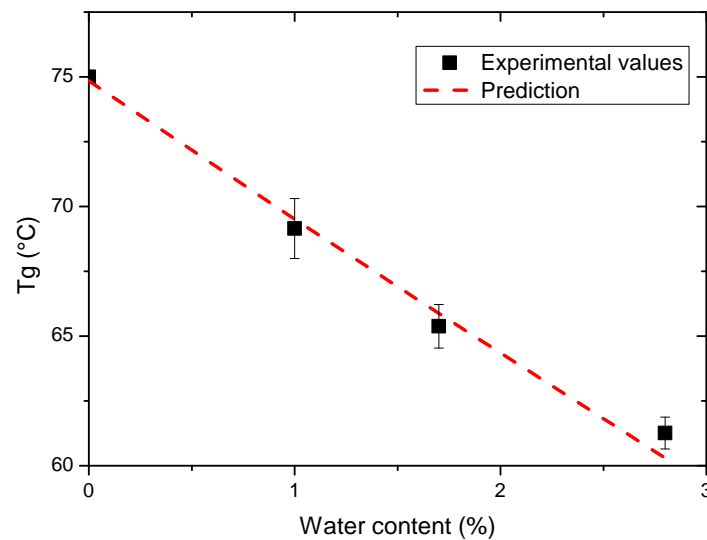


Figure 4.20 – Change in resin Tg as a function of water content, with Simha-Boyer prediction

From a mechanical point of view, the effect of water absorption was evaluated using the tensile properties. It appears that, as expected for this resin, plasticization occurs. This plasticization is illustrated by a decrease in maximum tensile stress and increasing strain to break. This behaviour is shown in Figure 4.21.

It is possible to plot a linear relationship between the measured maximum stress and the temperature difference between the Tg and the test temperature, that will be referred to as T. This relation can be calculated using the modified Kambour equation [175] as:

$$\sigma = A(T_g - T) + B \quad (4.4)$$

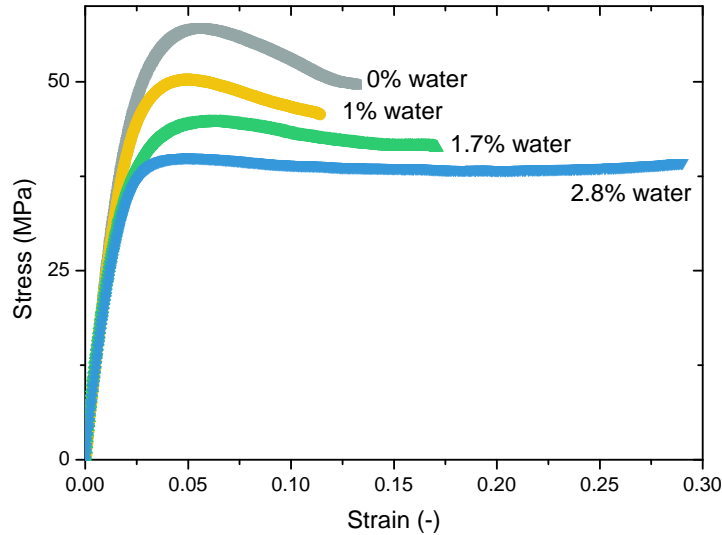


Figure 4.21 – Influence of water absorption on tensile behaviour

Here, the test temperature stays the same, as tests are performed in a 21 °C temperature-controlled test room. The value of T_g decreases as the water content increases. The A and B factors are material properties, A is often referred to as the proportionality factor expressed in $MPa.K^{-1}$. The prediction using Eq. (4.4) is in good agreement with the experimental values as shown in Figure 4.22.

Combining the two previous relationships with the modified Henry's law allows prediction of long term tensile properties of the resin (only the maximal stress without considering physical ageing here). Henry's law provides a mass to saturation for a certain value of water activity. This mass to saturation leads to a drop of the T_g which can be calculated by the Simha-Boyer equation. This drop of T_g induces a decrease in maximum stress that can be found using the Kambour equation. The parameters A and B of the Eq. (4.4) are found by performing tensile tests at different temperatures changing the T parameter and keeping the same T_g throughout.

As shown in the previous section, there is an influence of water saturation on the physical ageing behaviour. The next question is whether physical ageing has an influence on the plasticization behaviour. In order to investigate this, tensile specimens were placed in vacuum bags prior to water ageing. The reference "unaged" condition corresponds to a fully dried and physically aged sample. Then, specimens were placed in 40 °C seawater and a 50 % relative humidity chamber until fully saturated. The results from tensile tests for these ageing conditions are shown in Figure 4.23 with the addition of the fully saturated and physically unaged specimen for comparison to a fully plasticized resin response. It is clear that plasticization still has an effect on the maximal stress value. However, there is little effect on strain to break. The reason may be that the embrittlement induced by physical ageing has more effect than the strain increase induced by matrix plasticization.

Chapter 4. Accelerated ageing of the resin

As with physically unaged resin, water induces a decrease in the resin's T_g . Application of the Simha-Boyer expression shows a less good agreement compared to that found for the resin not physically aged, as shown in Figure 4.24.

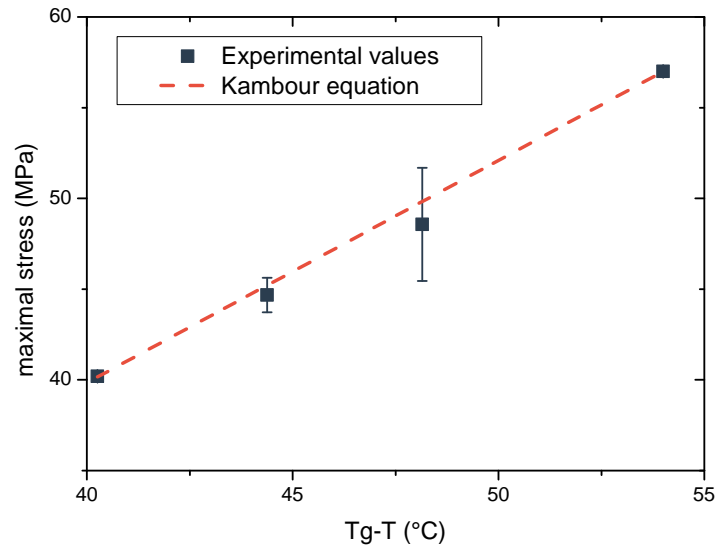


Figure 4.22 – Maximal tensile stress increase as a function of T_g-T temperature difference

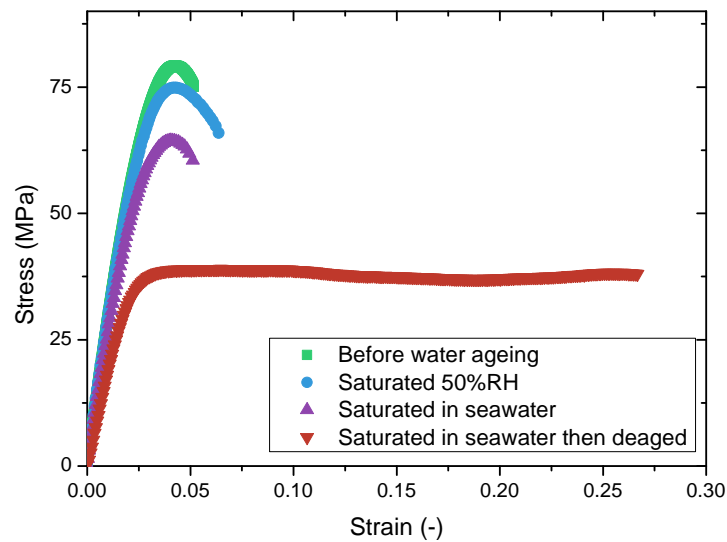


Figure 4.23 – Tensile response of water-saturated resin aged at 60 °C in inert atmosphere prior to water ageing

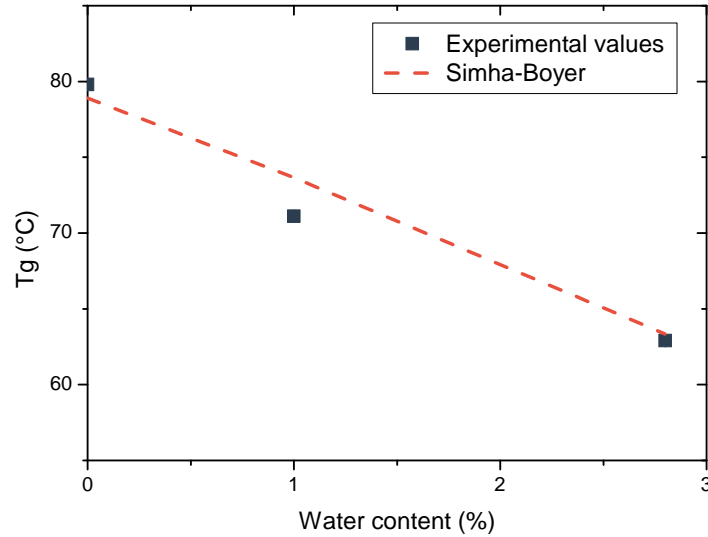


Figure 4.24 – Decrease in Tg induced by water absorption of a previously physically aged resin

Figure 4.25 represents the evolution of maximum stress as a function of the change in Tg value induced by water absorption for the resin physically aged and for the resin without physical ageing. It appears that the presence of physical ageing slightly attenuates the effect of water on the maximum stress decrease. This is characterised by the value of the proportionality constant being 0.84 MPa.K^{-1} for the previously physically aged resin whereas it is 1.23 MPa.K^{-1} for the resin without physical ageing. This change in proportionality constant is consistent with values recorded by Cook et al. [84, 85] which were in the range 0.5 to 1.5 MPa.K^{-1} but with different epoxy systems (anhydride-cured or ethylene diamine cured DGEBA epoxy resins).

As a conclusion to these sections, it was shown that the matrix resin is sensitive to two ageing phenomena; in addition to oxidation which was not mechanically highlighted here. These interact with each other, and have therefore been decoupled for better characterisation.

The first phenomenon, physical ageing, is activated by the temperature if kept below the material's Tg. The effect of physical ageing on the resin was found to be an embrittlement characterised by an increased maximum stress and a reduction of the strain to break. The maximum tensile stress increase was evaluated and correctly described by a modified KWW equation. The presence of water in the resin does change the kinetics of physical ageing which occurs more quickly when the resin is saturated, for the same ageing temperature. Physical ageing is fully reversible by subjecting the resin to above-Tg temperature.

The second ageing phenomenon is plasticization. The effect of plasticization on the resin showed good agreement with the Simha-Boyer and Kambour equations respectively

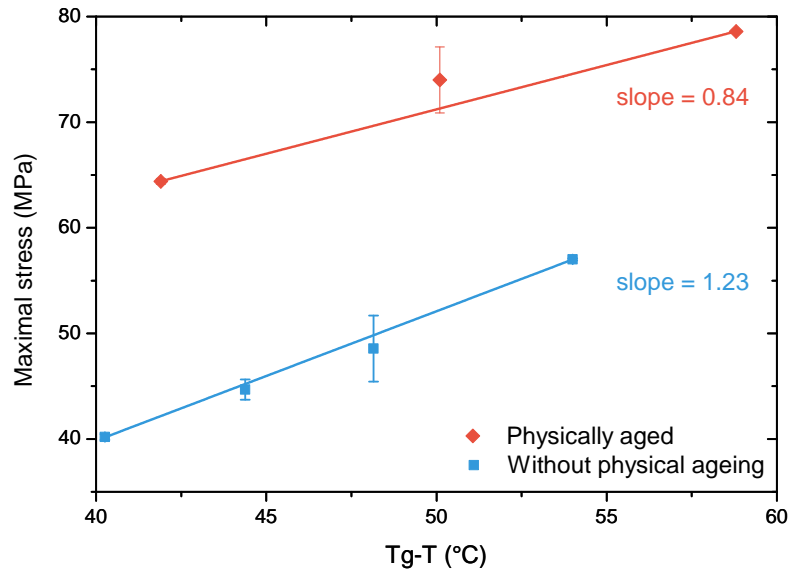


Figure 4.25 – Comparison with Kambour equation for resin with two physical ageing

for Tg and maximum stress decrease prediction. Plasticization effects were also evaluated for a previously physically aged resin. In this case the Kambour and Simha-Boyer equations are still in general agreement with the experimental values, even though the error was more important. Comparing the Kambour equations for the physically aged and not physically aged resin showed that physical ageing reduces the influence of water on maximum tensile stress.

This effect of physical ageing on the mechanical properties of the resin without fibre reinforcement raises questions as to the influence of this ageing mechanism on the composite properties, and particularly those governed by the matrix. This is the aim of the next section. The effect of water on the composite will then be discussed in later chapters.

4.2 Effect of physical ageing on composite

It was shown in the previous section that the resin used as the matrix for the composites in this study is sensitive to physical ageing when exposed to sub-Tg temperatures. The tensile behaviour of the neat resin becomes more brittle after physical ageing. It is therefore important to examine the effect of physical ageing on the composite properties. For composite structures, the three main damage mechanisms are transverse micro-cracking, fibre/matrix interface debonding and fibre breakage (see Figure 4.26). Of these three damage modes, two are matrix dependent, and so, could be affected by physical ageing. We therefore concentrated on mechanical tests that load the resin rather than the fibres. The effect of seawater on the other mechanical properties of the composite will be presented in later chapters.

The test samples were packed in vacuum bags and placed in 60 °C ovens for a period

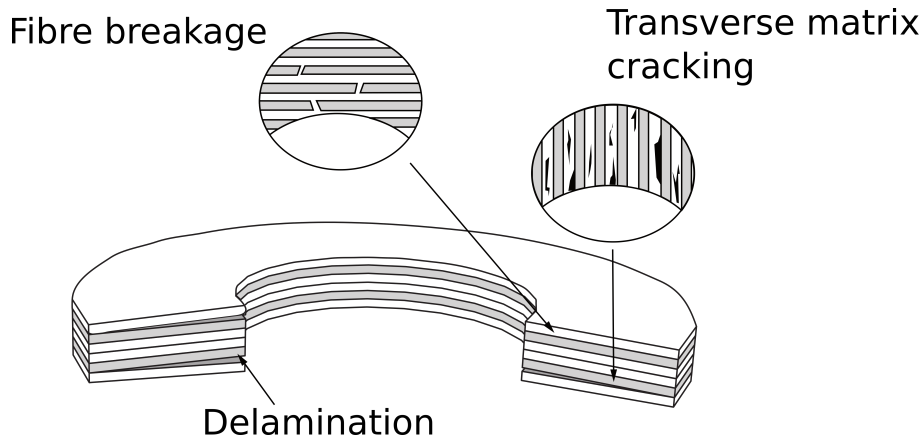


Figure 4.26 – Three main damage modes of unidirectional stacked composites [176]

of 1 week. At this temperature, the ageing time was considered long enough to consider the physical ageing to be complete or at least very close to a fully aged state. The initial reference state was obtained by performing a thermal rejuvenation (above- T_g + quenching) in order to eliminate any physical ageing that occurred prior to testing.

4.2.1 Effect of physical ageing on the composite transverse tensile properties

Transverse tensile tests are well known to be sensitive to the resin quality. With this orientation, the mechanical responses of the resin and the fibre/resin interface are predominant. Moreover, when designing composite structures, fibre orientations are optimized but there are often off-axis plies, which will be loaded in the transverse direction when other main load-bearing plies are loaded in the fibre direction. This can thus be a weak point in composite structures in service.

The result of physical ageing evaluated by transverse tensile tests, on 3 plies 90° specimens using the ASTM D3039 dimensions, shows a decrease in both strength and strain to break (Figure 4.27). The change in modulus is quite small even though it is visible on the stress-strain curves. We saw previously that physical ageing induced an embrittlement of the resin characterized by a decrease in strain to break and an increase in maximal stress. Here, the change in strength tends to decrease rather than the increase noted on the resin. However, as the resin breaks at lower strain and as modulus does not change significantly, specimens break at a lower stress. So the overall effect is again an embrittlement.

4.2.2 Evaluation of the influence of physical ageing on interlaminar shear strength

Delamination can occur by three different modes as discussed in Chapter 1. Mode II corresponds to shear loading, which can be induced by bending loads. Here, the sensitivity of shear strength to physical ageing was evaluated using the InterLaminar Shear Strength (ILSS) test method. The results from five physically unaged and five physically aged samples are summarized in Figure 4.28, which shows the average measured shear strengths.

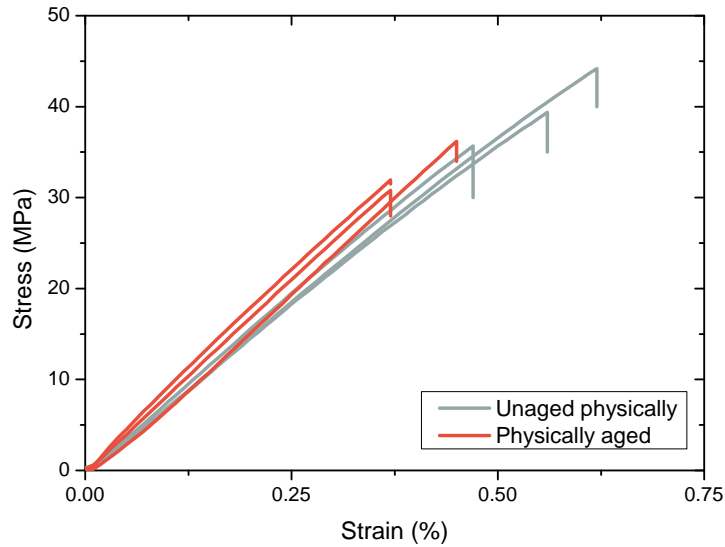


Figure 4.27 – Transverse tensile response of unidirectional composite subjected to physical ageing

The average values differ slightly but the high standard deviation for the physically unaged samples overshadows the possible change in interlaminar shear strength.

From these results, it appears that physical ageing has a limited influence on the composite properties. However, the fracture toughness of the composite was not studied under physical ageing. In fact, Chapter 6 will treat the delamination behaviour under mode I and mode II loading. The influence of physical ageing on these properties will be discussed there.

4.3 Conclusion

This chapter highlighted the fact that two ageing phenomena occur in the unreinforced epoxy matrix resin during accelerated seawater ageing. The first ageing phenomenon, plasticization, is well known when performing water ageing on polymers such as epoxy resins. The effect of plasticization is proportional to the amount of water in the polymer. This plasticization induces a decrease of the material T_g that results from water molecules entering between the polymer chains and increasing chain mobility. The decrease of T_g can be predicted using the Simha-Boyer equation. The effect of plasticization on resin tensile properties was evaluated. Plasticization induces a decrease in maximum stress with an increase in strain to break. The decrease in maximum stress as a function of T_g decrease was found to be in accordance with Kambour's equations. Finally, plasticization was found to be fully reversible after drying the resin.

The second ageing phenomenon recorded on the pure resin was identified as physical ageing. This ageing is induced by the matrix being exposed to sub- T_g temperatures. The

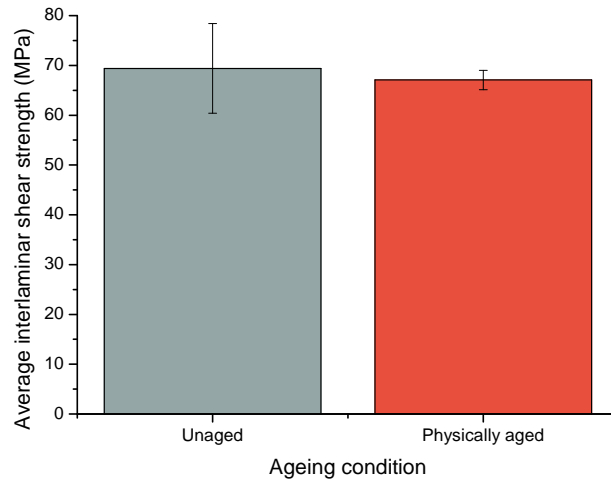


Figure 4.28 – Effect of physical ageing on the interlaminar shear strength of a 6 plies UD composite

level of physical ageing with time was evaluated by the maximum stress increase, even though physical ageing also induces a decrease in strain to break. In addition, a change in fracture surface confirmed that physical ageing induces an embrittlement of the resin. Physical ageing was found to progress in the same manner for both the dry and saturated resin, resulting in a maximum stress increase, a drop in strain to break and in a change in the fracture surface. The change in maximum stress with physical ageing time was described by a modified KWW equation with good agreement for both dry and saturated conditions. Characteristic relaxation times (τ) were different for the two water conditions. In fact, for the same ageing temperature, physical ageing is accelerated by a factor of 10 when the resin is saturated. There was also a change in the τ dependency on temperature, which could be estimated using an Arrhenius law. It appears that in the saturated state, temperature dependence is higher, as an activation energy of 160 kJ.mol^{-1} was recorded compared to 106 kJ.mol^{-1} in the dry state. The transition between the saturated and dry states, from a physical ageing point of view would need further investigation allowing integration of an additional parameter in the KWW equation, in order to take into account the amount of water. The same equation could then be used to describe the evolution of physical ageing.

The effect of physical ageing on the resin was evaluated and showed non-negligible variations for different mechanical properties. The sensitivity of the composite to physical ageing was evaluated, to understand if such a change on the resin could have an influence on the composite's properties. It appears that for interlaminar shear strength and transverse tensile strength, the physical ageing effect is limited, even though it cannot be neglected for transverse tensile properties. It may therefore be interesting to investigate the influence of physical ageing on the delamination properties, and this will be discussed in a later chapter.

Seawater ageing of composite materials

The main objective of this chapter is to study the long-term seawater ageing effect on mechanical properties of the composite under static and cyclic loading. The first question to be addressed is: What type of loading should be applied, in order to be as representative as possible of real load case scenarios of marine propeller blades. A first analysis was therefore performed on published studies for marine propellers, in order to define these. Then, based on published calculations and measurements, a first study of the fatigue behaviour under first quasi-static tensile then cyclic tensile-tensile loadings was carried out, with different ply orientations. In a second set of tests, flexural loading was applied to induce shear and compressive loads. The effect of long-term seawater ageing will be discussed for both cases.

5.1 Load cases for propeller blades

One of the consequences of using composite propeller blades, as discussed in Chapter 2, is the fact that when loaded to the propeller's designed rotational speed, there is deformation of the blades. An example of the measured tip deflection of a nylon propeller blade in a cavitation tunnel is shown in Figure 5.1 from Taketani et al. [9]. In this case, the tip deflexion was 5.4 mm. The same tests were run on a CFRP propeller leading to a tip deflection of 1.8 mm at 30 rpm and a water flow speed of 3 m.s^{-1} . This difference is due to the higher stiffness of CFRP.

This tip deflection can be taken into account and used to optimize the morphing of the blade. Optimizing the tip deflection and the blade deformations can result in fuel economy by reducing the required torque. To study this, combined FEM and CFD analysis studies have shown results of optimized propeller blades with their deformed shapes. Modern calculation facilities allow better definition of stress and strain resulting from complicated loadings such as those for propeller blades. For example, Young et al. [177] proposed an optimised propeller geometry and fibre orientation for a 2 foot (610 mm) diameter composite propeller. The result of such optimisation is multi-oriented deformations as shown in Figure 5.2. On this figure, the flexural loading is shown by sub figures a, b and c. The tip deflexion obtained experimentally by Tekatani et al. is magnified here, but it

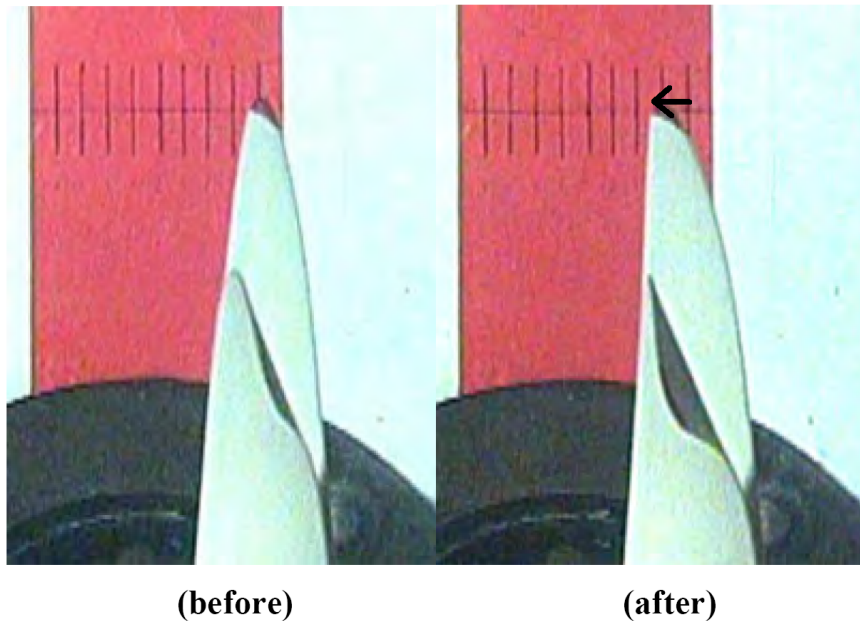


Figure 5.1 – Measured tip advance of 1.7 mm of a Nylon propeller at 10 rpm and 0.75 m.s^{-1} water speed in cavitation tunnel Taketani et al. [9]

shows that the deflection extends to up to 4/5 of the blade's length. On subfigures d and e are shown the strains in the transverse and in the fibre direction respectively.

Lin et al. [178] evaluated the possible failures that could occur for different stacking sequences for composite propeller blades. The main failures were matrix tension and delamination at the leading and trailing edges.

These studies present steady loading cases. Marine propeller blades are rotating parts that are obviously subjected to cyclic loadings. One assumption would be to consider the propeller rotation frequency as the loading frequency of the material. He et al. [16] studied the difference between metal and composite propeller blades under unsteady flow. The tip deflection according to the x, y and z axes as a function of blade angle is shown in Figure 5.3. Even if the strain values are low, frequency is high and it may induce high numbers of cycles that could cause early failures. The presence of such high frequency/small deflections can result from the high natural frequencies of the blade's shape and stiffness as discussed by Young et al. [177].

As a conclusion concerning these studies, propeller blades, whether they are made of composite or metal, are subjected to high cycle fatigue loading. Composite propeller blades have the advantage of being more flexible and so optimisation of the deformed geometry can be used to increase energy efficiency. However, deformation of the blade induces sequential and cyclic flexural, tensile and shear loadings. In order to propose improved designs and avoid early failures, it is important to evaluate the fatigue properties under these different loadings. It should also be noted that these studies do not take into account how the material's properties change after extended immersion in water and this is a key issue for marine propeller blades, which has received little attention to date.

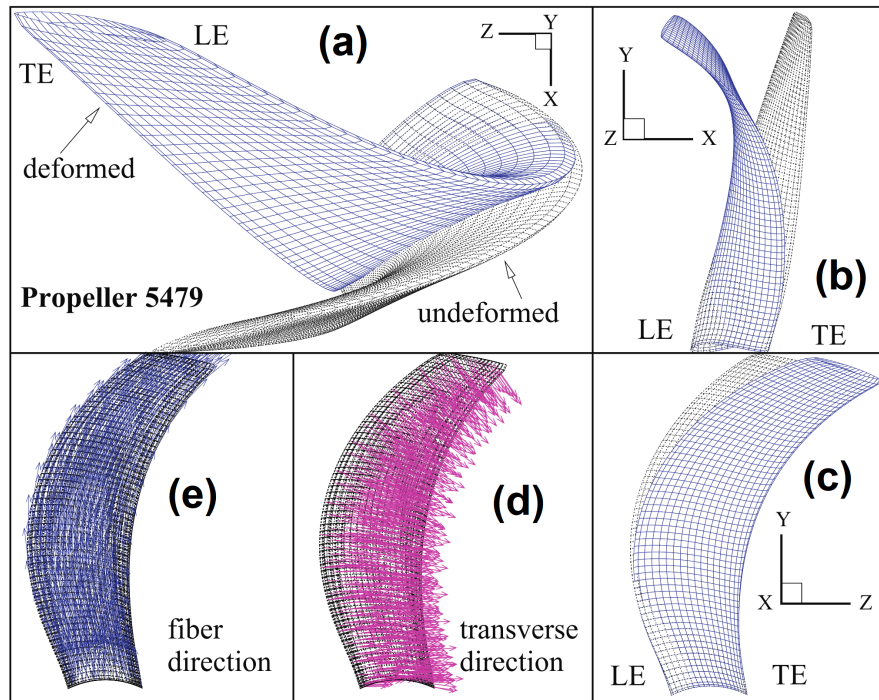


Figure 5.2 – Strain induced on a "flexible" design propeller blade at 909 rpm, $J=0.66$ (deformations magnified by 10) young et al. [177]

In this chapter, the long-term behaviour of the composite material under seawater ageing was evaluated under different loading configurations. A first section will discuss the behaviour under tensile loadings with three different fibre orientations and stacking sequences. Then the bending properties will be evaluated by four-point flexure fatigue tests. Delamination and crack propagation properties will be studied in a subsequent chapter.

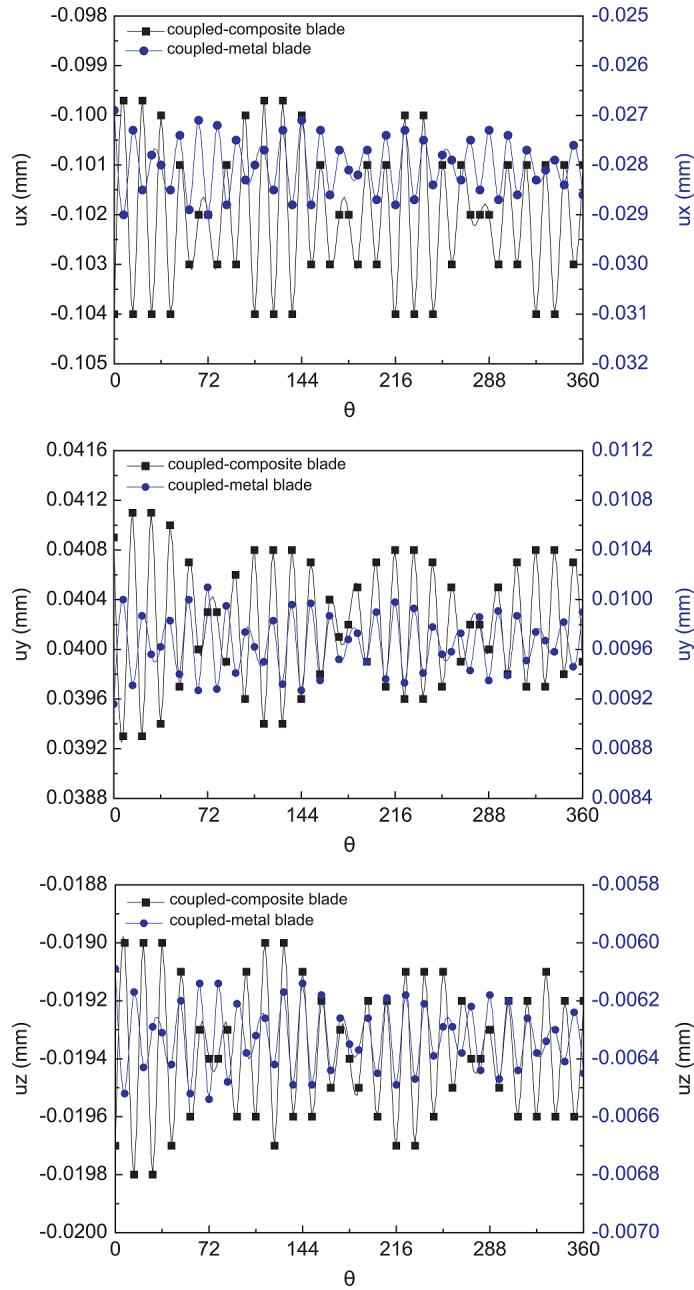


Figure 5.3 – Deflection of the blade's tip for a composite and a metal propeller calculated theoretically by He et al. [16]

5.2 Tensile loading

As discussed previously, tensile loadings are induced by blade deformation. The tensile loadings can come from the desired deformation of the blade, modal vibrations or from centrifugal forces. Tensile properties were evaluated in the fibre direction and in the transverse direction. In addition, in order to be representative of real stacking sequences, a cross-ply ($0/90^\circ$) composite, as presented in Chapter 2, was also studied. The effect of physical ageing, discussed in the previous chapter, is limited with respect to the tensile properties when 0° fibre reinforcement is present, so no special conditioning was needed for these tests.

5.2.1 Effect of seawater

Quasi-static tests

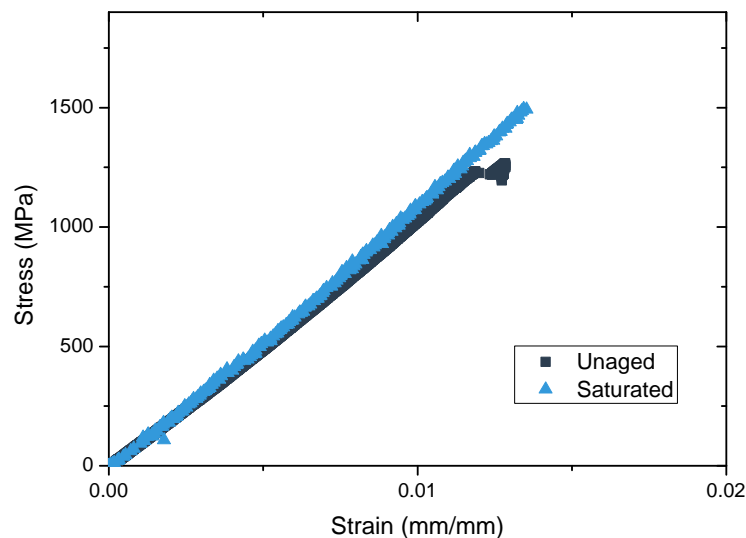


Figure 5.4 – Effect of seawater on 0° tensile behaviour of unidirectional composite

In order to perform fatigue tests, Ultimate Tensile Strengths (UTS) needed to be evaluated first for the three different ply orientations. Strain was measured using Digital Image Correlation. The recorded UTS in the fibre direction was measured to be higher after saturation, as shown in Figure 5.4. The ageing condition here was 3.5 months in seawater at 60°C . The measured average UTS for the unaged condition was recorded at 1190 MPa and reached 1450 MPa after 6 months seawater ageing.

At first sight, this result is surprising, as usually seawater tends to decrease material properties. However, there are differences in the test conditions for the two series. Glass-fibre tabs were used for the unaged condition whereas aluminium tabs were used for saturated specimens as shown in Figure 5.5. Glass fibre tabs were not used for the second

series, as when they are gripped they generate parasite noise, which is recorded by the acoustic emission apparatus. Performing these tests with aluminium tabs was used to answer this interrogation. 0 ° tensile tests on unidirectional specimens are very sensitive to load introduction conditions.

It is also important to note that the measured unaged UTS is half the theoretical value, that can be estimated as :

$$\sigma_{f_{max}} = (1 - V_f)\sigma_Y + V_f\sigma_{Rf} \quad (5.1)$$

In this equation, the composite's UTS, $\sigma_{f_{max}}$, is calculated from the UTS of the fibre σ_{Rf} , and the matrix σ_Y and the fibre volume ratio V_f . The failure stress of the resin, as measured in the previous chapter is equal to 57 MPa (dry) and 38 MPa (saturated). Fibre volume ratio of the tensile specimens was measured to be 47.5 % and the fibre UTS as provided by the supplier is equal to 4.9 GPa. Theoretical UTS of the composite in the fibre direction should therefore be around 2.3 GPa, the resin having a relatively low impact on the UTS in the fibre direction. From this estimation, it is clear that the unaged strength values are underestimated, and it is not possible to conclude on the influence of aging on these unidirectional composites.

A different observation can be made on the cross-ply sequence, that will be referred to as 0/90, the stacking sequence being $[0/90/0/90/0]_s$. Here, the measured UTS does change a little for the two ageing conditions (Figure 5.6).

The measured UTS is around 990 MPa for the unaged condition and 940 MPa in the saturated condition. For these tests, there was no change of tab material between the two ageing conditions. The slight decrease of the UTS could come from the change in maximal stress of the resin. For the cross-ply stacking sequence, the resin has more influence on the composite mechanical properties as the transverse, and thus matrix dominated, orientation represents 40 % of the loaded orientation (4 plies out of 10). With a fibre volume ratio of 50 % for this stacking sequence, the theoretical UTS unaged is estimated as:

$$\sigma_{0/90_{max}} = r_f\sigma_{f_{max}} + r_T\sigma_{TU} \quad (5.2)$$

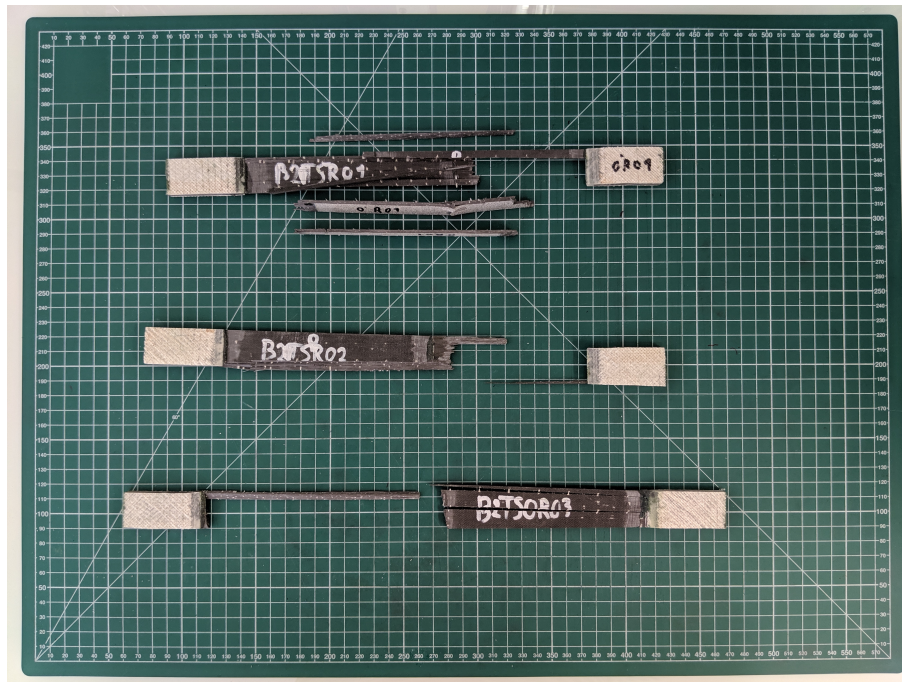
$$\sigma_{TU} = \frac{E_T\sigma_{MU}(1 - V_f^{\frac{1}{3}})}{E_M} \quad (5.3)$$

$$\frac{1}{E_T} = \frac{(1 - V_f)}{E_M} + \frac{V_f}{E_f} \quad (5.4)$$

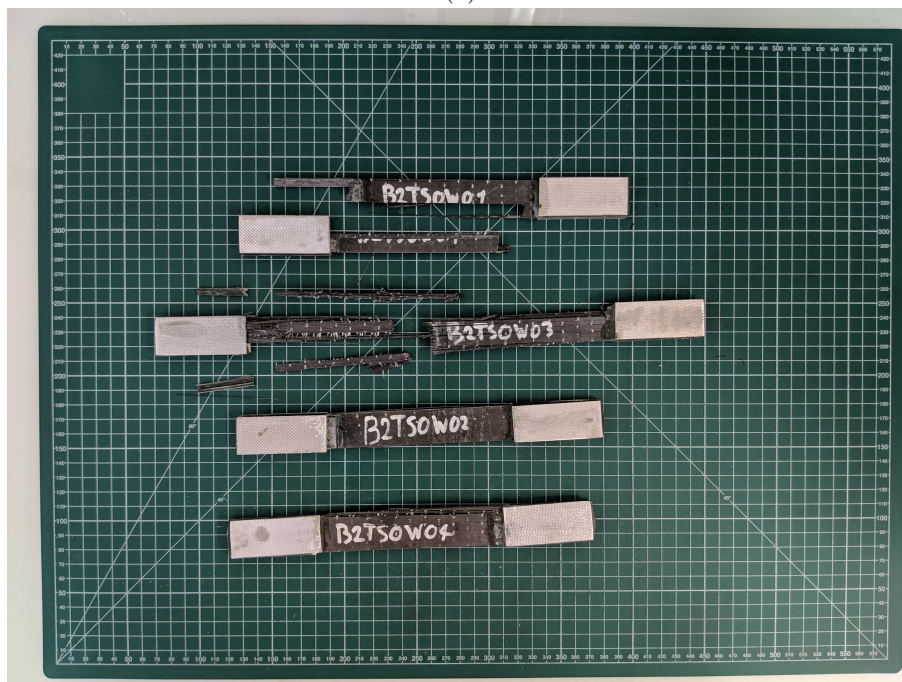
In Eq. (5.2), r_f and r_T are respectively the ratios of 0° and 90° plies, being 0.6 and 0.4 here; the transverse UTS, σ_{TU} , is calculated using the commonly adopted Eq. (5.3) with σ_{MU} being the UTS of the matrix, E_M the matrix' Young's modulus and the unidirectional transverse Young modulus, E_T , calculated with Eq. (5.4). The theoretical UTS of the 0/90 composite is equal to around 1300 MPa according to these equations regardless of the ageing condition as transverse UTS does not play a major role on the 0/90 composite's UTS. The results shown in Figure 5.6 show that even the unaged specimens have not achieved the expected strength; this may be related to the quality of the fibre/matrix interface or to the influence of stitching.

Finally, the UTS measured by tensile tests in the transverse direction to unidirectional fibres (90° tests) shows a decrease close to 50 % after saturation, Figure 5.7. The average

Chapter 5. Seawater ageing of composite materials



(a)



(b)

Figure 5.5 – Fractured unidirectional tensile specimens as unaged (a) and saturated (b) ageing conditions

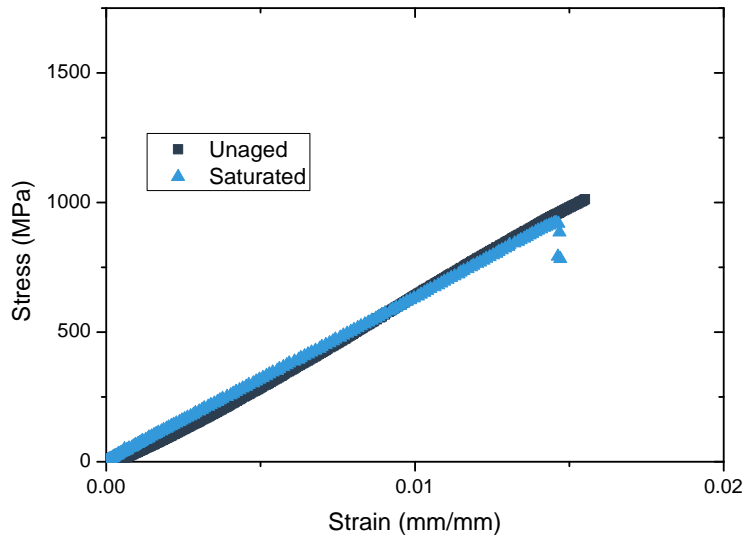


Figure 5.6 – Effect of seawater on tensile behaviour of 0/90° composite

unaged UTS was measured to be 42 MPa and the saturated UTS was measured to be 23 MPa. This decrease is coherent with the effect of plasticization shown in the previous chapter with an increased reduction of the maximum stress here.

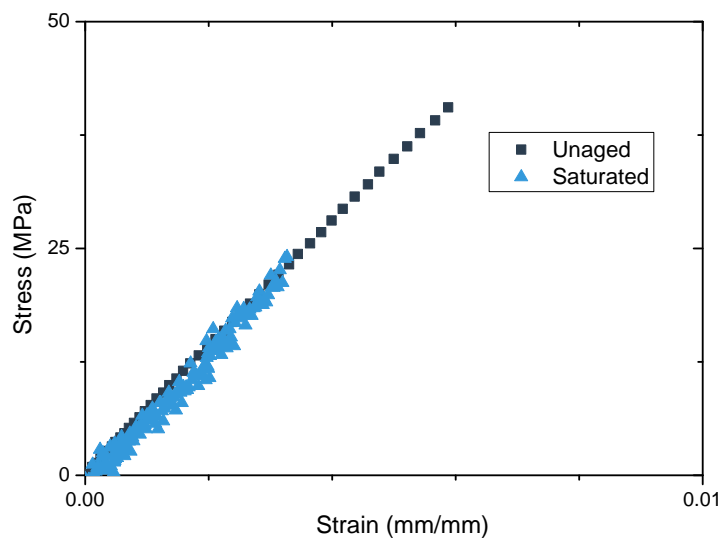


Figure 5.7 – Effect of seawater on tensile behaviour of unidirectional composite in the transverse direction

Cyclic tensile tests

The effect of seawater ageing on the quasi-static tensile properties has been evaluated for three different composite configurations: unidirectional in the fibre and transverse direction and cross-ply with the sequence $[0/90/0/90/0]_s$. The main measured effect of seawater was recorded on the transverse unidirectional specimens. This is not unexpected, as matrix resin is sensitive to seawater ageing whereas carbon fibres are known to be relatively inert. No change in Young's modulus was recorded for the three fibre orientations. Changes to the fibre/matrix interface region are not excluded, but alternative tests are needed to examine this area.

Fatigue tests were then performed for the three aforementioned stacking sequences. The same two ageing conditions were tested and referred to as "unaged" and "saturated". Fatigue tests were performed at a stress ratio of $R = 0.1$, which is representative of a propeller blade being deformed and then subjected to additional cyclic loadings. A 1 Hz frequency was chosen in order to limit self-heating. Ten specimens were prepared with a target number of four maximal stress levels. The replication of the six fatigue batches is shown in Table 5.1 and its calculation is:

$$N_R = 100 \times \left(1 - \frac{i}{Nb}\right) \quad (5.5)$$

In this equation, N_R is the calculated replication in percent, i is the number of stress levels tested and Nb is the total number of tested specimens. Replications of the presented tensile-tensile test data are between 50 and 62.5 % which is a bit low, but sufficient for a design allowable. Ten specimens were prepared for each test condition but there were some rejected specimens due to non-valid failures or test problems.

Table 5.1 – Replication of tensile-tensile test data

Test condition	i	Nb	N_R (%)
Unaged unidirectional	4	10	60
Saturated fibre direction	4	8	50
Unaged 0/90	4	9	55
Saturated 0/90	3	8	62.5
Unaged transverse	5	10	50
Saturated transverse	4	9	55

The statistical Whitney Pooling Scheme (WPS) was used to obtain fatigue curves for the three tested fibre orientations with a reliability of 95 %. This statistical approach is based on the assumption of power-law fitted data among with a Weibull distribution of time to failure. This approach was described in Chapter 2 and data was processed with a SciLab™ code (see Appendix B). The advantage of such an approach is that conservative results are obtained, compared to a more standard power law approach. Even though WPS was used to compare ageing behaviours, the standard power law parameters were calculated, and the parameters of both methods are presented in Table 5.2.

Unidirectional fatigue tests in the fibre direction presented a lot of variability in the unaged condition. Even though, for quasi-static tests, the UTS was higher in the saturated state, the fatigue data show a decrease in lifetime after saturation. In fact, based on the

Table 5.2 – Whitney’s pooling scheme and power law parameters of the tensile fatigue tests

Stacking sequence	Ageing condition	$\sigma = \sigma_0 e^{-\frac{1}{k}}$		Whitney Pooling Scheme		
		σ_0 (MPa)	$\frac{1}{k}$	σ_0 (MPa)	$\frac{1}{k}$	a_f
UD fibre direction	Unaged	978	0.0055	3342	0.1092	0.544
	Saturated	1463	0.0455	2463	0.1019	1.020
0/90	Unaged	1109	0.0377	1309	0.0518	1.848
	Saturated	1012	0.0314	1057	0.0354	3.043
UD transverse direction	Unaged	50.1	0.0798	54.6	0.0856	1.891
	Saturated	27.5	0.0607	37.3	0.0883	1.454

WPS curves, there is a loss of around 1 decade with similar curve slopes (Figure 5.8). Unfortunately, runout data were not taken into account for WPS calculation and the validity of the WPS could be questioned as the experimental data shows a high deviation of the number of cycles to failure. However, the stress levels at 10^6 cycles for both conditions are conservative if one refers to the WPS curves. Data variability may be due to the tested fibre orientation that is known to behave with high variability when dealing with carbon fibre reinforced composites.

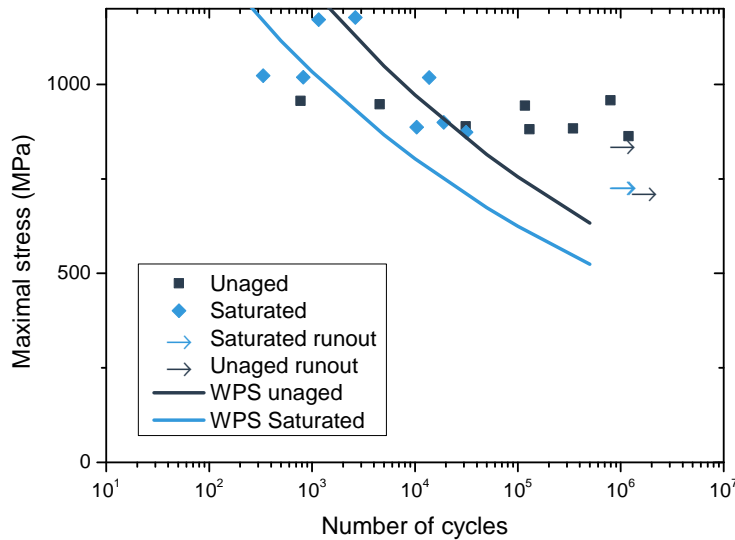


Figure 5.8 – Ageing effect on unidirectional composite in the fibre direction

As with quasi-static tests, the 0/90 composite showed only a slight change in fatigue behaviour after aging. As shown in Figure 5.9, there is a slight lowering in the curve slope

for the saturated composite. However, fatigue data does not fully differentiate between the two ageing conditions. No significant change is noted between unaged and saturated 0/90 composites.

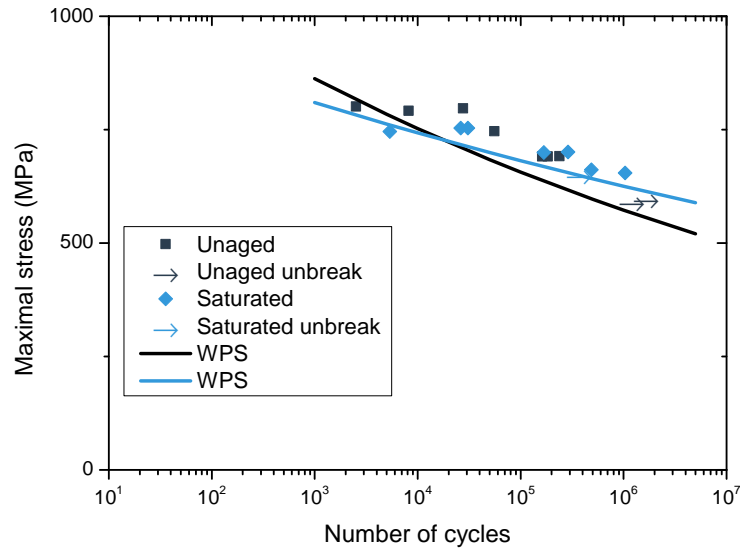


Figure 5.9 – Ageing effect on the fatigue behaviour of 0/90 composite

The fatigue response of transversely loaded unidirectional specimens shows a distinct influence of aging, as indicated previously for the quasi-static properties, (Figure 5.10). From a maximum stress point of view, to reach equivalent lifetimes, a 30 % lower average stress is needed after aging.

In conclusion, it is shown here that long-term seawater ageing induces a clear reduction in quasi-static and fatigue loading principally when considering transverse tensile loads. The decrease represents around 50 % in quasi-static and 30 % in fatigue tests. The use of WPS allows a better description of the fatigue data for 90° and 0/90 composites, while the data for unidirectional composite loaded in the fibre direction are very flat and show a lot more variation in lifetimes.

In terms of prediction, it is interesting to examine whether the decrease of the fatigue curve could be predicted from the decrease in static strength. To do so, the fatigue curve from Figure 5.10 was normalized by the static strength of the composite for the respective ageing condition (see Figure 5.11). There is still a small shift between the two conditions even though the trends are similar and there is some overlap.

All these data show an effect of ageing on the cycles to failure of the composite for different stress levels. However, this does not mean that failure occurs instantly. There is, usually, damage occurring throughout the specimen's lifetime. This will be studied in the next section.

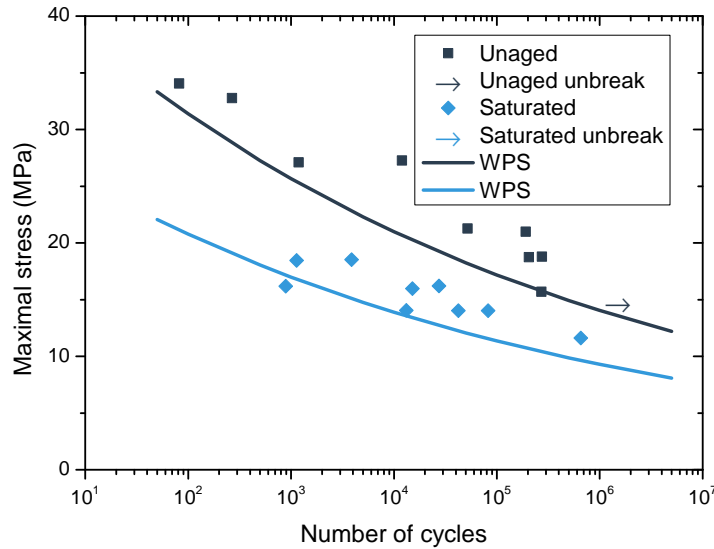


Figure 5.10 – Ageing effect on the fatigue behaviour of unidirectional transversely loaded composite

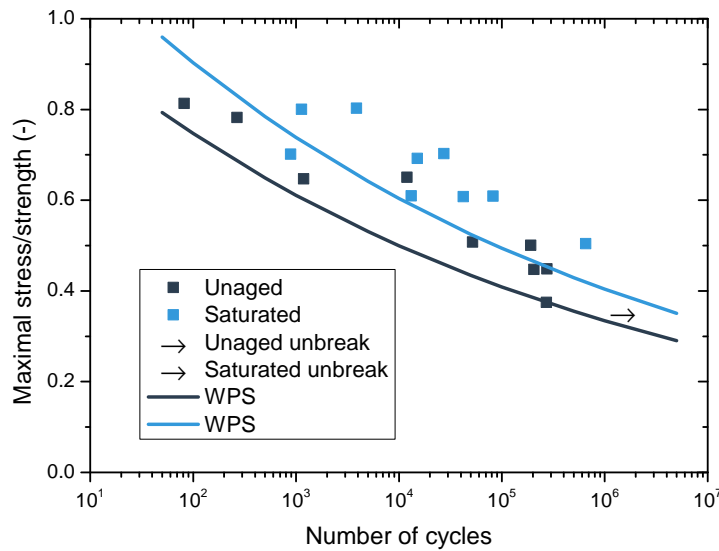


Figure 5.11 – Fatigue curves of tensile tests on 90° composite normalized by the strength

Damage sequence

Fatigue lifetime and quasi-static strengths are often used to characterize composites but damage can occur and propagate well before final failure. Thus, unbroken specimens

do not necessarily mean undamaged material. There is therefore a need to evaluate the damage evolution during the fatigue tests performed previously.

To do so, two damage measurement methods were chosen: stiffness degradation and acoustic emission. The stiffness degradation, R in $N.mm^{-1}$, was calculated by dividing the load by the displacement as:

$$K = \frac{F_{max} - F_{min}}{d_{max} - d_{min}} \quad (5.6)$$

F_{max} and F_{min} were measured by the load cell and d_{min} and d_{max} were measured by the LVDT of the test machine. Both measurements were recorded for every load cycle. It should be noted that these are global displacements, not gauge length extensometry values, so they are used for qualitative comparisons of behaviour here.

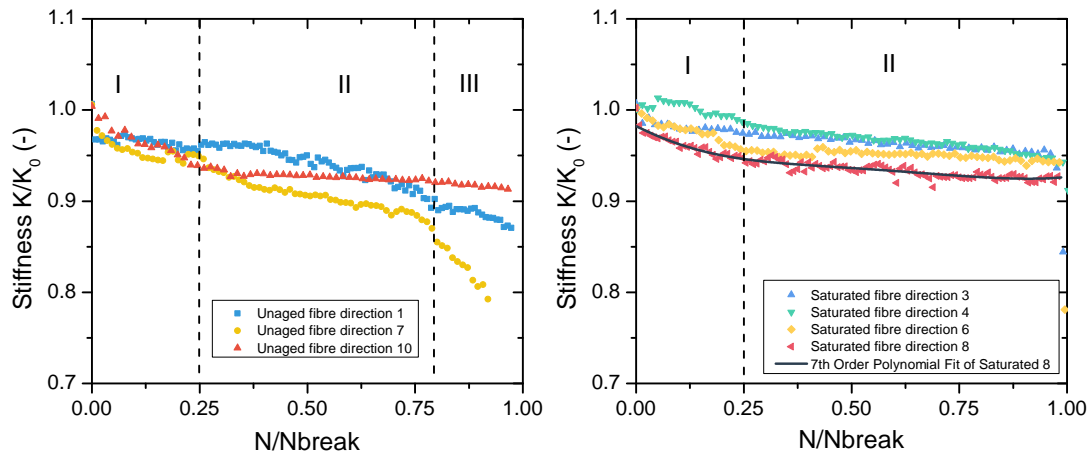


Figure 5.12 – Stiffness curves of unidirectional tensile tests unaged (left) and saturated (right)

Stiffness degradation, $\frac{K}{K_0}$, K_0 being the initial stiffness, for the 0° orientation showed different forms in the unaged state as shown in Figure 5.12. In this figure, and more generally for the other stiffness curves, different plots were selected to be representative of the entire set of stiffness curves. Most samples showed a two-phase degradation. This degradation was characterized by an initial stiffness reduction (around 5 %) until 25 % of the total lifetime followed by an almost stable degradation until failure. For the specimen number 7, a third phase occurred from around 80 % of the lifetime that is characterized by a significant final decrease of the stiffness resulting in specimen’s failure. For the saturated condition, only a two-phase degradation was recorded. The difference between unaged and saturated curves was that failure occurred with a final stiffness generally over 90 % for the saturated condition whereas prior-to-failure stiffness for the unaged state was lower, around 90 % or just below.

The damage behaviour for the cross-ply 0/90 composite showed only the three-phase stiffness degradation form, Figure 5.13. Here, the first degradation phase ended below 5 % of the total lifetime. This is much sooner and faster compared to the first degradation

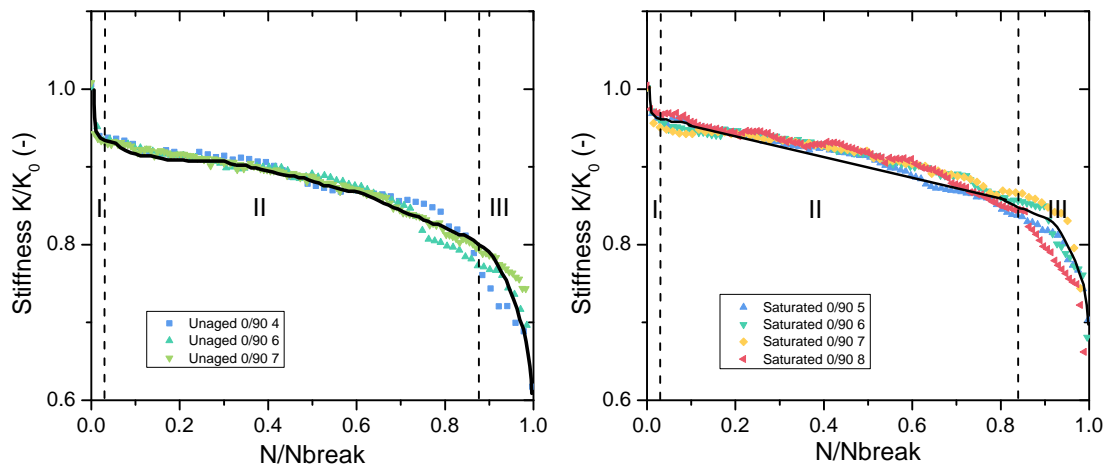


Figure 5.13 – Stiffness curves of 0/90 composite unaged (left) and saturated (right)

phase seen on the 0° tensile composite. This initial reduction was less important for the saturated composite as it represents around 2.5 % stiffness reduction whereas it was close to 5 % for the unaged condition. The transition between phases II and III seems to occur slightly earlier after seawater ageing even though a clear delimitation of the transition cannot be determined.

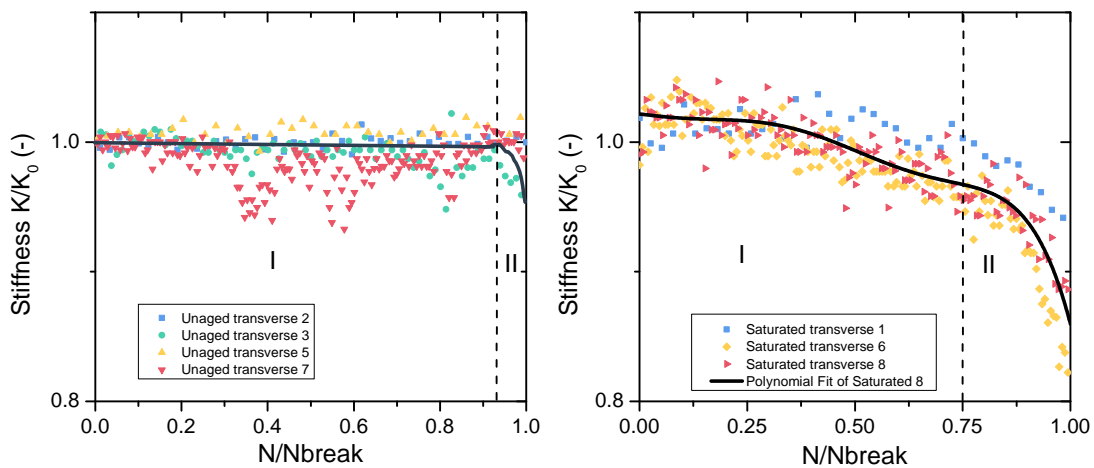


Figure 5.14 – Stiffness curves of transversely loaded unidirectional composite unaged (left) and saturated (right)

Finally, Figure 5.14 shows the stiffness degradation curves of the 90° composite, and a different behaviour is observed compared to unaged samples. This time, it seems that there is no initial degradation, only a constant stiffness in the case of unaged condition and a gradually decreasing stiffness for the saturated composite.

Prior to failure, the two conditions show a final subtle degradation. This final degradation ends at a relatively high stiffness in the case of the unaged composite. On the

contrary, it decreases a lot more for the saturated composite ending at around 80 % of the initial stiffness. The final transition before failure happens earlier for the saturated composite, as was noted for the cross-ply composite. The stiffness level at failure is coherent with the results of pure resin tensile tests for which it was shown that seawater induces plasticization of the resin, resulting in an increased strain at break.

By combining the behaviour of the three composite configurations, one could postulate that the characteristic phases of the cross-ply behaviour could be attributed to either the 0° or the 90° plies. This would mean that the initial decrease seen in the cross-ply 0/90 composite results from the 0° plies slightly degrading and final failure would result from the final failure of the resin. However, the normal fracture scenario (see Figure 1.8 from section 1.3.1) does not agree with the one theoretically exposed here.

In order to try to clarify this, acoustic emission was recorded for most of the fatigue tests. The fatigue samples were instrumented with two transducers, and a classification method was used on the recorded signals. This classification, based on the k-means method (see Chapter 2), allows the entire signal batch of a specimen to be classified in different clusters. These clusters correspond to signals having common features, such as similar released energy or peak frequencies. An example of clustering on the recorded signals of aged 0° composite is shown in Figure 5.15.

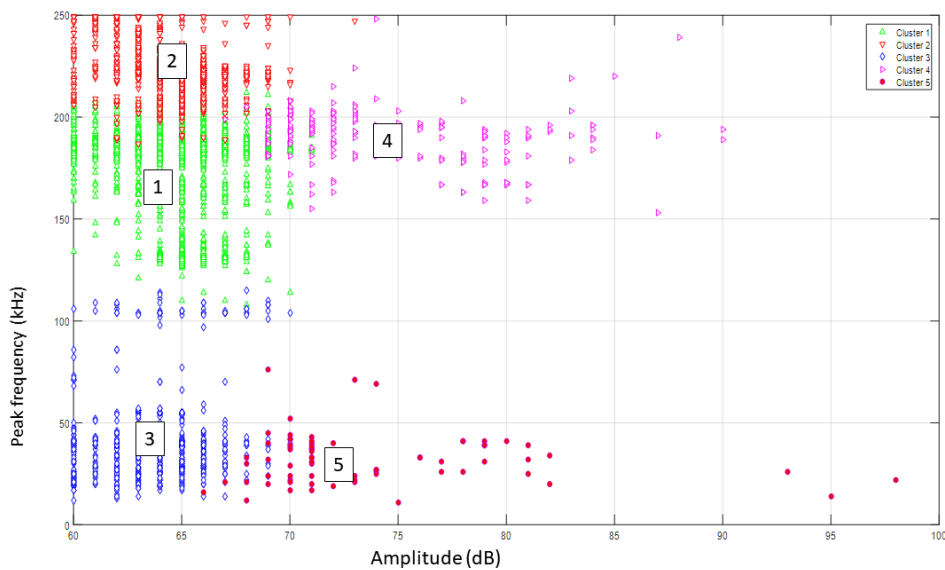


Figure 5.15 – Clustered signals of the 0° composite specimen n°6 saturated as a Peak frequency vs Amplitude layout

Interestingly, in the case of 0° specimens the occurrence of different clusters does not follow the stiffness degradation curve as shown in Figure 5.16. In fact, when considering the previously described two-phase stiffness degradation of the 0° composite, there was a first decrease until 25 % of the lifetime followed by a semi-stable phase. On the other hand, when considering acoustic emission, the occurrence of cluster-signals is low and

progressively increases from 25 % of the lifetime. This shows that even though stiffness does not change from 25 to 100 % of the lifetime, this does not mean that there is no damage during this phase.

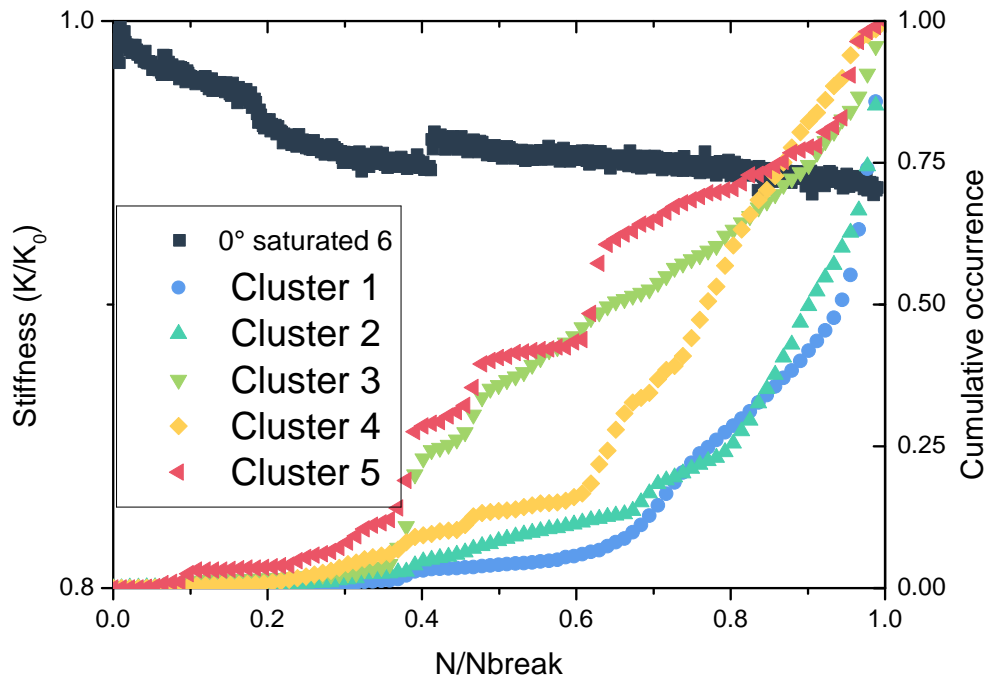


Figure 5.16 – Clustered signals of the 0° composite specimen n°6 saturated as a Peak frequency vs Amplitude layout

The same observations can be made for the 90° fatigue tests as shown in Figure 5.17. On this figure, clusters are not those from Figure 5.15, as 0° and 90° composites do not fail in the same way. Thus, another classification on the 90° specimens was performed and new clusters were found. During the first semi-stable phase, the cluster 1 signals are emitted throughout the lifetime, as with the cluster 2 on a lower level. This time, two clusters (n°3 and 4) seem to be indicative of final failure as they appear at the same place as that where the final stiffness decrease happens.

By performing further classification tests, it would be interesting to try to attribute one signal class to a specific failure such as fibre or matrix failure. This would be possible by classifying signals from quasi-static unidirectional composites in the fibre and transverse directions.

As a conclusion of this section, long-term seawater ageing does produce mechanical degradation, mainly for transverse tensile loading. A 50 % decrease in UTS was measured and the fatigue curve shifted down on the stress axis by 30 %. Long-term seawater ageing did not induce a large change in tests in the fibre direction nor for the 0/90 cross-ply composite. This was attributed to the fact that these fibre orientations rely mainly on the

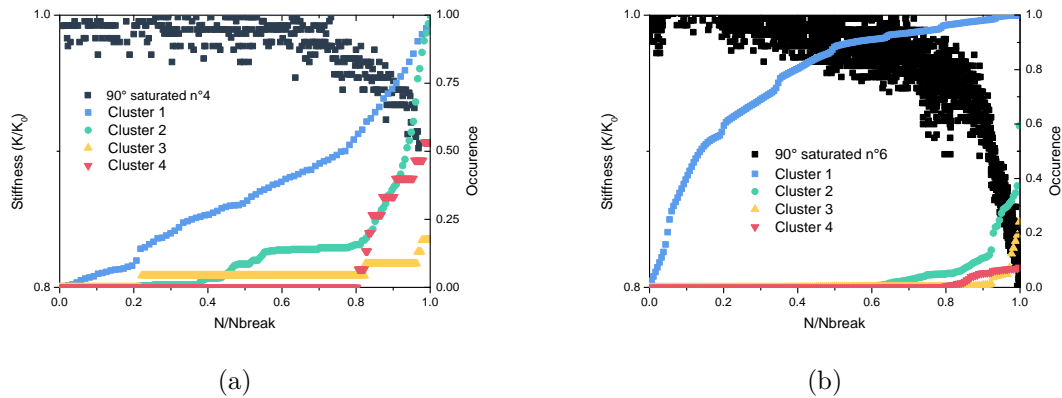


Figure 5.17 – Occurrence of clusters during 90° tensile fatigue tests on saturated specimens 3 (a) and 6 (b)

fibre properties that are known to be insensitive to seawater ageing.

When considering the stiffness degradation trends, there is a net difference between the three composite orientations with 0° and 90° composites both showing a two phase degradation behaviour. Both trends have a semi-stable phase, the 0° composite being stable after a small decrease of stiffness, the 90° having this semi-stable phase from the beginning of the lifetime before a second, decreasing phase. Acoustic emission showed that even though stiffness seems stable, it cannot be supposed that there is no damage formation during this phase. In fact, the presence of acoustic signals during this phase is indicative of damage occurring. On the other hand, the 0/90 cross ply does show a more classic three phase degradation trend.

After long-term seawater ageing, there are only small changes in the stiffness degradation trends. These small modifications were recorded mainly for the 0/90 cross-ply and 90° transverse orientations.

5.3 Cyclic four point flexure loading

As shown in the first section, marine propeller blades encounter both tensile and flexural stresses. The tensile properties were studied in the previous section. Flexure properties were then studied by four point bending tests. A first study on the frequency effect on the fatigue properties will be presented followed by the study of the ageing effect.

5.3.1 Effect of load frequency

Marine propellers rotate at different speeds depending on the propeller's diameter and the designed boat speed. The order of magnitude of the large marine propeller rotational speeds are in the range of 100 to 1000 rpm (1 to 16 Hz). On the other hand, resonant vibrations of the blade, as discussed in the first section, do occur at higher frequencies (100 Hz to 2 kHz). Unfortunately, the servo-hydraulic test machines available for this study were not designed to load at high frequencies such as those of the resonant frequencies.

Moreover, such frequencies with the low stresses involved would require studying the Very High Cycle Fatigue (VHCF) regime, which was not the aim of this thesis. This is another research area and some results are available for composites [179,180].

A first question to answer here is whether the load frequency has an impact on the fatigue properties. To do this, four frequencies were chosen to study this frequency dependency; 2, 4, 8 and 12 Hz. The self-heating of the specimens was expected to be limited, as all tests were performed immersed in seawater, as described in Chapter 2.

A first evaluation was performed on a unidirectional 10 ply thick composite. The quasi-static ultimate strengths were evaluated at different loading rates, which were chosen so that they would be representative of the highest loading rates at the corresponding frequency, as fatigue tests are load controlled. Considering the displacement in mm, $D(t)$, as a function of the time in seconds, t , resulting from the sine load signal, with a displacement amplitude A in mm and a load frequency f in Hz, this signal has the Eq. (5.7). The signal's derivate highest value, V , which corresponds to the highest load speed in mm/min, can be calculated as in Eq. (5.8).

$$D(t) = A \times \sin(2\pi ft) \quad (5.7)$$

$$V = A \times f \times 60 \quad (5.8)$$

$$(5.9)$$

The displacement amplitude was determined prior to the quasi-static tests to be $A = 3.2\text{mm}$. The quasi-static stress versus displacement curves at the four loading rates show that there is a small drop in the stress at break during four point bending as the rate is increased, as shown in Figure 5.18. These curves are the selected, most representative curves from three specimens tested at each loading rate.

Table 5.3 summarizes the results of these tests. It can be seen that changing the loading rate does not change the maximum stress value. Thus, for the fatigue tests, the S-N curves will be plotted with a maximal stress value normalized by the average stress at break of the quasi-static measured value.

The resulting fatigue plots as a function of load frequency were fitted with Whitney's Pooling Scheme as for the tensile fatigue curves. If one does not consider the 12 Hz fatigue curve, there seems to be a tendency of enhanced fatigue life by increasing the tests

Table 5.3 – Effect of loading rate on four point bending stress at break and modulus on unidirectional composite

Frequency(Hz)	equivalent displacement speed (mm.min^{-1})	Average stress at break (MPa)	Standard deviation (MPa)	Average calculated modulus (GPa)
2	384	1009	25	117
4	768	1062	24	123
8	1536	951	70	105
12	3072	947	91	104

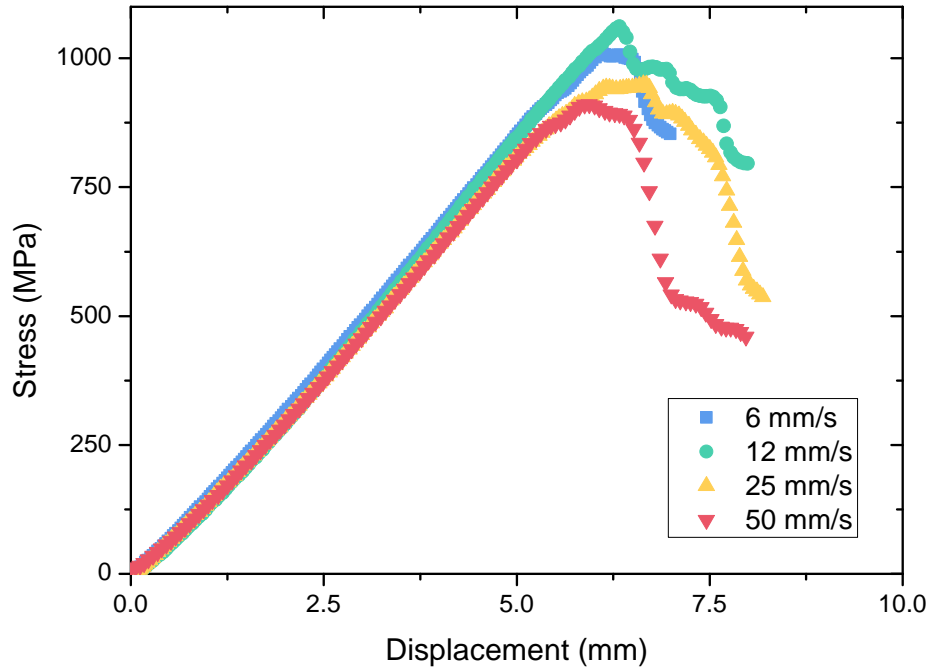


Figure 5.18 – Quasi-static four point bending for different displacement speeds on unidirectional composite

frequency (Figure 5.19). This tendency is more pronounced for the higher stress values. However, when considering the 12 Hz frequency, the fatigue curve seems to be close to the 2 Hz fatigue curve, but replication of the data seems poor. In fact, only a few specimens were available for this first study on unidirectional composite.

The same study was then applied to the cross-ply 0/90 composite. This time, data replication was guaranteed as 12 specimens per load frequency were tested with an average of 5 load levels. The resulting replication as calculated with Eq. (5.5) was at an average of 60 %. As with the unidirectional composite, the stress at break was equivalent at the four different load speeds. The fatigue curves were then normalized on the stress axis so that the fatigue curves are easier to compare.

Loading the 0/90 cross-ply composite at the four different load frequencies resulted in a different behaviour compared to that recorded on the 0° composite (Figure 5.20). Indeed, while the 0° fatigue curves shifted to longer lifetimes when increasing frequency from 2 to 4 and then to 8 Hz, this time increasing frequency did reduce lifetime, as fatigue curves tended to shift to fewer cycles to failure.

It is worth noticing that, as for the unidirectional composite, the 12 Hz and the 2 Hz fatigue curves seem to superpose. This similar fatigue life could be the result of a resonant frequency induced by the specimen's geometry. Indeed, tests at 12 Hz produced significant machine vibrations, which were not observed at lower frequencies so this may be

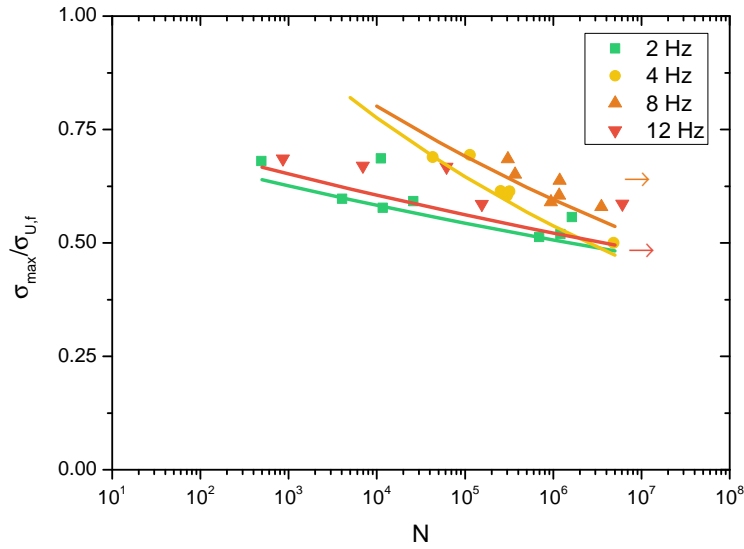


Figure 5.19 – Effect of load frequency on the fatigue of unidirectional composite

a machine-specific effect. A detailed model of the machine and fixture would be required to confirm this.

From this study, two observations are possible. The first one is that frequency has an

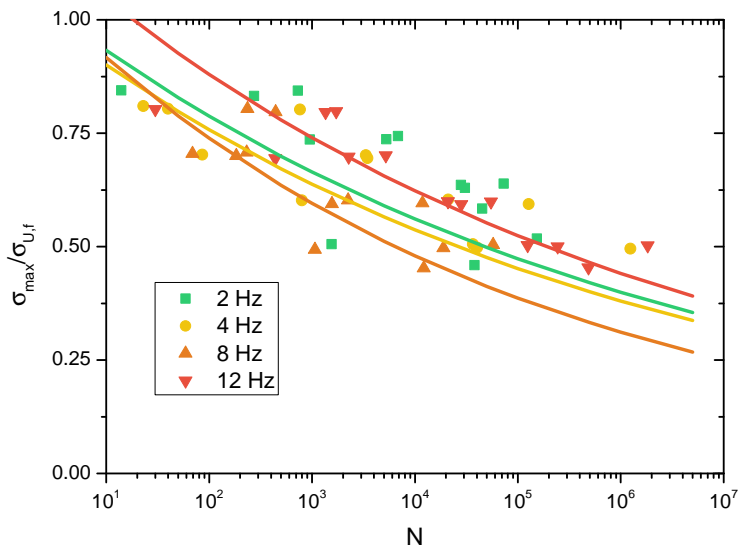


Figure 5.20 – Effect of load frequency on the fatigue of 0/90 cross-ply composite

impact on fatigue life of composites under flexure loading. Increasing frequency increased the fatigue life on unidirectional composite whereas it shortened this fatigue life for the 0/90 cross-ply composite. The latter could be induced by the presence of transverse plies, that are more sensitive to transverse micro-cracks which are affected by rate dependence of the resin. The second observation is that when considering only 12 and 2 Hz, fatigue life does not follow the tendency seen at the other studied frequencies, and there is no frequency sensitivity. It should also be noted that scatter is quite high, particularly for the cross-ply specimens.

As a result of this first study, the test method was adapted. Tests were started at 2 Hz and accelerated at 12 Hz when reaching 10^6 cycles. If specimens were still unbroken after 10^7 cycles, the test was stopped and counted as a runout.

5.3.2 Effect of long-term seawater ageing

As for tensile properties, before performing any cyclic tests, the ultimate quasi-static strength was evaluated. These tests were performed at 5 mm.min^{-1} as this results in a $1 \text{ \%}.\text{min}^{-1}$ surface strain rate with the selected geometry. In order to evaluate the possible effect of physical ageing on four point fatigue properties, the composite was aged at two different temperatures. The first temperature is $60 \text{ }^\circ\text{C}$ to be coherent with the seawater ageing performed for the tensile tests. As was shown in the previous chapter, as water absorption increases, the T_g decreases. Thus, performing seawater ageing at $60 \text{ }^\circ\text{C}$ would normally result in a rejuvenated composite with seawater. To evaluate if $60 \text{ }^\circ\text{C}$ is representative of the real ageing conditions, another batch of specimens was aged at $40 \text{ }^\circ\text{C}$ so that even with the decrease of T_g , physical ageing (PA) will not be rejuvenated. The samples aged at $60 \text{ }^\circ\text{C}$ took 3.5 months to saturate while those at $40 \text{ }^\circ\text{C}$ required over 400 days in seawater until reaching saturation. In terms of time, it took close to four times longer to age the samples at $40 \text{ }^\circ\text{C}$ compared to $60 \text{ }^\circ\text{C}$.

Figure 5.21 shows the displacement/stress curves for the three ageing conditions used for four point bending tests. The average flexural strength, $\sigma_{U,f}$ of the unaged composite is equal to $740 \pm 46 \text{ MPa}$. Ageing the composite at $40 \text{ }^\circ\text{C}$ shows a more pronounced decrease of the flexural strength compared to the composite aged at $60 \text{ }^\circ\text{C}$.

In fact, the average flexural strength measured for the composite aged at $60 \text{ }^\circ\text{C}$ was 680 MPa, whereas an average of 574 MPa was obtained after $40 \text{ }^\circ\text{C}$ aging, but with a higher standard deviation of 70 MPa. Specimens were not instrumented for strain measurements so no accurate measurement of the flexural modulus was obtained.

An explanation of the difference between 40 and $60 \text{ }^\circ\text{C}$ aged composite is that it took around 2 years to saturate specimens at $40 \text{ }^\circ\text{C}$ and only 4 months at $60 \text{ }^\circ\text{C}$. In addition to that, and as stated previously, at $60 \text{ }^\circ\text{C}$ there is a possible rejuvenation of the composite due to the decrease of T_g . This would mean that there is physical aging at $40 \text{ }^\circ\text{C}$ but not at $60 \text{ }^\circ\text{C}$.

However, when considering cyclic loadings, the same conclusions cannot be made, as shown in Figure 5.22. The fatigue curves show that when fully saturated, the composite loses some fatigue capacity after aging at both temperatures, characterized by a shift to lower numbers of cycles to failure. These shifts can be quantified in decades as the x-axis is expressed in a \log_{10} value. The shifts correspond to around 1.9 decades at a 500 MPa

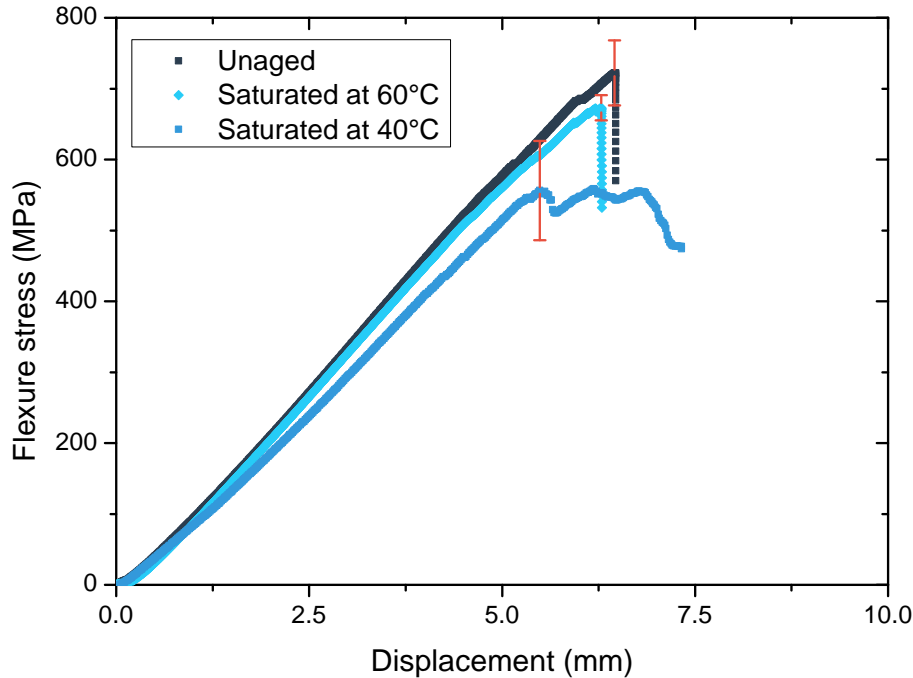


Figure 5.21 – Effect of seawater on ultimate four point bending strength of cross-ply specimens

maximal flexure stress. The difference between the composite aged at 40 °C and the one that was aged at 60 °C is here less obvious. Therefore, the effect of physical ageing on fatigue flexure properties is not confirmed and requires further investigation.

The main failure mode that occurred during these tests was delamination as shown in Figure 5.23. Delamination occurred for both unaged and saturated composites. One possible cause for delamination is the presence of transverse cracks, and the presence of micro-voids and defects can increase the probability for the formation of these transverse cracks.

The composite panels from which the four point flexure specimens were cut, have been inspected by ultrasonic C-scan. The result of these C-scans show that the quality of these composites, manufactured by RTM, was not optimal as shown in Figure 5.24. On this figure, the signal attenuation's scale goes from 0 to 8 dB. The red colour corresponds to low attenuation meaning that the presence of defects is low. On the other hand, blue to black colours signify that the ultrasound signal is attenuated to 8 dB and over. Where blue and black colours appear, there is a larger number/size of defects. This seems coherent with the void calculation presented in Chapter 2. It is worth noting the extraction point in the middle of the plate, characterized by the dark circle at the plate's central point. All the composites that were tested up to here were manufactured using the RTM process. RTM processing has the advantage of straightforward upscaling to larger component production,

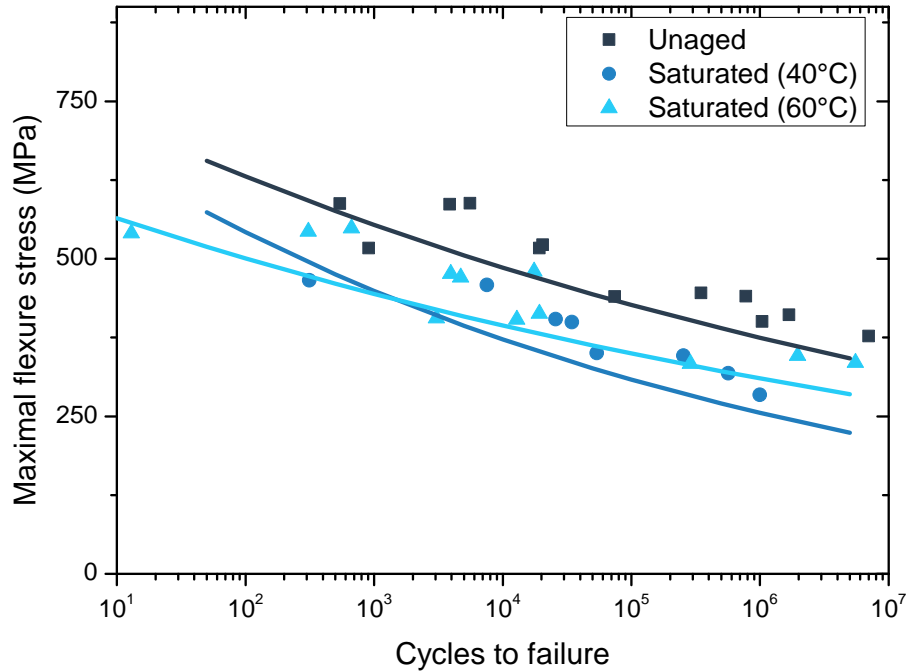


Figure 5.22 – Effect of seawater ageing on crossply composite in four point flexure

such as that planned for subsequent propeller blade manufacture. However, it is not the only possible manufacturing route and based on the previous results it was of interest to examine alternatives.

In order to compare the RTM process with a different process, composite plates were made from the same fibres and resin by infusion. The infusion process is more of a prototyping-oriented process as cheaper moulds can be used, even though mass production is possible. The advantage of RTM process over infusion would be a better repeatability of product design. However, in the present case the C-scan of the panel produced by the infusion process showed better quality. This is shown in Figure 5.25 with the same attenuation scale as for Figure 5.24. On this figure, one can clearly appreciate the very low occurrence of defects. This is accompanied by a calculated void fraction of 1 %, which confirms that the infused composite considered here has better manufacturing quality. In addition to the different process used, the fibres areal weight went from 300 to 600 $g.m^2$ for the infused composite. The cross-ply stacking sequence was adapted to obtain comparable thickness using the sequence: $[0/90/0]_s$, so the 90° proportion is reduced from 40 to 33 % compared to the RTM plates.

Four point flexure coupons were cut with the same dimensions as for the RTM composite. Seawater ageing was performed at 60 °C, as it was shown previously that fatigue behaviour after ageing at 60 and 40 °C did not seem to be strongly affected by physical ageing. The quasi-static four-point flexure results for the aged infused composites showed

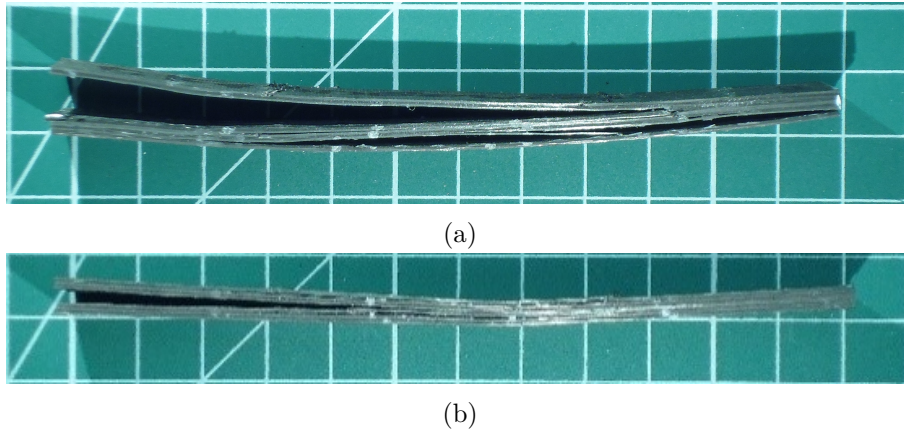


Figure 5.23 – Example of failure mode occurring during four point flexure unaged (a) and saturated (b)

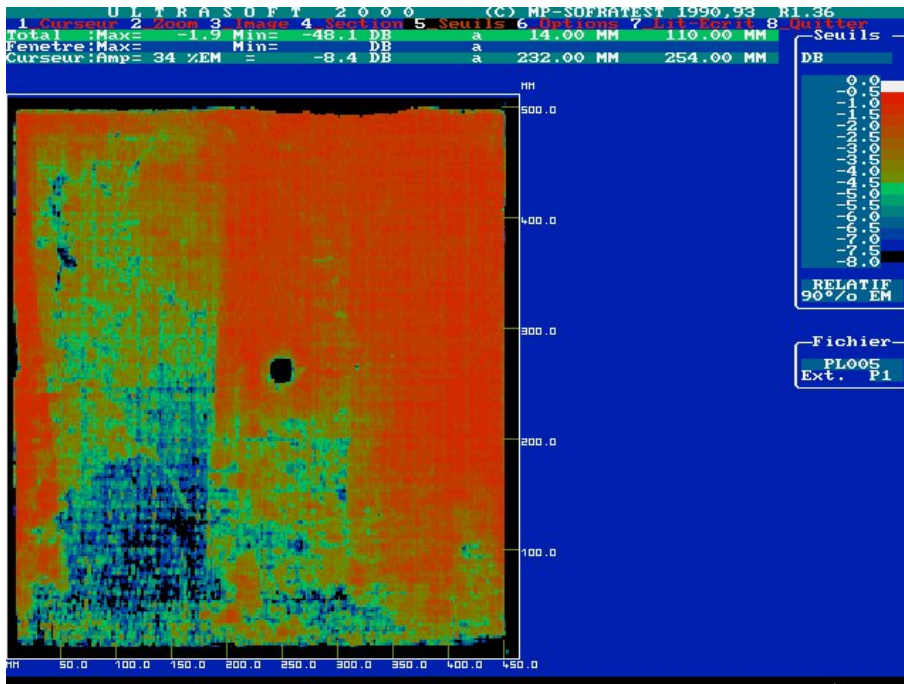


Figure 5.24 – C-Scan of RTM 0/90 cross ply composite

only a small decrease of 60 MPa going from an average flexure strength of 780 ± 50 MPa to an average of 715 ± 9 MPa (Figure 5.26). An additional ageing condition was then tested. This additional condition consisted of drying the composite once it was fully saturated. This, as for the pure resin previously, was intended to evaluate the reversibility of the aging process. The resulting saturated then dried flexural strength showed recovery of at least part of the initial flexure strength with an average 750 ± 45 MPa. This is within one standard deviation of the initial value.

The infused composite showed slightly higher flexure strength than the RTM. This can

Chapter 5. Seawater ageing of composite materials

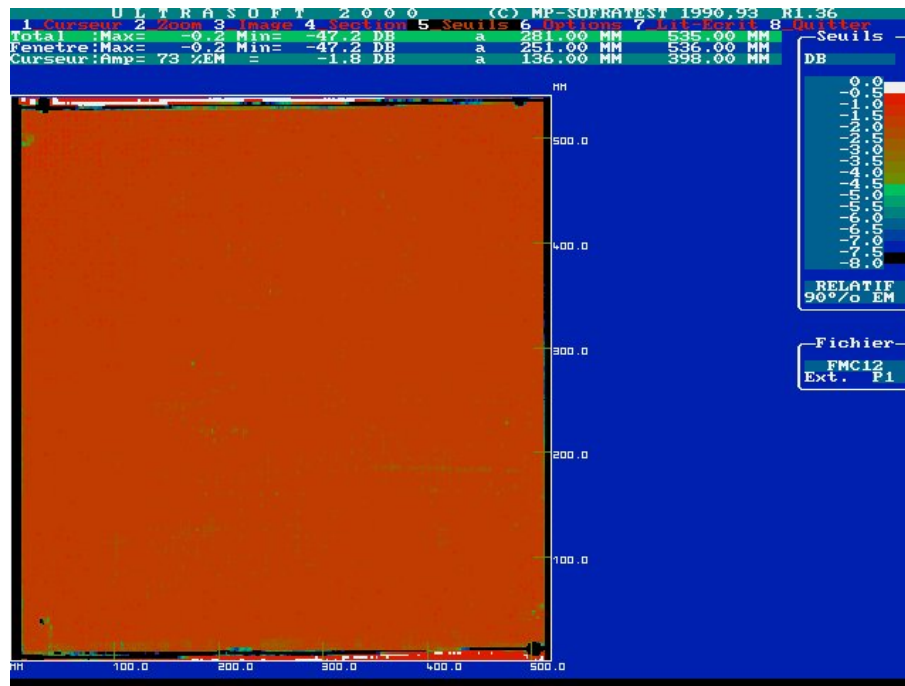


Figure 5.25 – C-Scan of infused 0/90 cross ply composite

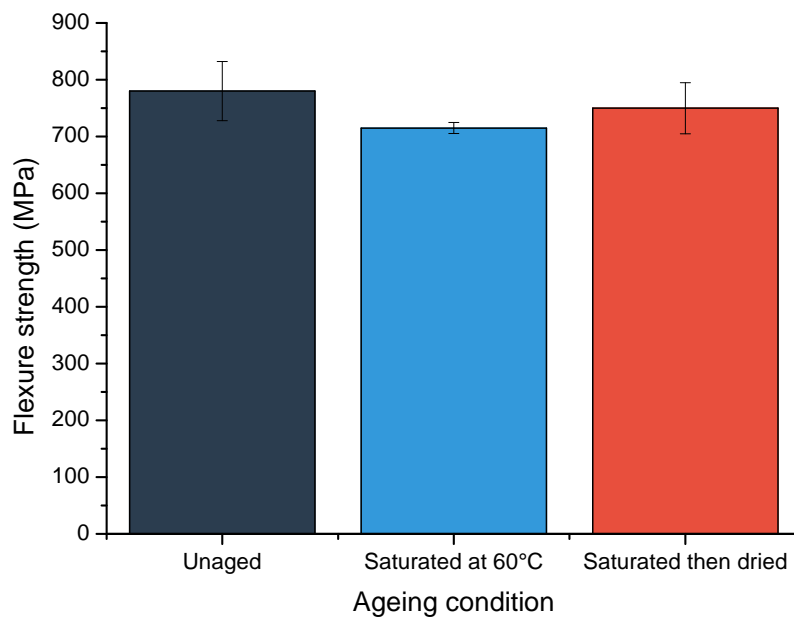


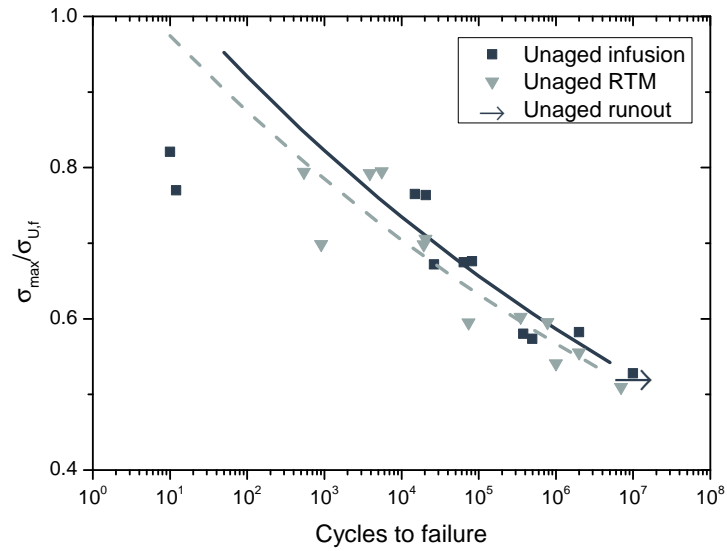
Figure 5.26 – Seawater ageing effect on infused cross-ply composite flexure strength

be explained by the fact that the fibre volume ratio of the infused composite was measured at close to 60 % whereas it was measured at 51 % for the RTM composite, together with the higher 0° fibre content.

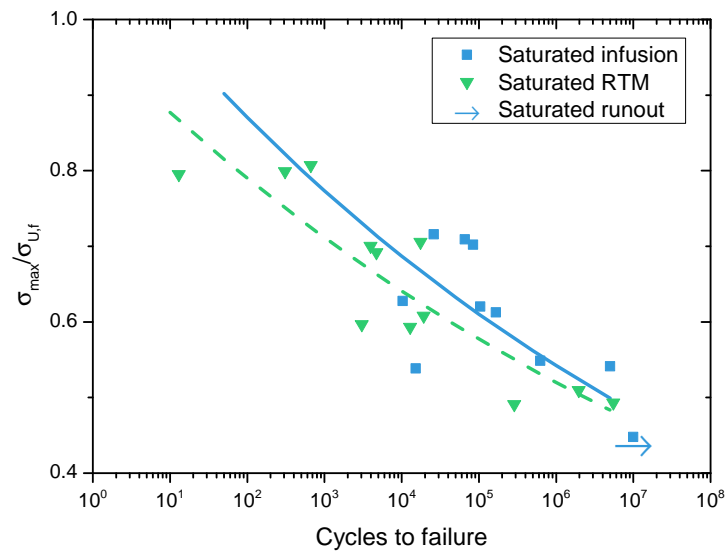
The difference in fatigue behaviour between the two composite is coherent with the measured quality. In fact, comparing the two unaged composites shows that the infused composite has longer lifetimes, by close to 0.2 decade at a stress level of $\frac{\sigma_{max}}{\sigma_{U,f}} = 0.7$. Comparing the saturated composites at the same stress level (both aged at 60 °C) shows an even higher shift of the fatigue curve by around 0.8 decade. The difference at high numbers of cycles seems less important however for the saturated condition. This is shown in Figure 5.27. Fatigue curves shown here are obtained from classical power laws.

Even though the infused composite shows better fatigue behaviour, it is not immune to seawater ageing. As shown in Figure 5.28, the fatigue curves of the infused composite shift to lower lifetimes in a similar way to the RTM composite. However, for the infused composite, this shift represents now 1.5 decades which is less than that observed for the RTM composite. Therefore, it could be concluded that this infused composite is less sensitive to seawater ageing when considering flexural stresses. This is coherent with the fact that fibre volume ratio is higher for the infused composite. As we saw before, seawater ageing tends to induce more damage for the properties where resin properties are important. The fact that the RTM composite has a higher resin ratio than the infused composite will increase its sensitivity to seawater.

The specimens cut from the infused composite were dried in order to evaluate reversibility of seawater ageing. This was done by placing previously saturated specimens in ovens with 0 % RH. The desorption curve of these specimens is shown in Figure 5.30, and the specimens return to their initial weight.



(a)



(b)

Figure 5.27 – Comparison between RTM and Infused 0/90° composite unaged (a) and saturated (b)

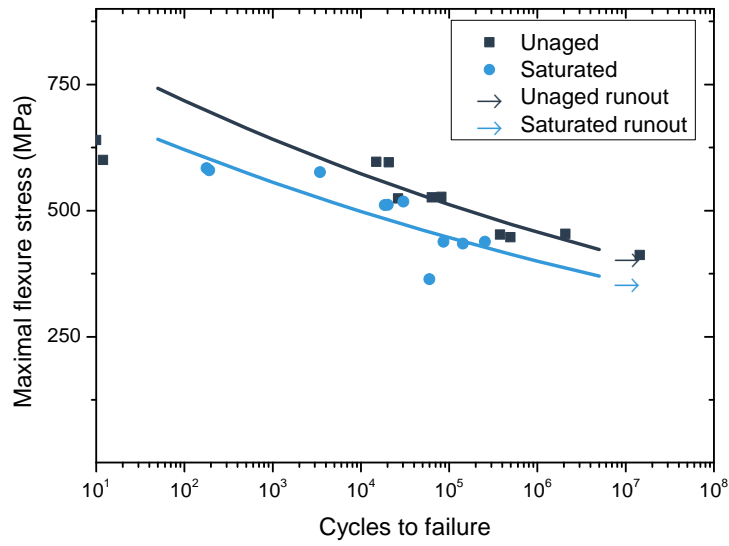


Figure 5.28 – S-N curves of unaged and saturated infused composite

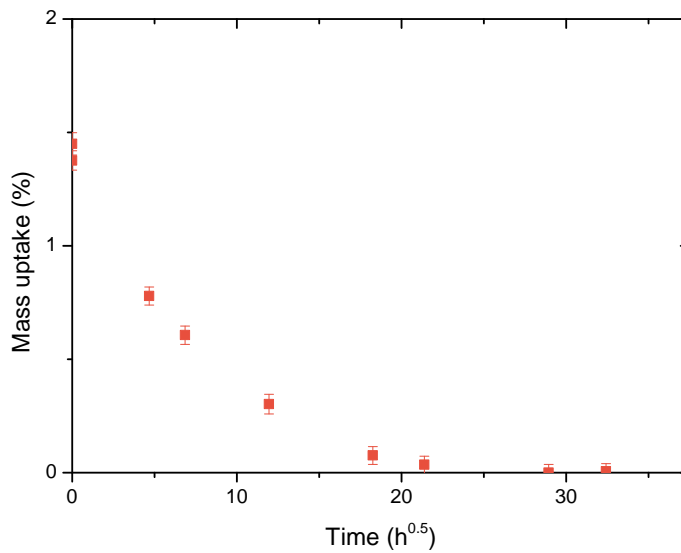


Figure 5.29 – Desorption curve of infused four point flexure cross-ply specimens

Figure 5.30 presents the fatigue curves of the unaged composite compared to the saturated then dried composite. One can see that initial properties seem to be recovered, as was the case for the pure resin when considering only plasticization. This would suggest that if the only two ageing phenomena occurring on the composite are physical ageing and plasticization, then PA does not have a major influence on the cyclic flexure properties. In fact, here the only de-ageing method was drying. No over-T_g exposure was applied. Thus, as initial properties are almost completely recovered, the effect of long-term seawater ageing is almost reversible. This is an important conclusion as it suggests that even under cyclic loading the main effect of water is as a plasticizer.

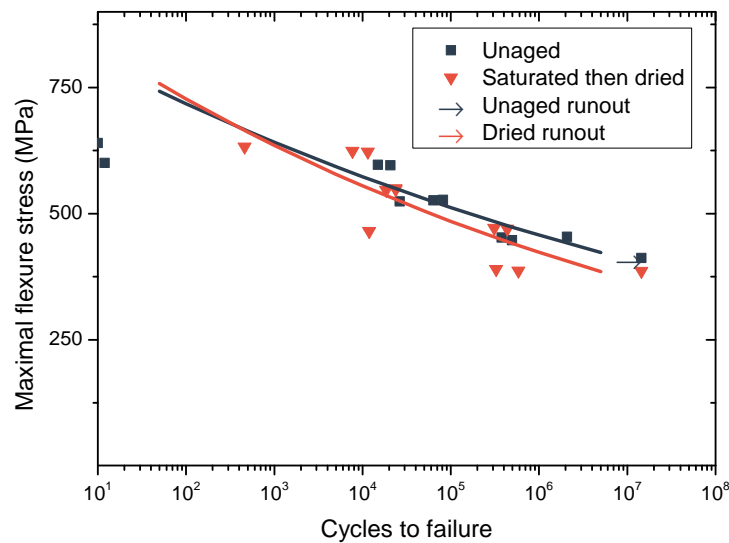


Figure 5.30 – Reversibility of ageing after drying, infused composite

For the infused composite, which had significantly less defects as shown by the C-scan maps, the main failure mode was also delamination. As shown in Figure 5.31, delamination occurred for all three ageing conditions. This would mean that either the composite has low crack resistance properties, or that the flexural test method encourages this failure mode. The aim of the next section is to analyse the damage sequence in the four point flexure tests in more detail.

As a conclusion to this section, cyclic flexure was found to be sensitive to load frequency for both unidirectional and cross-ply stacking sequences under certain conditions (2 to 8 Hz). At 12 Hz results were very close to those at 2 Hz, possibly due to a resonant frequency of the specimen/fixture/test machine combination.

The cross-ply composite was found to be sensitive to seawater ageing when loaded in flexure. This is important to note, as if only tensile-tensile testing had been performed, one could have concluded that the cross-ply sequence was hardly affected by seawater. This is even more important as propeller blades are expected to be loaded in flexure.

It was found that the infused composite has better flexure properties than RTM com-



Figure 5.31 – Delamination recorded during fatigue tests for unaged (a), saturated (b) and saturated then dried (c) of infused specimens

posite. The difference in flexure strength was attributed to the higher fibre volume ratio of the infused composite. The better fatigue properties may be attributed to the lower void volume ratio in concordance with lower defect levels seen by the C-scan method.

However, the cyclic failure mode was found to be delamination whether infused or RTM composite were tested. This means that the level of defects does not change the failure mode resulting from cyclic loading.

Damage sequence

In order to try to establish the sequence in which damage appeared during these flexure tests, a series of 16 infused specimens was loaded under different conditions and tests were stopped prior to failure. The number of cycles at which tests were interrupted was defined according to two strategies. The first is a “half-life” approach. This involved taking the fatigue curve of the unaged composite and stopping tests at the number of cycles corresponding to half of the mean lifetime at different load levels. Figure 5.32 illustrates the half-life curve as a red dashed curve. The half-life tests were performed at 80, 70, 60, 55 and 50 % of $\frac{\sigma_{max}}{\sigma_{U,f}}$. The second strategy was to load a series of samples at one stress level and to stop the tests after different proportions of the lifetime at that stress. This is illustrated on Figure 5.32 by the green dashed curve. The selected maximal stress was chosen to be 60 % and lifetimes were chosen at 10, 30, 50, 70 and 90 % of the predicted ultimate lifetime.

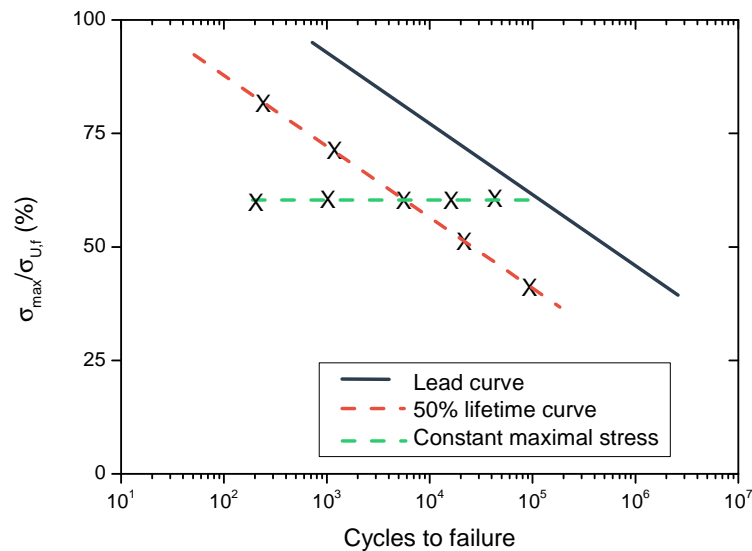


Figure 5.32 – Illustration of the interrupted tests

The stiffness curves obtained from the 60 % maximal stress specimen show a two-step damage trend (Figure 5.33). The first step shows no stiffness degradation. The second step was recorded to start at 70 % of total lifetime with a gentle decrease ending at 85 % of initial stiffness resulting to final specimen failure. Another two steps was recorded with

a different second step happening at around 90 % of total lifetime and this time a more sudden decrease of stiffness also decreasing to around 85 % of initial stiffness prior to final failure.

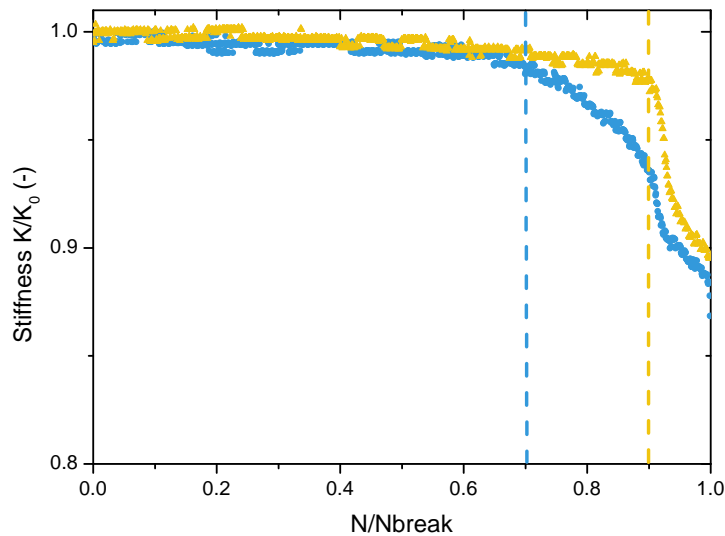


Figure 5.33 – Stiffness curves of two sample at 65 % of maximal stress

A parallel can be made between these stiffness curves and those of the tensile tests where there were stable stiffness steps for the different composite orientations. However, acoustic emission showed that even though there was no stiffness decrease, there was damage occurring during those phases. This time, acoustic instrumentation was not possible due to the test fixture used. So, in order to evaluate how damage developed during the interrupted tests, ultrasonic C-scan and X-ray micro-tomography were used on each specimen.

For the specimens loaded at 60 % of maximum stress, two specimens were tested per lifetime. One of the two specimens was scanned at every 10k cycles up to the corresponding number of cycles. The other specimen was loaded directly to the final desired lifetime and then scanned.

It appears that there is damage occurring under the load point very early, as shown in Figure 5.34. In fact, for the three specimens shown here, the upper load point appears on the C-scan as early as 10k cycles. For the first specimen (70 % of lifetime), there seems to be a delamination gradually appearing as shown by the round dark circle at the mid-width right at the load point. On the second specimen (50 % of lifetime) there is also damage occurring and spreading around the load point. One can see that there appears to be additional damage appearing on the second upper load point with one small dark circle appearing at 40k cycles. On the third specimen, there is clearly delamination occurring. This time again it starts from the first upper load point clearly appearing on the 20k cycles scan. Unfortunately, this specimen is biased as it has reached a damage

Chapter 5. Seawater ageing of composite materials

state corresponding to final failure. This is a difficulty with such analysis, as there is considerable variability in the lifetimes at a given stress level. Then, looking at the last sample, corresponding to a 30 % lifetime, we can clearly see the damage under the load point at 30k cycles but we can imagine this damage during the previous cycles based on the place where it finally happened.

From these observations, it appears that the load points induce damage on the samples.

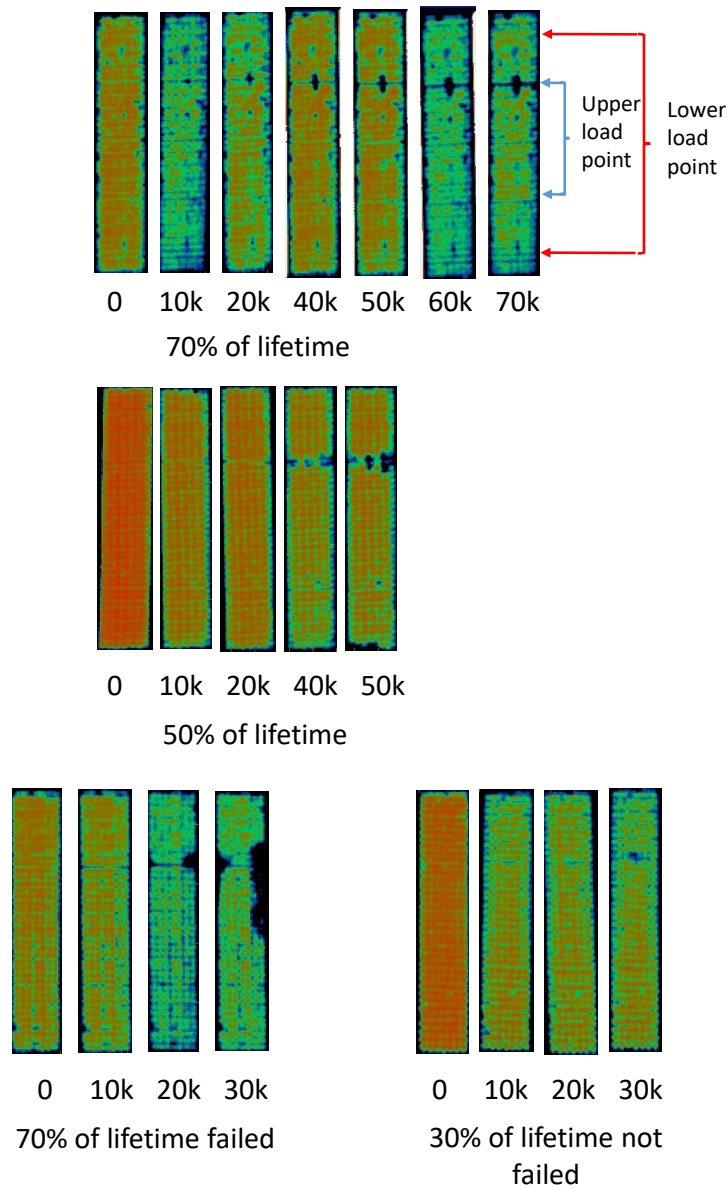


Figure 5.34 – Damage evolution in four point bending test on cross-ply composite

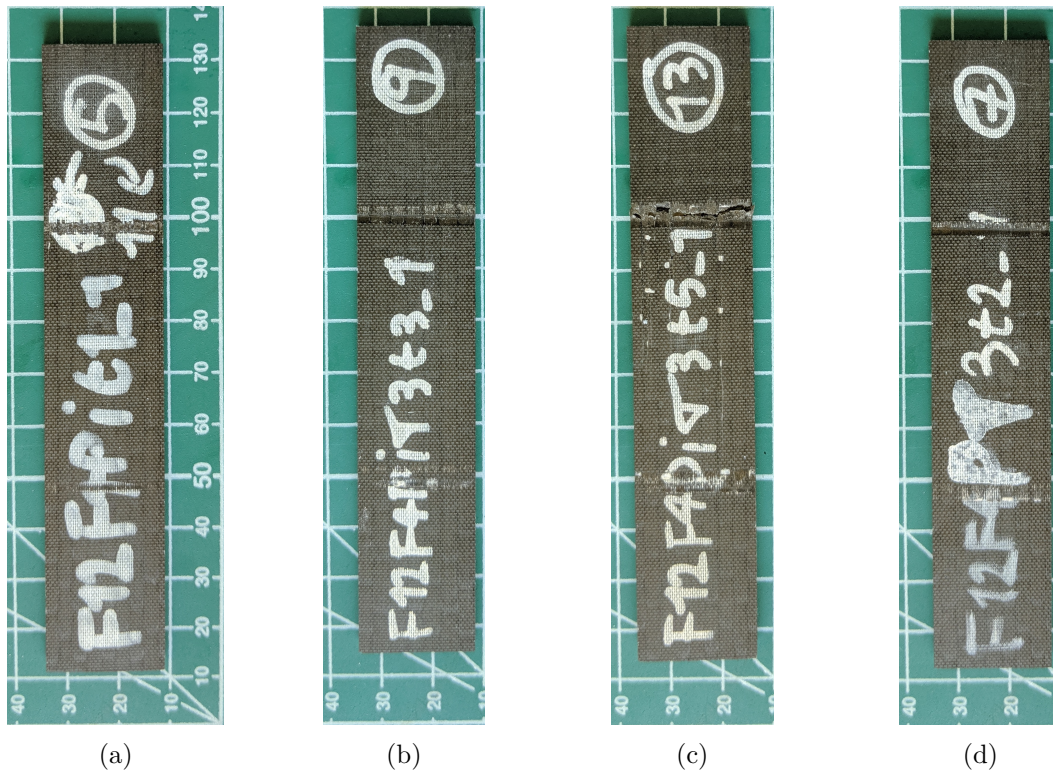
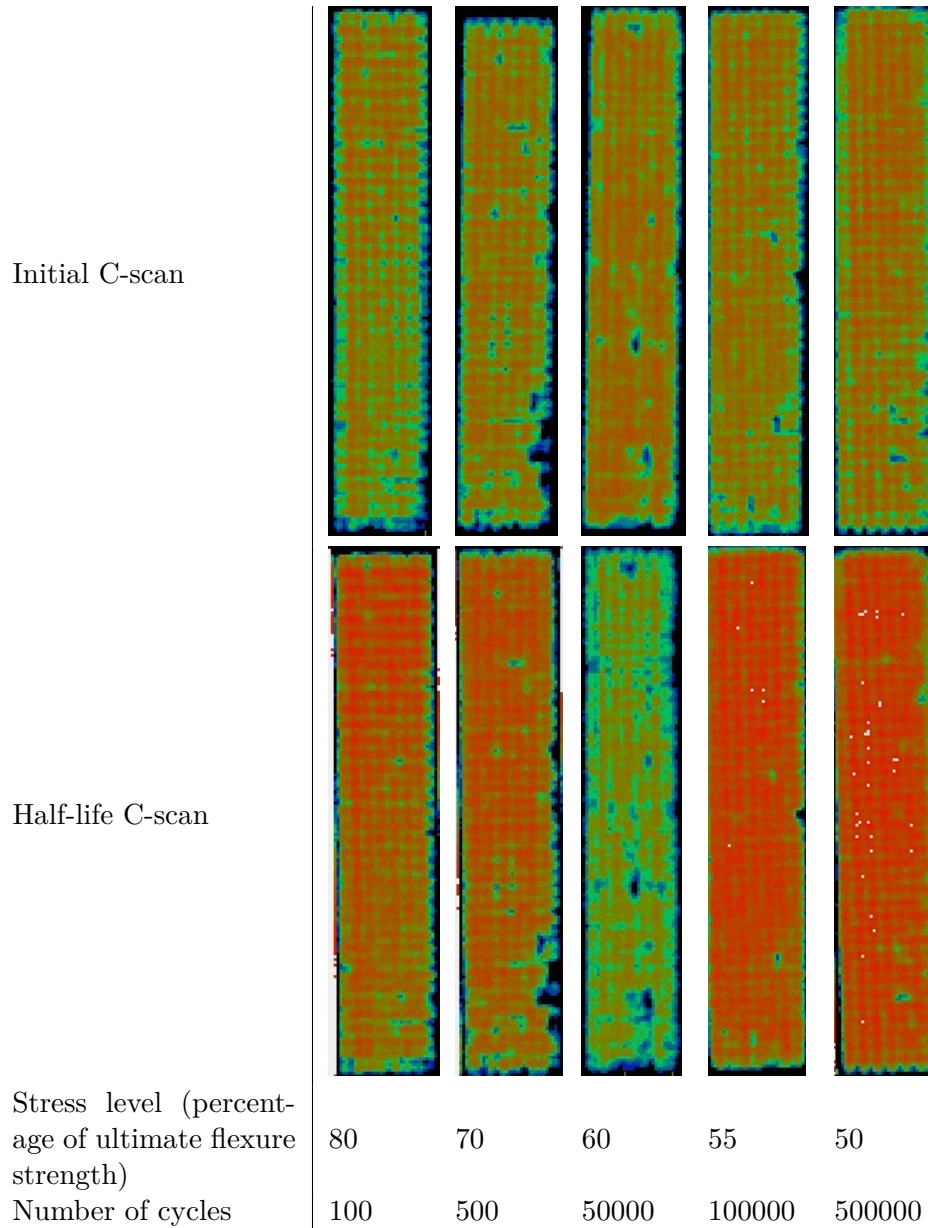


Figure 5.35 – Photographs of the final state of sample from Figure 5.34 (70 % of lifetime (a), 50 % of lifetime (b), 30 % of lifetime failed (c) and 30 % of lifetime non failed (d))

This is confirmed by the fact that the surface is marked by these load points as shown in Figure 5.35. The four pictures show the final state of the specimens that were scanned and presented in the Figure 5.34.

The damage induced by load points did not show up on the scans of the half-life samples. In fact, as shown by Table 5.4, there seems to be no damage below the load points. However, the samples show closer-to-red colour, which would signify a smaller signal attenuation. The reason may possibly come from the fact that as these tests were done immersed in seawater, there could be water absorbed by the sample during the tests. This was confirmed by weighing the samples prior to C-scans and resulted in water uptakes between 0.05 and 0.2 %. This might decrease the signal attenuation even more as water could penetrate defects and reduce contrast. This is the case for the sample at the 55 % stress level in Table 5.4 where the small defects that appeared in the initial state were attenuated during the final state scan. The samples were not dried prior to performing C-scans because water ingress coupled with flexural loading was investigated during this set of tests. However, the results from water uptake were not very conclusive, showing only little water absorption as referred previously. This may probably be due to the small amount of ageing time compared to the ageing times necessary to saturate the composite. In addition to that, there was partitioning of immersion due to loading, c-scan, re-loading; in particular, the samples were not loaded directly after the C-scans as some specimens were loaded while others were c-scanned. Therefore, no results from this investigation are

Table 5.4 – Half-life C-scans for different stress levels



presented here.

The way in which the loading points could induce damage in the samples can also be shown by examining the failure images of the specimens from Table 5.4. There are clear indentation marks at the load point as shown in Figure 5.36 especially for the highly cycled specimens (c, d and e).

The role of the load point in final failure must be questioned when examining these results. To examine this in more detail, the same samples were analysed by X-ray microtomography, before and after testing. Only the final state of the samples was analysed by

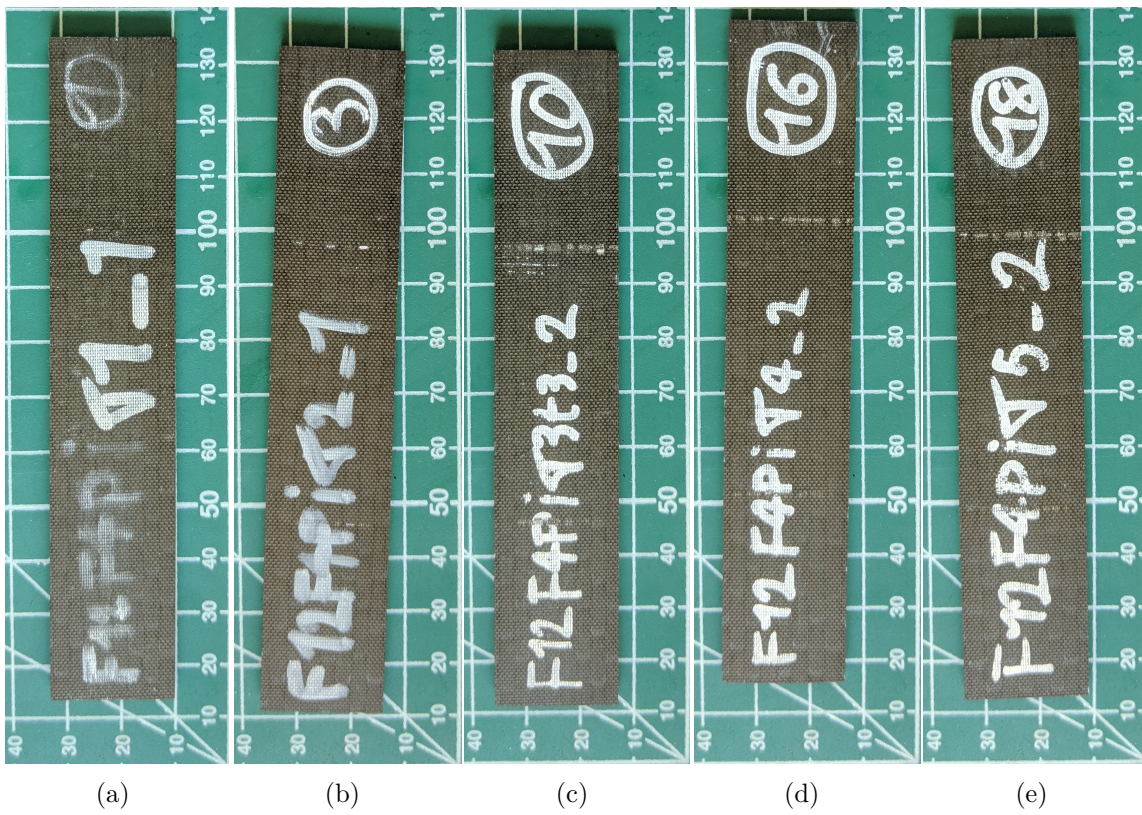


Figure 5.36 – Photographs of specimens presented in Table 5.4 in the same order

tomography. Qualitative analysis of the sample after 30 % of lifetime at 60 % maximum stress shows that delamination is not limited to one ply. Figure 5.37 shows the upper half part of this specimen. One delamination seems to have started from the load point (upper one) but the second one is on the second ply going from ply1/ply2 to ply2/ply3, across the transverse ply (Figure 5.38).

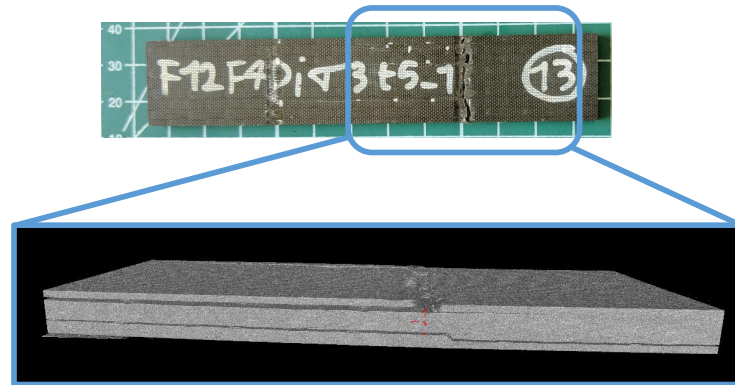


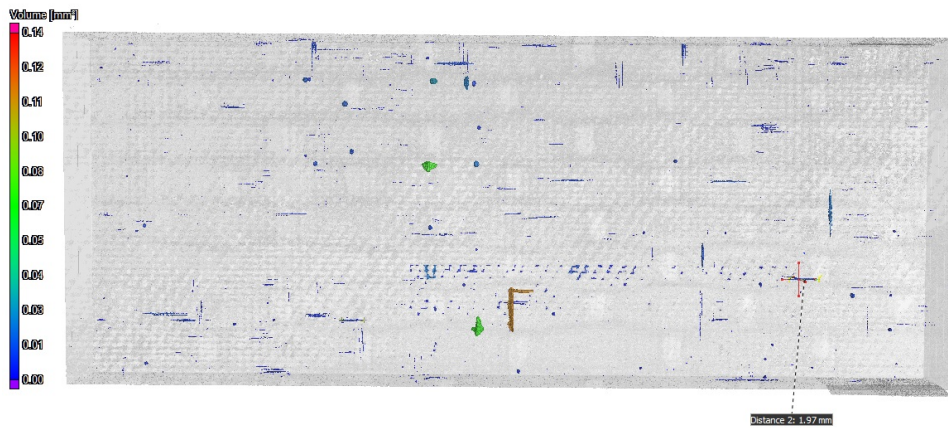
Figure 5.37 – 30 % of lifetime sample tomography showing two interlaminar delaminations



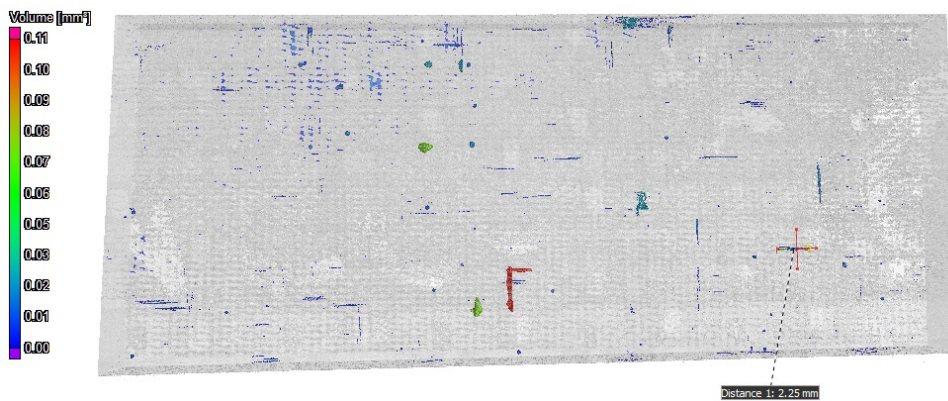
Figure 5.38 – Edge of specimen 13 showing delamination as seen in Figure 5.37

On the other samples, a threshold analysis was performed in order to identify the defects, cracks or delamination inside the material. Qualitative analysis of the identified volumes, can orientate the analysis on the presence of transverse cracks or interlaminar delamination. However, as shown by Figure 5.39, there can be no clear conclusions on the nature of the defect. The other option is to study the defects that were found by the tomography analysis. In fact, a threshold study of the imaging data can separate voids/defects from the actual material itself. Data acquired from this are defect properties such as the orientation, aspect ratio length according to a specific axis and so on.

Another approach consists of identifying the different types of defects based on the values extracted from tomography analysis. To do so, an unsupervised clustering method was applied to the sample (a) of Figure 5.35. The K means method was used to identify four different clusters as explained in Chapter 2. Figure 5.40 shows the distribution of longitudinal length of the defects as a function of their sphericity with respect to clusters differentiated by colours. Based on these results, the blue cluster shows the least spherical, most fibre-oriented defects. This cluster is representative of longitudinal defects that may lead to interlaminar delamination. One of these defects is shown in Figure 5.39, its position is marked by a cross on the two figures. This defect was also identified to belong to the blue cluster.



(a)



(b)

Figure 5.39 – Tomography picture of half of the specimen from figure 34 (a) as seen from above before (a) and after 70k cycles (b)

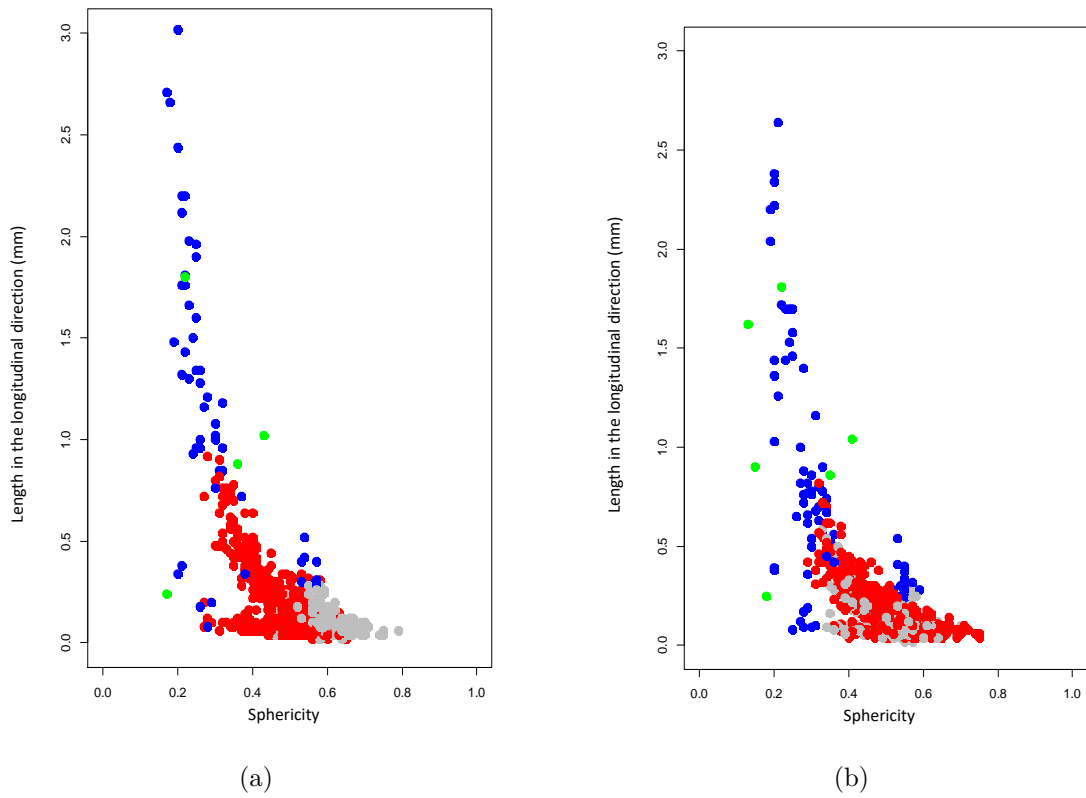


Figure 5.40 – Longitudinal length of defects as a function of sphericity, before (a) and after (b) fatigue tests

It is possible to follow the defects' positions on the thickness vs length plan. The tomography scan was performed only on one-half of the specimen. Then the planar distribution that will be discussed later is to be taken as illustrated on Figure 5.41. It is also important to notice that the length and thickness directions do not have the same scales.

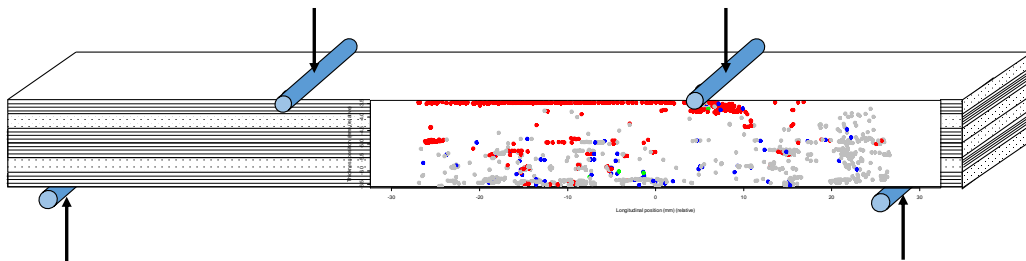


Figure 5.41 – Illustration of the position of planar distribution of the defects presented (scales are not respected)

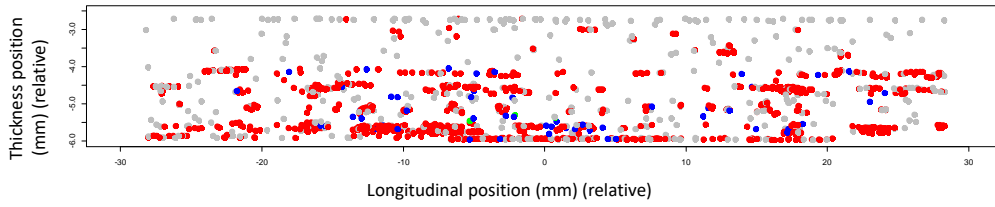
Figure 5.42 shows the spatial distribution of defects with respect to the cluster colours of Figure 5.40 in the same plane as in Figure 5.41. One can clearly identify the place where the test fixture loads the sample with the roller on the upper, yellow-rich zone. However, the most important observation is that there are defects distributed throughout the entire thickness of the specimen.

It is possible to isolate, on the same graphs, the longitudinal defects (blue cluster). In this case, we see that these defects are already present in the material prior to the fatigue tests, see Figure 5.43. However, by counting these defects, it appears that there are 76 defects of this kind after fatigue versus 54 before. This signifies that either these defects were too small for detection and that they extended during the fatigue tests, or that they extend from previous defects, which were not of this type, and fatigue loading enlarged them into longitudinal defects. This can be confirmed when comparing graphs on the Figure 5.40 where there are more longitudinal defects in the zone corresponding to below 1 mm in length. Another possibility is that they appear during fatigue loading. In this case, they are representative of damage appearing as it was measured by C-scans.

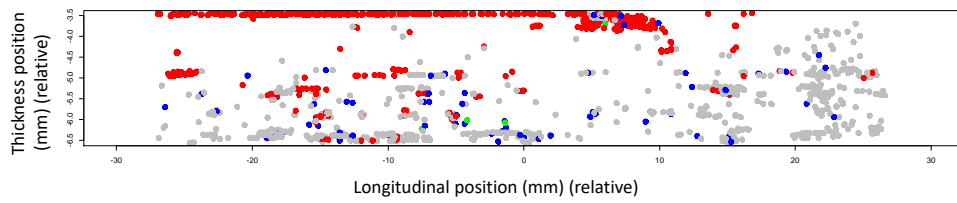
The main additional defects are found on the upper surface of the sample near the loading point. However, certain “new” defects were found throughout the sample’s thickness. This indicates that, even though the damage induced by the loading point is of great importance, the samples do also damage internally due to flexural loading.

As a conclusion on the four point flexure tests, different methods have been used to

Chapter 5. Seawater ageing of composite materials

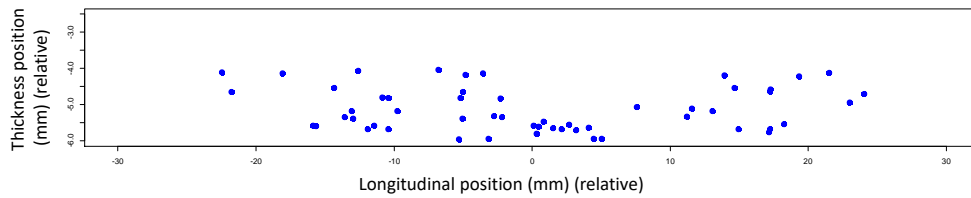


(a)

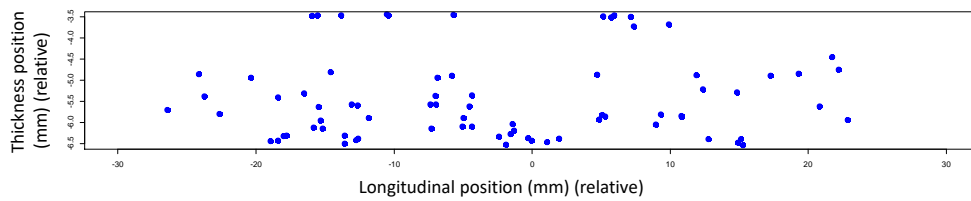


(b)

Figure 5.42 – Planar distribution of defects, all clusters before fatigue tests (a), after fatigue tests (b)



(a)



(b)

Figure 5.43 – Planar distribution of longitudinal defects before fatigue tests (a), after fatigue tests (b)

investigate the damage sequence occurring during these fatigue tests. It appears that the damage induced by the loading points plays a major role in the final failure of the specimens. Post-mortem analysis of the samples, tomography, and C-scans indicated that there was damage under the loading points. However, thanks to the tomography analysis, it was shown that damage also occurs both at the heart of the specimen and through the thickness.

The main final failure during those fatigue tests was delamination. The failure caused by the loading points did not always correspond to the location of the delaminated ply. Sometimes, there were delaminations in lower plies along with punching failure at the loading point with no connection between these two failures.

Therefore, during four point bending tests, there can be multiple failures induced by the fixture but also due to the loading mode (flexure and shear). In order to understand the long term behaviour it therefore appears important to be able to isolate the delamination mechanism and examine whether it is sensitive to wet ageing.

5.4 Conclusion

In this chapter, the effect of long-term exposure of the composite material to seawater was presented. It was shown that the effect of ageing on the composite could be considered as minor when fibre-dominated properties are considered. These include tensile properties of unidirectional and cross-ply 0/90 composites loaded in the fibre direction, for both quasi-static and cyclic loading in the saturated state. The flexural strength of the cross-ply 0/90° composite also shows little decrease in properties in the fully saturated state.

However, when looking at more resin-sensitive properties such as transverse tensile strength, exposure to seawater drastically changes the mechanical properties. A decrease of around 50 % of the ultimate transverse tensile strength was measured under quasi-static loading. In the meantime, a significant degradation of the fatigue properties of this material occurred, characterized by a reduction of the stress needed for a given lifetime by around 30 %.

It was also shown on the cross-ply composite that, even though seawater had a limited effect on the quasi-static flexure strength, it does affect the cyclic loading properties. This was quantified as a 1.8 decade shift for a composite produced by RTM, and a 0.9 decade shift for an infused composite. RTM composites were compared to infused composites because the main failure mode of the RTM composite was delamination. As cracks grow easily from defects, and the RTM panels showed quite high defect levels, the infused composite was expected to fail differently as it showed very few defects by C-scan. This quality difference, together with a higher fibre volume ratio and higher 0° content, had a positive effect on the fatigue properties but did not change the failure mode that was still delamination.

The effect of the test method was then evaluated by performing interrupted four point flexure tests on the infused composite. C-scans showed damage increasingly appearing beneath one of the upper load points then spreading across the specimen. Analysis of the outer surface of cycled specimens showed wear of the surface where it was loaded by the rollers. Thanks to X-ray tomography analysis, it was shown that damage induced by flexure tests is not restricted to below the load roller. Indeed, less spherical defects, that

are not thought to be voids resulting from manufacturing, were found to be distributed within the lower half thickness of the samples.

The effect of frequency on fatigue life was also evaluated on the UD and 0/90 cross-ply RTM composite. It was shown that there is a positive effect of raising frequency from 2 to 4 and 8 Hz mainly for the high stresses for the UD composite. On the cross-ply composite, the opposite behaviour was recorded. However, for both composites, 2 and 12 Hz showed similar fatigue life. This was used to pursue tests over 10^6 cycles by changing test frequency from 2 to 12 Hz at 10^6 cycles.

Independent of manufacturing, the majority of four point flexure specimens failed in delamination. Tomography confirmed that delamination-like defects form within the lower plies of the specimens and that they could result from new defects or previous non-longitudinal defects. Delamination is known to be a weakness of laminated composite materials, and so the key to improving the lifetime of composites for marine propellers is to be able to understand and quantify the delamination resistance of these materials. This is the aim of the following chapter.

Composite under delamination loading

One of the main weaknesses of laminated composites is their out-of-plane properties. In particular, delamination, or interlaminar crack development, is a frequent failure mode in highly loaded composite structures. We have seen in the previous chapter that final failure of four point flexure beams was dominated by delamination. This indicates that in order to guarantee the lifetime of the particular composite studied here for blade applications it is essential to understand this failure mechanism.

As shown in the previous chapter, bending of a blade structure may result in complex loadings ranging from in-plane shear to out-of-plane tensile. In addition, the water pressure seen by a propeller can add other particular loadings on the composite structure.

Testing real propeller parts will be necessary in the future but the results will be hard to analyse without detailed modelling due to this wide variety of loadings. For this reason in the present study, the delamination modes have been studied separately.

Note that, in this chapter, only the infused composite has been studied. This choice was made due to the better material quality obtained with this manufacturing route, as shown previously.

6.1 Seawater ageing under mode I

The effect of long-term seawater ageing was studied in the same way as it was evaluated during the four point bending tests. The composite was tested under three different ageing conditions; unaged, saturated in seawater, and fully dried after being saturated in seawater. In order to evaluate the mode I energy release rate, G_{Ic} , the Double Cantilever Beam (DCB) standard test was chosen. This corresponds to the test procedure and data reduction discussed in Chapter 2.

6.1.1 Quasistatic loading

A quasi-static value of strain energy release rate needs to be measured prior to cyclic loading. Figure 6.1 shows this energy release rate as a function of crack length, also known as the R-curve, for the composite in the unaged condition. There is significant scatter in the data, especially for the fourth specimen shown in yellow. The trend of the energy

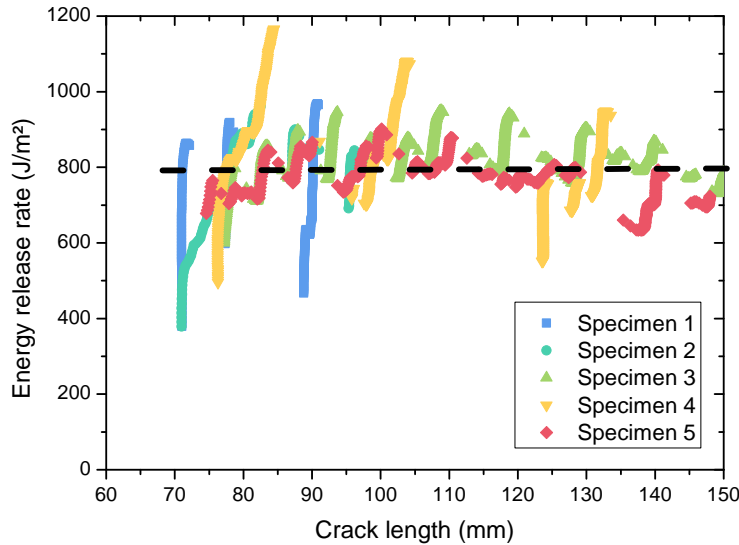


Figure 6.1 – R-curves of unaged composite in mode I

release rate indicates peaks and troughs, corresponding to a stick slip behaviour. This phenomenon was noted in early work on fracture mechanics testing [181] and attributed to a crack tip blunting mechanism. One way suggested to evaluate the energy release rate when the crack jumps are very large is to isolate peaks and valleys and present two values, one at the onset of propagation and one at arrest [182]. Here a global average was determined on the entire batch of specimens. The value found was determined to be around 800 J/m^2 with values reaching over 1000 J/m^2 and dropping below 600 J/m^2 . These values are slightly higher than those commonly reported in the literature for mode I energy release rates of CFRP composites [183,184]. Different factors could influence the value of the energy release rate such as the resin's fracture toughness but also interface parameters such as the type of carbon fibres, its areal weight and so on.

After 3 months of immersion in seawater at $60 \text{ }^\circ\text{C}$, and thus once the material had been fully saturated (i.e. 1.4 % weight gain in the case of the infused composite), the same tests were performed. Results, then, showed a decrease of the energy release rate, see Figure 6.2. As for the unaged composite, there is scatter in the results. The mean value of the propagation energy release rate was determined to be around 620 J/m^2 , which represents a decrease of 180 J/m^2 . This can be seen as contradictory to the idea of the resin being plasticized by seawater. Several studies have shown an increase in energy release rate due to plasticization of the resin induced by water immersion [28,65,67,71]. Thus, in this case, another behaviour is observed and has to be understood.

The reversibility was evaluated by finally drying a third set of specimens, which had been saturated. To do so, the specimens were placed in dry ovens at $60 \text{ }^\circ\text{C}$ for three month until being fully dried. In this case a further small decrease in the energy release rate of the dried specimens was measured. This decrease is less important than the decrease

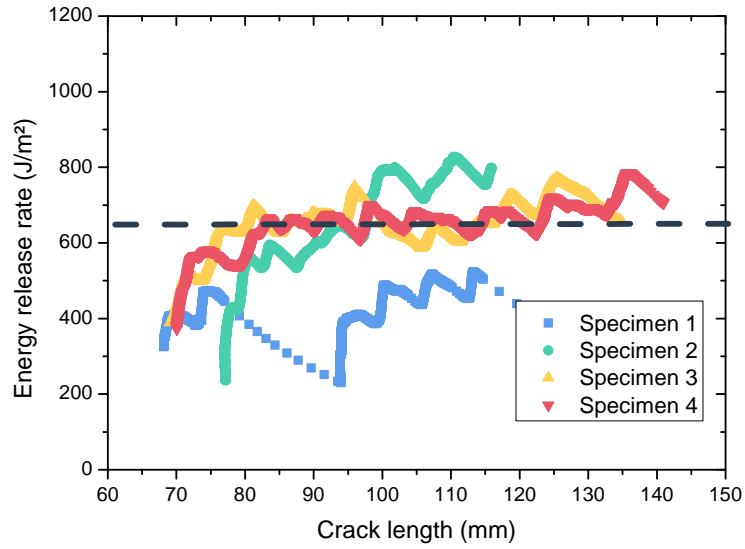


Figure 6.2 – R-curves of the saturated composite in mode I

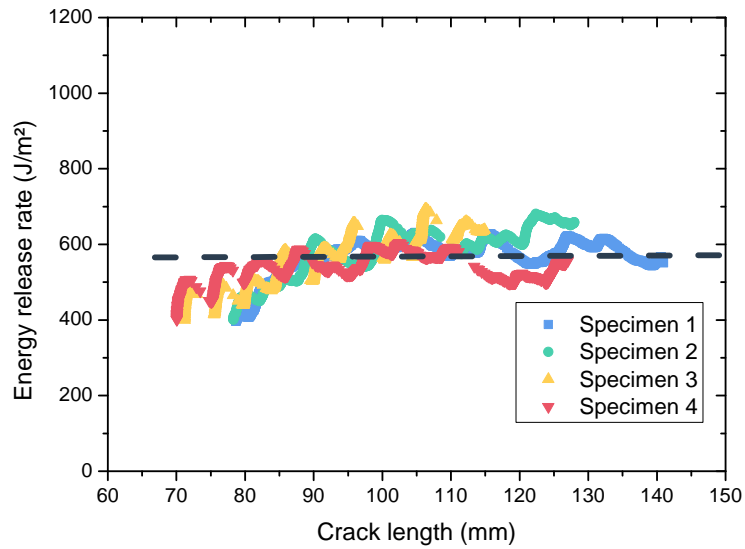


Figure 6.3 – R-curves of the saturated then dried composite in mode I

between unaged and saturated specimens. It results in a final overall decrease of around $210 J/m^2$ as the energy release rate for dried specimens was found to be close to $590 J/m^2$ (Figure 6.3).

It is possible to isolate one “representative” R-curve for each batch of specimens so

that a qualitative comparison can be made. Figure 6.4 shows this comparison. On this figure, one can also see that the energy release rate seems to stabilize after around 20 mm of propagation. This behaviour is quite classical and is attributed to the stabilization of the damage zone in front of the crack.

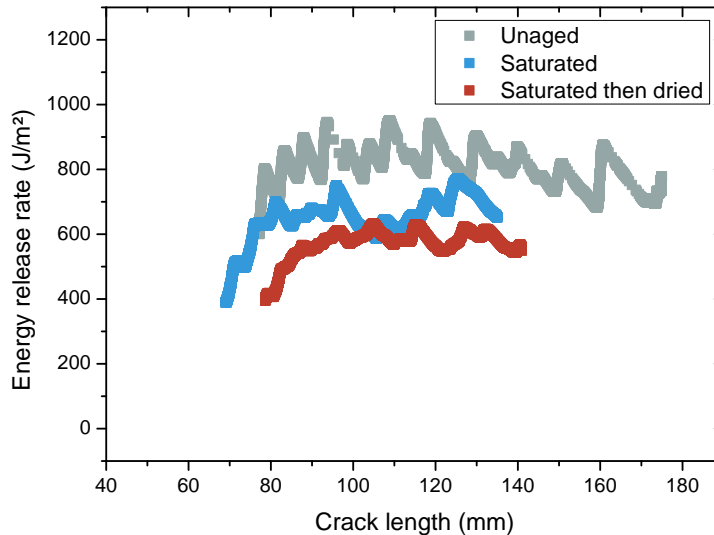


Figure 6.4 – Comparison of the three most representative R-curves from Figure 6.1 to Figure 6.3

These results show that wet aging and subsequent drying both result in a loss of toughness. The reasons for this will be discussed later.

6.1.2 Fatigue loading

The composite was then tested under cyclic mode I loading. The tests were performed under displacement control as explained in Chapter 2, so that a wide variety of energy release rates could be applied to the specimens. The results from these tests are curves that can be plotted as Paris (log crack growth rate versus log of applied strain energy release rate) plots. A Paris law can be fitted to the data obtained for all specimens. In our case, between four and five specimens were tested for each of the three different ageing conditions. The Paris law shown in each figure is the average of the four or five Paris laws previously fitted to each data curve.

The measured fatigue curves for the three different conditions (unaged, saturated and dried after saturation) are shown in Figure 6.5 to Figure 6.7. The values found for the unaged composite seem to be in accordance with round robin tests performed by Stelzer et al., with slopes of the Paris law and $G_{I_{max}}$ at 10^{-5} mm/cycle being in the same order of magnitude [128]. Here, the calculated slope is around 4 and value of $G_{I_{max}}$ at 10^{-5} mm/cycle is around 95 J/m².

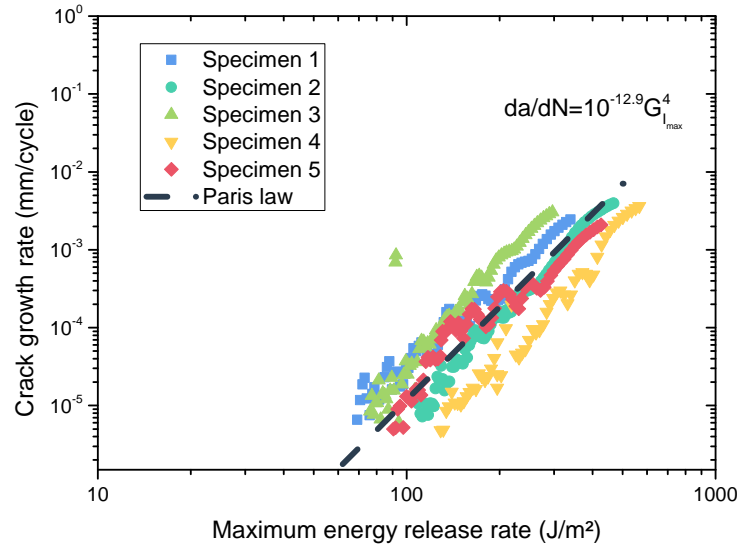


Figure 6.5 – da/dN curves of the unaged composite

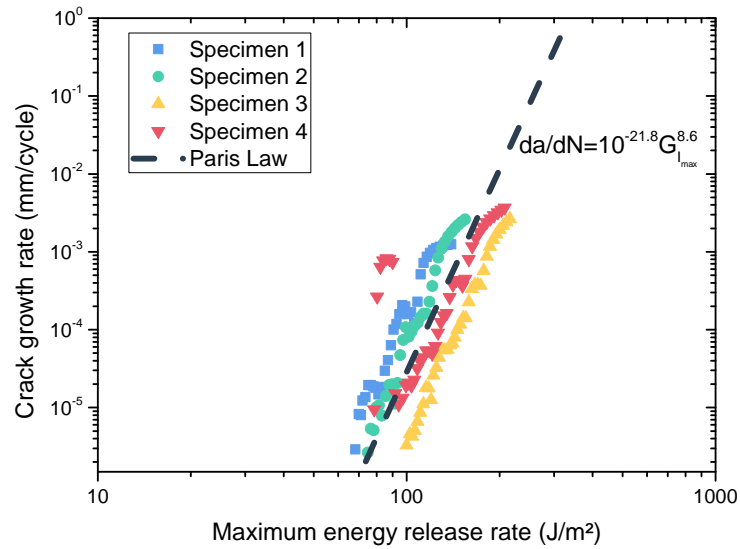


Figure 6.6 – da/dN curves of the saturated composite

After saturation, the slopes increase but at the same time, the curves shift to lower energy release rates, so the mechanical properties are degraded. This is shown in Figure 6.8 that compares the fatigue behaviour for the three ageing conditions. After drying, it can be noted that there is a slight recovery of the crack propagation resistance, characterized

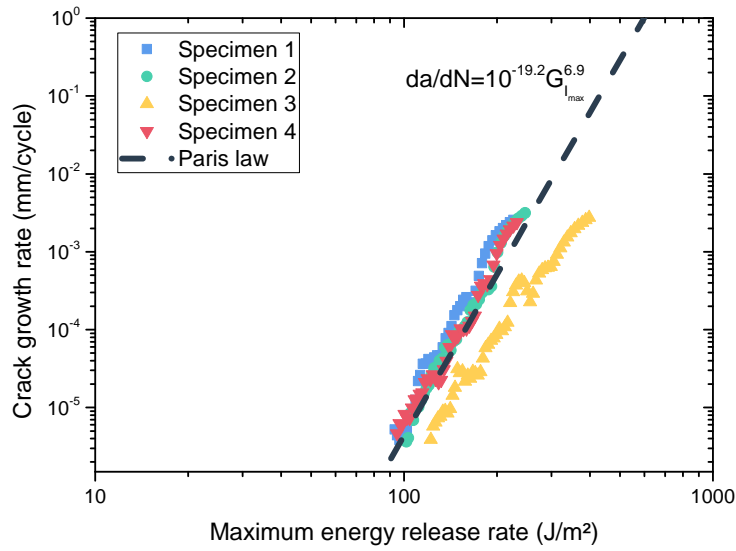


Figure 6.7 – da/dN curves of the saturated then dried composite

by the shift to higher energy release rates.

Another point to notice is that the effect of seawater seems to be more important at the higher crack growth rates. When comparing unaged and saturated specimens, at a

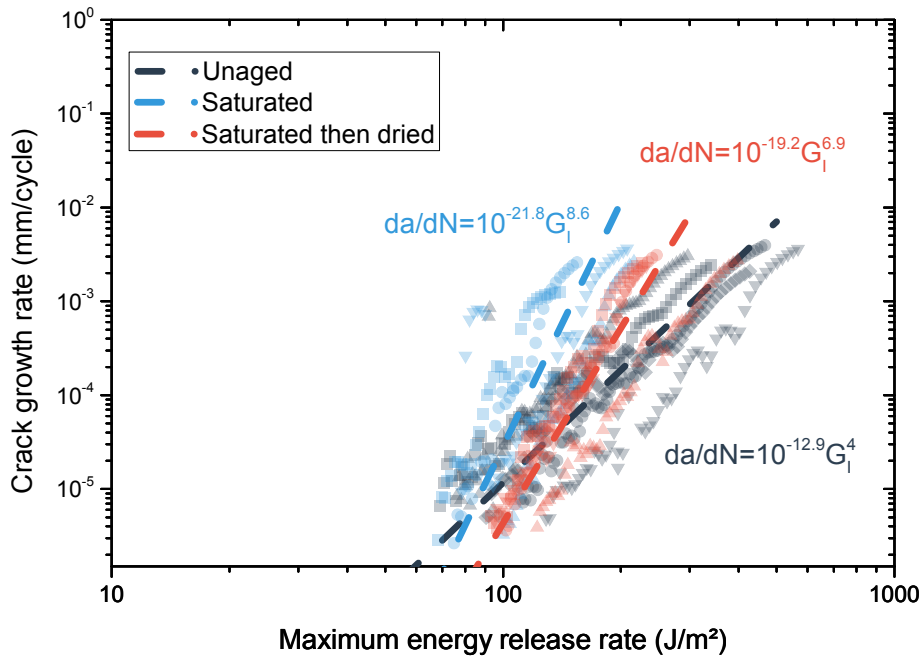


Figure 6.8 – da/dN curves of the three ageing conditions

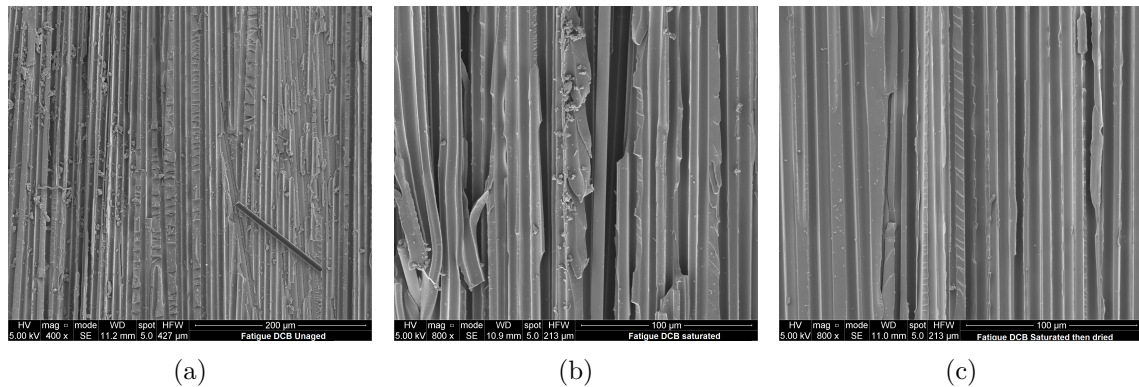


Figure 6.9 – SEM images of fracture surfaces of unaged (left) saturated (centre) and saturated the dried (right) composite, crack propagates from top to bottom

crack growth rate of 10^{-5} *mm/cycle*, the energy release rate decreases from a value of 95 to a value of 88 J/m^2 . On the other hand, at 10^{-3} *mm/cycle*, the difference is more important as the energy release decreases from 300 to 150 J/m^2 , which represents half the unaged value.

Overall, for mode I loading under both static and cyclic conditions the effect of seawater aging is to reduce the composite's resistance to crack propagation. After drying this effect is partially reversible for cyclic loading but permanent for static loads.

Comparing the fracture surfaces of specimens tested under the three conditions shows that the saturated composite surfaces seems more ductile than those for the other two conditions. In fact, the fracture surface shown in Figure 6.9b shows more deformation of the resin than for the two other conditions in Figure 6.9a and 6.9c. This would be in accordance with a plasticization of the resin, but does not explain the lower energy release rate values measured.

As suggested previously, plasticization does not explain these results, and the presence of another ageing phenomenon is likely. It was shown in Chapter 4 that physical ageing was coupled to plasticization of the resin. The results shown here could result from the same coupling, as a more brittle matrix behaviour might explain the lower energy release rates. This will be examined in a later section of this chapter but prior to that, the next section will discuss how seawater ageing affects the mode II crack propagation behaviour.

6.2 Seawater ageing under mode II

As with mode I crack tests, mode II was performed according to an international standard, ISO 15114 corresponding to the Calibrated Edge Loaded Split (C-ELS) test. This test method along with the data reduction method was presented in Chapter 2.

6.2.1 Quasistatic loading

Figures 6.10 to 6.12 show the mode II R-curves of the composite in the same three ageing conditions as those studied previously. One can clearly see the high variability obtained

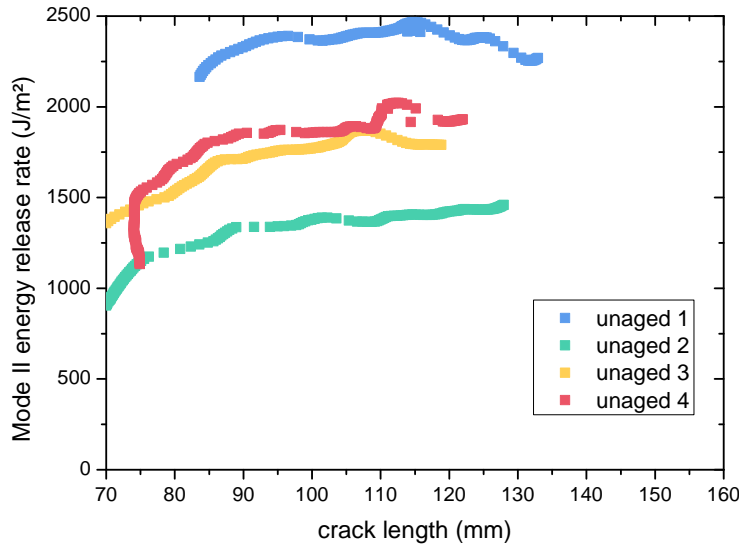


Figure 6.10 – R-curves of the unaged composite under mode II delamination

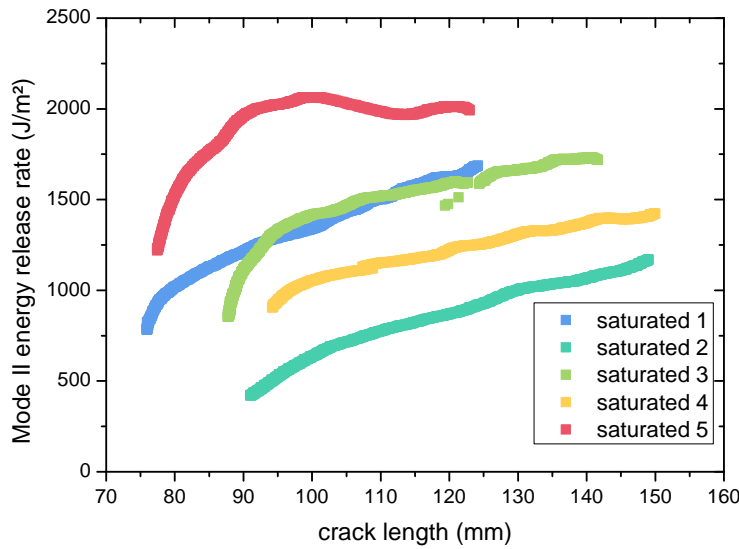


Figure 6.11 – R-curves of the saturated composite under mode II delamination

with this test method. First, when looking separately at each specimen, as crack length increases, the energy release rate (G_{IIc}) increases too. The difference compared to mode I measurements is that G_{IIc} does not seem to stabilize after a certain crack advance. However, there seems to be a first rising part leading to a more linear increase as shown

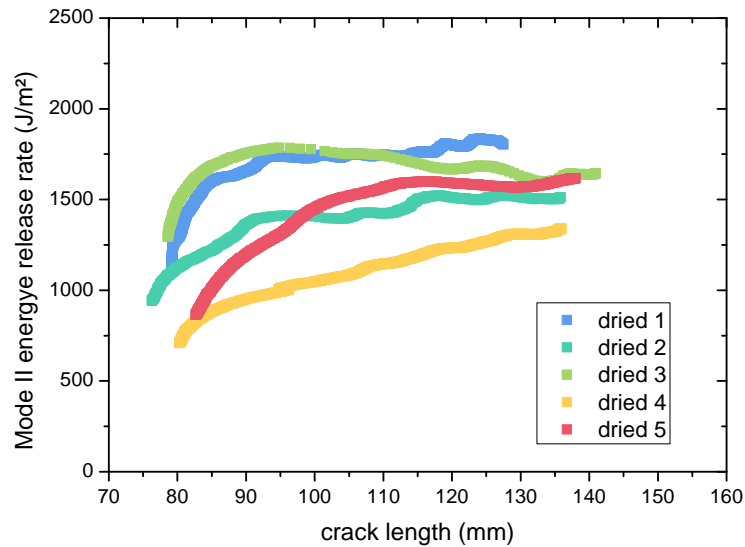


Figure 6.12 – R-curves of the saturated then dried composite under mode II delamination

schematically in Figure 6.13. It is worth noting that mode II pre-cracks were performed on all samples, so that the crack is no longer in the resin rich zone ahead of the PTFE insert. Longer pre-cracks may be necessary to reach a stabilized damage zone in front of the crack leading to a more stable R-curve. The constant increase of the R-curve, following the first curved increase, was also observed by Hojo et al. [143] and is attributed here to the particular layout of the test procedure. The contribution of friction which may increase as the length of fractured surfaces increases could result in a higher measured load and hence an increasing G_{IIc} value. Wang et al. proposed taking friction into account during 4ENF tests but their results showed that it only had a slight effect on the final G_{IIc} value [185].

In addition to this increasing trend of the R-curves, there is much more variability in the mode II results, compared to those obtained for mode I. Thus extracting a clear value of G_{IIc} for the three different conditions raises some difficulties. An approximation for G_{IIc} was made by determining the range of calculated G_{IIc} over the linear part of the R-curves.

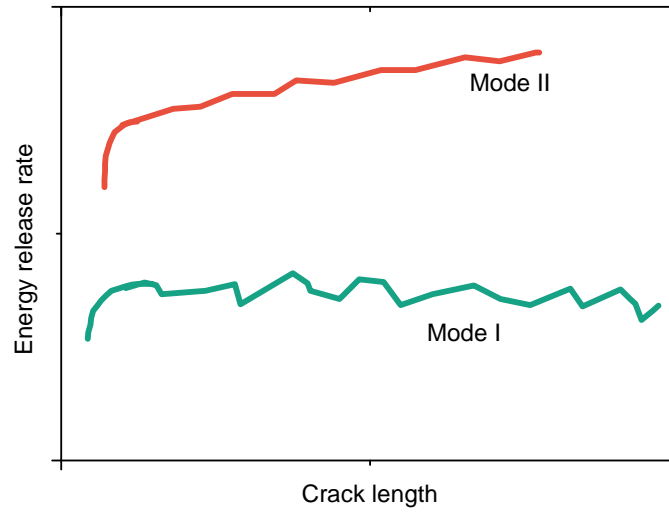


Figure 6.13 – Schematic representation of R-curves from mode I and mode II tests

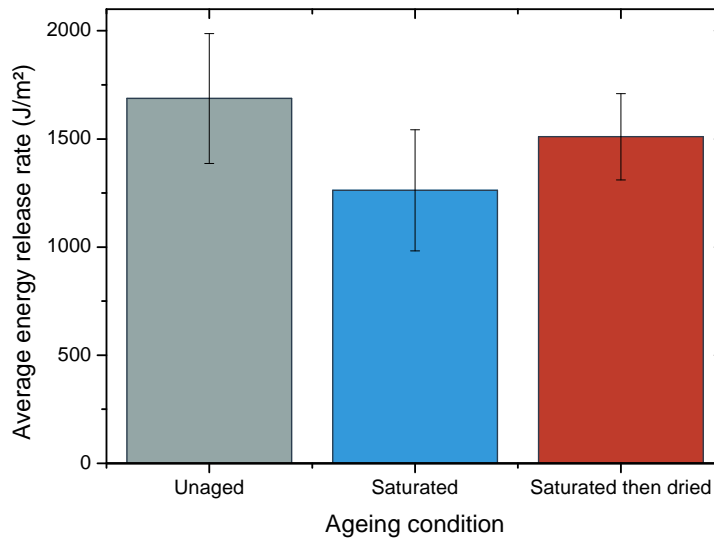


Figure 6.14 – Summary of average values of G_{IIc} of the composite under mode II delamination for different ageing conditions

6.2.2 Fatigue loading

Figure 6.14 summarizes the mean values of G_{IIc} that were determined from the R-curves presented previously. Although care needs to be taken with the values obtained with this procedure, unaged values are in the range of literature values [141, 142, 185, 186], Landry et al. even measured over 2 kJ/m^2 for CFRP prepreg composites [69]. The global trend does show a lowering of G_{IIc} induced by seawater ageing. However, the influence of water on mode II fracture resistance shows a different behaviour, compared to that of the mode I, as it seems to be partially reversible this time. This trend was also recorded by Landry et al. in the same study using distilled water as the ageing environment [69].

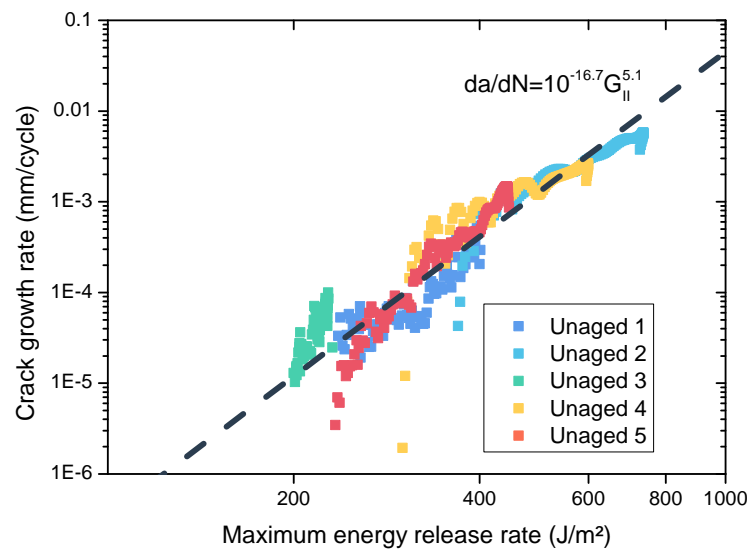


Figure 6.15 – Fatigue curve of unaged composite under mode II delamination

Figure 6.15 to 6.17 present the fatigue behaviour of the composite for the three different ageing conditions. It can be seen that there is less scatter in the data. Figure 6.18 summarizes the three conditions. A first observation is that there is less change in fatigue slopes. In fact, here the slope goes from 5 to 7.3 whereas for the mode I tests, slopes went from 4 to 8.6. In addition, the effect of seawater is more constant over the tested maximum G_{II} range. As for crack delamination in mode I, seawater shifts the fatigue curve to lower G_{II} values. However, the reversibility is total. The fatigue curve after drying is even slightly better than the initial fatigue curve. This time at 10^{-5} mm/cycle energy release rate decreases from 190 J/m^2 to 155 J/m^2 and recovers up to 235 J/m^2 . At 10^{-3} mm/cycle , the energy release rate of the unaged composite is around 480 J/m^2 dropping down to 290 J/m^2 and reaching once again a higher value after being dried, though the value for the latter is within the variability.

There is a net difference between the behaviour in mode I and mode II illustrated by the fatigue curve shifting. However, there is also a different behaviour between quasi-static and cyclic loading which is unexpected.

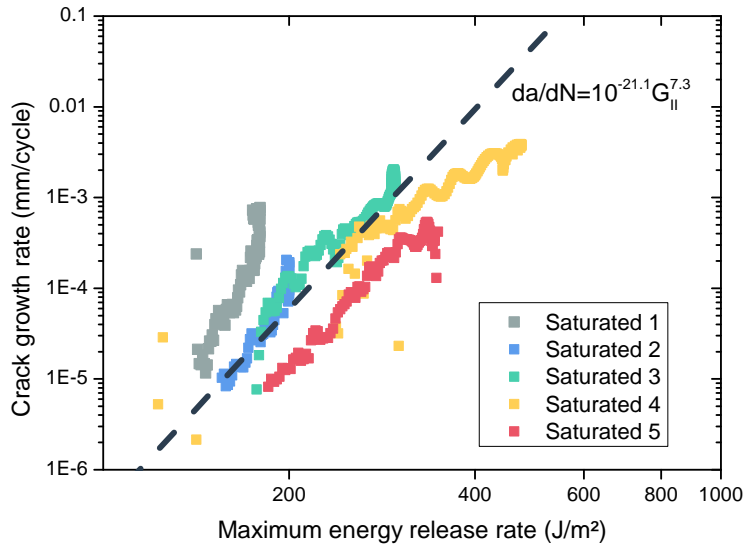


Figure 6.16 – Fatigue curve of seawater saturated composite under mode II delamination

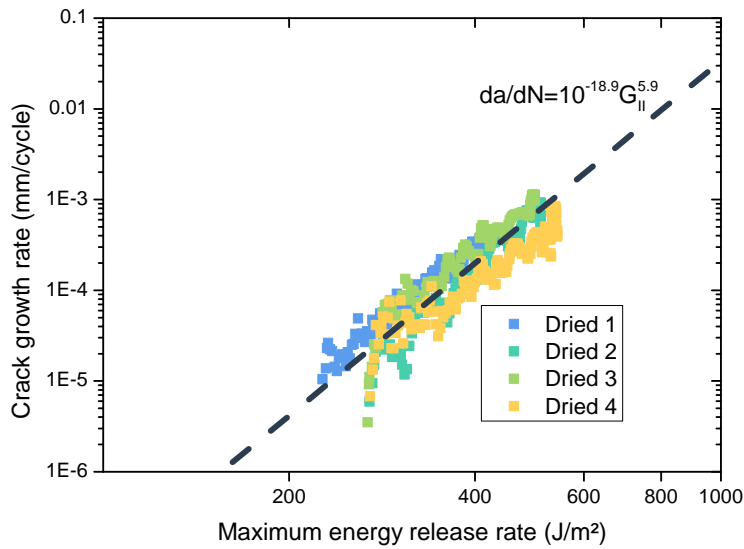


Figure 6.17 – Fatigue curve of seawater saturated then fully dried composite under mode II delamination

It is clear that there is another ageing phenomenon occurring in addition to plasticization. Plasticization induced by water absorption is completely reversible when water is removed, by drying the sample. Thus as the effect of seawater shows different degrees of

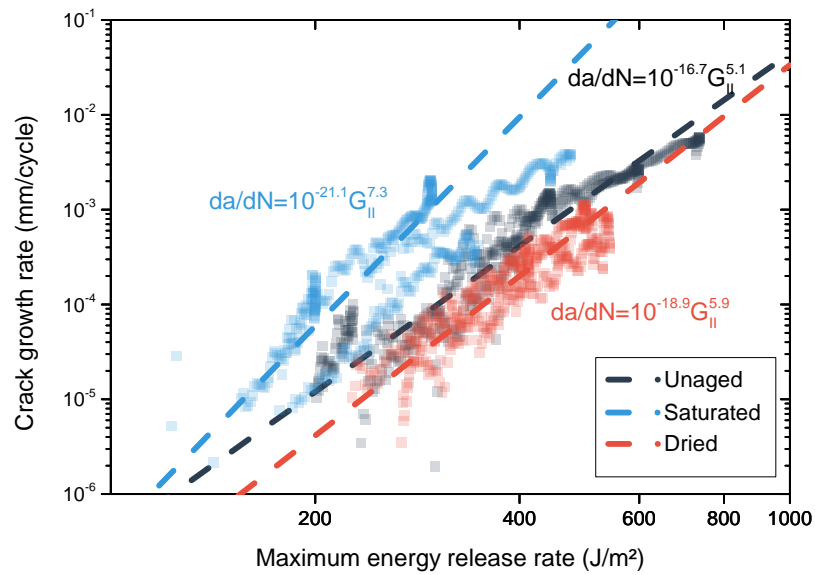


Figure 6.18 – Comparison of fatigue behaviour of the composite under mode II delamination for the three different ageing conditions

reversibility between the two loading modes studied, there is clearly an additional ageing phenomenon occurring.

It was noted previously that the influence of physical ageing on the mode I interlaminar fracture properties needed to be studied. Here, it is clear that it has to be studied in mode II too. So, in the next section of this chapter, the effect of physical ageing on mode I and mode II crack propagation will be studied.

The mode II fracture surfaces showed a similar trend to those shown previously for the mode I fatigue fracture surfaces. As shown in Figure 6.19b, the interlayer resin seems to have deformed more in the case of the saturated composite. For the two other conditions, the resin seems to break in a more brittle way.

In addition to that observation, it can be noticed that fracture surfaces of mode I and mode II specimens do not show the same features. This may be explained by the difference between mode I, where the fibre/matrix interface is highly loaded in tension, and mode II, where it is the interlayer matrix that is loaded in shear. This could also explain the difference in reversibility of ageing effects as the interface may be degraded permanently by water ingress whereas it was shown in Chapter 4 that the resin behaviour (and the interlayer matrix or interphase) could be recovered when water and physical ageing was removed. This is coherent with previous results. Nevertheless, the effect of physical ageing on crack propagation under the two different modes of loading needs to be isolated if it is to be understood. This is the purpose of the next subsection.

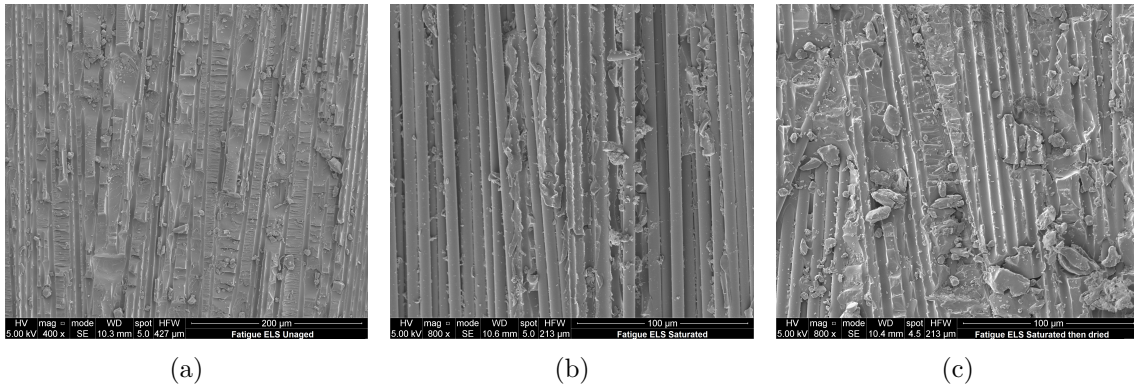


Figure 6.19 – SEM micrograph of fracture surfaces of fatigued mode II unaged (a), saturated (b) and saturated then dried (c) composite, crack propagate from top to bottom

6.3 Effect of physical ageing

In order to focus on how physical ageing affects crack propagation two series of specimens were prepared. The condition that will be referred to as “physically unaged” here corresponds to that of the composite being exposed to above- T_g (90 °C in water) during five minutes and quenched by plunging the specimens in 15 °C water. During exposure to above- T_g and quenching, the specimens were placed inside zip-bags so that water was not in contact with the samples.

For the condition that will be referred to as “physically aged”, the specimens were quenched with the same procedure as explained above. Then the specimens were placed in a vacuum oven at 60 °C for 1 month. According to the physical ageing kinetics studied previously, the “level” of physical ageing after this month at 60 °C would result in an elevated/fairly advanced level of physical ageing.

6.3.1 Mode I

The strain energy release rate required to propagate the crack in mode I was once again evaluated using the double cantilever beam standard test in exactly the same way as described in the previous section. The result of this test shows that physical ageing induces a decrease of around 200 J/m^2 in energy release rate. This decrease is in accordance with the conclusion of the previous subsection. As for the pure resin in tension the ductility decreases due to physical ageing and the critical strain energy release rate is lower. The reduction in the energy release rate for propagation drops from an average unaged value of 800 J/m^2 to 200 less, being 600 J/m^2 after being physically aged (see Figure 6.20).

Under cyclic mode I loading, the test results showed the same tendency as for quasi-static properties. The crack growth rates measured during the tests went from around $10^{-5} mm/cycle$ to just below $10^{-2} mm/cycle$. The curves shown in Figure 6.21 correspond to three specimens for each ageing condition. The two different da/dN curves show similar slopes but there is a clear, almost constant shift induced by physical ageing. It may be noted that at high crack growth rates, the difference in energy release rate is near 200 J/m^2 , which was the value measured under quasi-static loading.

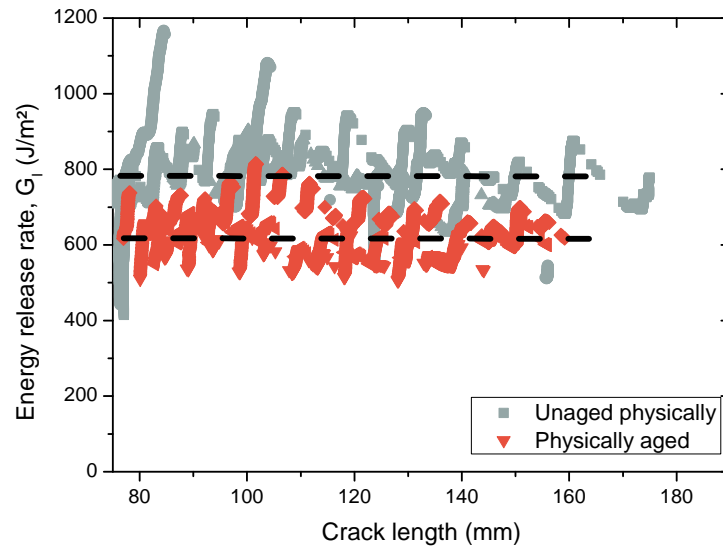


Figure 6.20 – Quasi-static mode I crack propagation in physically unaged and aged composites

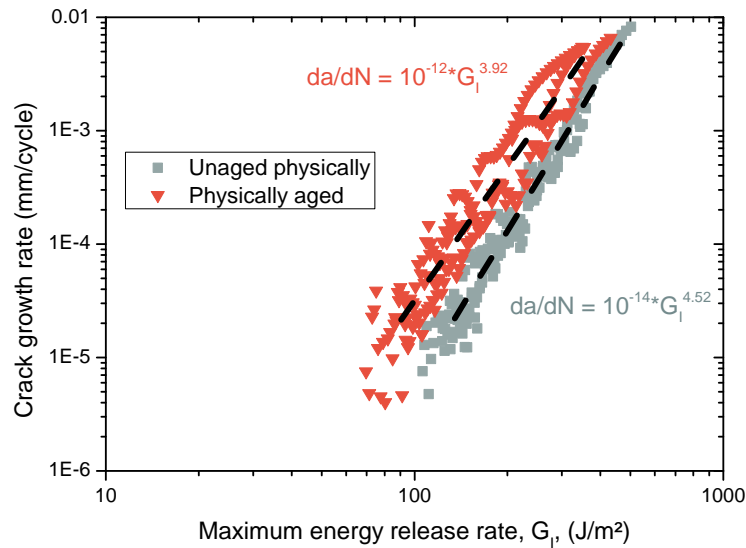


Figure 6.21 – Mode I fatigue curves for physically aged and unaged composites

Mode I fracture surfaces have been studied by SEM (Figure 6.22). The two different ageing conditions result in differences in fracture surfaces. They reveal a small change in roughness especially on the “thick” resin ridges, which show elongated scales for physically

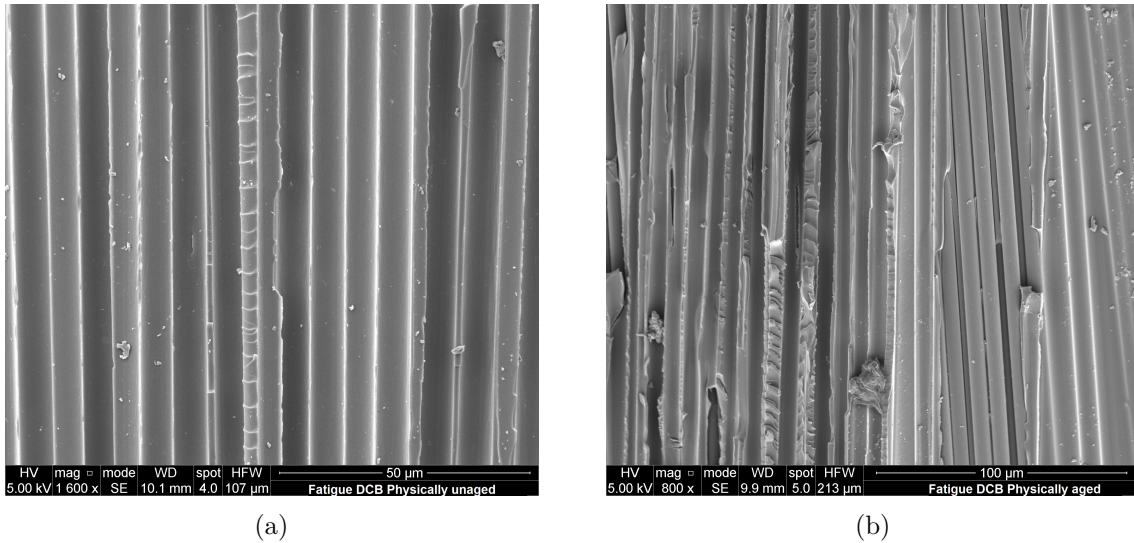


Figure 6.22 – Fracture surfaces of mode I fatigue composite physically unaged (a) and physically aged (b) crack propagates from top to bottom of the images

aged conditions whereas they appear smoother for the unaged conditions. One explanation could be that physical ageing induces multiple micro-cracks at the crack tip. As the crack propagates these coalesce, corresponding to the creation of a damage zone rather than matrix elongation, which is qualitatively coherent with resin embrittlement seen in the previous section 6.1.

6.3.2 Mode II

As in the previous section, the R-curves of mode II delamination tests on ELS specimens show high scatter, Figure 6.23. Nevertheless, it seems that the composite loses around $200 J/m^2$ in G_{IIc} during propagation after physical ageing. In the previous section the composite that was dried after being fully saturated did lose $200 J/m^2$ compared to the unaged condition. The presence of physical ageing on the dried specimens would explain this previous behaviour. An important point to note here is that G_{IIc} in the unaged condition measured in this set of tests is a little lower than the one that was measured in the previous section, the values being respectively 1300 and $1600 J/m^2$.

The difference between these values may come from the composite's quality and composition. In fact, the samples that were used for the seawater ageing trials were taken from two plates (plates n°3 and 6) which had good quality. However, the specimens that were taken for the physical ageing trials were all taken from another remaining plate (plate n°5) that had lower quality. For example, when comparing the C-scans from plate n°3 and 6 (Figure 6.24) and the plate 5 (Figure 6.25), the overall quality of plate n°5 shows lower quality. On these figures, the large black stripes that are visible on both sides of the plates are created by the plastic film that is placed at the mid-thickness to create the pre-crack. Looking at the C-scans, the plate n°5 seems to have poorer quality compared with the other two plates.

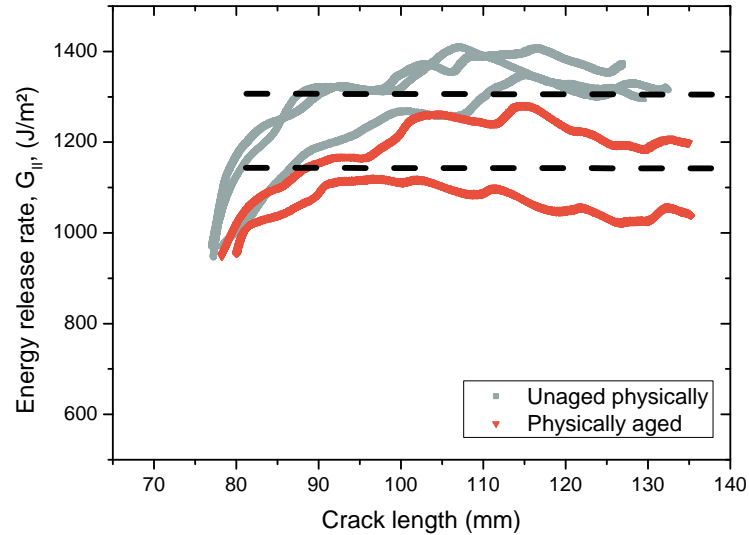


Figure 6.23 – R-curve of composite in mode II as a function of physical ageing

However, when looking at the composite's composition (Table 6.1, the difference between the plates does not seem to be that great. It is possible to notice that the void ratio of the plates 3 and 6 are respectively 1 and 0.6 % and that of the plate number 5 is only 1.3 %. Therefore, in terms of void ratios, the difference is not that big. However, the crack properties, as previously mentioned, depend strongly on the resin and fibre/resin interface. When looking at the values of fibre and resin ratios, the composition of the plate 5 shows a lower resin ratio compared to the two other plates. This may explain the lower values of G_{IIc} measured during these tests.

Additional investigations on the effect of fibre or resin ratio may enlighten this phenomenon.

Table 6.1 – Composition of the two plates that were used for mode I and mode II tests

	Fibre volume ratio (%)	Resin volume ratio (%)	Void volume ratio (%)
Plate 3	60.3	38.7	1.1
Plate 6	62.2	37.2	0.6
Plate 5	64.7	34	1.3

Regarding the scatter seen here, previous work has shown that as the mode II component in mixed mode loading increases so scatter in results also grows [187]. Friction contributions may explain this.

When considering the physical ageing effect on cyclic mode II loading, a different behaviour is noted compared to mode I results. In fact, the composite that was physically aged showed slightly better results after the physical ageing. This small enhancement of

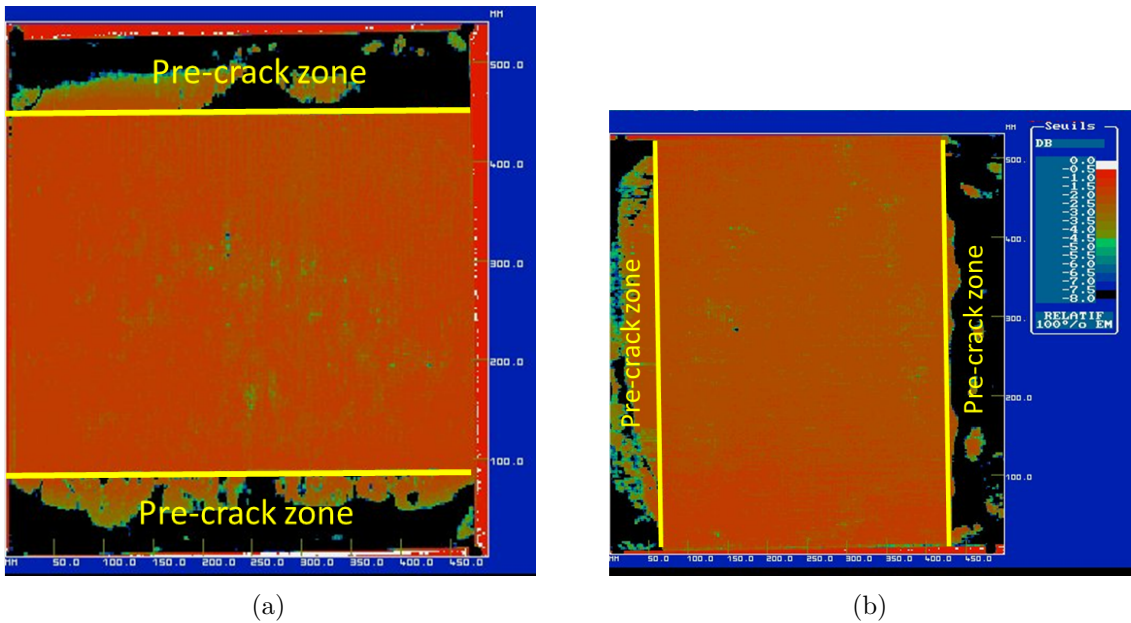


Figure 6.24 – C-scans of the two plates that were used for the mode I and mode II delamination tests, plate 3 (a) and plate 6 (b)

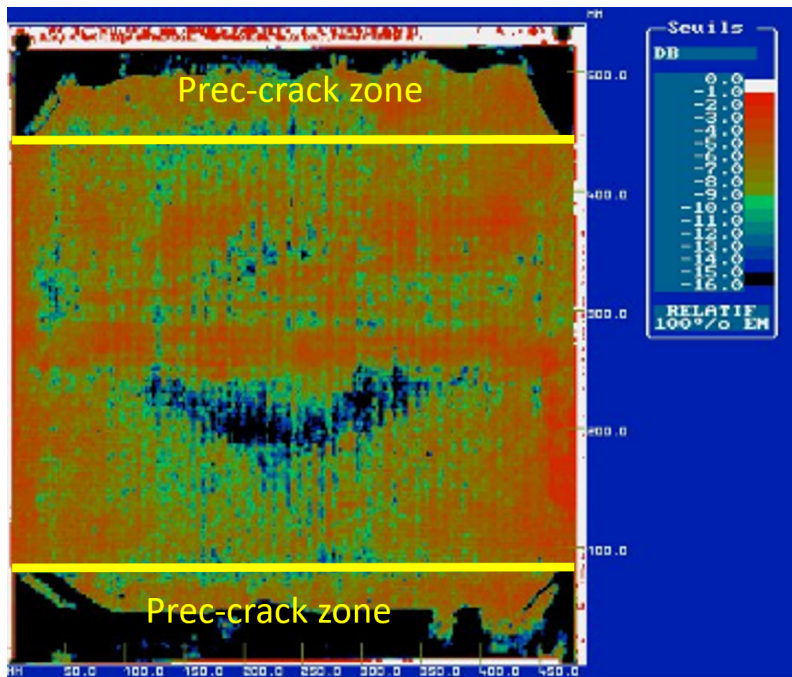


Figure 6.25 – C-scan of the composite panel used for the physical ageing trials (note larger attenuation scale)

the fatigue performance of the composite induced by PA is shown in Figure 6.26.

The fracture surfaces are shown in Figure 6.27. This time though, the effect of physical

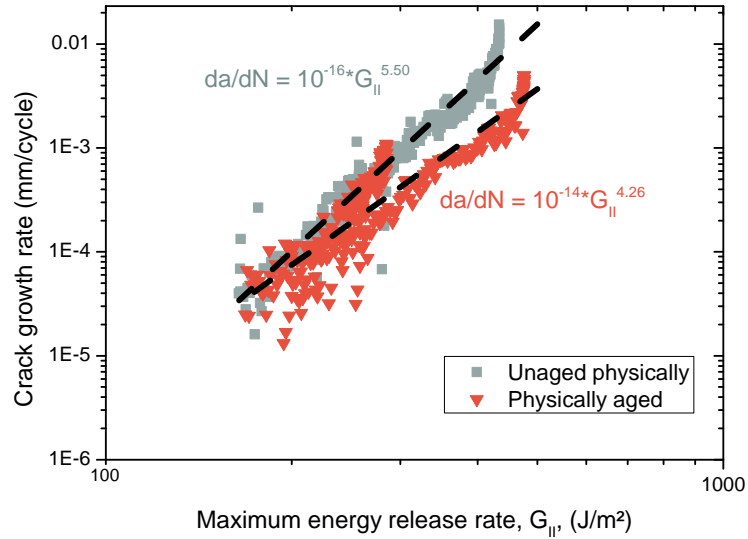


Figure 6.26 – Physical ageing effect on mode II fatigue

ageing appears to induce a more important change. The formation of larger scales could be explained by the embrittlement of the resin once again due to physical ageing. As illustrated in Figure 6.28, the damaged area near to the crack tip produces larger micro cracks when the composite is physically aged. Then when crack propagates, it produces deeper scales, such as those visible in the Figure 6.27b.

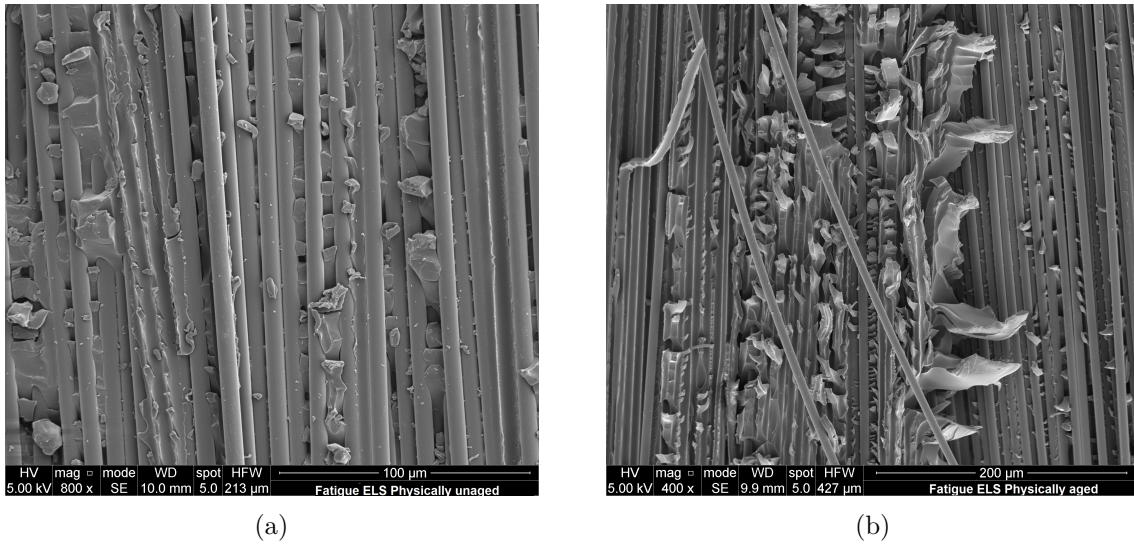


Figure 6.27 – Fracture surfaces from mode II fatigue with physically unaged material (a) and physically aged material (b) crack propagates from top to bottom of the images

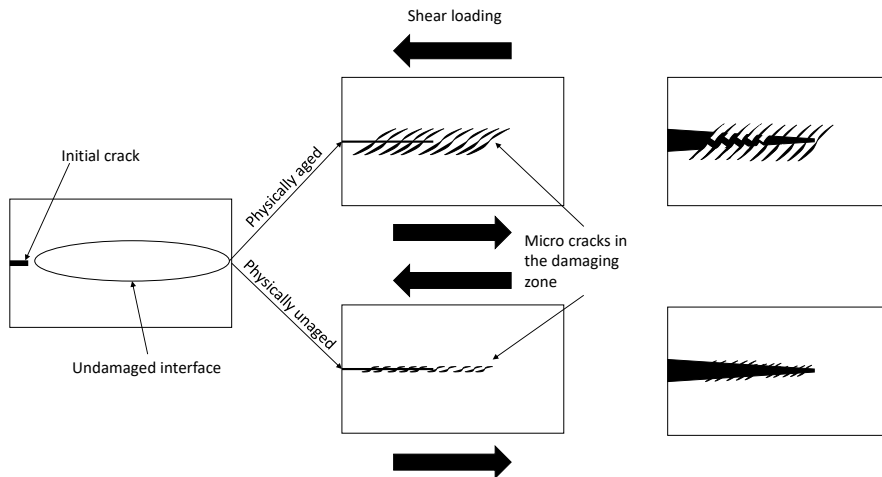


Figure 6.28 – Formation of fracture surfaces in mode II with physical ageing effect as shown by SEM micrographs

6.4 Discussion

The delamination tests described in this chapter have produced a large set of results, which are summarized in Table 6.2 below. The value taken to characterize fatigue is the value of energy release rate for a crack growth rate of 10^{-3} mm/cycle . The value was calculated based on the Paris law parameters of each conditions.

Table 6.2 – Summary of the values from delamination tests, arrows refer to the trend from the previous value (directly to the left)

Value	Unaged	Saturated	Saturated then dried	Physically unaged	Physically aged
$G_{Ic}(J/m^2)$	820	↘620	↘590	820	↘600
$G_{I_{max}}$ at $da/dN=10^{-3} \text{ mm/cycle}$ (J/m^2)	298	↘153	↗222	163	↘197
$G_{IIc} (J/m^2)$	1987	↘1262	↗1510	1350	↘1150
$G_{II_{max}}$ at $da/dN=10^{-3} \text{ mm/cycle}$ (J/m^2)	485	↘301	↗495	151	↗382

Analysis of these results is complicated by the fact that during accelerated seawater ageing, the material sees different water conditions but also different temperatures. There is also a question mark over the level of physical ageing of the “unaged” specimens as they are typically tested in the as received state. In our case, when unaged samples are placed in $60 \text{ }^\circ\text{C}$ seawater, so the temperature can induce physical ageing. Then as water diffuses into the composite, the T_g drops until reaching the value of $60 \text{ }^\circ\text{C}$ when fully saturated. As $60 \text{ }^\circ\text{C}$ is the ageing temperature and is now equal to the material’s T_g , the physical ageing present in the material should be “erased” in a similar way to the pure resin which was rejuvenated (Chapter 4). It is important to note that the glass transition temperature is not a net transition and the materials change from the glassy state to the rubbery state at around $\pm 10 \text{ }^\circ\text{C}$ around the measured T_g (see Figures 4.4 and 4.12). Therefore, when the material tested is fully saturated, it should no longer have physical ageing in it. Then, in order to remove the water, the specimens are placed in dry ovens at $60 \text{ }^\circ\text{C}$ once again so that drying is accelerated. This time, as water is removed from the composite, the T_g goes back up to $75 \text{ }^\circ\text{C}$ and physical ageing can occur. So when the material is tested as “saturated then dried”, it is also physically aged to a considerable degree, as we saw previously that the relaxation time of the pure resin at $60 \text{ }^\circ\text{C}$ was 12 hours and the drying period for the composites is around 4 months.

In both mode I and mode II, the dried G_c value was lower than the initial one. This is coherent with the physically aged G_c results showing a respective lower G_c after physical ageing. This is also coherent with results from tensile tests on the pure resin showing a more brittle behaviour and consequently leading to a lower energy release rate. In the literature, Chang and Brittain showed that physical ageing reduced the energy release rate of the pure resin [86], which confirms this hypothesis.

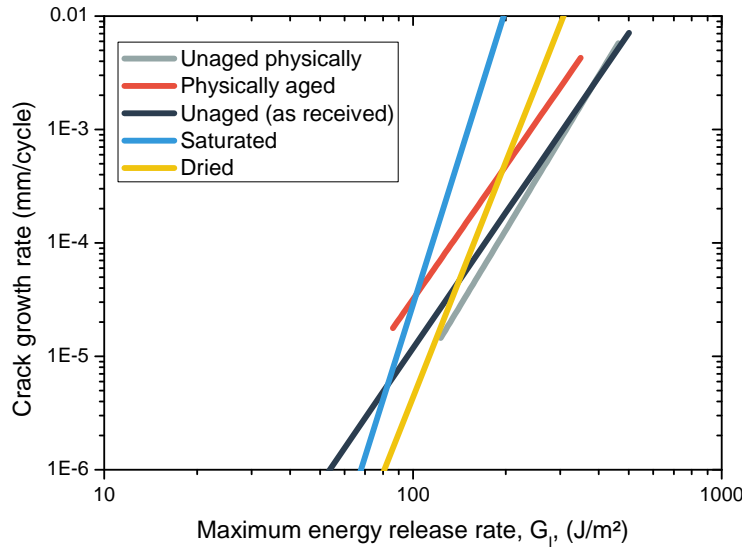


Figure 6.29 – Comparison of fitted Paris law curves from physical and seawater ageing in mode I

When looking at the fatigue curves in mode I (Figure 6.29), unaged curves from seawater ageing tests and physical ageing tests do show very similar values. The curves shown are those taken from the previous fatigue curve, only taking the Paris curves. However, the wet aged composite shows lower values than the physically aged composite. This suggests that there is a further embrittlement mechanism acting when water is involved, which may be related to swelling at the fibre-matrix interface. Recent work has shown that swelling may significantly affect local stress states, and may result in damage [188]. In addition to a shift to lower G_I , there is also an effect on the slope, which is not present for physical ageing. In fact, the values for physically aged composite are closer to those of the saturated-then-dried composite. In this case, this would confirm the presence of physical ageing in the dried specimens. It would have been interesting to expose saturated specimens to sub-T_g seawater at saturation, in the same way as was done for the pure resin. This would have shown whether physical ageing was present in the saturated specimens, and could be included in a future study.

A comparison of fatigue curves from mode II specimens exposed to physical and seawater ageing is shown in Figure 6.30. A first observation is that the physically unaged and saturated fatigue curves are quite similar. It was stated previously that physical ageing shifted the fatigue curve to the right of the unaged fatigue curve. Given this statement, it seems logical that, once again, the saturated then dried specimens were physically aged compared to the unaged specimens. However, comparing physically unaged and unaged specimens from the seawater ageing tests suggests that the initial state of the latter involved a high degree of physical aging.

If this is true, this would mean that water does not have a significant effect on the

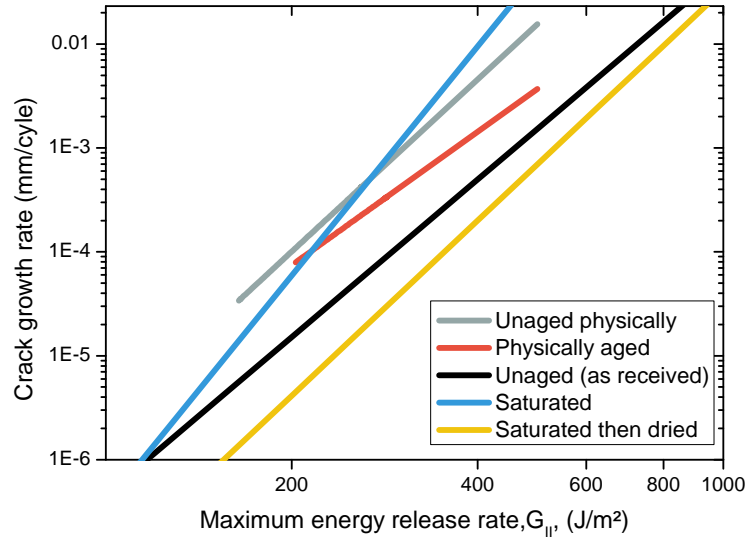


Figure 6.30 – Comparison of fitted Paris law curves from physical and seawater ageing in mode II

mode II fatigue behaviour of this composite, which is contrary to results presented by Landry et al. [69]. However, in the case of monotonic loading, the effect of physical ageing is to lower G_{IIc} . In addition, G_{IIc} from physically unaged samples was already measured to be lower than that of the unaged (from seawater ageing batch) specimens. Therefore, if physical ageing was present in the unaged specimens, they would have shown lower G_{IIc} values than those of the physically unaged specimens. However, the mode II results should be considered in the light of the large scatter in results for these tests and it is preferable to reserve judgement for this loading case. A complimentary set of tests under a mixed mode loading condition with a large mode II component would be very helpful to clarify these effects.

There is a counterintuitive result from this data. In fact, based on the resin's behaviour to physical ageing, the fact that under mode II loading physical ageing enhances the fatigue response is surprising. This is even more surprising when in mode I under fatigue loading this did not follow the same trend. As of now, there is no clear explanation for this behaviour.

A proposition can be made though. Starting from the assumption that resin is more brittle in the physically aged state and more ductile in the unaged state. There is no evidence that the resin's crack propagation behaviour is the same under tensile and shear loads. Therefore, there is no reason why physical ageing will behave in the same way under mode I and mode II. Studying the crack behaviour under tension and shear of the pure resin would possibly answer this question. In addition to that, the damage area in mode I may not be as large as in mode II as shear loading damage tends to remain at the interlaminar plane, whereas tension damage tends to extend in the out of plane direction

through the specimen thickness.

Leaving the mode I aside, when the resin behaves in a more brittle way, the damaged area may be larger, as represented in Figure 6.28. Hence, micro-cracks could reach other plies in the out of plane direction. However, in the case of this composite, the off-axis stitching constrains the macro-crack to stay at the mid-thickness and crack advance is not necessarily easier. On other composites, fibre bridging may show this behaviour where macro-cracks reach plies other than the mid-thickness one. Finally, there would be more energy released but at the end the crack advance would be the same. A post mortem analysis of the crack front by tomography might allow this damage area to be quantified. A representation of this theory inspired by Lee in [189] is shown in Figure 6.32.

This may be confirmed by the SEM from Figure 6.31 where one can see the microcracks extending beyond the first fibre layer.

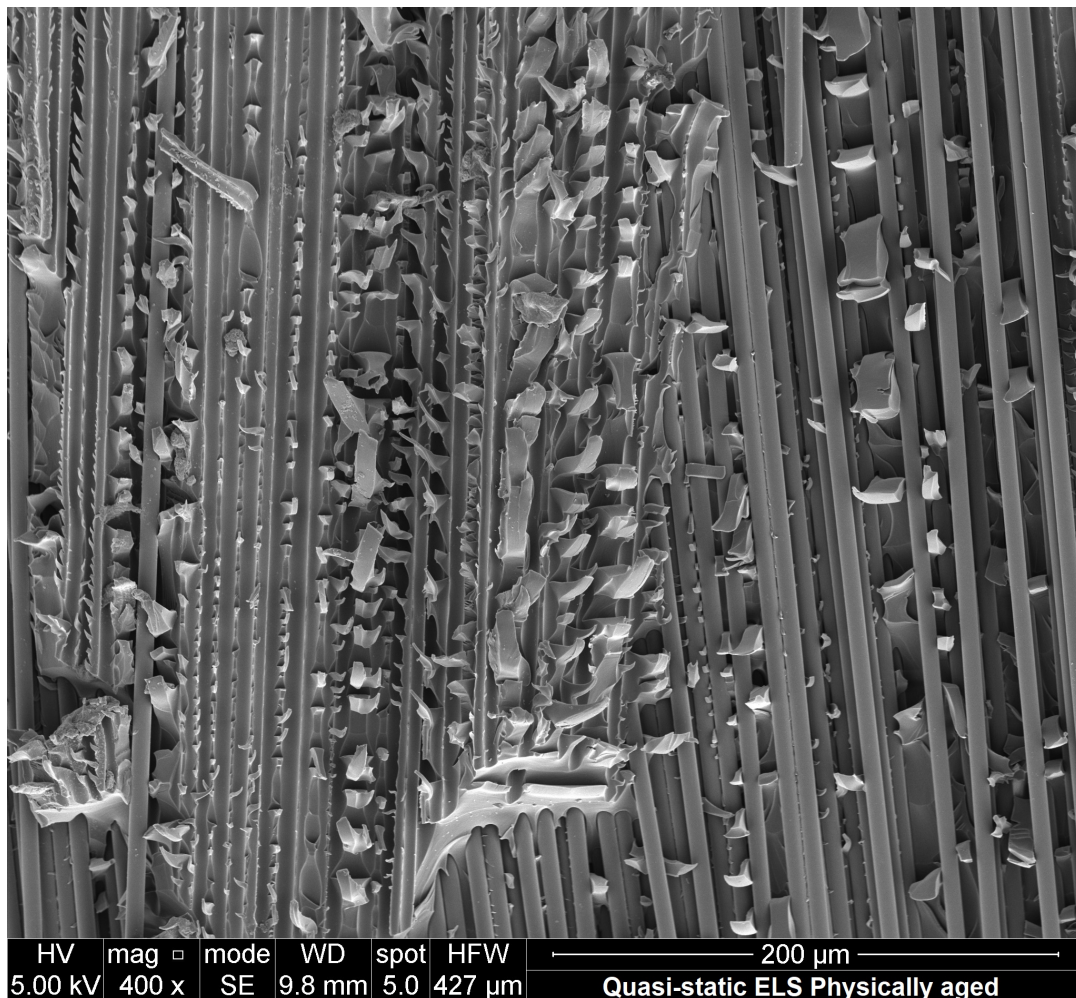


Figure 6.31 – SEM of the fracture surface of a physically aged and fatigued ELS specimen showing microcracks

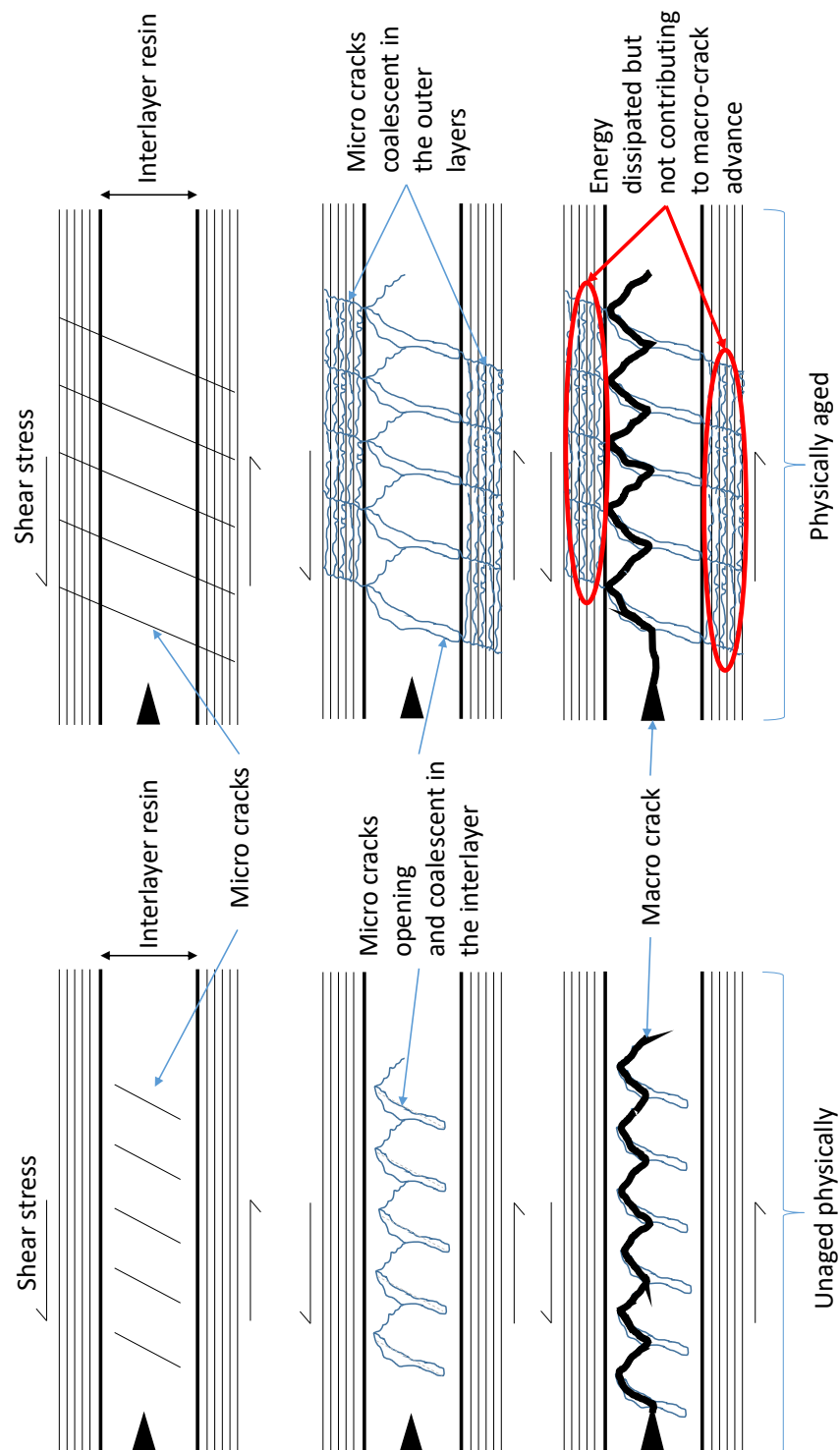


Figure 6.32 – Representation of possible micro-crack formation for a composite physically unaged versus physically aged

6.5 Conclusion

To conclude this chapter, the mode I and mode II crack properties were characterized with, respectively, DCB and ELS standard test methods. Both crack modes were tested under static and fatigue loads under three ageing conditions, these being unaged, saturated in seawater and finally saturated then dried.

The effect of seawater exposure induced a decrease of the energy release rates of crack propagation in both modes with respect to an initial unaged reference. Under fatigue loading, both curves shifted to lower energy release rates. This may seem contradictory with the idea of the resin being plasticized by seawater. Plasticization of the resin was shown in Chapter 4 to result in a decrease in maximal stress and increase in strain to failure, that could result in more or less energy dissipation when cracking the composite. The main effect noted for the composite here was for the saturated then dried condition, showing contradictory results according to whether fatigue or static loading was considered and also when comparing mode I and mode II delamination.

In the case of mode I delamination, the effect of seawater was found to be irreversible, whereas in fatigue it was found to be partially reversible. On the other hand, for mode II delamination, it was found to be partially reversible under static loading and fully reversible, (or even improved), under cyclic loading. This difference in reversibility behaviour was then studied.

First, mode I and mode II delamination are known to not load the interlayer region in the same manner. Mode I is known to be more dependent on fibre/matrix properties whereas mode II is more dependent of the interlayer matrix. It would be very interesting to pursue this study with tests on an MMB (Mixed Mode Bending) fixture [187,190,191], which allows the contributions of these two modes to be varied. A special MMB test fixture was designed and built so that such tests can be performed in seawater, and this will be used in a subsequent study.

Another possibility that was not taken into account when the first delamination tests were performed in this study (nor in most of the published studies on composite ageing in water), was that this composite might be sensitive to physical ageing. To examine this, the effect of physical ageing on the crack properties was studied under controlled conditions. It was found that under quasi-static loading for both mode I and mode II, physical ageing induced a reduction of the respective energy release rates. This result was coherent with that of Chapter 4 on the resin alone, showing a more brittle behaviour which will result here in a lower energy release rate. However, when the composite was loaded in fatigue, the behaviour differed between the two modes. While in mode I, physical ageing induced an embrittlement, characterized by a shift of the fatigue propagation curve to higher crack growth rates, in mode II, the fatigue curve shifted to lower crack growth rates which means better fatigue resistance to delamination. This last result may seem counterintuitive especially given the fact that the resin is more brittle when physically aged. However, this is coherent with previous results for the saturated then dried fatigue tests, which may suggest that the reversibility shown in the dried state includes a contribution from physical ageing.

This latter conclusion is of importance, as physical ageing is rarely taken into account when performing ageing tests, even though it is clearly shown here that it could affect

Chapter 6. Composite under delamination loading

mechanical properties. Thus, not considering physical ageing may result in misleading conclusions on the ageing behaviour of composite materials. Clearly further work is needed to fully explore these coupled effects in composites.

Conclusion

Conclusions of the study

The aim of this work is to investigate the long-term behaviour of composite materials subjected to a marine environment while loaded cyclically. This study was focused on a carbon fibre reinforced epoxy that was used in a parallel project, FabHeli, which ended in 2018. Having this application meant that the materials were commercially available systems. Therefore, the epoxy resin and the carbon fibres used were not model materials. The seawater ageing behaviour of both the pure resin and the composite was studied.

First, the water ingress in both materials was characterized. It was shown that the diffusion behaviour in the resin followed a Fickian behaviour excepting oxidation effects that were activated at the highest temperature used during accelerated seawater ageing. The diffusion in the composite was also identified as Fickian, and the diffusion parameters of the composite were predicted knowing those of the pure resin. It was shown that the diffusion coefficient was correctly predicted by the Rayleigh equation. The prediction of the mass to saturation of the composite based on that of the resin showed that water did not only diffuse in the resin. A proposition was made to obtain the values for the composite based on that of the resin by considering water diffusing in the micro-voids present in the composite. It was found that 25 % of the void volume needed to be taken into account to correlate maximal water absorption in composites.

The water ingress in the composite propeller blade from the FabHeli project was predicted based on an immersion in seawater at 15 °C. The prediction showed that more than a thousand years would be needed to fully saturate the propeller blade. However, it was shown that even after one year, the water had reached the fourth composite ply from the exterior. This is an important result because the value of time to saturation of the entire blade does not reflect the amount of water in the blade after one or five years. If this is neglected, early failure may initiate in the outer plies of the propeller blades. Additionally, the leading and trailing edges are parts of these thin parts of blades and they are highly sensitive to changes in mechanical response especially when considering vibrations of the propeller. For this reason, it is important to consider the mechanical behaviour when exposed to seawater.

The mechanical behaviour of the pure resin exposed to accelerated seawater ageing was studied. It appeared that there were two main ageing phenomena occurring during

these accelerated ageing tests. These were plasticization and physical ageing. When studying epoxy resin exposed to humidity and water, plasticization is not a surprising degradation process. However, the physical ageing was more unexpected. The coupling between physical ageing and plasticization was then studied and it was shown that the presence of water, i.e. plasticization, accelerated the physical ageing for the temperatures close to the material's T_g . This was demonstrated by modeling the effect of physical ageing on the maximal tensile stress at different temperatures using a KWW equation. The effect of physical ageing on the mechanical response of the epoxy was shown to be non-negligible. It was then studied on the composite under shear and transverse tension, with a notable effect on the latter.

The effect of seawater ageing on the quasi-static and fatigue behaviour of the composite was then studied using the same accelerated ageing as for the pure resin. The mechanical tests performed were tension, flexure and delamination.

In the case of tensile loads, the composite showed limited sensitivity to seawater when loaded in the fibre direction for unidirectional and for cross-ply 0/90 composites. This was seen for both quasi-static and fatigue. On the other hand, the influence of seawater on transverse tension showed a significant effect, decreasing the ultimate tensile strength by almost 50 %. The carbon fibres are not sensitive to seawater; they do not absorb water, while the response to loads perpendicular to the fibres is highly dependent on the matrix properties. As the mechanical properties of the pure resin were degraded by seawater, the degradation of the mechanical properties under transverse tension was expected. Acoustic emission showed that there was damage occurring during the entire fatigue life of unidirectional and cross-ply specimens even though stiffness degradation appeared to be stable during the middle life period.

The cross-ply composite was tested under four-point flexure. This time, the effect of seawater was significant. The fatigue curve shifted to lower lifetimes by between 1 and 2 decades showing an important effect of seawater. As a result the influence of the manufacturing process was studied, as delamination failure of the RTM composite was attributed to lower manufacturing quality. Infusion and RTM processes were then compared in flexural fatigue and, even though the infused composite showed better mechanical properties,—mainly due to higher fibre volume ratio and higher proportion of unidirectional fibres—it was still not insensitive to the presence of seawater. Additionally, the infused composite was dried after saturation and showed similar fatigue behaviour to the unaged composite. This suggested that as ageing was reversible by only removing seawater and that the only phenomenon playing a role in this case was plasticization; physical ageing did not show any effect. However, to confirm this postulate, additional trials are needed.

The damage sequence in four point flexure was investigated, as delamination was reported even with infused composite. Most of the fatigued samples also showed some damage under the loading points. It was shown that the load points play a major role in final failure but other damage appears throughout the fatigue life. This was clearly revealed by tomography analysis of interrupted fatigue test specimens. Finally, delamination behaviour was studied under two different loading modes: opening and in-plane shear (mode I and mode II). It was shown that seawater degraded the fracture toughness and fatigue crack resistance of the composite in both load cases. However, removing water from the saturated composite showed different results. In mode I, the static fracture toughness

Conclusion

decreased once again while the fatigue crack resistance did partially recover after drying. In the case of mode II, the static fracture toughness was partially recovered while fatigue crack resistance was completely recovered. These results did not consider physical ageing. The effect of physical ageing on these two delamination modes was then studied and showed results that could explain the difference between the results of seawater ageing on mode I and mode II. A conceptual proposition was made in order to explain the effect of physical ageing on the mode II fatigue response, as it is the least understood behaviour.

Recommendations for future work

Many aspects of the durability of carbon fibre reinforced epoxy were examined in this study. However, there are still many that need to be investigated. These aspects can be divided into three different areas:

- Test related
- Material related
- Ageing related

Tests and test methods

There are questions that still need further investigation regarding the test methods. In the first place, there are several aspects that were not studied here and that deserve further investigation. For example, the load ratio used for the fatigue tests here was kept to 0.1 but in reality, propeller and tidal turbine blades and, more broadly, composite parts are not loaded under a constant load ratio but with a wide variety of load ratios. In the same vein, even for marine propellers that are often designed for a particular rotational speed, the frequency seen by the actual propellers does not only correspond to the one it was designed for. In fact, the manoeuvres that the boat needs to perform whether it is for harbour approach, acceleration to reach cruise speed or avoidance manoeuvres involve a range of load frequencies. Therefore, studying the effect of the load speed/frequency would be an important aspect to consider. A very recent paper by Koshima et al. showed that the effect of seawater ageing was strongly dependent on the stress ratio [192]. This confirms the interest of such a study.

A set of results is presented here on the delamination resistance of the composite. These results showed that the mode II test still poses experimental problems. In fact, the results showed anomalies that were attributed to friction induced by the test method that involves the two delaminating faces to be in contact with one another.

A solution proposed during this study was to perform the tests under mixed mode bending with a high mode II component. This allows the composite to be characterized under loading dominated by mode II but with a little amount of mode I sufficient so that friction can be avoided. It would now be interesting to look at the seawater ageing effect with mixed mode loading. A titanium mixed mode bending fixture was designed and built at the end of this study, but there was a lack of time to set this test up. This titanium fixture would allow tests to be performed immersed in seawater as was done for the majority of the other tests during this study.

Another aspect that needs further attention is the damage occurring during the delamination tests. Tomographic analysis of the crack front may answer many questions that were raised in this study.

Finally, there are durability problems that were not studied here. One of those is the impact resistance. This is particularly critical for the applications considered in this study. In fact, whether it is at the sea-surface or by 20 metres depth, marine propellers and tidal turbine blades are exposed to unidentified object impacts. These objects can be containers, wood parts, marine wildlife, rocks or other debris. The damage caused by such impacts on composite parts could initiate delamination, which was studied here, or can even lead to total failure. A follow-up thesis is focusing on this aspect. Another point that was not considered here is the erosion caused by cavitation. In fact, it was shown that composite blades tend to reduce the level of cavitation but do not remove it completely. The effect of cavitation erosion can be seen as a particularly well located impacted zone. It may also lead to delamination and requires further investigations.

Material

The second point that requires further attention is related to the material. The applications cited here were shown to have a positive impact on the pollution and greenhouse gases emission. However, thermosetting matrices and carbon fibres are not the most environmental friendly materials available. Thermoset polymers have the disadvantage of being non-recyclable while carbon fibres can be recycled but are then used as either short or long fibres but with fairly low mechanical properties for the latter. Therefore, it would be interesting to study the life cycle assessment of such systems. On the same subject, it would be interesting to investigate the possibility to replace the matrix with a recyclable polymer such as a thermoplastic or with bio-sourced resin and also to examine other options for reinforcement (self-reinforced composite, natural fibres...).

The role of the material is predominant for this kind of application. Many factors could affect the results of this study significantly. First, it would be interesting to investigate the effect of the composite composition in terms of fibre and resin ratios. It is a common rule to consider that the higher the fibre volume ratio, the better the mechanical resistance of the composite is. This is true to a certain level of fibre volume and for certain load cases. For highly-resin-dependent properties such as the interlaminar properties that were discussed in this study, it would be interesting to investigate the positive or negative effect of increasing fibre content. On the same subject, the effect of void content was not considered in detail here. It is known that voids and defects cause stress concentrations, and in the case of fatigue loading, they are preferential areas for micro-cracks to propagate. It would be interesting to look at the effect of voids on both the water ingress and the mechanical properties discussed in this study.

A second key aspect is the manufacturing route. When manufacturing such thick composite parts, the control of cross-linking and curing is often difficult. This can result in heterogeneous cross-linking throughout the composite thickness. This non-uniform microstructure can have a great influence on both the mechanical response and also the ageing behaviour of the composite parts. During this study, the influence of curing level on water uptake was investigated by comparing non cured, cured to the manufacturer's

Conclusion

requirement, and totally cured conditions. Results showed a tendency to saturate at higher levels of weight gain when the resin was not fully cured but additional investigations are needed to fully characterize this behaviour. Taking this effect into consideration along with the prediction of curing level on the blade's thickness will allow a more accurate prediction of the water ingress in the real propeller blade.

The manufacturing effect on the mechanical properties was briefly considered here. The infusion and the RTM processes were compared but there was a change in fibre surface weight between the two composites, which induced additional differences. A more meticulous study on the effect of the manufacturing process would be interesting. In addition to these two manufacturing processes, it would be interesting to include more advanced processes such as Automated Fibre Placement (AFP), 3D woven composites or powder epoxy composites as studied in [193, 194].

Ageing aspects

An important conclusion of this study is the part that physical ageing plays in the mechanical behaviour of composite materials, and especially on resin-dominated mechanical properties. For classical seawater ageing tests, physical ageing is not taken into account. However, it was shown that its effect cannot be neglected. This raises two questions:

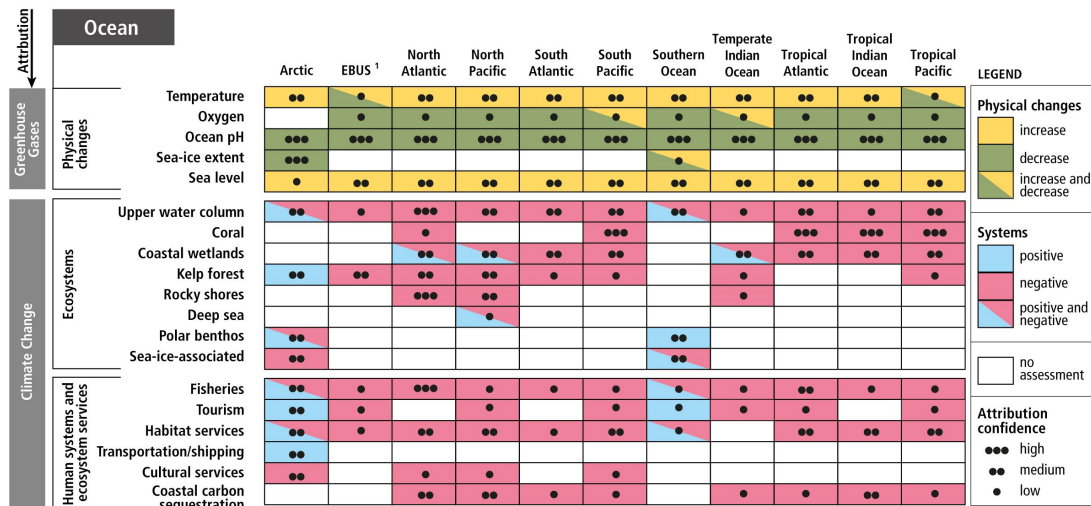
The first question is how representative are the accelerated ageing tests when investigating the effect of seawater. In fact, it is normally not recommended to perform seawater ageing tests at a temperature closer than 20 °C below the dry material's T_g. However, we saw that even at temperatures of 20 °C and more below the material's T_g, there was physical ageing occurring. When testing the composite materials at the different ageing conditions, we currently do not know what is the contribution of physical ageing to the response of the tested material.

Another question that can be raised is the level of physical ageing on the material on real structures. In fact, after being manufactured, the composite parts can be stored under different conditions. For example, when stored in containers, and the containers are exposed to the sun, the temperature inside could increase significantly and therefore induce physical ageing. One could argue that physical ageing has a positive influence on the resin behaviour as it increases the maximum stress. However, it was shown that on the composite it did not have such a positive influence mainly due to the more brittle behaviour generated. There is a need to quantify the "level" of physical ageing present in real structures. So, an interesting follow-up to this work would be to examine how to find a way to quantify, preferably in a non-destructive manner, the level of physical ageing in the material. A possibility would be to use acoustic emission as a more brittle material could have a different damping or a different speed of transmission of ultrasound. In the case of partially destructive analysis, calorimetry (DSC) might be a good candidate as it requires only a small amount of material and it is sensitive even to low levels of physical ageing.

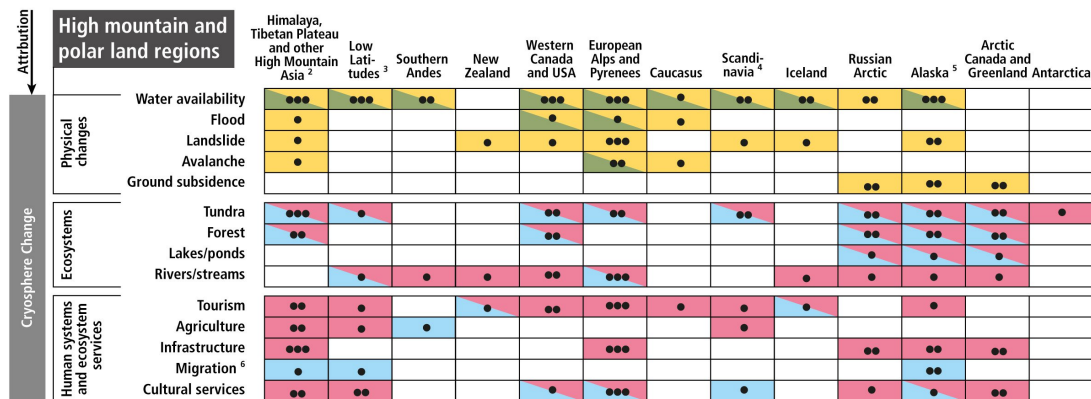
The present work has provided results in order to better design composite structure of which the final goal is to reduce global pollution. This will only work if these structures are reliable and durable.

At the time this thesis is finalized, a special report from the GIEC has been published [195]. This report points out the alarming effects of climate change on the ocean and cryosphere (see Figure 6.33). It is important for the scientific and engineering community to try to focus on projects that aims to act in a positive way for the climate and for government to support these projects.

Observed regional impacts from changes in the ocean and the cryosphere



¹ Eastern Boundary Upwelling Systems (Benguela Current, Canary Current, California Current, and Humboldt Current); [Box 5.3]



² including Hindu Kush, Karakoram, Hengduan Shan, and Tien Shan; ³ tropical Andes, Mexico, eastern Africa, and Indonesia;

⁴ includes Finland, Norway, and Sweden; ⁵ includes adjacent areas in Yukon Territory and British Columbia, Canada; ⁶ Migration refers to an increase or decrease in net migration, not to beneficial/adverse value.

Figure 6.33 – Summary of the observed changes due to global warming as reported by the 2019’s special GIEC report [195]

Extended French abstract

A.1 Introduction

L'impact de l'homme sur l'environnement n'est plus à démontrer. Un des indicateurs de ce changement est l'augmentation de la température aussi bien de l'air mais également de la mer. Cette augmentation de température s'est vue accélérée durant les dernières décennies, les gazes à effet de serre faisant entre autre parti des facteur jouant sur cette augmentation de température. Le CO_2 est l'un de ces gaz à effet de serre les plus connus de la communauté scientifique mais également de la population. Il existe une corrélation entre les quantités de CO_2 rejetées et l'augmentation de la température (Figure A.1). Dans ce contexte, de multiples travaux portent sur la réduction des émissions polluantes des systèmes actuels.

Parmi ces travaux, l'utilisation de matériaux composites pour fabriquer les hélices de navires est envisagée. Dans ces systèmes, les pales seraient fabriquées en matériaux composites à renforts fibres longues tels que les fibres de carbone. Les avantages sont multiples à commencer par la masse du système de propulsion qui pourrait se voir réduite de 50 %. Ceci est expliqué par le très bon rapport masse/propriété mécanique de ces matériaux composites. Un autre des avantages de ces hélices est la possibilité d'adapter le plan de drappage des fibres et ainsi obtenir des pales plus ou moins flexibles qui auraient une forme adaptée à la vitesse de rotation de l'hélice. Le couple de rotation requis pour faire tourner l'hélice et produire la poussée au bateau se verrait ainsi réduit, augmentant

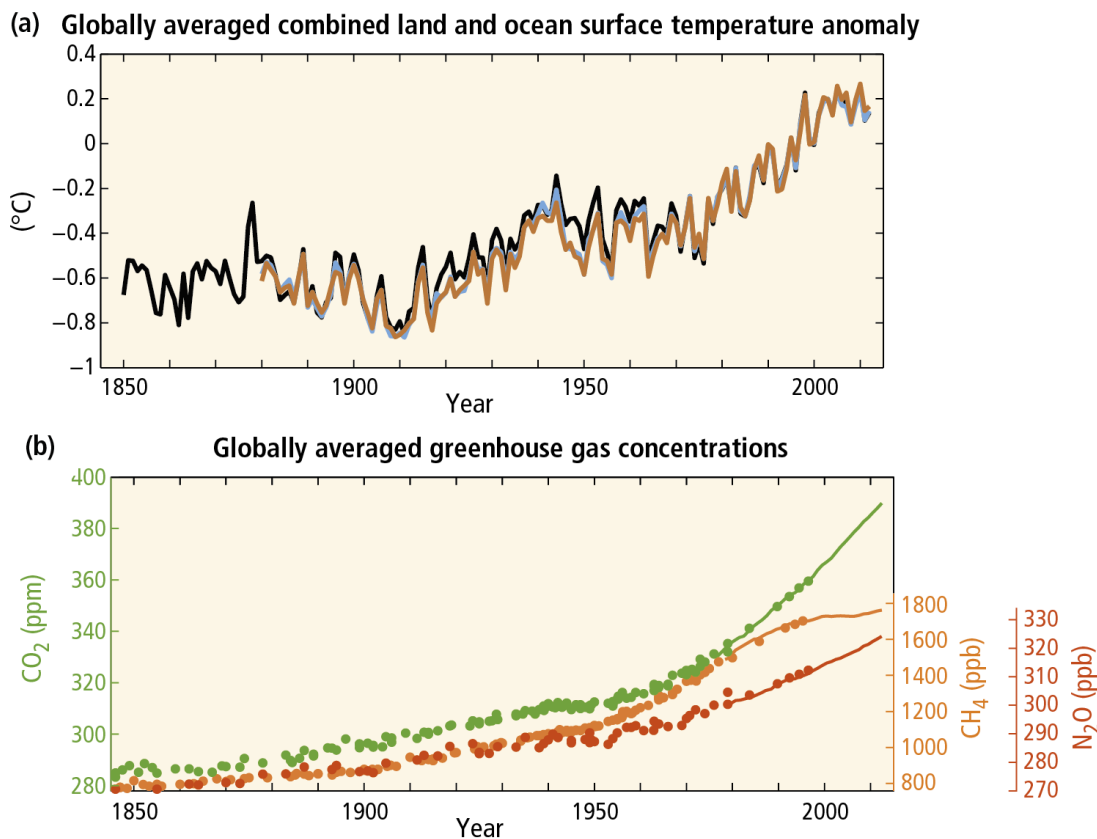


FIGURE A.1 – Emission de dioxyde de carbone [3]

le rendement de l'ensemble propulseur du navire et ainsi permettre la réduction de la consommation de ces navires. Des études expérimentales et numériques ont également investigué la possibilité de réduire la cavitation des pales, véritable fléau endommageant la surface des pales.

D'un autre côté, la production d'électricité grâce aux énergies renouvelables est également un sujet de recherche et développement important. Les principales sources d'énergies renouvelables actuelles sont l'éolien, le photovoltaïque et également l'énergie hydraulique issue des barrages. Cependant, de plus en plus de recherches portent aujourd'hui sur les énergies marines renouvelables (EMR) utilisant les énergies des marées, des courants, des vagues ou encore du potentiel thermique. Les hydroliennes sont parmi les prototypes les plus avancés dans ce domaine. Leur principe porte sur la conversion de l'énergie ciné-

tique des courants créés par les cycles des marées en énergie électrique en faisant tourner une génératrice. Différents systèmes existent pour faire tourner les génératrices, les hydroliennes à axe horizontal étant les plus répandues. Sur ces dernières, le rotor est animé par des pales du même principe que pour les éoliennes. L'utilisation de matériaux composites pour fabriquer les pales est souvent privilégiée bien qu'une partie des prototypes actuels utilisent des pales métalliques.

Ces deux systèmes utilisent des hélices multi-pales de diamètres allant du mètre à la dizaine de mètres. Leur fonctionnement se fait également en immersion en milieu marin. D'un point de vue matériaux, la question se pose donc quant à la tenue en fatigue de telles pièces composites soumises à des efforts importants, cycliques et prolongés.

L'objectif de cette étude est d'étudier le comportement à long terme des matériaux composites soumis à une charge cyclique en milieu marin. Cette étude s'est concentrée sur une résine époxy renforcée de fibres de carbone qui a été utilisée dans un projet parallèle, FabHeli, qui a pris fin en 2018. Le fait d'avoir cette application signifiait que les matériaux étaient des systèmes disponibles sur le marché. Par conséquent, la résine époxy et les fibres de carbone utilisées n'étaient pas des matériaux modèles. Le comportement de vieillissement à l'eau de mer de la résine pure et du composite a été étudié.

A.2 Prise en eau dans la résine et le composite

Tout d'abord, les cinétiques de diffusion de l'eau de mer dans la résine et dans le composite ont été caractérisées. Il a été montré que le comportement de diffusion dans la résine suivait une loi de Fick. Cependant, quelques déviations dues notamment à l'oxydation ont été observées aux températures les plus élevées utilisée lors des vieillissement accélérés en eau de mer (Figure A.3).

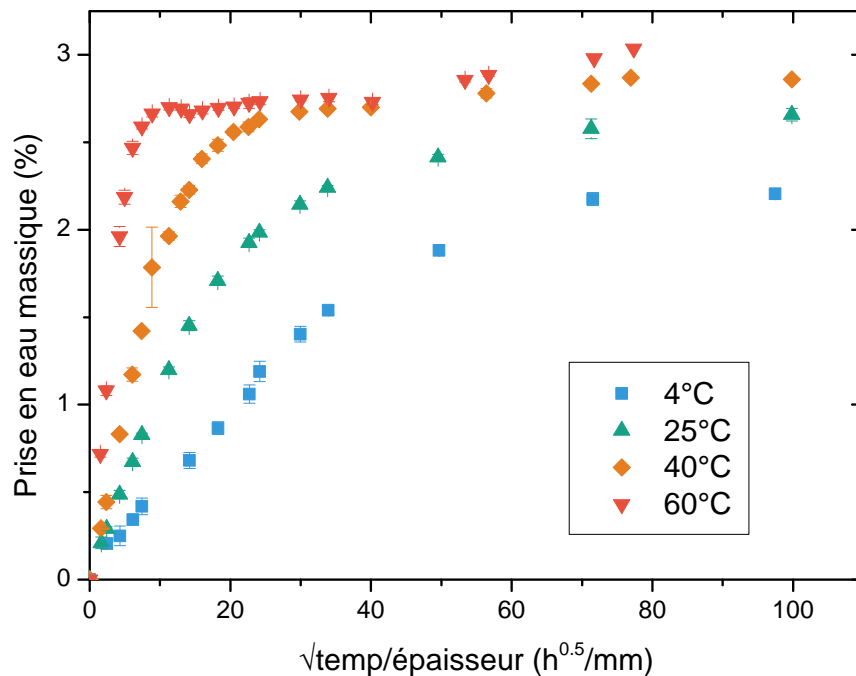


FIGURE A.2 – Prise en eau dans la résine à différentes températures

La diffusion dans le composite a également été identifiée comme suivant une loi de Fick, et les paramètres de diffusion du composite ont été prédits en connaissant ceux de la résine pure. Il a été montré que le coefficient de diffusion était correctement prédit par l'équation de Rayleigh. La prédiction de la masse à saturation du composite à partir de celle de la résine a montré que l'eau ne diffusait pas seulement dans la résine. Il a été proposé d'obtenir les valeurs de masses à saturation du composite à partir de celle de la

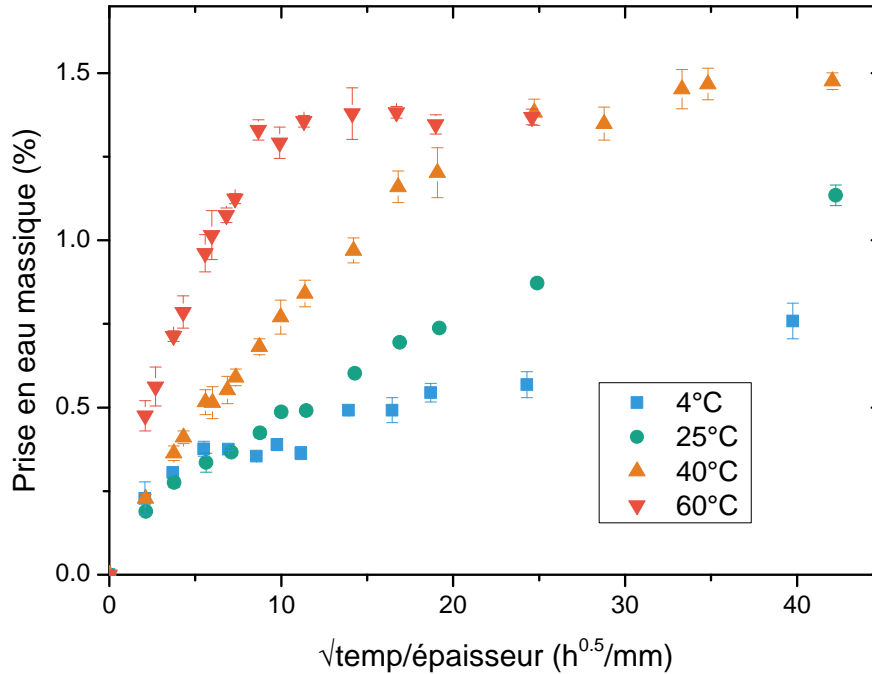


FIGURE A.3 – Prise en eau dans le composite à différentes températures

résine en considérant la diffusion de l'eau dans les micro-vides présents dans le composite. Il a été constaté que 25 % du volume de vide devait être pris en compte pour corrélérer l'absorption maximale d'eau dans les composites aux différentes températures.

L'absorption d'eau dans la pale d'hélice composite du projet FabHeli a été prédite sur la base d'une immersion dans l'eau de mer à 15 °C. La prédiction a montré qu'il faudrait plus de mille ans pour saturer complètement la pale de l'hélice. Cependant, comme montré dans la Figure A.5, après seulement un an, l'eau atteint le quatrième pli de composite en partant de l'extérieur.

Ce résultat est important car la valeur du temps de saturation de la pale entière ne reflète pas la quantité réelle d'eau dans les différentes couches de la pale après un ou cinq ans. Si cette précaution n'est pas respectée, une défaillance prématurée peut se produire dans les plis extérieurs des pales de l'hélice. De plus, les bords d'attaque et de fuite font partie des zones les plus minces des pales et ils sont très sensibles aux changements de

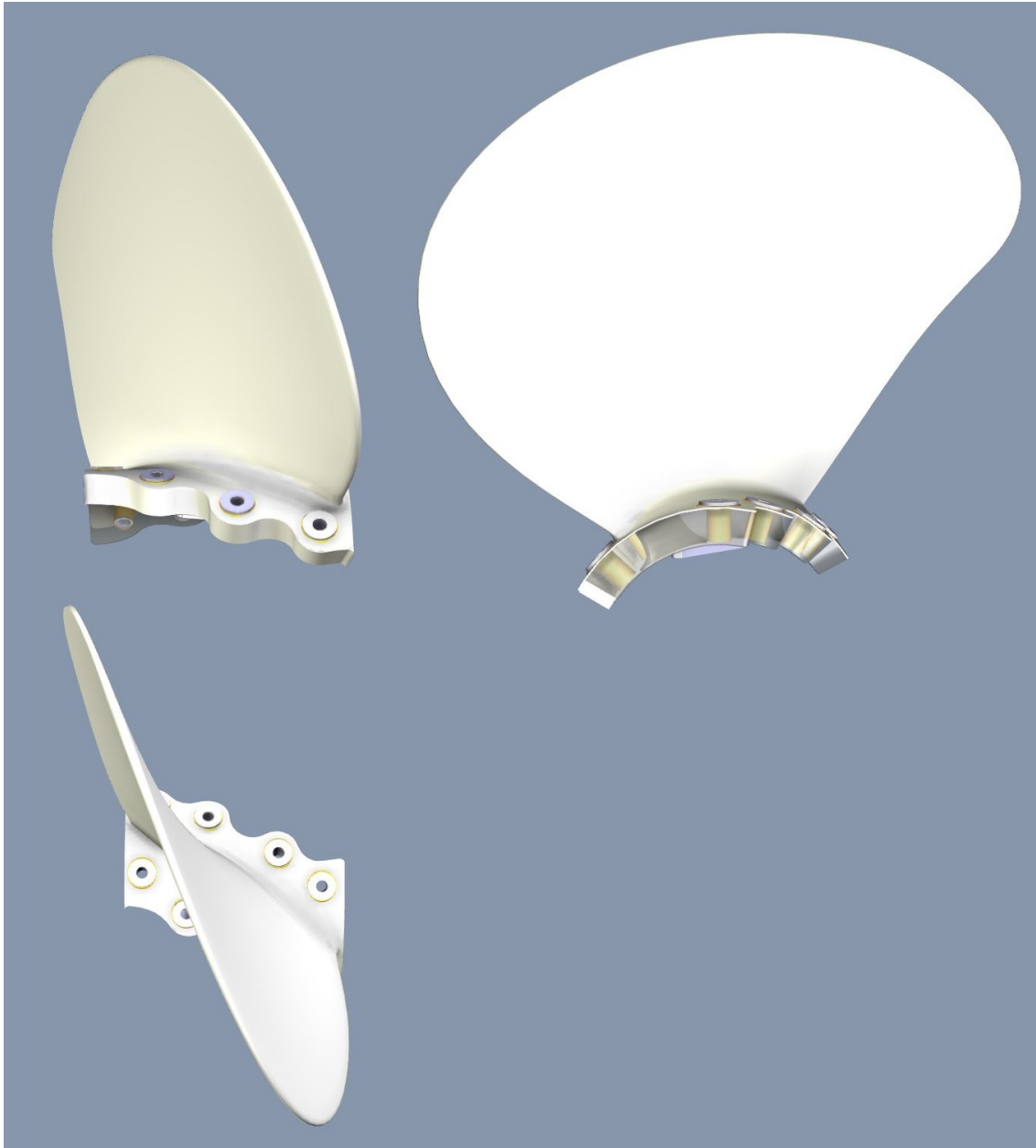


FIGURE A.4 – Vue en trois dimensions de la pale issue du projet FabHéli

réponse mécanique. Cela est d'autant plus vrai surtout si l'on considère les propriétés de vibration de l'hélice qui peuvent varier sensiblement. Pour cette raison, il est important de tenir compte du comportement mécanique du matériau à l'état saturé et prendre en compte ces possibles variations.

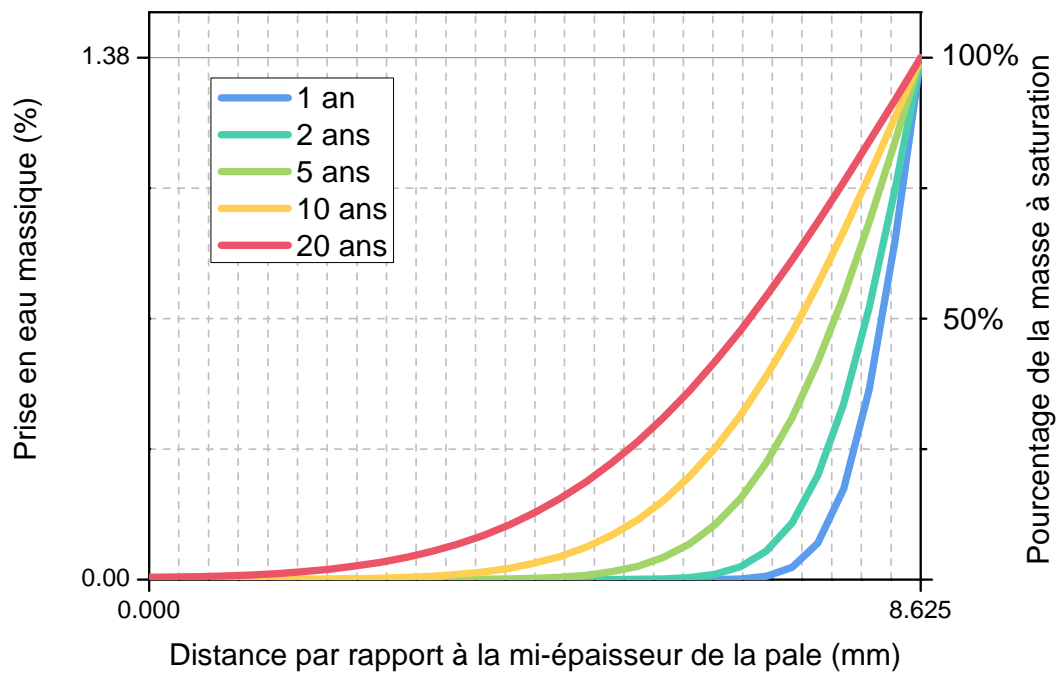


FIGURE A.5 – Répartition de la concentration d'eau dans une demi section de la pale FabHéli à différents temps

A.3 Plastification et vieillissement physique sur la résine pure

Le comportement mécanique de la résine pure exposée au vieillissement accéléré de l'eau de mer a été étudié. Il est apparu que deux phénomènes principaux se produisaient lors de ces vieillissements. Il s'agit de la plastification et du vieillissement physique.

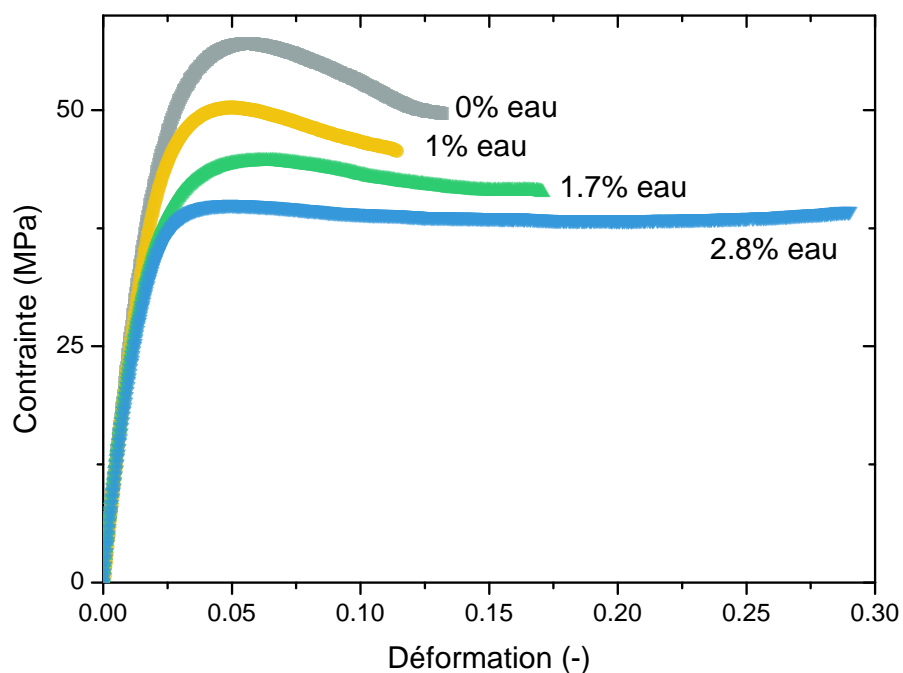


FIGURE A.6 – Effet de la plastification sur la réponse en traction sur la résine pure

La mise en évidence de la plastification s'est faite grâce à des prises en eau sur des éprouvettes de traction à différentes conditions d'humidité. En résulte des masses à saturation différentes en fonction de l'humidité de l'environnement de vieillissement. La quantité d'eau a été corrélée avec la diminution de la température de transition vitreuse (T_g). L'effet sur la réponse en traction de la résine est une diminution de la contrainte maximale, accompagnée d'une augmentation de l'allongement à la rupture (Figure A.6). La plastification de la résine par l'eau n'est pas un phénomène rare, il a été identifié précédemment

dans la littérature.

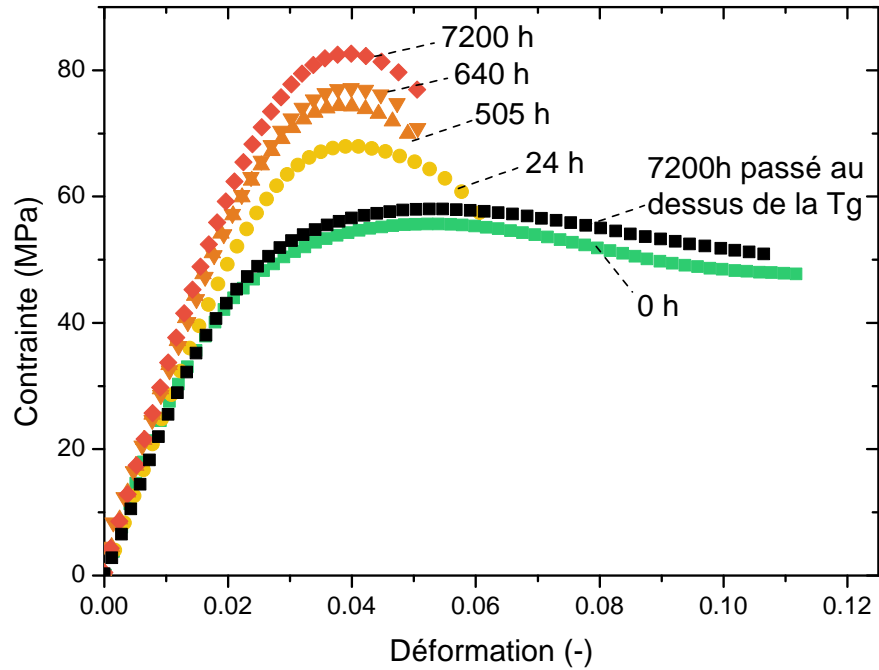


FIGURE A.7 – Effet du vieillissement physique sur la réponse en traction sur la résine pure

D'un autre côté, le phénomène de vieillissement physique était plus inattendu. Ce vieillissement a également été caractérisé par des essais de traction en plaçant les éprouvettes dans des sachets sous vide afin de limiter tout autre vieillissement susceptible d'entrer en jeu. L'effet sur les propriétés mécaniques est une augmentation de la contrainte maximale de traction ainsi qu'une réduction de l'allongement à la rupture. L'identification du vieillissement physique a été confirmé par le fait que les propriétés initiales étaient récupérées après exposition des éprouvettes à une température supérieure à la T_g (Figure A.7).

Le couplage entre vieillissement physique et plastification a finalement été étudié et il a été démontré que la présence d'eau, c'est-à-dire la plastification, accélère le vieillissement physique pour les températures proches de la T_g du matériau (Figure A.8). Ceci a été démontré en modélisant l'effet du vieillissement physique sur la contrainte de traction

maximale à différentes températures à l'aide d'une équation Kohlrausch Williams Watts (KWW).

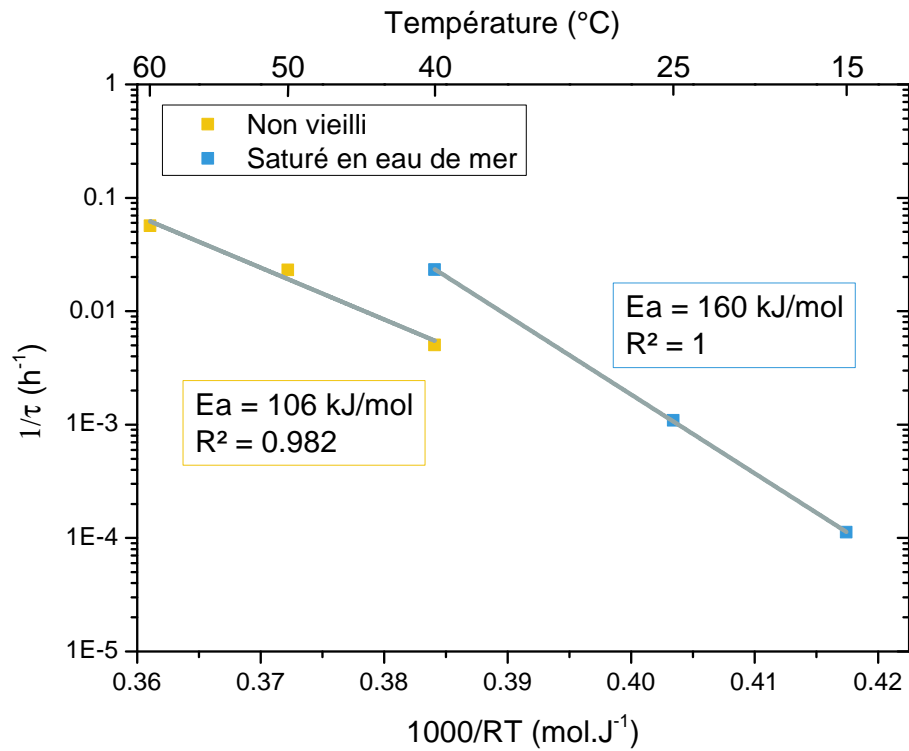


FIGURE A.8 – Courbe d'Arrhenius du temps de relaxation sur la résine pure

L'effet du vieillissement physique sur la réponse mécanique de l'époxy s'est révélé non négligeable. Il a ensuite été également étudié sur le composite sous cisaillement et sous tension transversale, avec un effet notable sur ce dernier.

A.4 Vieillissement à long terme du composite

L'effet du vieillissement à l'eau de mer sur le comportement quasi-statique et en fatigue du composite a ensuite été étudié en utilisant le même vieillissement accéléré que pour la résine pure. Les essais mécaniques effectués ont porté sur la traction, la flexion et le délaminage.

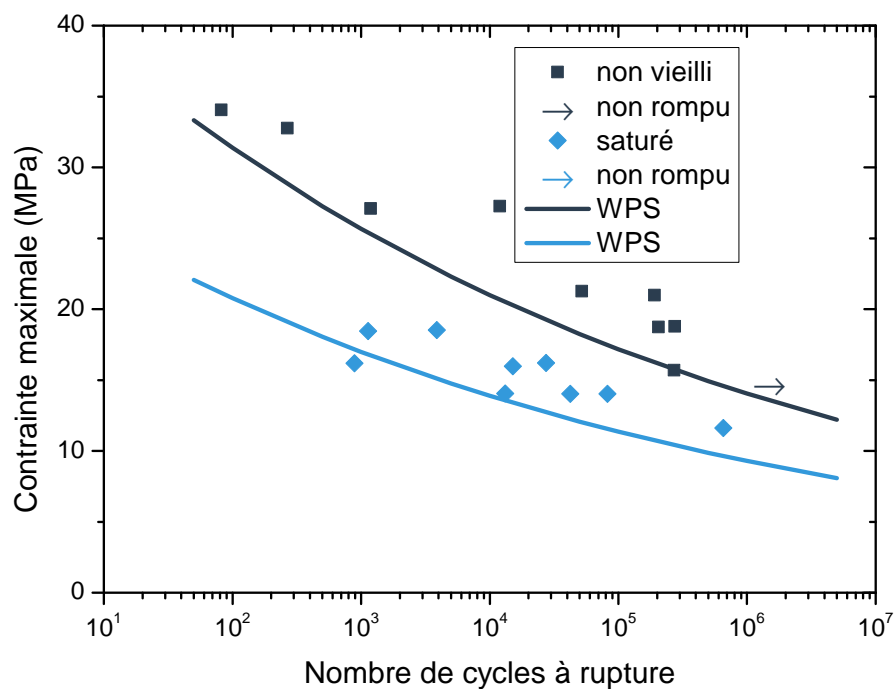


FIGURE A.9 – Courbe de fatigue de traction transverse, effet de l'eau

Dans le cas des charges de traction, le composite présentait une sensibilité limitée à l'eau de mer lorsqu'il était chargé dans le sens des fibres pour les composites unidirectionnels et les composites à plis croisés 0/90. Cela a été constaté tant sous chargement quasi-statique qu'en fatigue. D'autre part, l'influence de l'eau de mer sur la tension transversale a eu un effet significatif, diminuant la résistance à la traction finale de près de 50 % (Figure A.9). Les fibres de carbone ne sont pas sensibles à l'eau de mer ; elles n'absorbent pas l'eau. Cependant, la réponse aux charges perpendiculaires aux fibres dépend

fortement des propriétés de la matrice. Comme les propriétés mécaniques de la résine pure étaient dégradées par l'eau de mer, la dégradation des propriétés mécaniques sous traction transversale était prévue.

L'émission acoustique a montré que de l'endommagement se produit pendant toute la durée de vie en fatigue des éprouvettes unidirectionnelles et croisées, même si la perte de raideur semblait stable dans la phase intermédiaire de la durée de vie en fatigue.

Le composite à plis croisés a été testé sous flexion en quatre points. Cette fois, l'effet de l'eau de mer a été significatif. La courbe de fatigue s'est déplacée vers des durées de vie inférieures de 1 à 2 décades, ce qui montre un effet important de l'eau de mer. Lors de ces essais, une grande majorité des éprouvettes étaient rompues en délaminage. Par conséquent, l'influence du procédé de fabrication a été étudiée, la rupture en délaminage du composite RTM ayant été attribuée à une qualité de fabrication moindre.

Les procédés d'infusion et RTM ont ensuite été comparés en fatigue par flexion et, même si le composite infusé présentait de meilleures propriétés mécaniques, il n'était pas insensible à la présence d'eau de mer. De plus, le composite infusé a été séché après saturation et présentait un comportement à la fatigue similaire à celui du composite non vieilli. Cela suggère que le vieillissement est réversible par élimination de l'eau de mer et que le seul phénomène jouant un rôle dans ce cas est la plastification ; le vieillissement physique n'a pas montré d'effet. Cependant, pour confirmer ce postulat, des essais supplémentaires sont nécessaires.

La séquence d'endommagement en flexion quatre points a été étudiée, car la rupture par délaminage a été signalée même avec un composite infusé (Figure A.10). La plupart des échantillons fatigués présentaient également des dommages sous les points d'appuis. Il a été démontré que les points de charge jouent un rôle majeur dans la rupture finale, mais d'autres endommagements apparaissent tout au long de la durée de vie en fatigue au cœur des éprouvettes. C'est ce qu'a révélé l'analyse par tomographie des échantillons d'essai de fatigue interrompus.



FIGURE A.10 – Exemple de rupture par délaminage suite à un chargement de flexion 4 points en fatigue

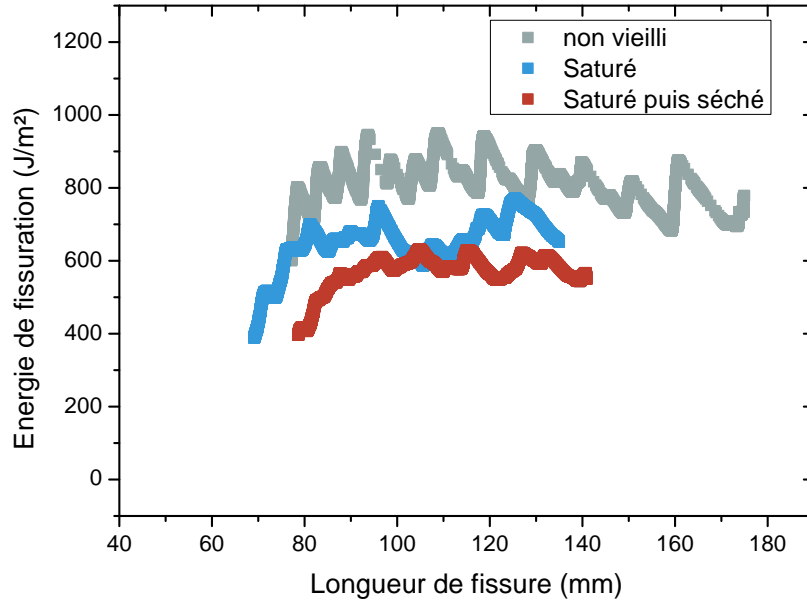
A.5 Composite sous chargement critique : délaminage

Le comportement de délamination a été étudié sous deux modes de charge différents : ouverture et cisaillement en plan (mode I et mode II).

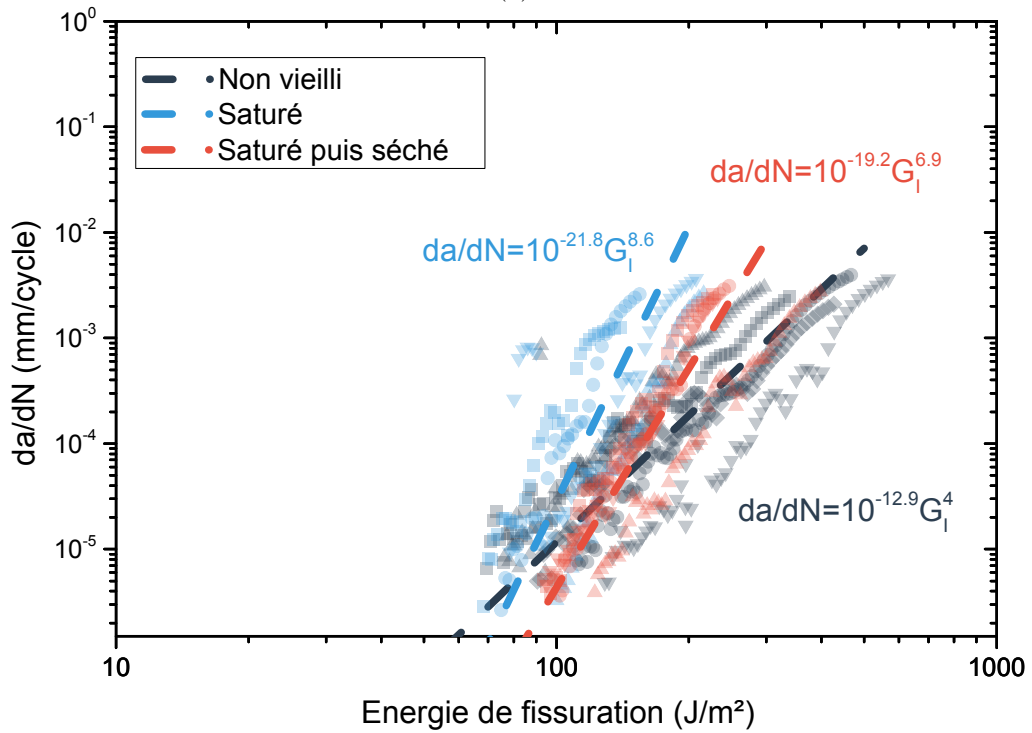
Il a été démontré que l'eau de mer diminue l'énergie de fissuration et la résistance à la fissuration par fatigue du composite dans les deux cas de charge. Cependant, l'élimination de l'eau du composite saturé a donné des résultats différents (Figures A.11 and A.12).

En mode I, la ténacité statique à la rupture a de nouveau diminué tandis que la résistance à la fissuration par fatigue a été partiellement récupérée après séchage. Dans le cas du mode II, la ténacité statique à la rupture a été partiellement retrouvée, tandis que la résistance à la fissuration par fatigue a été complètement retrouvée.

Ces résultats ne tiennent pas compte du vieillissement physique. L'effet du vieillissement physique sur ces deux modes de délaminage a donc ensuite été étudié et a donné des résultats qui pourraient expliquer la différence entre les résultats du vieillissement en eau de mer en mode I et en mode II. Une proposition conceptuelle a été faite afin d'expliquer l'effet du vieillissement physique sur la réponse de fatigue du mode II, car il a montré le comportement le moins intuitif.

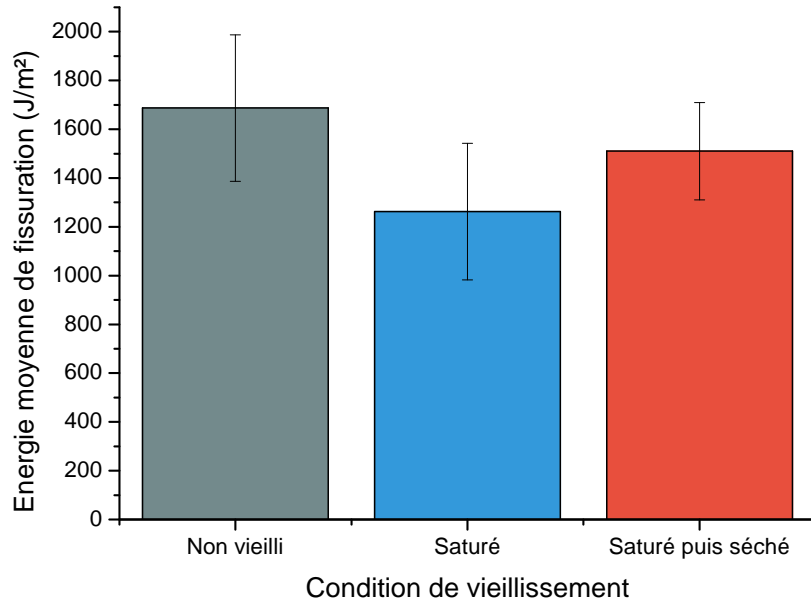


(a)

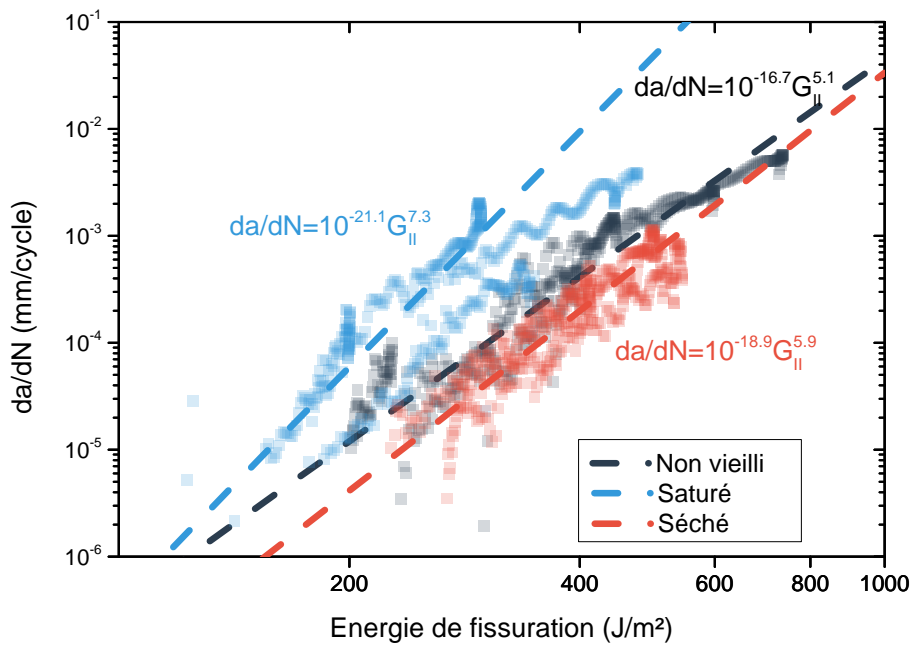


(b)

FIGURE A.11 – Effet de l'eau et du séchage sur la fissuration en mode I en quasi-statique (a) et en fatigue (b)



(a)



(b)

FIGURE A.12 – Effet de l'eau et du séchage sur la fissuration en mode II en quasi-statique (a) et en fatigue (b)

A.6 Perspectives

De nombreux aspects de la durabilité de l'époxy renforcé de fibres de carbone ont été examinés dans cette étude. Cependant, il reste des pistes qui doivent faire l'objet d'approfondissement. Ces aspects peuvent être divisés en trois domaines différents :

- Méthodes d'essais
- Matériaux
- Phénomènes de vieillissement

A.6.1 Méthodes et essais expérimentaux

Il y a des questions à approfondir en ce qui concerne les essais expérimentaux. Par exemple, le rapport de charge utilisé pour les essais de fatigue a été maintenu à 0,1, mais en réalité, les pales d'hélice et d'hydroliennes – et plus largement, les pièces composites – ne sont pas chargées sous un rapport de charge constant mais suivant une mixité variable selon différents facteurs. Un article récent de Koshima et al. a montré que l'effet du vieillissement de l'eau de mer était fortement dépendant du rapport de chargement [192]. Cela confirme l'intérêt d'une telle étude.

Dans le même registre, même pour les hélices de navires qui sont souvent conçues pour une vitesse de rotation particulière, la fréquence vue par les hélices réelles ne correspond pas seulement à celle pour laquelle elles ont été conçues. En effet, les manœuvres que le bateau doit effectuer, que ce soit pour l'amarrage, l'accélération pour atteindre la vitesse de croisière ou encore des manœuvres exceptionnelles d'évitement, impliquent toute une gamme de fréquences de chargement. Par conséquent, l'étude de l'effet de la vitesse/fréquence de la charge serait également un aspect important à considérer.

Un ensemble de résultats est présenté ici sur la résistance au délaminage du composite. Ces résultats ont montré que le test du mode II pose encore des problèmes expérimentaux. En effet, les résultats ont montré des anomalies attribuées au frottement induit par la méthode d'essai qui implique que les deux faces de délamination soient en contact l'une avec l'autre.

Une solution serait d'effectuer les essais sous flexion en mode mixte avec un composant de mode II élevé. Cela permettrait de caractériser le composite sous charge dominée par le mode II mais avec suffisamment de mode I pour éviter le frottement des faces l'une contre l'autre. Il serait ainsi intéressant d'examiner l'effet du vieillissement en eau de mer sous ces chargements en mode mixte. Un montage d'essai en mode mixte titane a été conçu et construit à la fin de cette étude, mais la mise en place de ce montage n'a pas eu le temps d'être faite. Ce support en titane permettrait d'effectuer des essais de fatigue immergés dans l'eau de mer, comme cela a été le cas pour la plupart des autres essais réalisés dans le cadre de cette étude.

Un autre aspect qui nécessite un intérêt supplémentaire est la caractéristique de la zone d'endommagement du front de fissure lors des essais de fissuration. Une analyse par tomographie d'éprouvettes fissurées permettrait la caractérisation de ce front de fissure qui apporterait certaines réponses soulevées dans cette étude.

Enfin, il y a des problèmes de durabilité qui n'ont pas été étudiés ici. L'un d'entre eux est la résistance à l'impact. Ceci est particulièrement important pour les applications considérées dans cette étude. En effet, que ce soit à la surface de la mer ou à une profondeur de 20 mètres, les hélices de navires ainsi que les pales d'hydroliennes sont exposées à des objets non identifiés. Ces objets peuvent être des conteneurs, des pièces de bois, des espèces marines, des roches ou d'autres débris. Les dommages causés par de tels impacts sur des pièces composites pourraient déclencher un délaminage, ou pourraient même conduire à une rupture totale des structures. Une nouvelle thèse démarrant au moment où celle-ci se termine se concentre notamment sur cet aspect important.

Un autre point qui n'a pas été abordé ici est l'érosion causée par la cavitation. En effet, il a été montré dans la littérature que les pales composites ont tendance à réduire le niveau de cavitation mais ne l'éliminent pas complètement pour autant. L'effet de l'érosion par cavitation peut être assimilé à une zone impactée de façon ponctuelle et répétée. Elle peut également entraîner du délaminage et nécessite donc d'être étudiée.

A.6.2 Matériaux

Le deuxième point qui nécessite une attention particulière est lié aux matériaux. Il a été démontré que les applications citées ici ont un impact positif sur la pollution et les émissions de gaz à effet de serre. Cependant, les matrices thermodurcissables et les fibres de carbone ne sont pas les matériaux les plus respectueux de l'environnement. Les polymères thermodurcissables ont l'inconvénient d'être non recyclables alors que les fibres de carbone peuvent être recyclées mais sont ensuite utilisées comme fibres courtes ou longues, avec généralement des propriétés mécaniques assez faibles. Il serait intéressant d'étudier l'analyse du cycle de vie de tels systèmes. Il serait également intéressant d'étudier la possibilité de remplacer la matrice par un polymère recyclable tel qu'un thermoplastique ou une résine bio-sourcée et d'examiner également d'autres options de renforcement (composite auto-renforcé, fibres naturelles...).

Le rôle du matériau est prédominant pour ce type de structures. De nombreux facteurs pourraient avoir une incidence importante sur les résultats de cette étude. Tout d'abord, il serait intéressant d'étudier l'effet de la composition du composite en termes de rapport fibre et résine. Il est d'usage de considérer que plus le rapport volumique des fibres est élevé, plus la résistance mécanique du composite est importante. Ceci est vrai jusqu'à un certain volume de fibres et pour certains cas de charge. Pour les propriétés fortement dépendantes de la résine, comme les propriétés interlaminaires dont il a été question dans cette étude, il serait intéressant d'étudier l'effet positif ou négatif d'une teneur accrue en fibres. Sur le même sujet, l'effet des porosités n'a pas été examiné en détail ici. On sait que les vides et les défauts provoquent des concentrations de contraintes et dans le cas des charges de fatigue ce sont des zones préférentielles pour la propagation des microfissures. Il serait intéressant d'examiner l'effet des vides à la fois sur la prise en eau mais également sur les propriétés mécaniques examinées dans cette étude.

Un deuxième aspect clé est le procédé de fabrication. Lors de la fabrication de pièces composites aussi épaisses, le contrôle de la réticulation et de la cuisson est souvent difficile notamment à cause des problèmes d'exothermie. Il peut en résulter une réticulation hétérogène sur l'épaisseur du composite. Cette microstructure non uniforme peut avoir une grande influence à la fois sur la réponse mécanique et sur le comportement au vieillissement

des pièces composites.

Au cours de cette étude, l'influence du niveau de durcissement sur l'absorption d'eau a été étudiée en comparant les conditions non cuit, cuit aux exigences du fabricant et totalement réticulé. Les résultats ont montré une tendance à saturer en eau à des niveaux plus élevés lorsque la résine n'était pas complètement durcie, mais des études supplémentaires sont nécessaires pour caractériser pleinement ce comportement. La prise en compte de cet effet ainsi que la prédiction du niveau de durcissement sur l'épaisseur de la pale permettra une prédiction plus précise de la prise en eau dans les pales d'hélice.

L'effet de la fabrication sur les propriétés mécaniques a été brièvement examiné ici. Les procédés d'infusion et RTM ont été comparés, mais il y a eu également un changement de grammage des fibres entre les deux composites, ce qui a induit une différence supplémentaire. Une étude plus méticuleuse sur l'effet du procédé de fabrication serait intéressante. En plus de ces deux procédés de fabrication, il serait intéressant d'inclure des procédés plus avancés tels que le Placement Automatisé des Fibres (AFP), les composites tissés 3D ou les composites époxy en poudre [193, 194].

A.6.3 Aspect vieillissement

Une conclusion importante de cette étude est le rôle que le vieillissement physique joue dans le comportement mécanique des matériaux composites, en particulier sur les propriétés mécaniques dominées par les résines. Pour les essais classiques de vieillissement en eau de mer, le vieillissement physique n'a pas été pris en compte. Toutefois, il a été démontré que son effet ne peut pas être négligé. Cela soulève deux questions :

La première question est de savoir dans quelle mesure les essais de vieillissement accéléré sont représentatifs de l'état réel du matériau à long terme. En fait, il n'est normalement pas recommandé d'effectuer des essais de vieillissement à une température de vieillissement plus proche que 20 °C de la Tg du matériau sec. Cependant, nous avons constaté que même à des températures de 20 °C et plus, il y avait un vieillissement physique. Lorsque nous testons les matériaux composites dans les différentes conditions de vieillissement, nous ne savons pas actuellement quelle est la part du vieillissement physique dans la réponse finale du matériau testé.

Une autre question que l'on peut se poser est celle du degré de vieillissement physique du matériau sur des structures réelles. En effet, après fabrication, les pièces composites peuvent être stockées dans des conditions différentes. Par exemple, les pièces peuvent être entreposées dans des conteneurs qui peuvent être exposés au soleil, la température à l'intérieur pourrait ainsi augmenter et provoquer un vieillissement physique.

On pourrait dire que le vieillissement physique a une influence positive sur le comportement de la résine car il augmente la contrainte maximale. Toutefois, il a été démontré que sur le composite, il n'a pas eu une telle influence positive, principalement en raison du comportement plus cassant.

Il est nécessaire de quantifier le "niveau" de vieillissement physique présent dans les structures réelles. Ainsi, une des perspectives de ces travaux serait de trouver une méthode permettant de quantifier, de préférence de manière non destructive, le niveau de vieillissement physique d'un matériau, si tant est qu'il y soit sujet. Une possibilité serait d'utiliser l'émission acoustique, car un matériau plus cassant pourrait avoir un amortissement différent ou une vitesse de transmission des ultrasons différente. Dans le cas d'une analyse partiellement destructive, la DSC pourrait être un bon candidat car elle ne nécessite qu'une petite quantité de matériau et, dans cette étude, elle s'est avérée sensible même à de faibles niveaux de vieillissement physique.

Appendix B

Identification procedures using scilab code

Fick's diffusion

You have first to create a 'Classeur.xls' file in the working directory. This xls file has to follow the architecture shown in Figure B.1. When Scilab reads the data from the xls file, it reads the columns until there is no more data in the column. There is a known issue with this code. If the scilab code is run with 24 values for example (as in the figure) and then the code is run with a new dataset of only 20 values (less than the previous dataset) it is required to delete the cells not by using the backspace or delete keyboard key but using right click>delete...>Delete, shift cells up.

```
1 //-----LEAST SQUARE
2 //-----Function to be fitted
3 function [a]=FICK(DM, e , x)
4     tmp=0;
5
6     for j=0:200
7         A= 8/((((2*j)+1)^2)*%pi^2);
8         B = exp(-((2*j+1)^2)*(%pi^2)*DM(1)*x/(4*(e^2)));
9         tmp=tmp+(A*B)
10    end
11    a=(1-tmp)*DM(2);
12 endfunction
13 //-----Comparing function
14 function er=myfun(DM, wm, e , ym, xm)
15     er = wm.*( FICK(DM,e , xm) - ym )
16 endfunction
17 //-----Function to plot Fick
18 function [a, b]=Trace_FICK(D, Minf, e)
19     t=((%pi/16)*(((e)^2)/D))*4; //estimated time to
20     saturation
21     tsat=t;
```

	A	B	C	D
1	Time (in h)	Mass uptake in %	thickness in mm	
2	0.0	0	1.15	
3	3.4	0.293876151		
4	7.5	0.443063878		
5	23.9333333	0.830984143		
6	48.6	1.172317836		
7	72.3	1.420488183		
8	103.3	1.785675649		
9	167.466667	1.963750163		
10	221.0	2.162431561		
11	264.1	2.227586382		
12	336.4	2.405478424		
13	438.25	2.483313432		
14	551.7	2.559660161		
15	672.8	2.588177243		
16	768.3	2.631301888		
17	1176.3	2.675817654		
18	1511.88333	2.691733136		
19	2112.8	2.699516365		
20	4204.1	2.780836382		
21	6725.65	2.835348302		
22	7825.23333	2.868931107		
23	13175.8833	2.85933602		
24	16036.6	2.864133564		
25				
26				
27				
28				

Figure B.1 – Architecture to be followed for the Classeur.xls file

```

21     j=int((tsat/3600)/24);
22     t=((tsat/3600)/24)-j;
23     h=int(tsat*24);
24     t=(tsat*24)-h;
25     m=int(tsat*60);
26     t=(t*60)-m;
27     s=int(tsat*60);
28     mprintf('Time to saturation is \n%i days , %i hours , %i
           minutes , %i secondes ' , j , h , m , s)
29     x=(0:t/20:t*50);
30     y=x;
31     DM=[D; Minf];
32     for i=1:length(x)
33         y(i)=FICK(DM,e,x(i));
34     end
35     a=(x^0.5)/e;
36     b=y;
37     plot(a,b,'r')

```

```

38 endfunction
39 //-----Main function
40 function a=fick(varargin)
41     timer();
42     clf();// clear the figure window
43
44     //-----Read of the experimental
         values in xls file .
45     [fd,SST,Sheetnames,Sheetpos] = xls_open('Classeur.xls');
46     [Value,TextInd] = xls_read(fd,Sheetpos(1));
47     mclose(fd);
48     //-----Variables declaration
49     xm=Value(2:$,1)*3600;           //---time in seconds
50     ym=Value(2:$,2);               //---mass uptake
51     e=Value(2,3)/1000;             //---thickness in meters
52     m = length(xm);
53     wm = ones(m,1);
54     //-----You can either call fick in the
         console without
55     //suggesting D and M value or you can guess this value by
         calling fick(D,M)
56     //using numerical values for D and M. D has to be guessed in
         10-13m2/s) and
57     //M in %
58     if argn(2) then
59         DM=[varargin(1)*10-13,varargin(2)];
60     else
61         DM=[10D-14;2.8];           //default values if not guessed
         when calling fick
62     end
63     disp(DM,'valeurs de dm');//to see in the shell what
         starting values are used
64     //-----
65     [f,xopt, gopt] = leastsq(list(myfun,wm,e,ym,xm),DM)
66     disp(f,xopt,'D and M values found')
67
68     [s,t]=Trace_FICK(xopt(1),xopt(2),e)//plotting the calculated
         fick curve
69     xm=(xm0.5)/e;
70     plot(xm,ym,'d')//plotting the experimental values
71     res=[s',t'];
72     EXP=[xm,ym];
73     //-----data export time in s0.5 /m
         and M in %
74     write_csv(res,'Fickmodel.csv',' ',' ',' ');

```

```

75     write_csv(EXP, 'experimental.csv', ',',' ','');
76     a=1
77     disp(timer(), 'computer_time_to_correlate_(s)')
78 endfunction

```

Kolrausch Williams Watts

An xls file has to be created in the working directory, the cells from column A are time in hours, and B are the maximal stress values in MPa.

```

1 // the KWW equation
2 function y=yth(t,x)
3     y = 42+(24)*(1-exp(-(t/x(3))^(1/3))) //42 is the initial
4         stress and 24 the stress increase
5     //It is possible to let Scilab determine all the values of
6         the equation this way:
7     //y = x(1)+(x(2))*(1-exp(-(t/x(3))^(x(4))))
8 endfunction
9
10 [fd,SST,Sheetnames,Sheetpos] = xls_open('val.xls');
11 [Value,TextInd] = xls_read(fd,Sheetpos(1));
12 mclose(fd);
13 //experimental variables
14 tm=Value(1:$,1);
15 ym=Value(1:$,2);
16 m = length(ym);
17 wm = ones(m,1);
18 // initial parameters guess
19 //x0=[S0, deltaSy, tau, beta]
20 x0 = [42; 24; 10; 0.33];
21 function e=myfun(x, tm, ym, wm)
22     e = wm.*(yth(tm, x) - ym)
23 endfunction
24
25 // we provide the Jacobian
26 function g=mydfun(x, tm, ym, wm)
27     a = wm.*1
28     b = wm.*exp(-(tm./x(3))^x(4))
29     c = wm.*(((x(2).*x(4).*exp(-(tm./x(3))^x(4)).*tm.*((tm./x(3))
30         )^(x(4)-1))))./(x(3)^2))
31     d = wm.*(-x(2).*exp(-(tm./x(3))^x(4)).*((tm./x(3))^(x(4))).*
32         log(tm./x(3)))
33     g = [a,b,c,d]
34 endfunction
35
36

```

```

32 //bound constraints in the order :[S0, deltaSy, tau, beta]
33 xinf = [1,0,0.1,0.1];
34 xsup = [100,100000,100000,1];
35
36 // without the Jacobian:
37 [f,xopt, gopt] = leastsq(list(myfun,tm,ym,wm),"b",xinf,xsup,x0)
38 disp(xopt,f)
39
40 // with the Jacobian :
41 //[f2,xopt2, gopt2] = leastsq(list(myfun,tm,ym,wm),mydfun,"b",
    xinf,xsup,x0)
42
43 clf()
44 tt = linspace(0,1.1*max(tm),500)';
45 yy = yth(tt, xopt);
46 //yyy = yth(tt, xopt2); //with the Jacobian
47 plot(tm, ym, "kx")
48 plot(tt, yy, "b-")
49 //plot(tt, yyy, "r-") //with the Jacobian

```

Whitney's Pooling Scheme

The following code gives the value of α and N_0 for a certain dataset. It is necessary to fit $\log(\sigma_i)$ versus $\log(N_0)$ (N_0 is given by the following scilab code) in order to obtain the values of σ_0 and $\frac{1}{k}$ as explained in chapter 1.

```

1 clear()
2 //One bracket correspond to one load level. In the bracket, the
    cycles to break of the correspond specimens need to be
    separated by a space as shown below
3 //Nij=list([N1_1 N1_2 N1_3],[N2_1 N2_2 N2_3],[...]);
4 //then press F5
5 Nij=list([15 31 110],[316 1050 1258],[7943 10000 5011],[100000 8
    9999 94999]);
6
7 //initial function
8 function a=A(x,m,i,Nb)
9     somme0=0
10    somme1=0
11    for(j=1:m)
12        somme0=somme0+((Nb(i)(j))^x * log(Nb(i)(j)));
13    end
14    for(j=1:m)
15        somme1=somme1+((Nb(i)(j))^x);
16    end

```

```

17     a=somme0/somme1
18 endfunction
19 //-----
    equation 3.13
20 function alpha=findalpha(a,m,i,Nb)
21     somme0=0;
22
23     for(j=1:m)
24         somme0=somme0+(log(Nb(i)(j)))
25     end
26     B=(1/m)*somme0;
27     C=1/a;
28     alpha=A(a,m,i,Nb)-B-C;
29 endfunction
30 //-----
    equation 3.14
31 function ni=findni(a,m,i,Nb)
32     somme0=0;
33     for(j=1:m)
34         somme0=somme0+(Nb(i)(j)^a)
35     end
36     ni=((1/m)*somme0)^(1/a)
37 endfunction
38
39 //final function
40 function a=Af(x,Nb)
41     somme0=0
42     somme1=0
43     for(i=1:length(Nb))
44         for(j=1:length(Nb(i)))
45             somme0=somme0+((Nb(i)(j))^x * log(Nb(i)(j)));
46         end
47     end
48     for(i=1:length(Nb))
49         for(j=1:length(Nb(i)))
50             somme1=somme1+((Nb(i)(j))^x);
51             nbep=nbep+1
52         end
53     end
54     a=somme0/somme1
55 endfunction
56 //-----
    equation 3.18
57 function alphaf=findalphaf(a,Nb)
58     somme0=0;

```

```

59     nbep=0;
60     for ( i=1:length(Nb) )
61         for ( j=1:length(Nb(i)) )
62             somme0=somme0+(log(Nb(i)(j)));
63             nbep=nbep+1;
64         end
65     end
66     B=(1/nbep)*somme0;
67     C=1/a;
68     alphaf=Af(a,Nb)-B-C;
69 endfunction
70 //-----
71     equation 3.19
72 function Q0=findQ0(a,Nb)
73     somme0=0;
74     nbep=0
75     for ( i=1:length(Nb) )
76         for ( j=1:length(Nb(i)) )
77             somme0=somme0+(Nb(i)(j)^a);
78             nbep=nbep+1;
79         end
80     end
81     Q0=((1/nbep)*somme0)^(1/a)
82 endfunction
83
84
85 m=0;
86 for ( i=1:length(Nij) )
87     m(i)=length(Nij(i));
88 end
89 a=0
90 //equation 3.13
91 for ( i=1:length(Nij) )
92     a(i)=fsolve(0.5,list(findalpha,m(i),i,Nij));
93 end
94 disp(a)
95 //equation 3.14
96 for ( i=1:length(Nij) )
97     n(i)=findni(a(i),m(i),i,Nij);
98 end
99 disp(n)
100 //equation 3.16
101 Qij=Nij;
102 for ( i=1:length(Nij) )

```

```

103     for (j=1:length(Nij(i)))
104         Qij(i)(j)=(Nij(i)(j))/n(i);
105     end
106 end
107
108
109
110 af=fsolve(0.1,list(findalphaf,Qij))
111 disp(af,'premier_af')
112
113 Q0=findQ0(af,Qij);
114 disp(Q0,'premier_Q0')
115
116 for (i=1:length(Nij))
117     n0(i)=Q0*n(i);
118 end
119 Qij=Nij;
120 for (i=1:length(Nij))
121     for (j=1:length(Nij(i)))
122         Qij(i)(j)=(Nij(i)(j))/n0(i);
123     end
124 end
125
126 af2=fsolve(0.1,list(findalphaf,Qij))
127
128
129 Q0=findQ0(af,Qij);
130 disp(Q0,'final_Q0')
131 disp(af2,'final_af')
132 disp(n0,'Values_of_N0')

```


Appendix C

Data processing using R

Tomographic classification

```
#empty memory
rm(list=ls())

#change of working directory
setwd("C:/Users/set your working directory here")
library(cluster)
library(fpc)
library("RColorBrewer") #for great colors

data<-read.csv(file="file.csv", header=TRUE, sep=";", dec=".")
#import parameters depend on your data to be opened

#centrering scaling
data.cr <- scale(data)

##### K-means #####

##Determination of appropriate number of clusters
##inertia
##This is a convergence study, the optimal number of clusters
##correspond to number at wich inertia does not increase significantly
inertie.expl <- rep(0,times=10)
for(k in 1:10){
  clus <-kmeans(data.cr ,centers=k, nstart=50,iter.max=20)
  inertie.expl[k] <- clus$betweenss/clus$totss
}
plot(1:10,inertie.expl,type="b",xlab="NB of clusters",
     ylab="% inertia explained")
```

```

##Calinski Harabasz criterion : the highest point correspond to the
##optimal number of clusters
sol.kmeans <- kmeansruns(data.cr , krange=1:20, criterion="ch")
plot(1:20, sol.kmeans$crit, type="b", xlab="NB of clusters",
     ylab="Calinski Harabasz score")

groupes.kmeans <- kmeans(data.cr , centers=4, nstart=50, iter.max=20)
print(groupes.kmeans)
clusplot(data.cr, groupes.kmeans$cluster, color = T, shade = T,
         labels = 2, lines = 0)

#statistics on clusters
stat.comp <- function(x,y){
  K <- length(unique(y))
  n <- length(x)
  m <- mean(x)
  TSS <- sum((x-m)^2)
  nk <- table(y)
  mk <- tapply(x,y,mean)
  BSS <- sum(nk * (mk - m)^2)
  result <- c(mk, 100.0*BSS/TSS)
  names(result) <- c(paste("G", 1:K), "% epl.")
  return(result)
}

print(sapply(data, stat.comp, y=groupes.kmeans$cluster))

acp <- princomp(data.cr , cor=T, scores=T)
plot(1:length(acp$sdev^2), acp$sdev^2, type="b")
biplot(acp, cex=1)

plot(acp$scores[,1], acp$scores[,2], col=brewer.pal(n=9,
name="Set1")[groupes.kmeans$cluster==4], xlim=c(-5,5), ylim=c(-5,5))

text(acp$scores[,1],
     acp$scores[,2],
     col=brewer.pal(n=9, name="Set1")[groupes.kmeans$cluster],
     cex=0.5,
     xlim=c(-5,5),
     ylim=c(-5,5))

library(wesanderson) #for colours
blanc <- rgb(1,1,1, alpha=0)

```

```

#plot of all the data as function of all parameters
pairs(data ,
      col=brewer.pal(n=12,name='Set3 ')[groupes.kmeans$cluster] ,
      diag.panel=panel.hist ,
      lower.panel=NULL)

#one can plot the clusters in the desired dimension as
plot(data[,1] ,
      data[,2] ,
      col=brewer.pal(n=12,name='Set3 ')[groupes.kmeans$cluster] ,
      cex=1.5,pch=19)

#it is also possible to export the data with the corresponding cluster
exp<-data.frame(C=groupes.kmeans$cluster , data)
write.table(exp , file="export.csv" , dec=".")

```

data processing of crack measurement

In this study, the data acquired was obtained via csv export from an acquisition system. It exported two lines per seconds, one for the maximum signal values and one for the minimum signal values. The reader is encouraged to modify this code to suit its need. For the DCB processing, the required data are:

- a0
- ap
- b
- h
- tps (which is the number of cycles but obtain with the measuring time in this case)
- Fmax
- Fmin
- dmax
- dmin

In the case of ELS data processing, the value of free length is required in addition to the previously cite data.

It is only necessary to have ap, af, b, h, L and

DCB

```

a0<-70 #initial crack length
ap<-73 #pre-crack length
af<-105 #final crack length
b<-21.535 #specimen width
h<-3.244 #specimen thickness

##file import
setwd("working directory")
data<-read.csv("file.csv", header=TRUE, sep=";", dec=".")

##variable attribution, here the data is cut in half : min and max values
tps <- 2*data[seq(1,length(data[,1]),2),1]
Fmax <- data[seq(2,length(data[,1]),2),2]
Fmin <- data[seq(1,length(data[,1]),2),2]
Dmax <- data[seq(2,length(data[,1]),2),3]
Dmin <- data[seq(1,length(data[,1]),2),3]

#this is to erase noise from the data
smousseFmin <- smooth.spline(tps,Fmin)
smousseFmax <- smooth.spline(tps,Fmax)
smousseDmin <- smooth.spline(tps,Dmin)
smousseDmax <- smooth.spline(tps,Dmax)

Fmins <- smousseFmin$y
Fmaxs <- smousseFmax$y
tps <- smousseFmax$x
Dmins <- smousseDmin$y
Dmaxs <- smousseDmax$y

#Compliance:
C <- (Dmaxs-Dmins)/(Fmaxs-Fmins)

#crack length calculation
Cp <- C[3]
Cf <- C[length(C)-1]
xi <- c(log10(ap), log10(af))
yi <- c(log10(Cp), log10(Cf))
res <- lm(yi~xi)
n <- as.numeric(res$coef[2])
d <- as.numeric(res$coef[1])
if(n>=3){print("attention danger n est superieur a 3")}
a<-10^((log10(C)-d)/n)
smoussea=smooth.spline(tps,a)

#calculation og the energy release rate at each cycle

```

```

g<-1000*(n*Fmax*Dmax)/(2*b*a)

#here, the data is refined after 50 cycles in order not to have 1M lines
exp<-data.frame(N=smoussea$x,A=smoussea$y,G=g,F=Fmax,D=Dmax)
EXP<-subset(exp,exp$N%%50==0)
write.table(exp[1:24,], file="export.csv",dec=".")
write.table(EXP, file="exportrefined.csv",dec=".")

ELS

a0<-60 #Crack length prior to pre-crack
ap<-74 #Crack length after pre-crack
af<-96 #final crack length
b<-20.48 #width
h<-3.24
L<-145

##_____file reading
setwd(working directory)
data<-read.csv("file.csv", header=TRUE, sep=";", dec=".")

##_____variable attribution

tps <- 2*data[seq(1,length(data[,1]),2),1]
Fmax <- data[seq(2,length(data[,1]),2),2]
Fmin <- data[seq(1,length(data[,1]),2),2]
Dmax <- data[seq(2,length(data[,1]),2),3]
Dmin <- data[seq(1,length(data[,1]),2),3]

#this is to erase noise from the data
smousseFmin <- smooth.spline(tps,Fmin)
smousseFmax <- smooth.spline(tps,Fmax)
smousseDmin <- smooth.spline(tps,Dmin)
smousseDmax <- smooth.spline(tps,Dmax)
Fmins <- smousseFmin$y
Fmaxs <- smousseFmax$y
tpss <- smousseFmax$x
Dmins <- smousseDmin$y
Dmaxs <- smousseDmax$y

#compliance:
C <- (Dmax-Dmin)/(Fmax-Fmin)

#calculation of E and delta

C0<-mean(C[1:5])

```

```

len<-length(C)
Cf<-mean(C[(len-5):len])
##E=100000
E=(3*((af^3)-(ap^3)))/(2*b*h*h*h*(Cf-C0))
delta=((2*b*(h^3)*E*Cf)-(3*(af^3)))^(1/3)-L

#calculation of the effective crack length
ae=((1/3)*((2*b*(h^3)*E*C)-((delta+L)^3)))^(1/3)
smoussea=smooth.spline(tps,ae)

#calculation of the energy release rate
g<-1000*(9*Fmax^2*ae^2)/(4*b^2*h^3*E)

#here, the data is refined after 50 cycles in order not to have 1M lines
exp<-data.frame(N=smoussea$x,A=smoussea$y,G=g,F=Fmax,D=Dmax)
EXP<-subset(exp,exp$N%%50==0)
write.table(exp[1:24,], file="export.csv",dec=".")
write.table(EXP, file="exportrefined.csv",dec=".")
plot(g,ae)

```

Appendix D

Water uptake of the infused composite

The infused composite was manufactured with different stacking sequences. In particular, there was $[0/90/0]$ and $[0/90/0]_s$ with thicknesses of respectively 1.8 and 3.3 mm. This allows performing water uptakes on different thicknesses as was done with the pure resin but not with the RTM composite.

The resulting water uptakes showed, as with the RTM composite, a Fickian diffusion of seawater with slight deviations. The Figures D.1 to D.4 show the water uptake from 4 to 60 °C with the Fick model. For the 4 and 25 °C conditions, the mass to saturation was fixed at 1.2 % as these conditions did not reach the plateau even for the 1 mm thick samples.

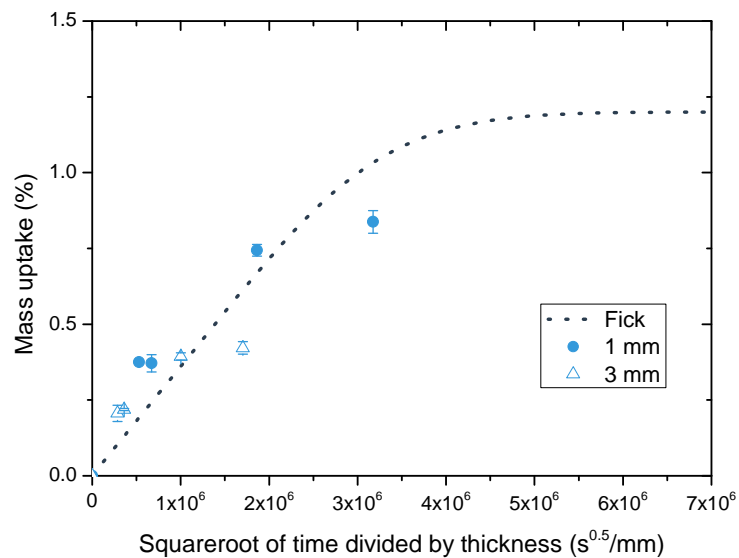


Figure D.1 – Water uptake of the infused composite at 4 °C

The mass to saturation found at 60 °C for the infused composite is $M_\infty \approx 1.2\%$. This

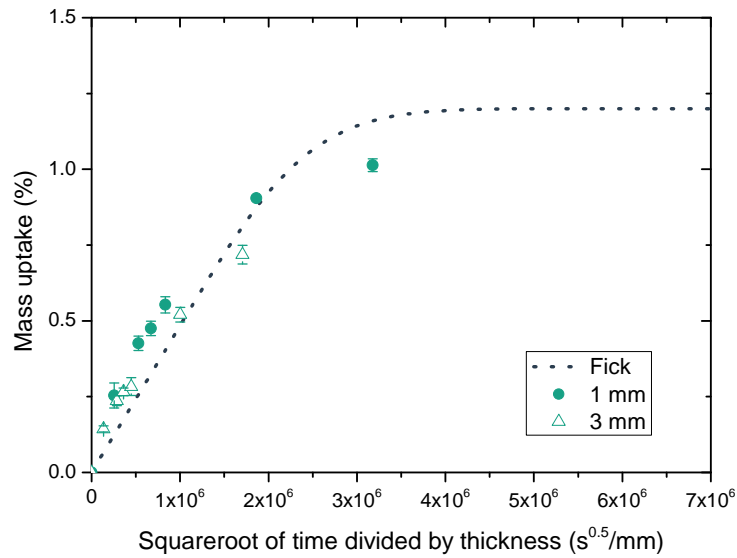


Figure D.2 – Water uptake of the infused composite at 25 °C

value is slightly lower than that of the RTM composite. This is due to the higher fibre volume ratio of the infused composite. The prediction of the mass to saturation of the composite with the value of the resin and taking a void volume ratio of 1.04 % into account will require 60 % of these void' volumes to be filled with water which is much more than that of the RTM composite.

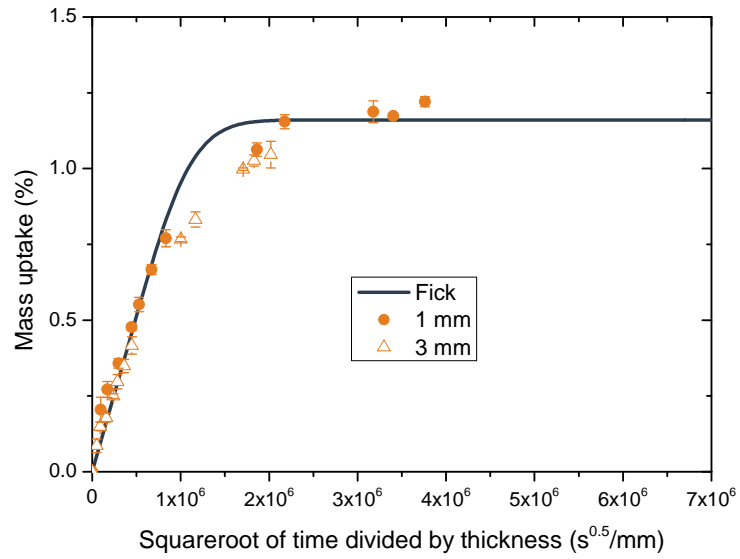


Figure D.3 – Water uptake of the infused composite at 40 °C

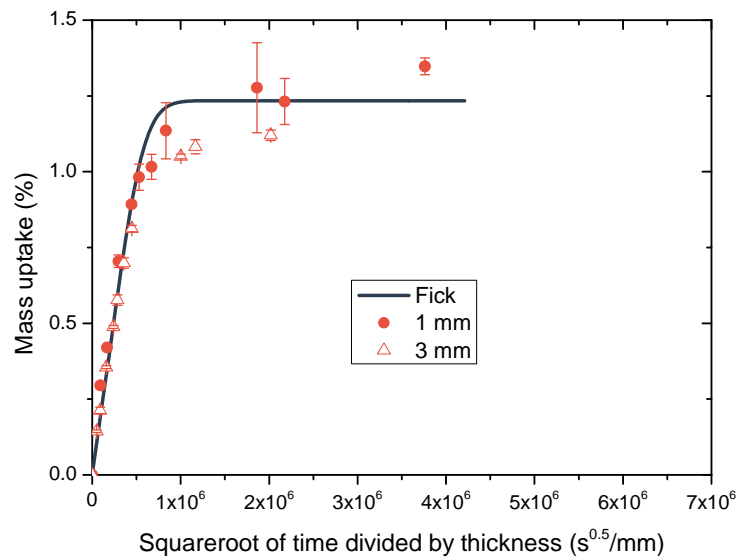


Figure D.4 – Water uptake of the infused composite at 60 °C

Appendix E

Crack gauges

The measurement of crack length during fatigue tests has been one of the difficulties of this study. There are different techniques that can be used. One option that has been investigated was to use crack gauges. This has the great advantage of giving a measured crack length at every cycle of the fatigue test. It was also expected to give better measurements of the crack length for the ELS quasi-static and fatigue tests as crack front is poorly distinguishable visually.

Two different gauge techniques were investigated in this study. The first one was set up by an intern student. The gauge consisted of a small ladder fabricated by 3D printing using electrical-conduction PLA (PolyLactic Acid). This ladder was bonded to the sample's edge. Then, the electrical resistance of the ladder was measured and as the crack length increases, the ladder steps break and crack length is correlated to the gauge resistance afterwards.



Figure E.1 – Crack gauge from Teksym™

The second gauge system investigated was a commercialised system from Teksym™ (see the gauge in Figure E.1). The principle is close to that of the gauge developed by this intern student. The main difference being that this gauge consists of a metallic foil instead of a plastic ladder. The advantage over the previous gauge is a continuous measurement of the resistance.

The electrical principle of this latter gauge is shown in Figure E.2. On this figure, the crack is represented in green. The resistance of R_6 and R_4 change as crack length increase. The sum from R_2 to R_8 is measured and converted to a 0-10V signal that can be read by an external acquisition system (see this system in Figure E.3).

There are multiple facts that pushed this study not to use the gauge system. The use of crack gauges raised some experimental difficulties for example. The metallic foil can debond from the thin plastic sheet that it is place on. This debond can happen during the bonding of the gauge on the specimen or also when welding cables to the gauge, heat

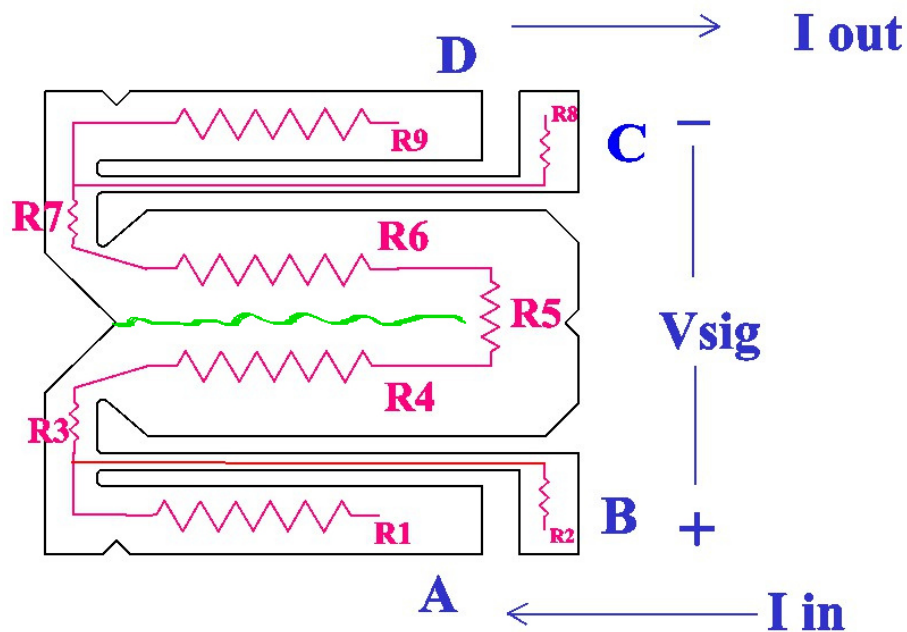


Figure E.2 – Schematic representation of the crack gauge principle ©Teksym



Figure E.3 – Gauge system with three specimens.

promoting this debonding. In addition, part of the fatigue tests was performed immersed in water and trials performed by Teksym™ showed some deviations on the measured crack length when it is immersed.

The validity of crack measurement on the edge can also be questioned. In fact, it

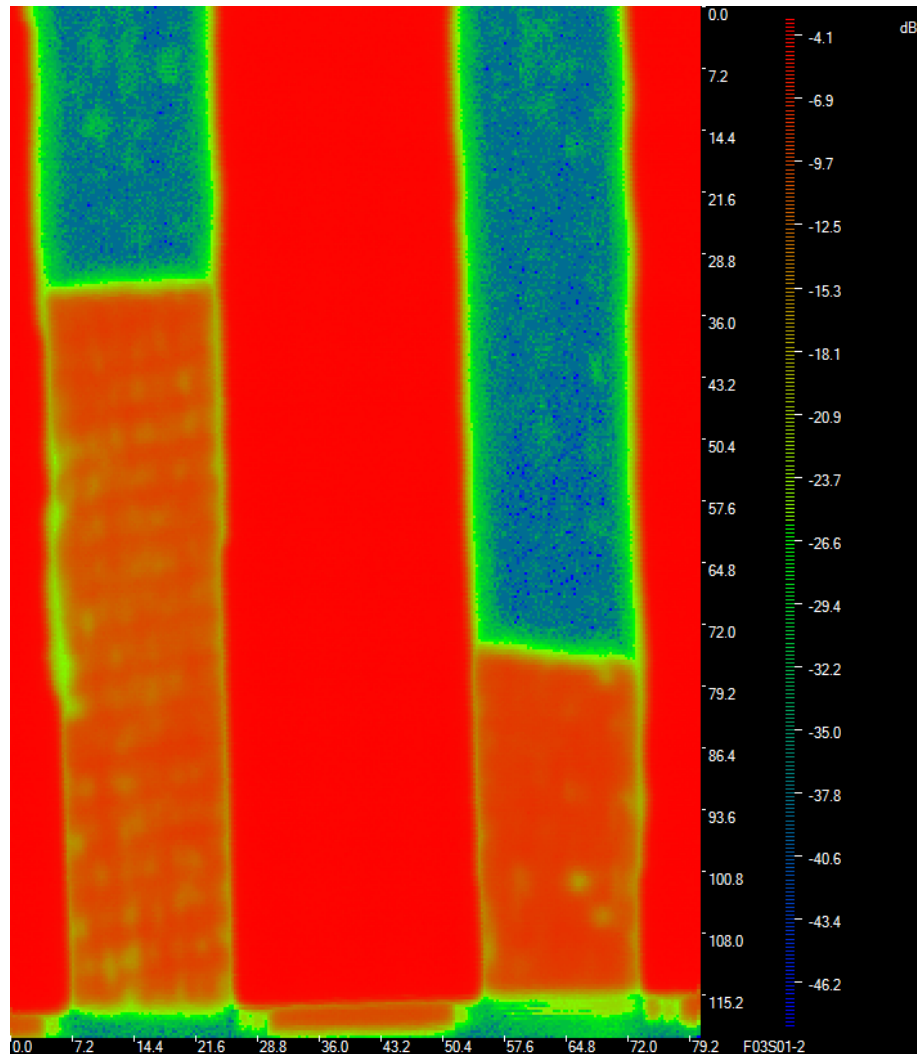


Figure E.4 – C-scan of crack front after fatigue test DCB on the left and ELS on the right, crack gauge was bonded on the left hand side of the specimens with regard to this scan, crack propagates from top to bottom

is well known that the crack front is not straight with regard to the specimen's width. In fact, many studies have shown that the crack front is longer at the mid-width of the specimen, resulting in a circular arc shape. However, this corresponds to a quasi-static crack front. The crack front of two specimens tested under mode I and mode II fatigue was inspected during this study by C-scan analysis. As shown in Figure E.4 there was no noticeable rounding of the crack front for both modes. One can see however, on the same picture that the crack front of the ELS specimen has a small angle to it.

This was seen for other ELS specimens tested with a gauge bonded to the specimen's edge with even higher angling of the crack front as shown in Figure E.5. It is believed that the addition of the crack resistance of the gauge, combined with that of the superglue used to bond the gauge, added resistance to the specimen's edge and therefore and increasing

the crack resistance on the edge where the gauge was bonded to. Unfortunately, the crack front from DCB specimens cannot be distinguished from the fracture surface but as shown by the C-scan, it did not show an angle.

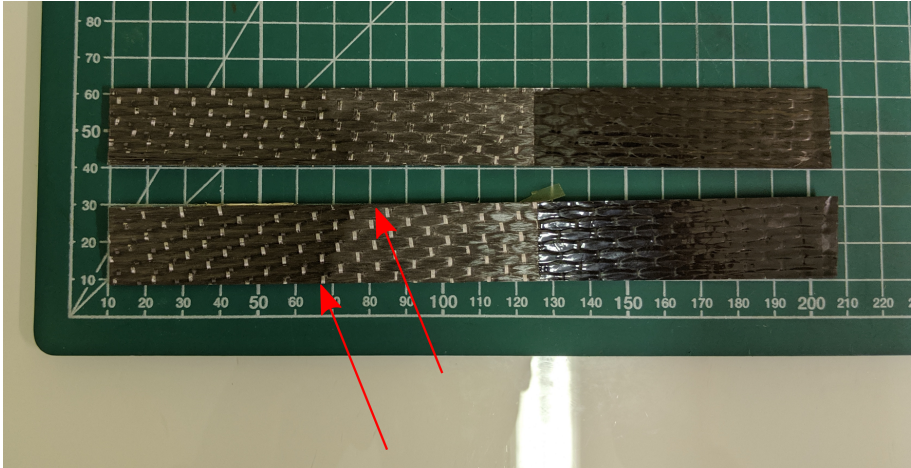


Figure E.5 – Fracture surface of a fatigued els specimen, red arrows point at the crack front delimitation

The determination of the crack length in this study was made thanks to the compliance, the entire methodology being explained in Chapter 2. It was possible to compare the value of crack length that can be calculated using the compliance and the one measured by the crack gauge. Figures E.6 and E.7 show the trend of the measured crack length versus the compliance during a mode I and a mode II fatigue test. The main purpose of this comparison is to show that the crack measured crack length is proportional to the compliance. It means that the value given by calculation can be used with a relatively good confidence.

The conclusion of these experiments was that the use of crack gauges for DCB fatigue tests can be an option to instrument these tests. However, the crack length measurement during ELS tests was found to induce bias on the results of the fatigue tests. The calculation of crack length using the compliance gives relevant values that can be used with fairly good confidence. For these aforementioned arguments, the use of compliance to determine crack length was adopted in this study.

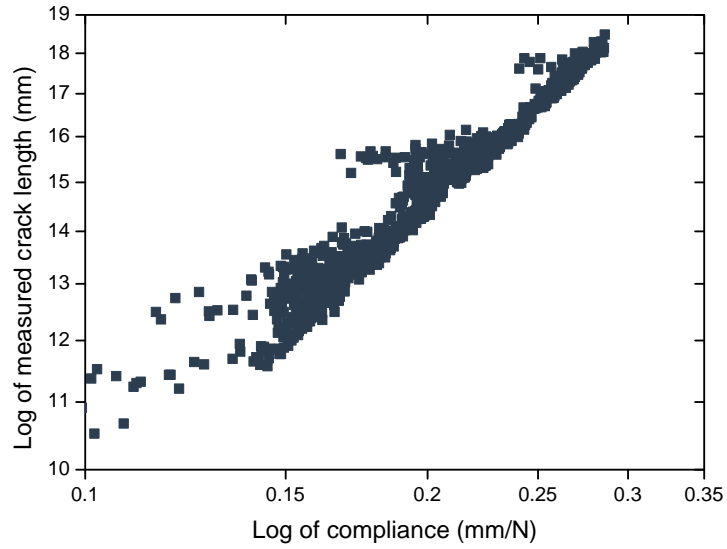


Figure E.6 – Crack length measured by the gauge as a function of specimen’s compliance during ELS fatigue test

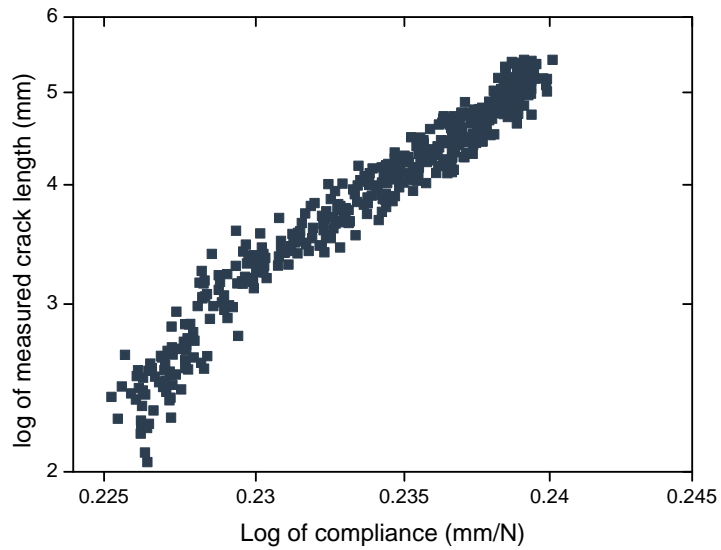


Figure E.7 – Crack length measured by the gauge as a function of specimen’s compliance during DCB fatigue test

Appendix **F**

Schematic drawings of the immersed fatigue fixtures

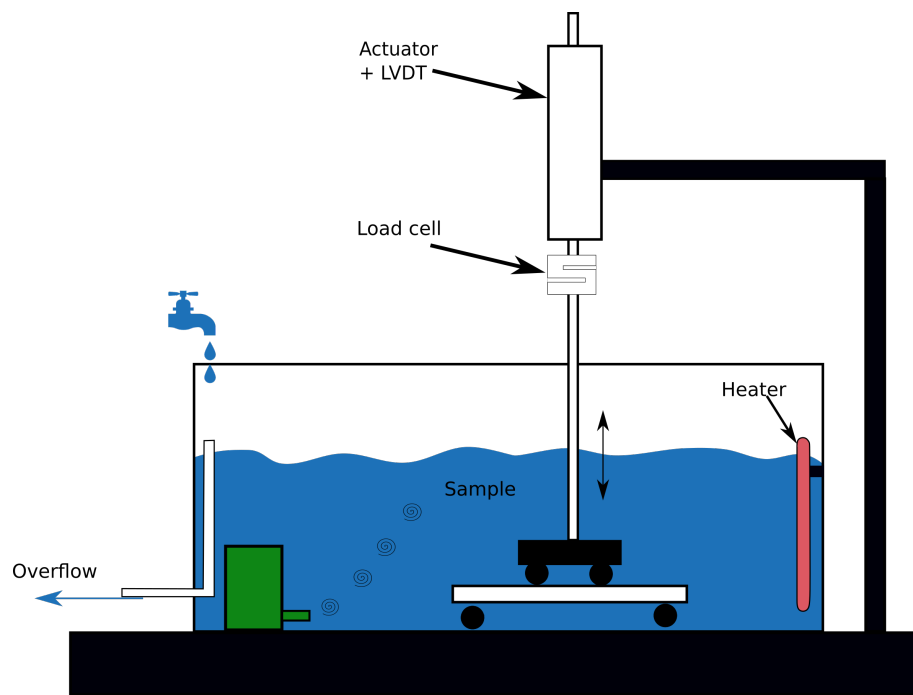


Figure F.1 – Drawing of the seawater immersed four point flexure fatigue fixture

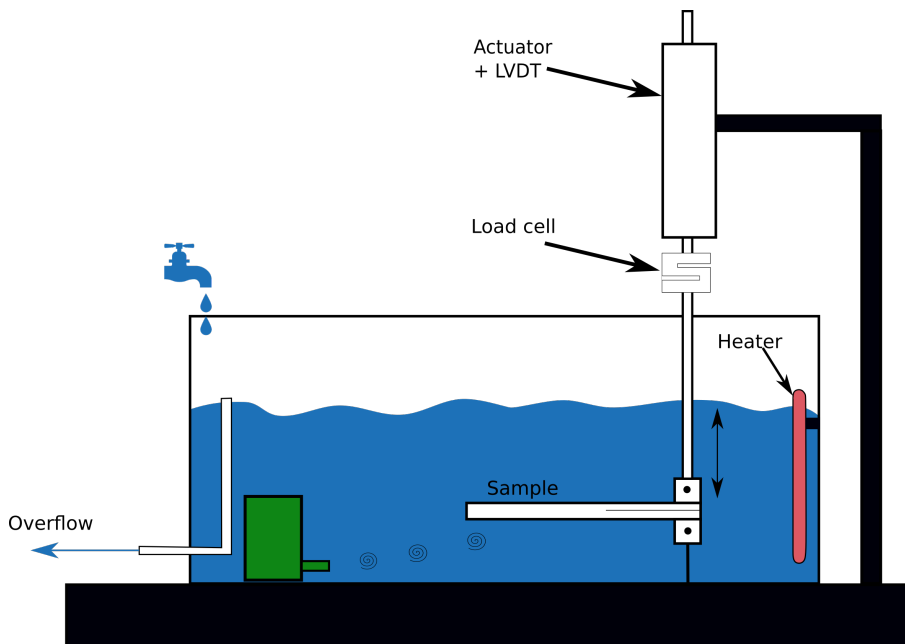


Figure F.2 – Drawing of the seawater immersed double cantilever beam fatigue fixture

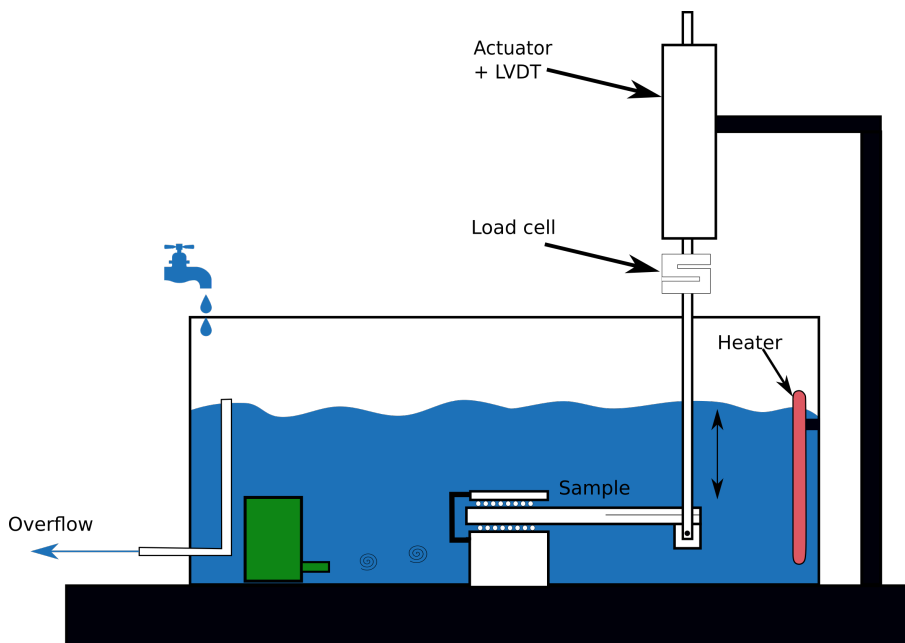


Figure F.3 – Drawing of the seawater immersed edge loaded split fatigue fixture

List of Figures

1	Global mean temperature anomaly in 1980, 1990, 2010 and 2018. Reference temperature is taken from 1951 to 1980 [1,2]	1
2	Increase of global temperature (a) and greenhouse gas concentrations (b) [3]	2
3	Francis Pettit Smith first (left) and amended (right) patent for the first marine screw propeller, taken from [4]	3
4	The different materials used to fabricate marine propellers from [5]	4
5	Example of tip and surface cavitation from [6]	5
6	FabHeli composite propeller blade [20]	6
7	Sabella D10 tidal turbine (picture from Sabella)	7
1.1	Gwalaz 7 meters multi-hull integrating flax fibres composite hulls, example of an impact on the structure, ©Ifremer	10
1.2	Reaction of amine curing agent with four epoxide groups [42]	11
1.3	Different manufacturing process of composite materials (a) wet-layup, (b) infusion, (c) Resin Transfer Moulding (RTM)	12
1.4	SEM micrographs of debonded carbon fibres dry (A) and exposed to 80°C water for 6 hours (B) [64]	15
1.5	Tg overshoot and endothermic peak as illustrated by [82]	16
1.6	$\pm 45^\circ$ tensile strength of a cfrp prepreg composite as a function of ageing time at 140°C [83]	18
1.7	Representation and correspondence of the different load ratios from [95]	19
1.8	Damage leading to fatigue failure of composite materials from [105]	20
1.9	Effect of 30 months at 30°C in seawater on a Quasi-isotropic glass/epoxy composite from [111]	20
1.10	Effect of seawater on CFRP composite under four-point flexure loading [25]	21
1.11	Damage accumulation theory with comparison of residual strength and stiffness trends [90]	22
1.12	Typical S-N curve and linear fit	22
1.13	Illustration of the Weibull survival probability on S-N data	23
1.14	Weibull distribution of normalized data	23
1.15	Result of the WPS approach	24
1.16	Illustration of the three modes of delamination	25
1.17	Design of the Double Cantilever Beam standard test	25

1.18	Typical delamination curve according to Paris relation	26
1.19	The different test methods for mode II delamination measurement [120] . . .	28
1.20	Comparison of data reduction methods according to round robin from [140]	28
1.21	Illustration of the document	30
2.1	Mould for pure resin	32
2.2	Effect of level of curing on water uptake of the pure resin in seawater at 40 °C	34
2.3	Charlyrobot® CNC machine	34
2.4	600 g/m ² carbon fibre fabric with off-axis glass fibre weaving	35
2.5	Measured composition of RTM composite plates	36
2.6	Measured composition of the infused composite plates	36
2.7	Temperature-controlled seawater ageing baths	38
2.8	Vacuum bagged resin tensile samples	39
2.9	Immersed fatigue four point bending test	40
2.10	Pure resin tensile specimen's dimensions	40
2.11	Example of random pattern on composite (a) pure resin (b)	41
2.12	Acoustic emission system on a composite fatigue tensile test	41
2.13	Crack length measurement by visual analysis regular (a) and negative (b) image	42
2.14	DCB immersed in water fatigue fixture	43
2.15	Water immersed C-ELS fatigue fixture	44
2.16	Example of a DCB-100 crack gage from Teksym®	45
2.17	Example ELS specimen being loaded showing the difficulty to measure the crack length precisely	45
2.18	X-ray tomography machine from CRT of Morlaix	48
2.19	Illustration of k-means clustering on a simple set of data [149]	48
2.20	Optimisation of the number of clusters with inertia criterion (a) and Calin- ski Harabasz criterion (b)	49
2.21	Illustration of the CH criterion: low value (a) high value (b)	50
3.1	Water uptake of pure resin; 1 mm thick coupons. (error bars are shown for all conditions)	52
3.2	Water uptake of pure resin at 40 °C in seawater	52
3.3	Coupons of 3 mm in thickness aged in seawater for up to 660 days at 60, 40, 25 and 4 °C (from left to right)	53
3.4	Arrhenius plot of diffusion coefficient for the pure resin in seawater	54
3.5	Arrhenius plot of the solubility for the pure resin in seawater	55
3.6	Water uptake on the pure resin at different relative humidities	55
3.7	Water uptake of RTM composite immersed in seawater	56
3.8	Water uptake of RTM composite in seawater at 40 °C	57
3.9	Arrhenius plot of diffusion coefficient for the RTM composite	57
3.10	Arrhenius plot of solubility of RTM composite in seawater	59
3.11	Illustration of the different cases of water in the composite	60
3.12	Comparison between predicted values of D and experimental value	61
3.13	Comparison of experimental and Rayleigh-calculated diffusion coefficients as Arrhenius plot	62

3.14	Design of the FabHéli composite blade (the propeller has 5 blades)	63
3.15	Different propeller blade sections considered for water ingress prediction, section 1 on the left, section 2 in the middle and section 3 on the right . . .	64
3.16	Water profile for the mid-thickness of section 1	64
3.17	Water profile for the mid-thickness of section 2	65
3.18	Water profile for the mid-thickness of section 3	65
4.1	Tensile behaviour of pure resin aged at 40 °C in seawater then dried	70
4.2	Tensile behaviour of pure resin aged at 40 °C in inert atmosphere	71
4.3	Fracture micrographs from resin tensile test of physically unaged (a) and aged during 620h at 40 °C (b), aged 14 hours at 50 °C (c) and rejuvenated after 166 hours at 50 °C (d).	73
4.4	DSC measurements performed on in-situ thermally aged pure dry resin at 60 °C	74
4.5	Change of maximal tensile stress during thermal ageing at 40 °C	74
4.6	Change of maximal tensile stress during thermal ageing at 50 °C	75
4.7	Change of maximal tensile stress during thermal ageing at 60 °C	75
4.8	Comparison of the maximal tensile stress changes at 3 different tempera- tures during thermal ageing	76
4.9	Temperature dependence of τ expressed as an Arrhenius plot	76
4.10	Tensile behaviour of physically aged fully saturated resin at 40 °C	77
4.11	Fracture surfaces for the saturated resin as physically unaged (a), physically aged during 500 hours (b), 475 days (c) and finally, rejuvenated after 500 hours of physical ageing at 40 °C (notice the porous aspect in (c))	78
4.12	DSC measurements performed on in-situ thermally aged saturated resin at 40 °C	79
4.13	Evolution of maximal stress of saturated resin thermally aged at 15 °C . . .	80
4.14	Evolution of maximal stress of saturated resin thermally aged at 25 °C . . .	80
4.15	Evolution of maximal stress of saturated resin thermally aged at 40 °C (truncated from 600 to 10000 hours)	81
4.16	Change in maximal stress as a function of logarithm ageing time, saturated resin	81
4.17	Arrhenius plot of the physical ageing relaxation time for the saturated resin	82
4.18	DSC plots of saturated and dry resin thermally aged for 24 hours at 40 °C .	83
4.19	Arrhenius plot of physical relaxation time as a function of ageing tempera- ture gap with respect to T_g	83
4.20	Change in resin T_g as a function of water content, with Simha-Boyer prediction	85
4.21	Influence of water absorption on tensile behaviour	86
4.22	Maximal tensile stress increase as a function of $T_g - T$ temperature difference	87
4.23	Tensile response of water-saturated resin aged at 60 °C in inert atmosphere prior to water ageing	87
4.24	Decrease in T_g induced by water absorption of a previously physically aged resin	88
4.25	Comparison with Kambour equation for resin with two physical ageing . .	89
4.26	Three main damage modes of unidirectional stacked composites [176]	90

4.27	Transverse tensile response of unidirectional composite subjected to physical ageing	91
4.28	Effect of physical ageing on the interlaminar shear strength of a 6 plies UD composite	92
5.1	Measured tip advance of 1.7 mm of a Nylon propeller at 10 rpm and 0.75 m.s^{-1} water speed in cavitation tunnel Taketani et al. [9]	94
5.2	Strain induced on a "flexible" design propeller blade at 909 rpm, $J=0.66$ (deformations magnified by 10) young et al. [177]	95
5.3	Deflection of the blade's tip for a composite and a metal propeller calculated theoretically by He et al. [16]	96
5.4	Effect of seawater on 0° tensile behaviour of unidirectional composite	97
5.5	Fractured unidirectional tensile specimens as unaged (a) and saturated (b) ageing conditions	99
5.6	Effect of seawater on tensile behaviour of $0/90^\circ$ composite	100
5.7	Effect of seawater on tensile behaviour of unidirectional composite in the transverse direction	100
5.8	Ageing effect on unidirectional composite in the fibre direction	102
5.9	Ageing effect on the fatigue behaviour of $0/90$ composite	103
5.10	Ageing effect on the fatigue behaviour of unidirectional transversely loaded composite	104
5.11	Fatigue curves of tensile tests on 90° composite normalized by the strength	104
5.12	Stiffness curves of unidirectional tensile tests unaged (left) and saturated (right)	105
5.13	Stiffness curves of $0/90$ composite unaged (left) and saturated (right)	106
5.14	Stiffness curves of transversely loaded unidirectional composite unaged (left) and saturated (right)	106
5.15	Clustered signals of the 0° composite specimen n°6 saturated as a Peak frequency vs Amplitude layout	107
5.16	Clustered signals of the 0° composite specimen n°6 saturated as a Peak frequency vs Amplitude layout	108
5.17	Occurrence of clusters during 90° tensile fatigue tests on saturated specimens 3 (a) and 6 (b)	109
5.18	Quasi-static four point bending for different displacement speeds on unidirectional composite	111
5.19	Effect of load frequency on the fatigue of unidirectional composite	112
5.20	Effect of load frequency on the fatigue of $0/90$ cross-ply composite	112
5.21	Effect of seawater on ultimate four point bending strength of cross-ply specimens	114
5.22	Effect of seawater ageing on crossply composite in four point flexure	115
5.23	Example of failure mode occurring during four point flexure unaged (a) and saturated (b)	116
5.24	C-Scan of RTM $0/90$ cross ply composite	116
5.25	C-Scan of infused $0/90$ cross ply composite	117
5.26	Seawater ageing effect on infused cross-ply composite flexure strength	117

5.27	Comparison between RTM and Infused 0/90° composite unaged (a) and saturated (b)	119
5.28	S-N curves of unaged and saturated infused composite	120
5.29	Desorption curve of infused four point flexure cross-ply specimens	120
5.30	Reversibility of ageing after drying, infused composite	121
5.31	Delamination recorded during fatigue tests for unaged (a), saturated (b) and saturated then dried (c) of infused specimens	122
5.32	Illustration of the interrupted tests	123
5.33	Stiffness curves of two sample at 65 % of maximal stress	124
5.34	Damage evolution in four point bending test on cross-ply composite	125
5.35	Photographs of the final state of sample from Figure 5.34 (70 % of lifetime (a), 50 % of lifetime (b), 30 % of lifetime failed (c) and 30 % of lifetime non failed (d))	126
5.36	Photographs of specimens presented in Table 5.4 in the same order	128
5.37	30 % of lifetime sample tomography showing two interlaminar delaminations	129
5.38	Edge of specimen 13 showing delamination as seen in Figure 5.37	129
5.39	Tomography picture of half of the specimen from figure 34 (a) as seen from above before (a) and after 70k cycles (b)	130
5.40	Longitudinal length of defects as a function of sphericity, before (a) and after (b) fatigue tests	131
5.41	Illustration of the position of planar distribution of the defects presented (scales are not respected)	132
5.42	Planar distribution of defects, all clusters before fatigue tests (a), after fatigue tests (b)	133
5.43	Planar distribution of longitudinal defects before fatigue tests (a), after fatigue tests (b)	133
6.1	R-curves of unaged composite in mode I	138
6.2	R-curves of the saturated composite in mode I	139
6.3	R-curves of the saturated then dried composite in mode I	139
6.4	Comparison of the three most representative R-curves from Figure 6.1 to Figure 6.3	140
6.5	da/dN curves of the unaged composite	141
6.6	da/dN curves of the saturated composite	141
6.7	da/dN curves of the saturated then dried composite	142
6.8	da/dN curves of the three ageing conditions	142
6.9	SEM images of fracture surfaces of unaged (left) saturated (centre) and saturated the dried (right) composite, crack propagates from top to bottom	143
6.10	R-curves of the unaged composite under mode II delamination	144
6.11	R-curves of the saturated composite under mode II delamination	144
6.12	R-curves of the saturated then dried composite under mode II delamination	145
6.13	Schematic representation of R-curves from mode I and mode II tests	146
6.14	Summary of average values of G_{IIc} of the composite under mode II delamination for different ageing conditions	146
6.15	Fatigue curve of unaged composite under mode II delamination	147

6.16	Fatigue curve of seawater saturated composite under mode II delamination	148
6.17	Fatigue curve of seawater saturated then fully dried composite under mode II delamination	148
6.18	Comparison of fatigue behaviour of the composite under mode II delamination for the three different ageing conditions	149
6.19	SEM micrograph of fracture surfaces of fatigued mode II unaged (a), saturated (b) and saturated then dried (c) composite, crack propagate from top to bottom	150
6.20	Quasi-static mode I crack propagation in physically unaged and aged composites	151
6.21	Mode I fatigue curves for physically aged and unaged composites	151
6.22	Fracture surfaces of mode I fatigue composite physically unaged (a) and physically aged (b) crack propagates from top to bottom of the images . . .	152
6.23	R-curve of composite in mode II as a function of physical ageing	153
6.24	C-scans of the two plates that were used for the mode I and mode II delamination tests, plate 3 (a) and plate 6 (b)	154
6.25	C-scan of the composite panel used for the physical ageing trials (note larger attenuation scale)	154
6.26	Physical ageing effect on mode II fatigue	155
6.27	Fracture surfaces from mode II fatigue with physically unaged material (a) and physically aged material (b) crack propagates from top to bottom of the images	156
6.28	Formation of fracture surfaces in mode II with physical ageing effect as shown by SEM micrographs	156
6.29	Comparison of fitted Paris law curves from physical and seawater ageing in mode I	158
6.30	Comparison of fitted Paris law curves from physical and seawater ageing in mode II	159
6.31	SEM of the fracture surface of a physically aged and fatigued ELS specimen showing microcracks	160
6.32	Representation of possible micro-crack formation for a composite physically unaged versus physically aged	161
6.33	Summary of the observed changes due to global warming as reported by the 2019's special GIEC report [195]	170
A.1	Emission de dioxyde de carbone [3]	172
A.2	Prise en eau dans la résine à différentes températures	174
A.3	Prise en eau dans le composite à différentes températures	175
A.4	Vue en trois dimensions de la pale issue du projet FabHéli	176
A.5	Répartition de la concentration d'eau dans une demi section de la pale FabHéli à différents temps	177
A.6	Effet de la plastification sur la réponse en traction sur la résine pure	178
A.7	Effet du vieillissement physique sur la réponse en traction sur la résine pure	179
A.8	Courbe d'Arrhenius du temps de relaxation sur la résine pure	180
A.9	Courbe de fatigue de traction transverse, effet de l'eau	181

A.10	Exemple de rupture par délaminage suite à un chargement de flexion 4 points en fatigue	183
A.11	Effet de l'eau et du séchage sur la fissuration en mode I en quasi-statique (a) et en fatigue (b)	185
A.12	Effet de l'eau et du séchage sur la fissuration en mode II en quasi-statique (a) et en fatigue (b)	186
B.1	Architecture to be followed for the Classeur.xls file	194
D.1	Water uptake of the infused composite at 4 °C	207
D.2	Water uptake of the infused composite at 25 °C	208
D.3	Water uptake of the infused composite at 40 °C	209
D.4	Water uptake of the infused composite at 60 °C	209
E.1	Crack gauge from Teksym™	211
E.2	Schematic representation of the crack gauge principle ©Teksym	212
E.3	Gauge system with three specimens.	212
E.4	C-scan of crack front after fatigue test DCB on the left and ELS on the right, crack gauge was bonded on the left hand side of the specimens with regard to this scan, crack propagates from top to bottom	213
E.5	Fracture surface of a fatigued els specimen, red arrows point at the crack front delimitation	214
E.6	Crack length measured by the gauge as a function of specimen's compliance during ELS fatigue test	215
E.7	Crack length measured by the gauge as a function of specimen's compliance during DCB fatigue test	215
F.1	Drawing of the seawater immersed four point flexure fatigue fixture	217
F.2	Drawing of the seawater immersed double cantilever beam fatigue fixture	218
F.3	Drawing of the seawater immersed edge loaded split fatigue fixture	218

List of Tables

2.1	Resin's pre-polymer composition	32
2.2	Resin's pre-polymer composition	33
3.1	Theoretical time to saturation of the composite and pure resin for different ageing temperatures	58
3.2	Prediction and experimental value of mass to saturation of the composite (*estimated values)	60
3.3	Calculated diffusion coefficient according to Dana et al. [159],(* calculated using an extrapolated M_{∞} value based on an Arrhenius law)	61
4.1	Mass to saturation as a function of ageing condition	84
5.1	Replication of tensile-tensile test data	101
5.2	Whitney's pooling scheme and power law parameters of the tensile fatigue tests	102
5.3	Effect of loading rate on four point bending stress at break and modulus on unidirectional composite	110
5.4	Half-life C-scans for different stress levels	127
6.1	Composition of the two plates that were used for mode I and mode II tests	153
6.2	Summary of the values from delamination tests, arrows refer to the trend from the previous value (directly to the left)	157

Acronyms

4ENF	Four point Edge Notched Flexure
AE	Acoustic Emission
AFP	Automated Fibre Placement
C-scan	Computer aided scan Mapping
CBTE	Corrected Beam Theory with Effective crack length
CC	Compliance Calibration
CENS	Compact Edge Notched Shear
CFD	Computational Fluid Dynamics
CH	Calinski Harabasz
CRAN	Comprehensive R Archive Network
DCB	Double Cantilever Beam
DIC	Digital Image Correlation
DSC	Differential Scanning Calorimetry
ECM	Experimental Compliance Method
ELS	Edge Loaded Split
ENF	Edge Notched Flexure
FEM	Finite Element Method
FRP	Fibre Reinforced Polymers
ILSS	InterLaminar Shear Strength
KWW	Kohlrausch-Williams-Watts
MBT	Modified Beam Theory
MCC	Modified Compliance Calibration
ONF	Over Notched Flexure
R-curve	Resistance curve
S-N	Stress versus Number of cycles to failure
SBT	Simple Beam Theory
SENF	Stabilized Edge Notched Flexure
SEM	Scanning Electron Microscopy
T_g	glass transition temperature
TGA	ThermoGravimetric Analysis
TTSP	Time Temperature Superposition Principle
UD	UniDirectional

UTS Ultimate Tensile Strength
VHCF Very High Cycle Fatigue
WPS Whitney's Pooling Scheme

Tabular abstract

Material	Material configuration	Experimental test	Condition studied	Observation	Reversibility	Page		
Resin	Pure resin	Quasi-static tensile	seawater	Decrease maximal stress, increase strain to break	Reversible	86, 87		
			sub-Tg ageing	Increase maximal stress, decrease strain to break		71, 77		
Infused UD	UD	Quasi-static transverse tensile	sub-Tg ageing	Slight decrease	Not tested	91		
		ILSS		No effect		92		
RTM Composite	UD 0°	Quasistatique tensile	Seawater	Slight increase of UTS	Not tested	97		
		Fatigue tensile		Discutable shift of fatigue curve		102		
	Crossply 0/90	Quasi-static tensile	Seawater	Slight decrease of UTS		100		
		Fatigue tensile		No effect		103		
	UD 90°	Quasi-static tensile	Seawater	Decrease of UTS		100		
		Fatigue tensile		Shift of the fatigue curve		104		
	UD	Four point flexure quasi-static	Frequency	No effect on UTF		111		
		Four point flexure fatigue		Shift of fatigue curve		112		
	Crossply 0/90	Four point flexure fatigue	Seawater	Shift of the fatigue curve		112		
		Four point flexure quasi-static		Slight decreas of the UFS		114		
	Crossply 0/90	Four point flexure fatigue	Seawater	Shift of the fatigue curve		115		
		Four point flexure Fatigue		Process RTM versus Infusion		Slight shift of the fatigue curve	119	
		UD	DCB quasistatic	Seawater		Shift of the fatigue curve	Reversible	120, 121
				Fatigue fixture		Damage caused by load point		125
Infused	UD	DCB quasistatic	Seawater	Decrease	Not reversible	140		
		DCB fatigue			Partially reversible	142		
		ELS quasistatic			Partially reversible	146		
		ELS fatigue			fully reversible	149		
	UD	DCB quasistatic	Sub-Tg ageing	Decrease	Not tested	151		
		DCB fatigue		Shift to lower mechanical properties		151		
		ELS quasistatic		Decrease		153		
		ELS fatigue		Shift to higher mechanical properties		155		

Bibliography

- [1] N. J. Lenssen, G. A. Schmidt, J. E. Hansen, M. J. Menne, A. Persin, R. Ruedy, and D. Zyss, “Improvements in the gistemp uncertainty model,” *Journal of Geophysical Research (Atmospheres)*, vol. 124, pp. 6307–6326, 2019.
- [2] G. Team, “Giss surface temperature analysis (gistemp),” *NASA Goddard Institute for Space Studies. Dataset accessed*, pp. 06–16, 2016.
- [3] R. K. Pachauri, M. R. Allen, V. R. Barros, J. Broome, W. Cramer, R. Christ, J. A. Church, L. Clarke, Q. Dahe, P. Dasgupta, *et al.*, *Climate change 2014: synthesis report. Contribution of Working Groups I, II and III to the fifth assessment report of the Intergovernmental Panel on Climate Change*. Ipcc, 2014.
- [4] J. Bourne, *A Treatise on the Screw Propeller: With Various Suggestions of Improvement*. Longman, Brown, Green, and Longmans, 1855.
- [5] J. Carlton, *Marine propellers and propulsion*. Butterworth-Heinemann, 2018.
- [6] A. Asnaghi, U. Svennberg, and R. E. Bensow, “Numerical and experimental analysis of cavitation inception behaviour for high-skewed low-noise propellers,” *Applied Ocean Research*, vol. 79, pp. 197–214, 2018.
- [7] B.-G. Paik, G.-D. Kim, K.-Y. Kim, H.-S. Seol, B.-S. Hyun, S.-G. Lee, and Y.-R. Jung, “Investigation on the performance characteristics of the flexible propellers,” *Ocean engineering*, vol. 73, pp. 139–148, 2013.
- [8] C.-C. Lin, Y.-J. Lee, and C.-S. Hung, “Optimization and experiment of composite marine propellers,” *Composite structures*, vol. 89, no. 2, pp. 206–215, 2009.
- [9] T. Taketani, K. Kimura, S. Ando, and K. Yamamoto, “Study on performance of a ship propeller using a composite material,” in *The Third International Symposium on Marine Propulsors smp*, vol. 13, 2013.
- [10] J. P. Blasques, C. Berggreen, and P. Andersen, “Hydro-elastic analysis and optimization of a composite marine propeller,” *Marine Structures*, vol. 23, no. 1, pp. 22–38, 2010.

- [11] M. Motley, Z. Liu, and Y. Young, “Utilizing fluid–structure interactions to improve energy efficiency of composite marine propellers in spatially varying wake,” *Composite Structures*, vol. 90, no. 3, pp. 304–313, 2009.
- [12] D. Buchler, “Composite propeller new features and properties specific design and experiences,” in *Propellers/Shafting 2006 Symposium*, vol. 9, pp. 9–1 – 9–6, SNAME, 2006.
- [13] D. Zou, J. Zhang, N. Ta, and Z. Rao, “The hydroelastic analysis of marine propellers with consideration of the effect of the shaft,” *Ocean Engineering*, vol. 131, pp. 95–106, 2017.
- [14] H. Das and S. Kapuria, “On the use of bend–twist coupling in full-scale composite marine propellers for improving hydrodynamic performance,” *Journal of Fluids and Structures*, vol. 61, pp. 132–153, 2016.
- [15] M. P. Kishore and R. Behera, “Base line study for determination of effect of stacking sequence on vibration characteristics of composite propeller blade,” *Aquatic Procedia*, vol. 4, pp. 458–465, 2015.
- [16] X. He, Y. Hong, and R. Wang, “Hydroelastic optimisation of a composite marine propeller in a non-uniform wake,” *Ocean engineering*, vol. 39, pp. 14–23, 2012.
- [17] Y. Hara, T. Yamatogi, H. Murayama, K. Uzawa, and K. Kageyama, “Performance evaluation of composite marine propeller for a fishing boat by fluid structure interaction analysis,” in *18TH international conference on composite materials*, 2011.
- [18] M. P. Kishore, R. Behera, S. Pradhan, and P. Parida, “Effect of material behavior on dynamic characteristics determination of marine propeller blade using finite element analysis,” *Procedia Engineering*, vol. 144, pp. 767–774, 2016.
- [19] S. K. Tamunoiyala, O. S. Khaled, O. A. Unyime, and E. N. Merv, “Review of composite propeller developments and strategy for modeling composite propellers using pvast,” *Defence R&D Canada Atlantic*, 2012.
- [20] S. Durand and P. Muller, “Fabheli,” E-Lass Seminar Day, 2018.
- [21] M. Khan, G. Bhuyan, M. Iqbal, and J. Quaicoe, “Hydrokinetic energy conversion systems and assessment of horizontal and vertical axis turbines for river and tidal applications: A technology status review,” *Applied energy*, vol. 86, no. 10, pp. 1823–1835, 2009.
- [22] D. M. Grogan, S. B. Leen, C. Kennedy, and C. Ó. Brádaigh, “Design of composite tidal turbine blades,” *Renewable Energy*, vol. 57, pp. 151–162, 2013.
- [23] H. Li, Z. Hu, K. Chandrashekhara, X. Du, and R. Mishra, “Reliability-based fatigue life investigation for a medium-scale composite hydrokinetic turbine blade,” *Ocean Engineering*, vol. 89, pp. 230–242, 2014.

- [24] E. M. Fagan, C. R. Kennedy, S. B. Leen, and J. Goggins, “Damage mechanics based design methodology for tidal current turbine composite blades,” *Renewable energy*, vol. 97, pp. 358–372, 2016.
- [25] P. Davies, G. Germain, B. Gaurier, A. Boisseau, and D. Perreux, “Evaluation of the durability of composite tidal turbine blades,” *Philosophical Transactions of the Royal Society A: Mathematical, Physical and Engineering Sciences*, vol. 371, no. 1985, p. 20120187, 2013.
- [26] Z. Zhou, F. Sculler, J. F. Charpentier, M. Benbouzid, and T. Tang, “An up-to-date review of large marine tidal current turbine technologies,” in *2014 International Power Electronics and Application Conference and Exposition*, pp. 480–484, IEEE, 2014.
- [27] Z. Zhou, M. Benbouzid, J.-F. Charpentier, F. Sculler, and T. Tang, “Developments in large marine current turbine technologies—a review,” *Renewable and Sustainable Energy Reviews*, vol. 71, pp. 852–858, 2017.
- [28] N. Tual, N. Carrere, P. Davies, T. Bonnemains, and E. Lolive, “Characterization of sea water ageing effects on mechanical properties of carbon/epoxy composites for tidal turbine blades,” *Composites Part A: Applied Science and Manufacturing*, vol. 78, pp. 380–389, 2015.
- [29] S. A. Energy, “Our tidal power project & operations | atlantis ressources @ONLINE,” Sept. 2019.
- [30] C. S. Smith, *Design of marine structures in composite materials*. Elsevier London, 1990.
- [31] D. Chalmers, “The potential for the use of composite materials in marine structures,” *Marine structures*, vol. 7, no. 2-5, pp. 441–456, 1994.
- [32] P. Davies and Y. D. Rajapakse, *Durability of composites in a marine environment*, vol. 208. Springer, 2014.
- [33] W. C. Tucker and T. Juska, “Marine applications,” in *Handbook of Composites* (S. T. Peters, ed.), pp. 916–930, Boston, MA: Springer US, 1998.
- [34] A. P. Mouritz, E. Gellert, P. Burchill, and K. Challis, “Review of advanced composite structures for naval ships and submarines,” *Composite structures*, vol. 53, no. 1, pp. 21–42, 2001.
- [35] A. Boisseau, *Etude de la tenue à long terme de matériaux composites immergés pour structures de récupération d’énergie marines*. PhD thesis, Université de Franche-Comté, 2011.
- [36] N. Tual, *Durability of carbon/epoxy composites for tidal turbine blade applications*. PhD thesis, Brest, 2015.

- [37] M. Arhant, P. Davies, S. Paboef, and E. Nicolas, “Reliability of composite tidal turbine blades,” in *ICCM22*, 2019.
- [38] J. Graham-Jones and J. Summerscales, *Marine applications of advanced fibre-reinforced composites*. Woodhead Publishing, 2015.
- [39] CELC, *Flax & Hemp Fiber Composites, a market reality - The biobased solutions for the industry*. JEC Group.
- [40] E. Gellert and D. Turley, “Seawater immersion ageing of glass-fibre reinforced polymer laminates for marine applications,” *Composites Part A: Applied Science and Manufacturing*, vol. 30, no. 11, pp. 1259–1265, 1999.
- [41] P. Davies, F. Mazeas, and P. Casari, “Sea water aging of glass reinforced composites: shear behaviour and damage modelling,” *Journal of composite materials*, vol. 35, no. 15, pp. 1343–1372, 2001.
- [42] L. S. Penn and H. Wang, “Epoxy resins,” in *Handbook of Composites* (S. T. Peters, ed.), pp. 48–74, Boston, MA: Springer US, 1998.
- [43] H. Q. Pham and M. J. Marks, “Epoxy resins,” in *Encyclopedia of Polymer Science and Technology*, American Cancer Society.
- [44] G. Gibson, “Chapter 27 - epoxy resins,” in *Brydson’s Plastics Materials (Eighth Edition)* (M. Gilbert, ed.), pp. 773 – 797, Butterworth-Heinemann, eighth edition ed., 2017.
- [45] D. Gay, *Composite materials: design and applications*. CRC press, 2014.
- [46] S. T. Peters, *Handbook of composites*. Springer Science & Business Media, second edition ed., 1998.
- [47] A. Fick, “Ueber diffusion,” *Annalen der Physik*, vol. 170, no. 1, pp. 59–86, 1855.
- [48] J. Crank *et al.*, *The mathematics of diffusion*. Oxford university press, 1979.
- [49] P. Bonniau, , and A. Bunsell, “A comparative study of water absorption theories applied to glass epoxy composites,” *Journal of Composite Materials*, vol. 15, no. 3, pp. 272–293, 1981.
- [50] E. Morel, V. Bellenger, and J. Verdu, “Structure-water absorption relationships for amine-cured epoxy resins,” *Polymer*, vol. 26, no. 11, pp. 1719–1724, 1985.
- [51] C. Humeau, P. Davies, and F. Jacquemin, “Moisture diffusion under hydrostatic pressure in composites,” *Materials & Design*, vol. 96, pp. 90–98, 2016.
- [52] C. Humeau, P. Davies, and F. Jacquemin, “An experimental study of water diffusion in carbon/epoxy composites under static tensile stress,” *Composites Part A: Applied Science and Manufacturing*, vol. 107, pp. 94–104, 2018.

- [53] R. J. Morgan and J. E. O’neal, “The durability of epoxies,” *Polymer-Plastics Technology and Engineering*, vol. 10, no. 1, pp. 49–116, 1978.
- [54] J. El Yagoubi, G. Lubineau, S. Saghir, J. Verdu, and A. Askari, “Thermomechanical and hygroelastic properties of an epoxy system under humid and cold-warm cycling conditions,” *Polymer degradation and stability*, vol. 99, pp. 146–155, 2014.
- [55] P. Nogueira, C. Ramirez, A. Torres, M. Abad, J. Cano, J. Lopez, I. López-Bueno, and L. Barral, “Effect of water sorption on the structure and mechanical properties of an epoxy resin system,” *Journal of Applied Polymer Science*, vol. 80, no. 1, pp. 71–80, 2001.
- [56] P. Moy and F. Karasz, “Epoxy-water interactions,” *Polymer Engineering & Science*, vol. 20, no. 4, pp. 315–319, 1980.
- [57] M. A. Abanilla, Y. Li, and V. M. Karbhari, “Durability characterization of wet layup graphite/epoxy composites used in external strengthening,” *Composites Part B: Engineering*, vol. 37, no. 2-3, pp. 200–212, 2005.
- [58] P. Davies and Y. D. Rajapakse, eds., *Durability of Composites in a Marine Environment 2*, vol. 245 of *Solid Mechanics and Its Applications*. Springer International Publishing.
- [59] L. Norwood and A. Marchant, “Recent developments in polyester matrices and reinforcements for marine applications, in particular polyester/kevlar composites,” in *Composite structures*, pp. 158–181, Springer, 1981.
- [60] P. Davies, P. Le Gac, and M. Le Gall, “Influence of sea water aging on the mechanical behaviour of acrylic matrix composites,” *Applied Composite Materials*, vol. 24, no. 1, pp. 97–111, 2017.
- [61] L. V. da Silva, F. W. da Silva, J. R. Tarpani, M. M. de Camargo Forte, and S. C. Amico, “Ageing effect on the tensile behavior of pultruded cfrp rods,” *Materials & Design*, vol. 110, pp. 245–254, 2016.
- [62] M. Arhant, P.-Y. Le Gac, M. Le Gall, C. Burtin, C. Briançon, and P. Davies, “Effect of sea water and humidity on the tensile and compressive properties of carbon-polyamide 6 laminates,” *Composites Part A: Applied Science and Manufacturing*, vol. 91, pp. 250–261, 2016.
- [63] K. Berketis, D. Tzetzis, and P. Hogg, “The influence of long term water immersion ageing on impact damage behaviour and residual compression strength of glass fibre reinforced polymer (gfrp),” *Materials & Design*, vol. 29, no. 7, pp. 1300–1310, 2008.
- [64] V. M. Karbhari and G. Xian, “Hygrothermal effects on high vf pultruded unidirectional carbon/epoxy composites: Moisture uptake,” *Composites Part B: Engineering*, vol. 40, no. 1, pp. 41–49, 2009.

- [65] R. Selzer and K. Friedrich, “Influence of water up-take on interlaminar fracture properties of carbon fibre-reinforced polymer composites,” *Journal of materials science*, vol. 30, no. 2, pp. 334–338, 1995.
- [66] G. LaPlante and B. Landry, “The effect of hygrothermal aging on mode i fatigue delamination growth in a carbon/epoxy composites,” *Journal of Advanced Materials*, vol. 43, no. 2, pp. 79–86, 2011.
- [67] A. Garg and O. Ishai, “Hygrothermal influence on delamination behavior of graphite/epoxy laminates,” *Engineering fracture mechanics*, vol. 22, no. 3, pp. 413–427, 1985.
- [68] D. J. Wilkins, “A comparison of the delamination and environmental resistance of a graphite-epoxy and a graphite-bismaleimide.,” Tech. Rep. NAV-GD-0037, GENERAL DYNAMICS FORT WORTH TX FORT WORTH DIV, 1981.
- [69] B. Landry, G. LaPlante, and L. R. LeBlanc, “Environmental effects on mode ii fatigue delamination growth in an aerospace grade carbon/epoxy composite,” *Composites Part A: Applied Science and Manufacturing*, vol. 43, no. 3, pp. 475–485, 2012.
- [70] L. LeBlanc, G. LaPlante, and C. Li, “Moisture effects on mixed-mode delamination of carbon/epoxy composites,” in *Design, Manufacturing and Applications of Composites Tenth Workshop 2014: Proceedings of the Tenth Joint Canada-Japan Workshop on Composites, August 2014, Vancouver, Canada*, p. 115, DEStech Publications, Inc, 2015.
- [71] L. Asp, “The effects of moisture and temperature on the interlaminar delamination toughness of a carbon/epoxy composite,” *Composites Science and Technology*, vol. 58, no. 6, pp. 967–977, 1998.
- [72] A. I. Gagani, A. E. Krauklis, E. Sæter, N. P. Vedvik, and A. T. Echtermeyer, “A novel method for testing and determining ilss for marine and offshore composites,” *Composite Structures*, vol. 220, pp. 431–440, 2019.
- [73] P. Sun, Y. Zhao, Y. Luo, and L. Sun, “Effect of temperature and cyclic hygrothermal aging on the interlaminar shear strength of carbon fiber/bismaleimide (bmi) composite,” *Materials & Design*, vol. 32, no. 8-9, pp. 4341–4347, 2011.
- [74] S. Pavlidou and C. Papaspyrides, “The effect of hygrothermal history on water sorption and interlaminar shear strength of glass/polyester composites with different interfacial strength,” *Composites Part A: applied science and manufacturing*, vol. 34, no. 11, pp. 1117–1124, 2003.
- [75] P. Davies and M. Arhant, “Fatigue behaviour of acrylic matrix composites: influence of seawater,” *Applied Composite Materials*, vol. 26, no. 2, pp. 507–518, 2019.
- [76] F. Ramirez, L. Carlsson, and B. Acha, “Evaluation of water degradation of vinylester and epoxy matrix composites by single fiber and composite tests,” *Journal of materials science*, vol. 43, no. 15, pp. 5230–5242, 2008.

- [77] D. A. Biro, G. Pleizier, and Y. Deslandes, "Application of the microbond technique: effects of hygrothermal exposure on carbon-fiber/epoxy interfaces," *Composites science and technology*, vol. 46, no. 3, pp. 293–301, 1993.
- [78] Y. Joliff, L. Bélec, M. Heman, and J. Chailan, "Experimental, analytical and numerical study of water diffusion in unidirectional composite materials–interphase impact," *Computational Materials Science*, vol. 64, pp. 141–145, 2012.
- [79] W. Bradley and T. Grant, "The effect of the moisture absorption on the interfacial strength of polymeric matrix composites," *Journal of Materials Science*, vol. 30, no. 21, pp. 5537–5542, 1995.
- [80] L. C. E. Struik, "Physical aging in amorphous polymers and other materials," 1977.
- [81] J. M. Hutchinson, "Physical aging of polymers," *Progress in polymer science*, vol. 20, no. 4, pp. 703–760, 1995.
- [82] G. M. Odegard and A. Bandyopadhyay, "Physical aging of epoxy polymers and their composites," *Journal of Polymer Science Part B: Polymer Physics*, vol. 49, no. 24, pp. 1695–1716, 2011.
- [83] E. S.-W. Kong, "Physical aging in epoxy matrices and composites," in *Epoxy Resins and Composites IV*, pp. 125–171, Springer, 1986.
- [84] W. D. Cook, A. E. Mayr, and G. H. Edward, "Yielding behaviour in model epoxy thermosets—ii. temperature dependence," *Polymer*, vol. 39, no. 16, pp. 3725–3733, 1998.
- [85] W. Cook, M. Mehrabi, and G. Edward, "Ageing and yielding in model epoxy thermosets," *Polymer*, vol. 40, no. 5, pp. 1209–1218, 1999.
- [86] T. Chang and J. Brittain, "Studies of epoxy resin systems: Part d: Fracture toughness of an epoxy resin: A study of the effect of crosslinking and sub-tg aging," *Polymer Engineering & Science*, vol. 22, no. 18, pp. 1228–1236, 1982.
- [87] C. G. Sell and G. B. McKenna, "Influence of physical ageing on the yield response of model dgeba/poly (propylene oxide) epoxy glasses," *Polymer*, vol. 33, no. 10, pp. 2103–2113, 1992.
- [88] E. S.-W. Kong, G. L. Wilkes, J. E. McGrath, A. Banthia, Y. Mohajer, and M. Tant, "Physical aging of linear and network epoxy resins," *Polymer Engineering & Science*, vol. 21, no. 14, pp. 943–950, 1981.
- [89] V.-T. Truong and B. Ennis, "Effect of physical aging on the fracture behavior of crosslinked epoxies," *Polymer Engineering & Science*, vol. 31, no. 8, pp. 548–557, 1991.
- [90] A. P. Vassilopoulos and T. Keller, *Fatigue of fiber-reinforced composites*. Springer Science & Business Media, 2011.

- [91] P. Alam, D. Mamalis, C. Robert, C. Floreani, and C. M. Ó. Brádaigh, “The fatigue of carbon fibre reinforced plastics-a review,” *Composites Part B: Engineering*, 2019.
- [92] B. Harris, *Fatigue in composites: science and technology of the fatigue response of fibre-reinforced plastics*. Woodhead Publishing, 2003.
- [93] V. Carvelli, A. Jain, S. V. Lomov, *et al.*, *Fatigue of textile and short fiber reinforced composites*. Wiley Online Library, 2017.
- [94] K. L. Reifsnider, *Fatigue of composite materials*, vol. 4. Elsevier, 2012.
- [95] G. Sims, “2 - fatigue test methods, problems and standards,” in *Fatigue in Composites* (B. Harris, ed.), Woodhead Publishing Series in Composites Science and Engineering, pp. 36 – 62, Woodhead Publishing, 2003.
- [96] “Standard test method for tensile properties of polymer matrix composite materials, astm international,” standard, ASTM International, West Conshohocken, PA, 2017.
- [97] “Standard test method for tension-tension fatigue of polymer matrix composite materials,” standard, ASTM International, West Conshohocken, PA, 2019.
- [98] S. Ogihara, N. Takeda, S. Kobayashi, and A. Kobayashi, “Effects of stacking sequence on microscopic fatigue damage development in quasi-isotropic cfrp laminates with interlaminar-toughened layers,” *Composites Science and Technology*, vol. 59, no. 9, pp. 1387–1398, 1999.
- [99] N. Takeda, S. Kobayashi, S. Ogihara, and A. Kobayashi, “Effects of toughened interlaminar layers on fatigue damage progress in quasi-isotropic cfrp laminates,” *International journal of fatigue*, vol. 21, no. 3, pp. 235–242, 1999.
- [100] K. Tohgo, S. Nakagawa, and K. Kageyama, “Fatigue behavior of cfrp cross-ply laminates under on-axis and off-axis cyclic loading,” *International Journal of Fatigue*, vol. 28, no. 10, pp. 1254–1262, 2006.
- [101] T. Jeannin, M. Berges, X. Gabrion, R. Léger, V. Person, S. Corn, B. Piezel, P. Ienny, S. Fontaine, and V. Placet, “Influence of hydrothermal ageing on the fatigue behaviour of a unidirectional flax-epoxy laminate,” *Composites Part B: Engineering*, p. 107056, 2019.
- [102] C. Hochard, Y. Thollon, *et al.*, “Fatigue of laminated composite structures with stress concentrations,” *Composites Part B: Engineering*, vol. 65, pp. 11–16, 2014.
- [103] H. Liu, A. Ojha, Z. Li, C. C. Engler-Pinto Jr, X. Su, Q. Sun, H. Kang, W. Wen, and H. Cui, “Fatigue modeling for carbon/epoxy unidirectional composites under various stress ratios considering size effects,” *International Journal of Fatigue*, vol. 120, pp. 184–200, 2019.
- [104] J. Payan and C. Hochard, “Damage modelling of laminated carbon/epoxy composites under static and fatigue loadings,” *International Journal of Fatigue*, vol. 24, no. 2-4, pp. 299–306, 2002.

- [105] T. Wu, W. Yao, and C. Xu, “A vhc life prediction method based on surface crack density for frp,” *International Journal of Fatigue*, vol. 114, pp. 51–56, 2018.
- [106] “Standard test methods for flexural properties of unreinforced and reinforced plastics and electrical insulating materials,” standard, ASTM International, West Conshohocken, PA, 2017.
- [107] “Standard test method for flexural properties of unreinforced and reinforced plastics and electrical insulating materials by four-point bending,” standard, ASTM International, West Conshohocken, PA, 2017.
- [108] A. Chambers, J. Earl, C. Squires, and M. Suhot, “The effect of voids on the flexural fatigue performance of unidirectional carbon fibre composites developed for wind turbine applications,” *International journal of fatigue*, vol. 28, no. 10, pp. 1389–1398, 2006.
- [109] A. Boisseau and C. Peyrac, “Long term durability of composites in marine environment: Comparative study of fatigue behavior,” *Procedia Engineering*, vol. 133, pp. 535–544, 2015.
- [110] A. Zhang, D. Li, D. Zhang, H. Lu, H. Xiao, and J. Jia, “Qualitative separation of the effect of voids on the static mechanical properties of hygrothermally conditioned carbon/epoxy composites,” *eXPRESS Polymer Letters*, vol. 5, no. 8, 2011.
- [111] C. R. Kennedy, V. Jaksic, S. B. Leen, and C. M. Brádaigh, “Fatigue life of pitch-and stall-regulated composite tidal turbine blades,” *Renewable energy*, vol. 121, pp. 688–699, 2018.
- [112] R. Selzer and K. Friedrich, “Mechanical properties and failure behaviour of carbon fibre-reinforced polymer composites under the influence of moisture,” *Composites Part A: Applied Science and Manufacturing*, vol. 28, no. 6, pp. 595–604, 1997.
- [113] K. W. Furrow, A. C. Loos, and R. J. Cano, “Environmental effects on stitched rtm textile composites,” *Journal of reinforced plastics and composites*, vol. 15, no. 4, pp. 378–419, 1996.
- [114] M. Nakada and Y. Miyano, “Accelerated testing for long-term fatigue strength of various frp laminates for marine use,” *Composites Science and Technology*, vol. 69, no. 6, pp. 805–813, 2009.
- [115] B. Harris, “1 - a historical review of the fatigue behaviour of fibre-reinforced plastics,” in *Fatigue in Composites* (B. Harris, ed.), Woodhead Publishing Series in Composites Science and Engineering, pp. 3 – 35, Woodhead Publishing, 2003.
- [116] C. Hochard and Y. Thollon, “A generalized damage model for woven ply laminates under static and fatigue loading conditions,” *International Journal of Fatigue*, vol. 32, no. 1, pp. 158–165, 2010.

- [117] N. Dimitrov, A. Der Kiureghian, and C. Berggreen, “Bayesian inference model for fatigue life of laminated composites,” *Journal of Composite Materials*, vol. 50, no. 2, pp. 131–143, 2016.
- [118] H. Krüger and R. Rolfes, “A physically based fatigue damage model for fibre-reinforced plastics under plane loading,” *International Journal of Fatigue*, vol. 70, pp. 241–251, 2015.
- [119] A. P. Vassilopoulos and T. Keller, “Statistical analysis of fatigue data,” in *Fatigue of Fiber-reinforced Composites* (A. P. Vassilopoulos and T. Keller, eds.), Engineering Materials and Processes, Springer Science & Business Media, London, 2011.
- [120] P. Davies, “Review of standard procedures for delamination resistance testing,” in *Delamination behaviour of composites*, pp. 65–86, Elsevier, 2008.
- [121] R. H. Martin, “Evaluation of the split cantilever beam for mode iii delamination testing,” in *Composite Materials: Fatigue and Fracture (Third Volume)*, ASTM International, 1991.
- [122] “Standard test method for mode i interlaminar fracture toughness of unidirectional fiber-reinforced polymer matrix composites,” standard, ASTM International, West Conshohocken, PA, 2013.
- [123] I. C. Secretary, “Fibre-reinforced plastic composites — determination of mode i interlaminar fracture toughness, G_{Ic} , for unidirectionally reinforced materials,” Standard ISO 15024:2001(E), International Organization for Standardization, Geneva, CH, 2001.
- [124] T. K. O’Brien and R. H. Martin, “Round robin testing for mode i interlaminar fracture toughness of composite materials,” *Journal of Composites, Technology and Research*, vol. 15, no. 4, pp. 269–281, 1993.
- [125] T. K. Obrien, “Results of ASTM round robin testing for mode 1 interlaminar fracture toughness of composite materials,” tech. rep., Nov. 1992.
- [126] “Standard test method for mode i fatigue delamination growth onset of unidirectional fiber-reinforced polymer matrix composites,” standard, ASTM International, West Conshohocken, PA, 2019.
- [127] A. Brunner, N. Murphy, and G. Pinter, “Development of a standardized procedure for the characterization of interlaminar delamination propagation in advanced composites under fatigue mode i loading conditions,” *Engineering Fracture Mechanics*, vol. 76, no. 18, pp. 2678–2689, 2009.
- [128] S. Stelzer, A. Brunner, A. Argüelles, N. Murphy, and G. Pinter, “Mode i delamination fatigue crack growth in unidirectional fiber reinforced composites: Development of a standardized test procedure,” *Composites Science and Technology*, vol. 72, no. 10, pp. 1102–1107, 2012.

- [129] M. Hojo, S. Matsuda, M. Tanaka, S. Ochiai, and A. Murakami, “Mode i delamination fatigue properties of interlayer-toughened cf/epoxy laminates,” *Composites Science and Technology*, vol. 66, no. 5, pp. 665–675, 2006.
- [130] L. Yao, R. Alderliesten, M. Zhao, and R. Benedictus, “Bridging effect on mode i fatigue delamination behavior in composite laminates,” *Composites Part A: Applied Science and Manufacturing*, vol. 63, pp. 103–109, 2014.
- [131] O. Al-Khudairi, H. Hadavinia, A. Waggott, E. Lewis, and C. Little, “Characterising mode i/mode ii fatigue delamination growth in unidirectional fibre reinforced polymer laminates,” *Materials & Design (1980-2015)*, vol. 66, pp. 93–102, 2015.
- [132] R. Khan, R. Alderliesten, L. Yao, and R. Benedictus, “Crack closure and fibre bridging during delamination growth in carbon fibre/epoxy laminates under mode i fatigue loading,” *Composites Part A: Applied Science and Manufacturing*, vol. 67, pp. 201–211, 2014.
- [133] F. Lahuerta, T. Westphal, R. Nijssen, F. Van Der Meer, and L. Sluys, “Measuring the delamination length in static and fatigue mode i tests using video image processing,” *Composites Part B: Engineering*, vol. 63, pp. 1–7, 2014.
- [134] I. Simon, L. Banks-Sills, and V. Fourman, “Mode i delamination propagation and r-ratio effects in woven composite dcb specimens for a multi-directional layup,” *International Journal of Fatigue*, vol. 96, pp. 237–251, 2017.
- [135] A. Sjögren and L. E. Asp, “Effects of temperature on delamination growth in a carbon/epoxy composite under fatigue loading,” *International Journal of Fatigue*, vol. 24, no. 2-4, pp. 179–184, 2002.
- [136] M. Manca, C. Berggreen, and L. A. Carlsson, “G-control fatigue testing for cyclic crack propagation in composite structures,” *Engineering Fracture Mechanics*, vol. 149, pp. 375–386, 2015.
- [137] “Standard test method for determination of the mode ii interlaminar fracture toughness of unidirectional fiber-reinforced polymer matrix composites,” standard, ASTM International, West Conshohocken, PA, 2019.
- [138] I. C. Secretary, “Fibre-reinforced plastic composites — determination of the mode ii fracture resistance for unidirectionally reinforced materials using the calibrated end-loaded split (c-els) test and an effective crack length approach,” Standard BS ISO 15114:2014, International Organization for Standardization, Geneva, CH, 2014.
- [139] P. Davies, G. Sims, B. Blackman, A. Brunner, K. Kageyama, M. Hojo, K. Tanaka, G. Murri, C. Rousseau, B. Gieseke, *et al.*, “Comparison of test configurations for determination of mode ii interlaminar fracture toughness results from international collaborative test programme,” *Plastics, rubber and composites*, vol. 28, no. 9, pp. 432–437, 1999.

- [140] B. Blackman, A. Brunner, and J. Williams, “Mode ii fracture testing of composites: a new look at an old problem,” *Engineering Fracture Mechanics*, vol. 73, no. 16, pp. 2443–2455, 2006.
- [141] I. Maillet, L. Michel, F. Souric, and Y. Gourinat, “Mode ii fatigue delamination growth characterization of a carbon/epoxy laminate at high frequency under vibration loading,” *Engineering Fracture Mechanics*, vol. 149, pp. 298–312, 2015.
- [142] J. Sousa, A. Pereira, A. Martins, and A. de Moraes, “Mode ii fatigue delamination of carbon/epoxy laminates using the end-notched flexure test,” *Composite Structures*, vol. 134, pp. 506–512, 2015.
- [143] M. Hojo, T. Ando, M. Tanaka, T. Adachi, S. Ochiai, and Y. Endo, “Modes i and ii interlaminar fracture toughness and fatigue delamination of cf/epoxy laminates with self-same epoxy interleaf,” *International journal of fatigue*, vol. 28, no. 10, pp. 1154–1165, 2006.
- [144] A. Brunner, S. Stelzer, G. Pinter, and G. Terrasi, “Mode ii fatigue delamination resistance of advanced fiber-reinforced polymer–matrix laminates: Towards the development of a standardized test procedure,” *International journal of fatigue*, vol. 50, pp. 57–62, 2013.
- [145] I. C. Secretary, “Fibre-reinforced plastics — determination of fatigue properties under cyclic loading conditions,” Standard ISO 13003:2003(E), International Organization for Standardization, Geneva, CH, 2003.
- [146] I. C. Secretary, “Plastics — determination of tensile properties of plastics — part 2: Testing conditions for moulding and extrusion plastics,” Standard ISO 524-2:2012(F), International Organization for Standardization, Geneva, CH, 2012.
- [147] I. C. Secretary, “Fibre-reinforced plastic composites — determination of apparent interlaminar shear strength by short-beam method,” Standard BS EN ISO 14130:1998, International Organization for Standardization, Geneva, CH, 2004.
- [148] I. C. Secretary, “Carbon-fibre-reinforced composites — determination of the resin, fibre and void contents,” Standard ISO 14127:2008, International Organization for Standardization, Geneva, CH, 2008.
- [149] C. Chesneau, *Eléments de classification*. Université de Caen, mars 2017.
- [150] L. Li, S. V. Lomov, and X. Yan, “Correlation of acoustic emission with optically observed damage in a glass/epoxy woven laminate under tensile loading,” *Composite structures*, vol. 123, pp. 45–53, 2015.
- [151] L. Li, Y. Swolfs, I. Straumit, X. Yan, and S. V. Lomov, “Cluster analysis of acoustic emission signals for 2d and 3d woven carbon fiber/epoxy composites,” *Journal of Composite Materials*, vol. 50, no. 14, pp. 1921–1935, 2016.

- [152] M. Diakhate, N. Tual, N. Carrere, and P. Davies, “Cracking and durability of composites in a marine environment,” in *Challenges in Mechanics of Time Dependent Materials, Volume 2*, pp. 1–8, Springer, 2017.
- [153] M. Diakhate, E. Bastidas-Arteaga, R. M. Pitti, and F. Schoefs, “Cluster analysis of acoustic emission activity within wood material: Towards a real-time monitoring of crack tip propagation,” *Engineering Fracture Mechanics*, vol. 180, pp. 254–267, 2017.
- [154] E. Richaud, F. Djouani, B. Fayolle, J. Verdu, and B. FLACONNECHE, “New insights in polymer-biofuels interaction Avancées dans la compréhension des interactions polymères-biocarburants,” *Oil & Gas Science and Technology - Revue d'IFP Energies nouvelles*, vol. 70(2), pp. 317–333., 2015.
- [155] J. Delozanne, N. Desgardin, M. Coulaud, N. Cuvillier, and E. Richaud, “Failure of epoxies bonded assemblies: comparison of thermal and humid ageing,” *The Journal of Adhesion*, pp. 1–24, 2018.
- [156] A. C. Loos and G. S. Springer, “Moisture absorption of graphite-epoxy composites immersed in liquids and in humid air,” *Journal of Composite Materials*, vol. 13, no. 2, pp. 131–147, 1979.
- [157] I. Merdas, F. ThomINETTE, A. Tcharkhtchi, and J. Verdu, “Factors governing water absorption by composite matrices,” *Composites Science and technology*, vol. 62, no. 4, pp. 487–492, 2002.
- [158] M. L. Costa, M. C. Rezende, and S. F. M. De Almeida, “Effect of void content on the moisture absorption in polymeric composites,” *Polymer-Plastics Technology and Engineering*, vol. 45, no. 6, pp. 691–698, 2006.
- [159] H. R. Dana, A. Perronnet, S. Fréour, P. Casari, and F. Jacquemin, “Identification of moisture diffusion parameters in organic matrix composites,” *Journal of Composite Materials*, vol. 47, no. 9, pp. 1081–1092, 2013.
- [160] L. Rayleigh, “Xix. on the instability of cylindrical fluid surfaces,” *The London, Edinburgh, and Dublin Philosophical Magazine and Journal of Science*, vol. 34, no. 207, pp. 177–180, 1892.
- [161] Argo, “Argo float data and metadata from global data assembly centre (argo gdac),” *SEANOE.*, 2000.
- [162] C. R. Kennedy, S. B. Leen, and C. M. Brádaigh, “A preliminary design methodology for fatigue life prediction of polymer composites for tidal turbine blades,” *Proceedings of the Institution of Mechanical Engineers, Part L: Journal of Materials: Design and Applications*, vol. 226, no. 3, pp. 203–218, 2012.
- [163] B. De’Nève and M. Shanahan, “Water absorption by an epoxy resin and its effect on the mechanical properties and infra-red spectra,” *Polymer*, vol. 34, no. 24, pp. 5099–5105, 1993.

- [164] S. Sugiman, I. K. P. Putra, and P. D. Setyawan, “Effects of the media and ageing condition on the tensile properties and fracture toughness of epoxy resin,” *Polymer Degradation and Stability*, vol. 134, pp. 311–321, 2016.
- [165] W. Loh, A. Crocombe, M. A. Wahab, and I. Ashcroft, “Modelling anomalous moisture uptake, swelling and thermal characteristics of a rubber toughened epoxy adhesive,” *International journal of adhesion and adhesives*, vol. 25, no. 1, pp. 1–12, 2005.
- [166] N. Fredj, S. Cohendoz, X. Feugas, and S. Touzain, “Some consequences of saline solution immersion on mechanical behavior of two marine epoxy-based coatings,” *Progress in Organic Coatings*, vol. 69, no. 1, pp. 82–91, 2010.
- [167] G. B. McKenna and S. L. Simon, “The glass transition: Its measurement and underlying physics,” *Handbook of thermal analysis and calorimetry*, vol. 3, pp. 49–109, 2002.
- [168] A. Lee and G. B. McKenna, “Effect of crosslink density on physical ageing of epoxy networks,” *Polymer*, vol. 29, no. 10, pp. 1812–1817, 1988.
- [169] B. C. Hancock and G. Zograf, “The relationship between the glass transition temperature and the water content of amorphous pharmaceutical solids,” *Pharmaceutical research*, vol. 11, no. 4, pp. 471–477, 1994.
- [170] F. N. Kelley and F. Bueche, “Viscosity and glass temperature relations for polymer-diluent systems,” *Journal of Polymer Science*, vol. 50, no. 154, pp. 549–556, 1961.
- [171] M. Broudin, P.-Y. Le Gac, V. Le Saux, C. Champy, G. Robert, P. Charrier, and Y. Marco, “Water diffusivity in pa66: Experimental characterization and modeling based on free volume theory,” *European Polymer Journal*, vol. 67, pp. 326–334, 2015.
- [172] V. Velikov, S. Borick, and C. Angell, “The glass transition of water, based on hyperquenching experiments,” *Science*, vol. 294, no. 5550, pp. 2335–2338, 2001.
- [173] G. Johari, A. Hallbrucker, and E. Mayer, “The glass–liquid transition of hyperquenched water,” *Nature*, vol. 330, no. 6148, p. 552, 1987.
- [174] G. Johari, “Does water need a new t_g ?,” *The Journal of Chemical Physics*, vol. 116, pp. 8067–8073, 05 2002.
- [175] R. Kambour, “A review of crazing and fracture in thermoplastics,” *Journal of Polymer Science: Macromolecular Reviews*, vol. 7, no. 1, pp. 1–154, 1973.
- [176] L. Gornet, “Généralités sur les matériaux composites.” Lecture, Ecole Centrale de Nantes, 2008.
- [177] Y. L. Young, “Fluid–structure interaction analysis of flexible composite marine propellers,” *Journal of Fluids and Structures*, vol. 24, no. 6, pp. 799–818, 2008.

- [178] H. J. Lin, J. Lin, and T.-J. Chuang, “Strength evaluation of a composite marine propeller blade,” *Journal of reinforced plastics and composites*, vol. 24, no. 17, pp. 1791–1807, 2005.
- [179] D. Backe, F. Balle, and D. Eifler, “Fatigue testing of cfrp in the very high cycle fatigue (vhcf) regime at ultrasonic frequencies,” *Composites Science and Technology*, vol. 106, pp. 93–99, 2015.
- [180] M. Gude, W. Hufenbach, I. Koch, and R. Koschichow, “Fatigue testing of carbon fibre-reinforced polymers under vhcf loading,” *Materials Testing*, vol. 54, no. 11-12, pp. 756–761, 2012.
- [181] A. Kinloch and J. Williams, “Crack blunting mechanisms in polymers,” *Journal of Materials Science*, vol. 15, no. 4, pp. 987–996, 1980.
- [182] P. Davies and D. Moore, “Glass/nylon-6.6 composites: delamination resistance testing,” *Composites Science and Technology*, vol. 38, no. 3, pp. 211–227, 1990.
- [183] L. Yao, Y. Sun, L. Guo, X. Lyu, M. Zhao, L. Jia, R. Alderliesten, and R. Benedictus, “Mode i fatigue delamination growth with fibre bridging in multidirectional composite laminates,” *Engineering Fracture Mechanics*, vol. 189, pp. 221–231, 2018.
- [184] N. Sato, M. Hojo, and M. Nishikawa, “Novel test method for accurate characterization of intralaminar fracture toughness in cfrp laminates,” *Composites Part B: Engineering*, vol. 65, pp. 89–98, 2014.
- [185] W.-X. Wang, M. Nakata, Y. Takao, and T. Matsubara, “Experimental investigation on test methods for mode ii interlaminar fracture testing of carbon fiber reinforced composites,” *Composites Part A: Applied Science and Manufacturing*, vol. 40, no. 9, pp. 1447–1455, 2009.
- [186] C. Schuecker and B. D. Davidson, “Evaluation of the accuracy of the four-point bend end-notched flexure test for mode ii delamination toughness determination,” *Composites Science and Technology*, vol. 60, no. 11, pp. 2137–2146, 2000.
- [187] J. R. Reeder and J. Crews, “Redesign of the mixed-mode bending delamination test to reduce nonlinear effects,” *Journal of Composites, Technology and Research*, vol. 14, no. 1, pp. 12–19, 1992.
- [188] H. Obeid, A. Clément, S. Fréour, F. Jacquemin, and P. Casari, “On the identification of the coefficient of moisture expansion of polyamide-6: Accounting differential swelling strains and plasticization,” *Mechanics of Materials*, vol. 118, pp. 1–10, 2018.
- [189] S. M. Lee, “Mode ii delamination failure mechanisms of polymer matrix composites,” *Journal of materials science*, vol. 32, no. 5, pp. 1287–1295, 1997.
- [190] M. L. Benzeggagh and M. Kenane, “Measurement of mixed-mode delamination fracture toughness of unidirectional glass/epoxy composites with mixed-mode bending apparatus,” *Composites science and technology*, vol. 56, no. 4, pp. 439–449, 1996.

- [191] M. Kenane and M. Benzeggagh, “Mixed-mode delamination fracture toughness of unidirectional glass/epoxy composites under fatigue loading,” *Composites Science and Technology*, vol. 57, no. 5, pp. 597–605, 1997.
- [192] S. Koshima, S. Yoneda, N. Kajii, A. Hosoi, and H. Kawada, “Evaluation of strength degradation behavior and fatigue life prediction of plain-woven carbon-fiber-reinforced plastic laminates immersed in seawater,” *Composites Part A: Applied Science and Manufacturing*, p. 105645, 2019.
- [193] C. Robert, D. Mamalis, P. Alam, A. D. Lafferty, C. Ó. Cadhain, G. Breathnach, E. D. McCarthy, and C. M. Ó. Brádaigh, “Powder epoxy based ud-cfrp manufacturing routes for wind and tidal turbine blades,” 2018.
- [194] C. Floreani, C. Robert, P. Alam, P. Davies, and C. M. Brádaigh, “Characterization of mode i interlaminar properties of novel composites for tidal turbine blades,” in *Reuropean Wave and Tidal Energy Conference*, vol. 13, 2019.
- [195] I. 2019, H.-O. Portner, D. Roberts, V. Masson-Delmotte, P. Zhai, M. Tignor, E. Poloczanska, K. Mintenbeck, M. Nicolai, A. Okem, J. Petzold, B. Rama, and N. Weyer, “Summary for policymakers,” *IPCC Special Report on the Ocean and Cryosphere in a Changing Climate*, vol. In press, p. 15, 2019.

Titre : Vieillissement en milieu marin et fatigue des pâles d'hélices en carbone/époxy

Mots clés : composite, fatigue, vieillissement marin, délaminage

Résumé : Les travaux présentés portent sur l'étude du vieillissement en milieu marin d'un composite carbone époxy pour applications pâles d'hélice de navires. La caractérisation de la prise en eau dans la résine pure et le composite a montré un comportement Fickien. La présence d'eau dans les porosités du composite a également été mise en évidence analytiquement. Le vieillissement accéléré de la résine a mis en évidence trois phénomènes : l'oxydation, le vieillissement physique et la plastification. L'effet mécanique des ces deux derniers a été particulièrement étudié. La présence d'eau et donc d'une résine plastifiée a eu l'effet d'accélérer le vieillissement physique. L'effet du vieillissement accéléré sur le composite a ensuite été étudié sous différentes sollicitations quasistatiques et de fatigue.

Peu d'effets de l'eau ont été relevés pour les sollicitations de traction sur des orientations sens fibres. Cependant, des pertes de plus importantes des propriétés mécaniques ont été observés en traction sens transverse aussi bien en statique que en fatigue. Ces mêmes résultats ont été trouvés sous sollicitations de flexion grâce à l'essai de flexion quatre points. Ce dernier a été discuté du fait de l'endommagement qu'il provoque. Enfin, le composite a été étudié sous sollicitations de délaminage suivant deux modes de fissuration: ouverture et cisaillement dans le plan. La présence d'eau a eu pour effet de diminuer l'énergie de fissuration dans les deux modes. Ce même résultat a été trouvé sous chargement de fatigue. L'influence du vieillissement physique sur les propriétés mécaniques du composite a également été démontré, son effet étant négatif, il nécessite d'être pris en compte.

Title : Marine ageing and fatigue of carbon/epoxy composite propeller blades

Keywords : Composite materials, fatigue, marine ageing, delamination

Abstract: The current document presents the long term seawater ageing effect on the fatigue properties of carbon fibre reinforced epoxy marine propeller blades. Seawater uptake in the resin and the composite was identified to correspond to a Fickian diffusion. Calculations of the mass to saturation of the composite based on that of the resin reveal the presence of water in the composite's porosities. Accelerated ageing of the pure resin highlighted three ageing phenomena: oxidation, plasticization and physical ageing. The last two were mechanically characterised separately and coupled with one another. Above all, it was shown that the presence of seawater accelerated the physical ageing kinetics by reducing the relaxation time. The composite was studied under different quasistatic and cyclic loadings.

Few effects of seawater have been found for tensile stresses on fibre oriented loadings. This was not the case for transversely loaded composite that showed a non-negligible decrease of the mechanical properties for both static and fatigue loadings. This was also the case for flexure loading which was studied under four-point flexure. This latter test method was particularly studied due to the particular induced damage. The composite was studied under two delamination loadings: crack opening and in-plane shear. It was observed that seawater decreased the critical strain energy release rates for both load cases as well of the fatigue resistance of both crack modes. Finally, the effect of physical ageing on the composite was studied and found to be non-negligible, demonstrating the necessity of taking it into account for both ageing and mechanical design.